

## **Acknowledgement**

I would to express my sincere gratitude to Prof. A. B. Seddon and Prof. T. M. Benson for their excellent supervision, consistent guiding, advice and encouragement throughout the study. They always advise me how to drive the project forward. Under their supervision, my project went progressively. Also, they sought every opportunity to enhance my experience and spread my insight. They taught me not just in science but also professional skills which are priceless and transferable to my future career.

I would also express my sincere gratitude to Dr. David Furniss for his excellent tutoring in experimental work, and his utmost patience in guiding and explanation. His wealth of experience in the laboratory helped me tackle the problems faced on numerous occasions. Also, my horizon has been broadened from his creative manner and inventive enthusiasm.

I would also thank all of my colleagues for their support during the research. The period of collaboration when we encouraged each other to tackle and conquer the challenges in scientific problem is memorable.

Last, but not the least, I appreciate my parents for their support on emotion, education and finance all the time. Their expectation is the endless resource of strength for me to tackle the obstacle to try to achieve the MPhil degree. Also, I thank my girlfriend for her understanding and waiting for me to allow me to pursue my research dream in a foreign country.

## **Abstract**

Chalcogenide glasses offer transmission windows within the far-visible, near- and mid-infrared (IR) range. They exhibit potentially excellent linear and large nonlinear optical properties, photosensitivity and their low phonon energies are conducive to efficient dopant rare earth transitions. These properties enable many potential infrared applications: large-scale optics; fibreoptics; integrated optics; optical imaging; optical data storage and all-optical switching. Two lines of experimental work were followed in this project based on chalcogenide glasses, as below:

(1) Antimony was used to replace arsenic, to form the ternary Ge-Sb-Se glass system. Nine compositions of Ge-Sb-Se glasses were synthesised and characterised to reveal their glass forming abilities, thermal properties and optical properties. Glass pairs, with close thermal properties and relatively high refractive index contrast, were developed for fabricating core-clad. structure step index fibre and microstructured optical fibres (MOFs).

(2) Fabrication of an all-solid chalcogenide glass microstructured fibre (MOF), which was designed as a mimic of the holey suspended structure silica MOF, was carried out. A cane-drawing technique and a real-time contactless diameter monitor of the chalcogenide canes were developed to improve the precision of the fabrication. Stacking equipment was designed to improve the technique of the chalcogenide preform stacking.

# Content

<b>Glossary of Symbols and Abbreviations</b> .....	4
<b>Chapter 1 Introduction</b> .....	6
<b>1.1 Motivation of the research</b> .....	6
<b>1.2 Objectives</b> .....	7
<b>1.3 Layout of the thesis</b> .....	7
<b>Chapter 2 Literature Review</b> .....	10
<b>2.1 Chalcogenide glasses</b> .....	10
<b>2.1.1 Glass science and technology</b> .....	10
<b>2.1.2 Properties of chalcogenide glasses</b> .....	14
2.1.2.1 Glass structure and thermal properties .....	14
2.1.2.2 Optical transparency and loss.....	16
2.1.2.3 Refractive index.....	18
2.1.2.4 Nonlinear optical properties.....	20
<b>2.2 Ge-Sb-Se glass system</b> .....	22
<b>2.3 Background of MOF</b> .....	26
<b>2.3.1 Microstructured Optical Fibres (MOF) in silica glass, comparison between conventional structure and MOF</b> .....	26
<b>2.3.2 Light guiding in a PCF</b> .....	29
<b>2.3.3 Design parameters required for different applications</b> .....	31
<b>2.3.4 Propagation mode of MOF</b> .....	34
2.3.4.1 Endlessly single mode.....	34
2.3.4.2 Large mode area.....	35
2.3.4.3 High nonlinear with highly confined mode area.....	36
<b>2.4 Supercontinuum (SC) mechanism and the benefit of SC with MOF</b> .....	38
<b>2.4.1 Nonlinear phenomena in SC mechanism</b> .....	40
<b>2.4.2 Summary of SC mechanisms in specific experimental conditions</b> .....	43
2.4.2.1 Pumped in normal and abnormal dispersion area .....	44
2.4.2.2 SC of different pulse duration .....	45
<b>2.5 Novel glass for SC generation</b> .....	50
<b>2.6 Advances in the fabrication of novel glass microstructured optical fibres (MOFs)</b> ..	53
<b>2.6.1 Preform fabrication</b> .....	53
<b>2.6.2 Fibre drawing</b> .....	56
<b>2.7 Summary</b> .....	57
<b>Chapter 3 Experimental</b> .....	59
<b>3.1 Chalcogenide glass preparation</b> .....	59
<b>3.1.1 Ampoule preparation</b> .....	59
<b>3.1.2 Purification of batch elements.</b> .....	62
<b>3.1.3 Batching.</b> .....	65
<b>3.1.4 Operation of the vacuum system to seal the batch inside the silica glass ampoule under vacuum.</b> .....	66
<b>3.1.5 Operation of sealing the ampoule.</b> .....	68
<b>3.1.6 Glass melting, quenching, and annealing.</b> .....	69

3.1.7 Annealing furnace temperature profile.....	71
3.1.8 Sample preparation: cutting, grinding and polishing.....	75
3.2 Glass characterisation .....	76
3.2.1 X-ray diffraction (XRD).....	76
3.2.2 Differential thermal analysis (DTA).....	77
3.2.3 Thermomechanical analysis (TMA).....	80
3.2.3.1 Viscosity / temperature relationship.....	80
3.2.3.2 Thermal expansion coefficient ( $\alpha$ ).....	84
3.2.4 Optical microscopy.....	86
3.2.5 Environmental scanning electron microscope (ESEM) with energy dispersive X-ray spectroscopy (EDX).....	87
3.2.6 Fourier transform infrared spectrometry (FTIR).....	90
3.2.7 Refractive index .....	92
3.3 Preparation of chalcogenide glass preforms.....	95
3.3.1 Glass preparation prior to shaping.....	95
3.3.2 Extrusion of unstructured and core-clad chalcogenide glass rods.....	95
3.3.3 Cane-drawing.....	98
3.3.4 Rotational casting of chalcogenide glass tubes.....	99
3.3.5 Chalcogenide glass preform assembly and fibre drawing.....	102
3.3.5.1 Assembly of MOF preforms .....	102
3.3.5.2 MOF (microstructured optical fibre) drawing.....	103
3.4 Conclusions.....	105
<b>Chapter 4 Thermal and optical characterisation of a glass pair in the Ge-Sb-Se chalcogenide glass family .....</b>	<b>106</b>
4.1 Background and motivation.....	106
4.2 Glass synthesising.....	113
4.3 Re-melting of glasses to obtain correctly sized samples for TMA measurement of viscosity / temperature behaviour .....	118
4.4 Results of glass characterisation .....	119
4.4.1 DTA .....	119
4.4.2 X-ray diffraction .....	123
4.4.3 Field emission gun environmental scanning electron microscope-energy dispersive X-ray analysis (FEG-ESEM-EDS) .....	127
4.4.4 Thermal properties: viscosity / temperature relations.....	130
4.4.5 Thermal properties: thermal expansion coefficient .....	132
4.4.6 Optical properties: Fourier transform infrared spectroscopy .....	136
4.4.7 Optical properties: refractive indices at 1.463 $\mu\text{m}$ wavelength.....	138
4.5 Development of a glass pair with matched thermal properties and disparate refractive indices.....	140
4.5.1 Glass $T_g$ stability and properties in comparison with the previous literature.....	141
4.5.2 In view of the average coordination number.....	147
4.5.3 Adjusting the optical properties.....	149
4.6 Selecting a chalcogenide Ge-Sb-Se glass pair with matched thermal properties and disparate refractive indices .....	150

4.7 Conclusions.....	153
<b>Chapter 5 Improvement on the fabrication of chalcogenide microstructured optical fibres (MOFs) and MOFs fabrication .....</b>	<b>155</b>
5.1 Research on the fabrication of rotationally casted tube .....	155
5.1.1 Straightforward rotational casting of tube ID $\geq 4.5$ mm.....	156
5.1.2 Rotational casting of tube ID $< 4.5$ mm .....	157
5.1.3 ‘Two chamber silica glass ampoule’ method for tube ID $< 4.5$ mm.....	159
5.1.4 Suggested additional method for tube making by casting.....	160
5.2 Fabrication and characterisation of all-solid MOF005 .....	162
5.2.1 Fabrication of all-solid MOF005. ....	163
5.2.1.1 Glass pair of $As_{40}Se_{60}$ and $Ge_{10}As_{23.4}Se_{66.6}$ .....	163
5.2.1.2 Preparation of preform for MOF005.....	164
5.2.1.3 Fibre drawing for MOF005.....	169
5.2.2 Characterisation of all-solid MOF005.....	170
5.2.2.1 Optical microscopy. ....	171
5.2.2.2 SEM. ....	172
5.2.3 Summary regarding MOF005.....	173
5.3 Improvement in fabrication of MOF preforms. ....	174
5.3.1 Diameter monitor for cane drawing and cane-drawer system for cane $> 0.5$ mm diameter and $< 3.00$ mm diameter. ....	174
5.3.1.1 Explanation of system solution .....	174
5.3.1.2 Development of LabView software solution.....	178
5.3.2 Stacking mechanism design for assembly of the microstructure. ....	180
5.4 Fabrication and characterisation of all-solid MOF006. ....	183
5.4.1 Fabrication of all-solid MOF006. ....	183
5.4.1.1 Preparation of preform for MOF006.....	183
5.4.1.2 Fibre drawing for MOF006.....	191
5.4.2 Characterisation of all-solid MOF006.....	191
5.4.2.1 Reflection optical microscopy.....	191
5.4.2.2 SEM characterisation. ....	193
5.4.2.3 Light guiding characterisation of MOF006.....	195
5.6 Conclusion. ....	197
<b>Chapter 6 Conclusion and Future Work.....</b>	<b>198</b>
6.1 Properties of Ge-Sb-Se glass and fibre fabrication .....	198
6.2 The technique of MOF fabrication and the solution for application.....	199
<b>References: .....</b>	<b>201</b>
<b>Appendix I .....</b>	<b>215</b>
<b>Appendix II .....</b>	<b>217</b>

## Glossary of Symbols and Abbreviations

### Chemicals

Al	Aluminium
As	Arsenic
Ge	Germanium
H	Hydrogen
O	Oxygen
S	Sulfur
Sb	Antimony
Se	Selenium
Si	Silicon
Te	Tellurium

### Techniques

BSE	Back scattering electron
DTA	Differential thermal analysis
EDX	Energy Dispersive X-Ray Analysis
ESEM	Environmental scanning electron microscopy
FTIR	Fourier transform infrared spectroscopy
SEI	Secondary electron imaging
TEM	Transmission electron microscopy
TMA	Thermomechanical analysis
XRD	X-ray diffractometry

## Properties and Miscellaneous

c	Velocity of light in a vacuum
d	Inter-planar spacing
D	Dispersion
h	Planck's constant
HF	Hydrofluoric acid
I	Intensity of light
ID	Internal diameter
IR	Infrared
K	Force constant
$k_o$	Wavenumber in vacuum
MOF	Microstructured optical fibre
n	Refractive index
$n_{eff}$	Effective-refractive-index
OD	Outer diameter
PCF	Photonic crystal fibre
$\langle r \rangle$	Average coordination number
SEM	Scanning electron microscopy
SCG	Supercontinuum generation
t	Time
$T_c$	Crystallisation temperature
$T_m$	Fictive temperature
$T_g$	Glass transition temperature
$T_l$	Liquidus temperature
V	Volume
$V_{feed-out}$	Drum take-up speed
$V_{feed-in}$	Preform feed-in speed
ZDW	Zero dispersion wavelength
$\alpha$	Thermal expansion coefficient
$\beta$	Modal propagation constant
$\delta$	Minimum deviation angle
$\epsilon_o$	Free space permittivity
$\eta$	Viscosity / poise
$\lambda$	Wavelength
$\chi$	Susceptibility of a medium
$\omega$	Angular velocity

# Chapter 1 Introduction

## 1.1 Motivation of the research

Light at near- and mid-infrared wavelengths has many potential applications, e.g, optical imaging, fast communication and power delivery. The aim of this project is to explore chalcogenide glass pairs suitable for fabricating into chalcogenide microstructured optical fibres for guiding light in the near- and far-infrared wavelength range. Chalcogenide glasses, contain one or more of the chalcogen elements S, Se or Te [1.1], and are inorganic glasses. Chalcogenide glasses are considered as good candidate materials for optical applications because of their wide transparency in near- and mid-infrared region, high refractive indices, high optical nonlinearity and photosensitivity.

Ge-Sb-Se glasses system were first explored in 1966 [1.2] as a good candidate for applications in the near- and mid-infrared regions. In the present project, the Ge-Sb-Se glasses system was studied, and pairs in this glass system were investigated in order potentially to make use of these glasses in fibre fabrication.

Our previous studies reported one route of fabrication of microstructured chalcogenide optical fibres [1.3]. Microstructured optical fibres were invented by Russell [1.4]. The development of Microstructured Optical Fibre (MOFs) in silica glass usually utilises a large refractive index difference fibre drawn from preform based on periodically arranged hollow glass canes to form the cladding. An attempt to fabricate an all-solid suspended-core structure MOF based on chalcogenide glasses was also made in this project.

## **1.2 Objectives**

Successfully fabrication of an all-solid chalcogenide MOF requires the two glass compositions to have similar glass transition temperatures ( $T_g$ ), thermal expansion coefficients and a viscosity / temperature match. The difficulty was to choose two glass compositions which fulfilled the above requirements while being robust glass formers.

In order to produce all-solid chalcogenide glass Microstructured Optical Fibre (MOF) with a small core, a rotational casting method was developed to fabricate  $As_{40}Se_{60}$  (at%) tubes with a wall thickness ranging from 1 mm to 3 mm. The chalcogenide glass cane-drawing procedure using a contactless, real-time cane diameter monitor was developed to achieve a more precise control of the diameter of the chalcogenide canes, which ranged from 0.5 mm to 2 mm. The canes were then stacked as a preform and drawn to MOF. The difficulties were to achieve accuracy and precision of the cane's diameter in the order of microns and maintain the desired MOF preform structure during fibre-drawing. This was both essential to realise the desired light guiding behaviour.

## **1.3 Layout of the thesis**

In chapter 2, the glass science and technology, especially the properties of chalcogenide glasses will be introduced. Literature about the development of Microstructured Optical Fibre (MOF) is discussed, including the materials that have

been used and the fabrication methods. The principle of supercontinuum generation in silica MOF and its application are also summarised.

In chapter 3, the experimental techniques applied in this Project are described, thus: 1) the procedure of chalcogenide glass melting, quenching, annealing and polishing; 2) the schedule and the purpose of chemical precursor purification; 3) the methods for glass characterisation, i.e. Differential Thermal Analysis (DTA) for examining the glass  $T_g$ , X-ray Diffraction (XRD) for checking the amorphicity of glass, Thermomechanical Analysis (TMA) for measuring the thermal expansion coefficient ( $\alpha$ ) of the glass and viscosity / temperature relation of the supercooled glass melt, Environment Scanning Electron Microscopy (ESEM) for viewing and imaging the sample at the micro-scale and the Fourier Transform Infrared Spectroscopy (FTIR) for finding the transparent window of certain chalcogenide glasses; 4) the methodology and the experimental setup for the fabrication of Microstructured Optical Fibres (MOFs), this requires the four steps which were: rotational casting of chalcogenide glass tubes, extrusion of chalcogenide glass fibreoptic preforms, cane-drawing of chalcogenide glass canes and chalcogenide glass optical fibre drawing.

In chapter 4, nine glass compositions in the Ge-Sb-Se glass system are reported in the aspects of their glass forming ability, thermal properties and optical properties. Glass pairs were developed for fabricating chalcogenide microstructured optical fibre and core-clad. step index fibre.

In chapter 5, the attempted fabrication of a suspended structure all-solid chalcogenide Microstructured Optical Fibres (MOFs) will be described. Based on the procedure and techniques used in the previous work [1.5], improvement was made in cane-drawing equipment, a real-time cane-diameter-monitoring system and MOF preform stacking equipment was developed. Then subsequently fibre drawing of the suspended all-solid chalcogenide MOF preform was carried out to produce a MOF.

Chapter 6 is a summary of the key conclusions reached throughout the Project and contains suggestions for future work.

## **Chapter 2 Literature Review**

In the chapter 2, a literature review of the chalcogenide glasses (section 2.1) and a more detailed discussion of the Ge-Sb-Se glass system (section 2.2) are presented. This is followed by a review of the principles of microstructured optical fibre (section 2.3) and the mechanism of supercontinuum generation based on microstructured optical fibre is described (section 2.4). The application of chalcogenide optical glasses for supercontinuum generation is discussed in section 2.5. Finally, the fabrication techniques of chalcogenide microstructured optical fibres are reviewed in section 2.6.

### **2.1 Chalcogenide glasses**

In this section, the principle of glass formation is discussed in section 2.1.1. In section 2.1.2, the properties of chalcogenide glasses are introduced in the aspect of thermal properties, optical transparency, (from visible to infrared and beyond dependant on composition), as low-phonon-energy-materials, photosensitivity to visible light and shorter intrinsic nonlinear response time together with highly nonlinear optical behaviour.

#### **2.1.1 Glass science and technology**

The definition of glass described by the Committee of the U.S. National Research Council in 1976 is quoted as: ‘Glass is an X-ray amorphous material which exhibits the glass transition, this being defined as that phenomenon in which a solid amorphous phase exhibits with changing temperature a more or less sudden change in the

derivative thermodynamic properties, such as heat capacity and expansion coefficient, from crystal-like to liquid-like values' [2.1]. In terms of the structure, glass is also defined as 'an amorphous solid completely lacking in long range, periodic atomic structure' [2.2].

The glass formation scheme for chalcogenide glasses has been investigated extensively in the literature. There are two critical properties for shaping, which are the viscosity / temperature relation and the thermal expansion coefficient. Also it is important to understand the glass stability, and glass forming behaviour and accordingly to choose a temperature scheme for glass processing to avoid crystallisation.

The process of glass formation is presented schematically in figure 2.1. The relation of enthalpy versus temperature is shown for different glass formation processes.

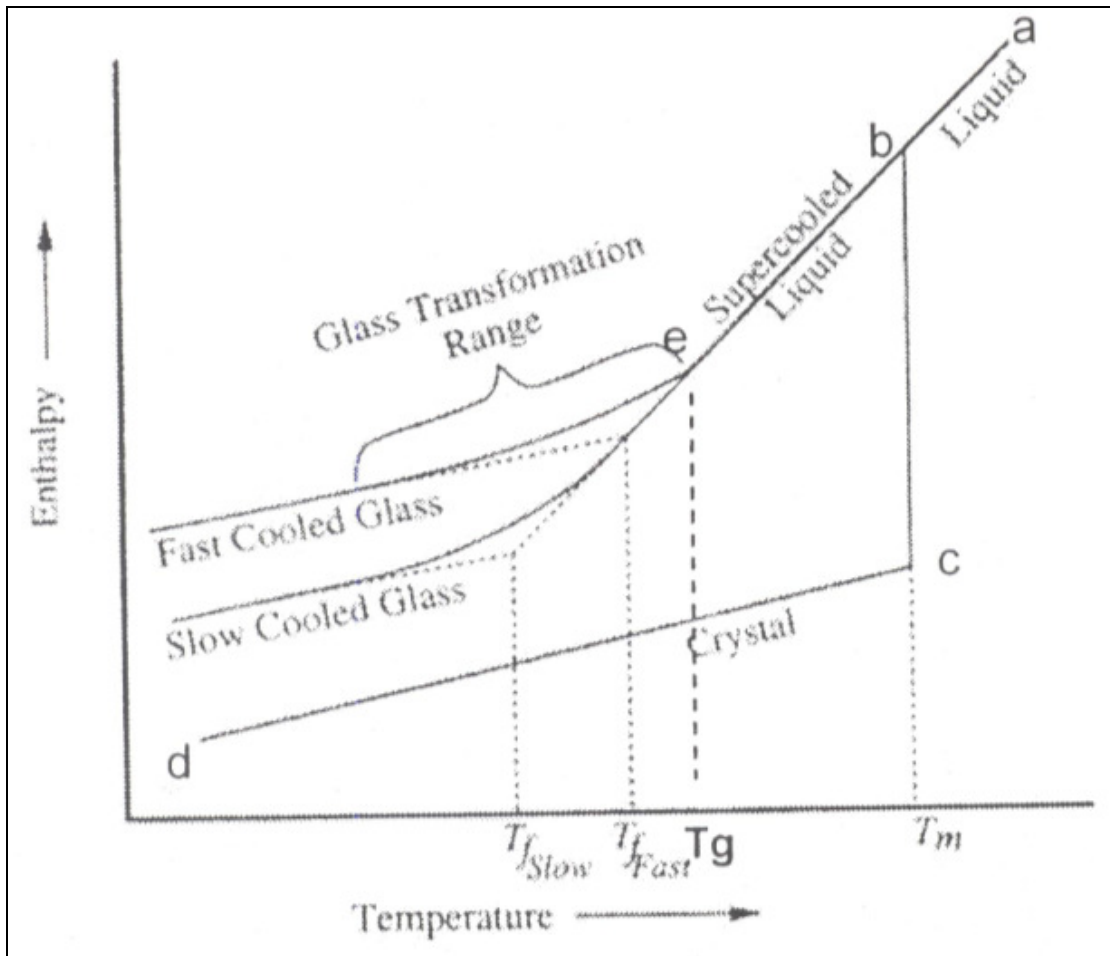


Figure 2.1 Glass formation process diagram [2.1].

The glass formation process by melt-quenching depicted in figure 2.1 can be divided into stages by several temperature points as below:

liquidus temperature ( $T_l$ ): the lowest temperature at normal pressure at which (section ab of the line in figure 2.1) every constituent of the system is in the liquid state is defined as the liquidus (extrapolation of line bc to temperature axis in figure 2.1).

The cooling rate should be large enough to ensure there is not enough time for crystallisation to occur. The viscosity of the super-cooled liquid increases as

temperature decreases until at  $T_g$  its viscosity becomes so high that no more changes occur. Glass transition range ( $T_g$ ):  $T_g$  is a temperature range within which the rate of change of enthalpy for volume per unit mass of the supercooled melt deviates from the quasi equilibrium cooling curve. The numerical value of  $T_g$  is to some extent dependent on the cooling rate utilised and the method of measurement. It can be viewed in figure 2.1 that the glass transition temperatures  $T_{fFast}$  and  $T_{fSlow}$  corresponded to a fast cooled glass and a slow cooled glass, respectively. The targeted glass is attained after cooling below the glass transition range, to ambient temperature.

Fictive temperature:  $T_m$  is the extrapolated cross-point of the equilibrium cooling curve and the glass curve in figure 2.1, above which the melt is in the supercooled-liquid phase. The supercooled liquid can be considered to be cooled immediately and with increasing the viscosity such that the molecular motion is hindered in order to produce a glass.

The viscosities of the above points have been designated as reference points for glass forming melts (Table 2.1).

Table 2.1 Viscosity reference for glass melting [2.2].

Name of reference temperature	Viscosity / Pas
Practical melting temperature	~1-10
Working point	$10^3$
Littleton softening point	$10^{6.6}$
Dilatometric softening temperature	$10^8$ - $10^9$
Glass transformation temperature	$\sim 10^{11.3}$
Annealing point	$10^{12}$ or $10^{12.4}$
Strain point	$10^{13.5}$

It is recognised that any material will form a glass if cooled so rapidly that insufficient time is provided to allow the nucleation and crystal growth required for crystallization; a compound or mixture that can form a glass with a moderate cooling rate is considered to be a good glass former [2.1, 2.2].

### 2.1.2 Properties of chalcogenide glasses

Chalcogenide glasses are based on the chalcogen elements S, Se, and Te, and are usually formed by the addition of other elements such as Ge, As, Sb, Ga and so on [2.3].

#### 2.1.2.1 Glass structure and thermal properties

The structure of the glass is the fundamental issue that affects the glass formability and thermal properties. As the study in [2.4], chalcogenide glasses are based on weakly

covalent bonded chains of 2-coordinated chalcogenide (group VI) atoms (e.g. Se, Te, S), with cross-linking provided by 3 or 4-coordinated group V and IV atoms (e.g. As, Sn, Ge), and the Van der Waals bonding between the atoms is even weaker.

The average coordination number ( $\langle r \rangle$ ) and R-value [2.2] are two measures to indicate the structure of the glasses. It is suggested by Phillip's constraint theory [2.1] that a covalently bonded glass is made up of under cross-linked floppy and overly constrained rigid networks. The average coordination number,  $Z$ , of glass  $A_xB_yC_z$  (where A, B and C are group IV, V and VI elements respectively) is given by [2.5]

$$Z = \frac{(4x + 3y + 2z)}{(x + y + z)} \quad (2.1)$$

There is a critical composition at which the number of constraints acting on the network is balanced by the degrees of freedom available to the atoms. This critical composition is called the rigidity percolation threshold (RPT) and corresponds to an average coordination number for the chalcogenide glasses,  $Z = 2.4$ . Glasses with  $Z < 2.4$  are under cross-linked and 'floppy', glasses with  $Z > 2.4$  are rigidly connected. The R-value is the ratio of covalent bonding possibilities of the chalcogen atoms to the covalent bonding possibilities of the non-chalcogenide atoms. It is given by [2.5]:

$$R = \frac{2z}{(4x + 3y)} \quad (2.2)$$

When  $R = 1$  the glass can become chemically ordered and contain only strong heteronuclear bonds; these are known as stoichiometric compositions.

Compared to oxide glasses, chalcogenide glasses are less robust and have relatively

lower  $T_g$  due to their higher atomic mass and hence weaker bonding strength.

#### 2.1.2.2 Optical transparency and loss

The optical loss of the chalcogenide glasses consists of intrinsic loss and extrinsic loss. The former is inherent to the material; it is unavoidable. The latter is due to the absorption and scattering of impurity and contamination which could be removed by improving the glass synthesis and fabrication techniques. These optical loss properties act together to determine the transparency of a glass.

Because of the weaker bonding strength, chalcogenide glasses are low-phonon-energy materials compared to oxide glasses. Thus, they are the ideal host to dope with rare earth elements. Chalcogenide glasses are near and mid-infrared transparent and their transmission window, which is restricted by the optical band gap (also called electronic absorption edge) and multi-phonon edge, may be tailored by changing the composition of the glass.

A comparison of the transparency windows of different glass series is shown in figure 2.2. Note, reference [2.6] does not give any information on the individual absorption bands.

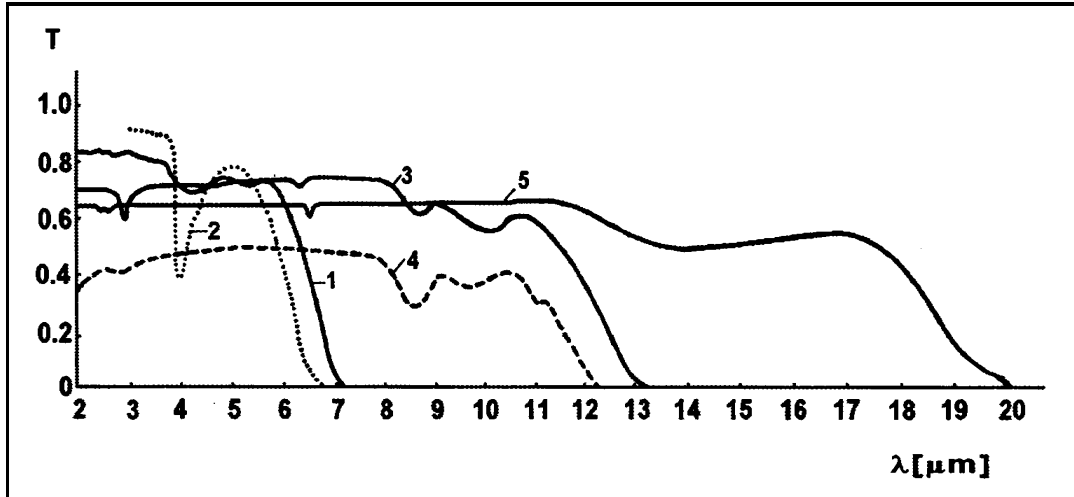


Figure 2.2 Transmission characteristics of various glasses: 1, PbO-GeO<sub>2</sub> glass; 2, CaO-Al<sub>3</sub>O<sub>3</sub>-SiO<sub>2</sub> glass; 3, As<sub>2</sub>S<sub>3</sub> glass; 4, As<sub>2.75</sub>Te<sub>0.25</sub> glass and 5, As<sub>2</sub>Se<sub>3</sub> glass [2.6].

Figure 2.2 shows that, compared to several known binary and ternary oxide-glass systems, the windows of common chalcogenides, e.g. As<sub>2</sub>Se<sub>3</sub>, inherently extend from the near-infrared (IR) to the mid-IR region covering at least 20 μm. To understand the long wavelength cut-off of glasses, equation 2.3 is given, which is explained by lattice absorptions due to the atomic network's vibrations and is known as the multiphonon edge [2.13]. The fundamental absorption frequency  $V$  in equation 2.3 can be approximately calculated for a diatomic molecule, assuming it performs simple harmonic motion, consisting of two point masses  $m_1$  and  $m_2$ ; connected by a bond (like a spring):

$$V = \frac{1}{2\pi} \left( K / M_{GMM} \right)^{\frac{1}{2}} \quad (2.3)$$

where,  $K$  is the force constant and  $M_{GMM}$  is the geometric mean mass which is given by:

$$M_{GMM} = \left( \frac{1}{m_1} + \frac{1}{m_2} \right) \quad (2.4)$$

It can be seen from equations 2.3 and 2.4 that the larger the atomic masses and the weaker the bonding, the lower the frequency (longer wavelength) of the fundamental absorption. Thus, the long wavelength transmission limit will be extended further into the infrared region [2.13]. Hence, the differences in the transparency windows of different glass systems in figure 2.2 can be explained. A chalcogenide glass containing a large percentage of the element with a heavier relative atomic mass (RAM) than the other chalcogenide elements, such as tellurium, will tend to transmit further into the infrared than sulphide or selenide glasses.

#### 2.1.2.3 Refractive index

The refractive index of a glass at a specified wavelength is the velocity of light in the vacuum divided by its velocity in this glass. The variation of refractive index versus wavelength is termed dispersion. In a core-clad. optical fibre, light can be confined mainly to the core region by the effect of refractive index contrast between the core and cladding regions of the fibre [2.28]. The propagation of light may be controlled by adjusting the refractive index profile of the optical fibre [2.3, 2.28]. In this Project, chalcogenide glass pairs in the As-Se and Ge-As-Se glass systems, and also in the Ge-Sb-Se system, have been investigated to make microstructured optical fibre, similar to those studied in silica glass in Russell's paper [2.25], with chalcogenide optical glasses. Generally, the composition with the heavier and more polarisable atoms has higher refractive index, for instance refractive index increases as  $S < Se < Te$  in the chalcogen group. The addition of germanium can decrease the refractive

index. An experimental study has been done to determine how much variation in refractive index can be achieved by adjusting the composition.

In this project,  $\text{As}_{40}\text{Se}_{60}$  and  $\text{Ge}_{10}\text{As}_{23.4}\text{Se}_{66.6}$  were used for fabricating microstructured optical fibres (MOFs) by the author in conjunction with Dr Z.G. Lian (PhD student Faculty of Engineering, University of Nottingham 2006 - 2010).  $\text{As}_{40}\text{Se}_{60}$  is a well studied glass composition, which consists of only two components and both elemental precursors can have extra purification to form highly purified glass.  $\text{As}_{40}\text{Se}_{60}$  has a relatively high refractive index compared with Ge-containing chalcogenide compositions. It was demonstrated that  $\text{As}_{40}\text{Se}_{60}$  and Ge-containing chalcogenide glasses could be used as a pair for achieving waveguiding in the higher refractive index  $\text{As}_{40}\text{Se}_{60}$  glass [2.7]. The refractive index of  $\text{As}_{40}\text{Se}_{60}$  was measured, using the minimum deviation method by Dr. W.J. Pan and Dr. Z.G. Lian in our laboratory [2.7, 2.8], to be 2.828 at 1.3  $\mu\text{m}$  wavelength. This result compares well with that of the group of Sanghera [2.9] who reported the refractive index of  $\text{As}_{40}\text{Se}_{60}$  to be 2.81 at a wavelength of 1.55  $\mu\text{m}$ .

The investigation of a glass pair in a non-arsenic-containing glass system has also been done in this project. Some previous studies on the refractive index of non-arsenic-containing chalcogenide glasses are listed in Table 2.2.

Table 2.2 Summary of the refractive index of non-arsenic-containing chalcogenide glasses taken from the literature.

Composition	T <sub>g</sub> / °C	Refractive index (@ wavelength /μm)	Reference
Ge <sub>13</sub> Sb <sub>7</sub> Se <sub>80</sub>	151	2.64 (1.064)	[2.22]
Ge <sub>16</sub> Sb <sub>14</sub> Se <sub>70</sub>	214	2.68 (1.064)	[2.22]
Ge <sub>23</sub> Sb <sub>7</sub> Se <sub>70</sub>	246	2.62 (1.064)	[2.22]
Ga <sub>5</sub> Ge <sub>25</sub> Sb <sub>10</sub> Se <sub>60</sub>	283	2.6709 ± 0.0001(2) 2.6198 ± 0.00025(12) 2.628(10.6)	[2.16, 2.20]
Ge <sub>28</sub> Sb <sub>7</sub> Se <sub>65</sub>	287	2.59 (1.064)	[2.22]
Ge <sub>28</sub> Sb <sub>12</sub> Se <sub>60</sub>	277	2.62 (5) 2.6163 (3)	[2.12, 2.13]
Ga <sub>2</sub> Ge <sub>30</sub> Sb <sub>8</sub> Se <sub>60</sub>	290	2.615 (1.5) 2.61(1.6)	[2.21]
Ga <sub>2</sub> Ge <sub>30</sub> Sb <sub>8</sub> Se <sub>55</sub> (CsI) <sub>5</sub>	294	2.587 (1.5) 2.58(1.6)	[2.21]
Ge <sub>35</sub> Sb <sub>7</sub> Se <sub>58</sub>	299	2.58 (1.064)	[2.22]

#### 2.1.2.4 Nonlinear optical properties

Linear optical properties of glasses are important when explaining reflection, refraction, dispersion and scattering, whereas nonlinear optical properties are important for explaining wavelength conversion of light and all-optical switching of light. The optical power polarisation vector  $P$  is assumed to be proportional to the optical field strength  $E$  of the instant optical wave:

$$P = \epsilon_0 \chi E \quad (2.5)$$

where  $\epsilon_0$  is the free space permittivity and  $\chi$  is the susceptibility of a medium [2.10].

However, for an intense optical light beam, the linear term in this equation should be replaced by a power series:

$$P = \epsilon_0 [\chi^{(1)} E + \chi^{(2)} EE + \chi^{(3)} EEE + \dots] \quad (2.6)$$

where,  $\chi^{(1)}$ ,  $\chi^{(2)}$  and  $\chi^{(3)}$  are the first order (linear), second order (nonlinear) and third order (nonlinear) susceptibilities [2.10]. Nonlinear optical power terms that appear in propagation can be predicted by substituting (2.6) into Maxwell's equations [2.28].

Chalcogenide glasses exhibit highly nonlinear optical properties compared to silicate glasses because of consisting of heavy, polarisable elements [2.80], so they may benefit applications requiring compact device dimensions and highly nonlinear optical properties.

However, there are also some drawbacks of the chalcogenide glasses, which limit the applications of this glass system and provide barriers to fabrication using this glass system. It is well known that chalcogenide glasses tend to exhibit weak chemical bonding. This leads to several drawbacks of the chalcogenide glasses which should be taken into account [2.1 to 2.4, 2.14, 2.17 to 2.20]: (1) they exhibit lower  $T_g$  and steeper viscosity / temperature curves than silica glass and so it is hard to maintain the glass structure and shape during fabrication; (2) they contain toxic elements calling for safety measures; (3) they are prone to surface corrosion by oxidation and hydrolysis and (4) they are not widely transparent in the visible wavelength range (350nm-750nm approximately). So, a lot of research should be done to overcome these drawbacks and balance the tricky fabrication schemes against the required optical quality of the glasses.

## 2.2 Ge-Sb-Se glass system

In this section, a brief literature review is presented on the Ge-Sb-Se glass system, which can avoid the toxic element As in the glass forming system for safety considerations. The purpose is to predict a glass pair in the Ge-Sb-Se system instead of the glass pair of  $\text{Ge}_{10}\text{As}_{23.3}\text{Se}_{66.6}/\text{As}_{40}\text{Se}_{60}$ , which was applied in the published in-house-prepared MOF [2.11] from this work. The potential candidate glass pair should have a relatively large refractive index ( $n$ ) contrast, similar glass transition temperature ( $T_g$ ) and viscosity at the glass shaping temperature and similar thermal expansion coefficient, which will enable the expected light guiding property and a stable fibre shaping procedure. Moreover, a small contrast of thermal expansion coefficient is helpful considering the strength of the fibre. In order to achieve a strong fibre, the central part is expected to expand more than the cladding when heated to the softening temperature and shrink more than the clad. (clad. is the stand shorthand for cladding.) to cause residual compression in the surface layers when the fibre is cooled below the glass transition region. So, it is desirable that the material in the core region (higher  $n$  for a core-clad fibre and can be lower  $n$  for a MOF preform) has a slightly higher thermal expansion coefficient than the surrounding layer material (lower  $n$  for a core-clad fibre and higher  $n$  for a MOF preform).

The Ge-Sb-Se glass system has been investigated since the 1960s [2.12, 2.13] when a series of As based chalcogenide glass systems was also proposed. The As based glass

system exhibits good glass formability and good transparency, especially from 2 $\mu\text{m}$  to 10  $\mu\text{m}$  wavelength [2.14]. However, the Ge-Sb-Se glass forming system takes its advantage from a relatively lower vapour pressure compared to the Ge-As-Se system [2.16], and better transmission between 10 $\mu\text{m}$  ~ 14 $\mu\text{m}$  because the Sb helps to shift the multiphonon edge to longer wavelengths. So the Sb-rich glass system is of benefit for applications at 10.6 $\mu\text{m}$ , such as CO<sub>2</sub> laser power transmitting glass fibre [2.15]. With the addition of a few atomic % Ga, the Ge-Sb-Se glass system can be explored as a host glass for rare earth doping [2.16]. Also, some research has been done to introduce alkaline halide additions into these glasses system to enable them to become transparent in the visible region, while maintaining good transparency to ~ 14 $\mu\text{m}$  [2.17].

The glass forming ability of the Ge-Sb-Se system has also been researched on both experimental and theoretical sides. Based on the previous literature [2.18 - 2.20], a variety of compositions with their glass transformation temperatures is listed in Table A.(i) of Appendix I (to thesis).

It is known from the literature [2.21] that for the Ge-Sb-Se ternary system, the thermal expansion coefficient, molar volume and heat capacity of glasses and liquids depend on the average coordination number and it is thought that the glass forming liquid at  $\langle r \rangle = 2.4$  has minimised configurational changes, a characteristic which extends to the supercooled liquid region so as to minimise the tendency for crystallisation [2.12,

2.13].

The glass forming region diagram (figure 2.3) has been given in the literature [2.12, 2.13], in which the glass transition temperature  $T_g$  is plotted. Along the plotted  $T_g$  line in the glassy region, it would be possible to select two candidates of composition as being suitable candidates on which to carry out a series of glass characterisation to find their thermal properties, mechanical properties and optical properties for potential use in MOF design and fabrication. Many reported Ge-Sb-Se compositions from the literature have been tabulated with regards to their thermal optical properties in Table A.(i) in Appendix 1. The conclusion can be obtained that the refractive index is monotonically decreasing when the concentration of Ge increases and Sb performs the reverse of Ge. So, it seemed possible to find a glass pair with large refractive index contrast and similar thermal properties on the isotherm of 220°C.

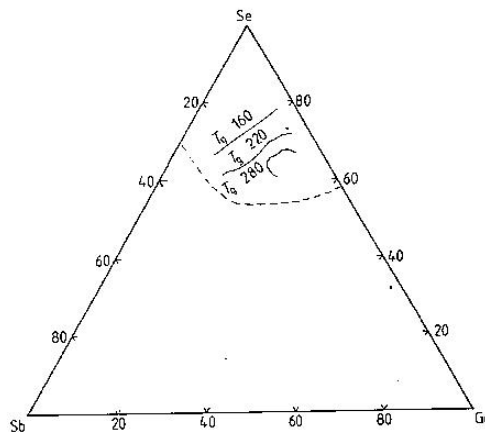


Figure 2.3 An early report (1975) of the glass forming region versus atomic % for Ge-Sb-Se glasses system illustrating the range of glass transition temperature  $T_g$  as isotherms [2.12, 2.13].

The research in [2.12] was referred to in the later investigation of [2.18], in which the

desired glasses with Sb contents  $\geq 5\%$  and Ge contents  $\geq 10\%$  and a  $T_g \geq 150^\circ\text{C}$  were within the glass forming area. From figure 2.3, the compositions located near the dashed edge, which, as reported in [2.12 and 2.13], is the boundary of the glass forming region shown in figure 2.3, tend to become partially crystalline during synthesising [2.12].

In order to synthesise a glass that resists the tendency to crystallise and with high purity, a suitable material purification treatment and glass melting schedule are critical. In the literature of [2.16 - 2.18], the experimental results of research on the purification on glass and a glass forming scheme are presented. The vapour pressure of antimony and its oxide are compared to that of selenium and its relevant oxide in Table 2.3. It is difficult to purify elemental antimony due to the very small vapour pressure contrast between antimony and its oxide close to the melting point, as shown in Table 2.3. So, generally, the technique of distillation of the compound is applied to the glass system; however it is commented in [2.18] that a physical purification technique is viable if special care is taken.

Table 2.3 Vapour pressure of Se, Sb and their oxides [2.18].

Temperature (°C)	Vapour pressure (mm Hg)			
	Se	SeO <sub>3</sub>	Sb	Sb <sub>2</sub> O <sub>3</sub>
200	0.004	1.89	-	-
275	0.096	74.0	-	-
300	0.24	200.07	-	-
550	-	-	0.01	0.41
600	-	-	0.06	1.94
630	-	-	0.16	4.50

In summary, from the literature it appears possible to find a glass pair with relatively large refractive index contrast and similar thermal properties in the Ge-Sb-Se glass system. It will offer a more safe material for the research and application into chalcogenide glasses based optical components than that of arsenic-based material.

## 2.3 Background of MOF

### 2.3.1 Microstructured Optical Fibres (MOF) in silica glass, comparison between conventional structure and MOF

Microstructured optical fibres (MOF), have compact and designable properties, to enable a broad diversity of potential applications and have so attracted extensive attention worldwide [2.24]. Photonic Crystal Fibre (PCF), which can be addressed by MOF, enables the key advantage of controlling the properties of dispersion, nonlinear optics, and birefringence, which benefit applications such as lasing systems, amplifiers,

dispersion compensating engineering and nonlinear-optics.

The conventional step index, core-clad fibre has two shortcomings, which restrict its widely used in many applications. The first is the small refractive index difference between the core and cladding glasses certainly for silica glass, which limits the capacity of manipulating the group velocity dispersion (GVD) and birefringence [2.28]. Secondly, because the conventional core-clad. fibre guide light is based on total internal reflection (TIR), thus, the guiding light has to go all the way through the solid medium in which attenuation cannot be avoided due to intrinsic absorption and e.g. Rayleigh scattering introduced from the solid medium of the core area [2.23].

Due to the mechanism of guiding in the fibre, PCFs can be divided as total internal reflection (TIR) PCF and photonic band gap (PBG) PCF [2.24]. A PCF based on TIR is similar to the step index core-clad fibre. The central capillary in an air-hole lattice is replaced by a defect to form the core, in which the refractive index is larger than the cladding area. The cladding area for silica fibres has usually comprised of a lattice of air capillaries. Such PCFs, known as modified TIR, have many different properties with respect to conventional optical fibres. The flexible design geometry can offer larger refractive index variations than conventional fibre, so the light is confined more tightly in the core. The first solid core “holey” PCF, based on TIR, was reported in 1995 by Russell and his colleagues [2.25], and it just transmitted the fundamental mode with low intrinsic losses, because of no doping elements were present in the core.

Ten times the large mode area was achieved compared with that of the standard single-mode fibre (SMF), consequently guaranteeing a considerable increase in input power level, because the power density (for same power in) is decreased with larger mode area.

A PCF based on a PBG is formed by a negative refractive index variation between core and clad. Usually an air capillary is inserted into the centre to realise the defect. Light guidance within a photonic band gap is an analogue of the mechanism known as the electron conduction within an energy-band structure. If the two dimensional lattice structure can be designed properly, light with a wavelength similar to the lattice constant, which is the distance between adjacent holes in the lattice, could be blocked in the lattice area. In 1999, a demonstration of light guiding, which was based on PBG and in an air defect, showed that a few central capillaries were removed from a hexagonal lattice leaving a large hole filled with air [2.26]. It showed that the PBG mechanism was robust and light confined well in the fibre even if tight bends were formed. Moreover, the ideal hollow air core can avoid intrinsic material attenuation.

The refractive index of the core and cladding of a conventional step index fibre is less wavelength dependent than the effective refractive index of the MOF cladding. The reason is that in the MOF, for short wavelengths relative to the pitch, the field can resolve the individual air holes and mainly exist in the high index regions, which causes the effective index of the cladding region to approach that of the pure cladding

material. In contrast, for relatively long wavelengths, the effective index will approach the average of the glass index and air, weighted with the air filling fraction [2.27].

The research of MOF, can thus be usefully classified into two types, solid-core MOF and hollow-core MOF.

### 2.3.2 Light guiding in a PCF

The propagation constant is a useful property that describes the guided mode in the fibre [2.10].  $\beta$  is the component of the propagation constant along the fibre axis, whose highest value:  $\beta = nk_0$  can be achieved in homogeneous media with refractive index  $n$ .  $k_0$  represents the free-space propagation constant. In the mechanism of TIR, the light can be confined in the core material propagating with an angle  $\theta$  to the axis when  $\beta < nk_0$ , where  $\beta = k_0 n \cos \theta$  [figure 2.4 (a)]. The light is evanescent if  $\beta > nk_0$ , where  $\beta$  is now imaginary. Two regimes of PBG can be defined. In figure 2.4(b), the light propagates in the centre high index layer and the assembly of a number of TIR waveguides opens up the band gap by resonant tuning which lets the leakage through adjacent high index layers. Among these high index layers, one smaller layer with a mode in the band gap, which is not resonant and frustrates the light leakage by tuning, thus, the mode is guided by PBG named frustrated tunneling. Another kind of PBG is the Bragg form of BPG, in which  $\beta < k_0 n_2$  and so the light is guided in all layers. A band gap occurs as a result of interference and multi-scattering, as shown in figure 2.4(c). Three different ways of guiding are explored with the one or

two dimensional waveguide geometry in figure 2.4.

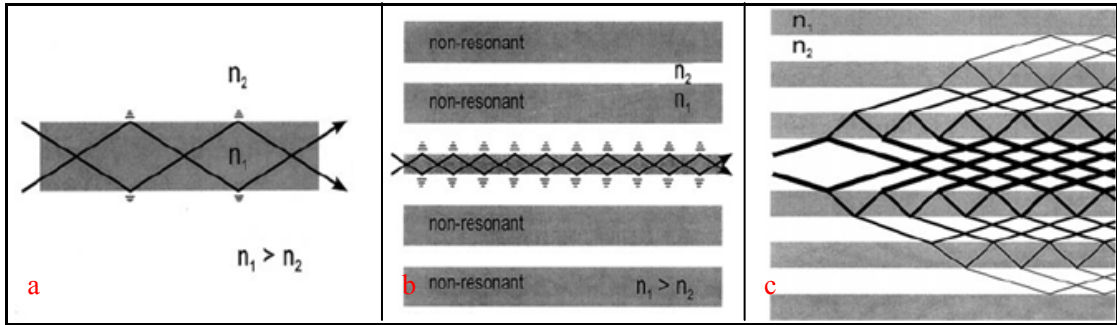


Figure 2.4 Propagation in optical fibres: (a) total internal reflection; (b) frustrated tunnelling PBG guidance; (c) Bragg BPG guidance [2.25].

The wave equation that governs the electromagnetic wave propagation in a PCF is derived from Maxwell's equation as [2.28]:

$$(\nabla^2 + k_0^2 n^2)h + \nabla(\ln n^2) \times (\nabla \times h) = \beta^2 h \quad (2.7)$$

where  $h(x, y)$  represents a transverse component of the magnetic field,  $n^2(x, y)$  is the dielectric function of the cladding structure in the transverse direction,  $ck_0$  is the angular frequency ( $\omega$ ) of the radiation and  $\beta$  is the propagation constant as introduced above. A series of numerical methods, such as plane wave expansion, the beam propagation method, multipole method and finite element method has been adapted to solve the propagation equation for practical geometries [2.29]. The aim for each case is to solve for the propagation constant, the effective mode area for each mode supported in the fibre. If the band gap achieved from hollow core PCF crosses the air line, on which the light travels with the propagation constant of vacuum ( $\beta = k_0$ ), the light could be guided along the central axis in the hollow core [2.30]. Some hollow-core PCFs based on the two types of band gap have been reported, respectively [2.29, 2.30]. The band gap of type-I, which is with a material (silica) of n

of 1.5 promising transparency across visible wavelengths, is appreciable at high air fractions of 80%. The type-II, which is for a material with  $n > 2.0$  promises transparency in the mid- and far-IR, is appreciable at a relative low air fraction of about 60%. The potential to explore the type-II band gap in this project is because it is suitable for manufacture with soft glass such as chalcogenide and tellurite glasses [2.30].

### 2.3.3 Design parameters required for different applications

PCFs are usually formed in terms of periodically arranged capillaries with a defect which is realised by removing the central unit. The effective refractive index  $n_{eff}$  (defined as  $\beta/k_0$ ) is the main parameter of a fibre. The material and geometry in fact act as two contributions affecting the  $n_{eff}$ . When the material is fixed, only the geometry can be influenced. The imaginary part of  $n_{eff}$  contains information on the loss, and the real part supplies the dispersion information, given by [2.31]:

$$L = \frac{40\pi}{\ln(10)\lambda} \text{Im}(n_{eff}) \quad (2.8)$$

and:

$$D = -\frac{\lambda}{c} \frac{\partial^2 \text{Re}(n_{eff})}{\partial \lambda^2} \quad (2.9)$$

where  $L$  is the loss in  $\text{dBm}^{-1}$  and  $D$  is the dispersion. The method to achieve the second differential term in equation (2.9) is to use a polynomial fit to the data and to differentiate, rather than to do it directly using a numerical method such as a finite difference method [2.31].

The structure parameter of a PCF are the diameter of air hole ( $d$ ) and the hole-to-hole spacing  $\Lambda$  (the distance between the cores of the holes) which is called the pitch. The ratio of  $d/\Lambda$  can be chosen over a large range, so it enables a large flexibility in design to match the different applications. The number of rings of capillaries (“holes”) around the core is another vital design parameter which can determine the confinement loss to high degree, while the effective mode area is independent of the ring number. Many researchers indicate that the two parameters of  $d/\Lambda$  and  $\lambda/\Lambda$  should affect the effective core radius [2.25, 2.31, 2.32]. Furthermore, the number of modes supported in a PCF is dependent on the  $d/\Lambda$  ratio [2.32], because the air filling fraction determines the limit of the V-parameter (see equation 2.10) which governs the guided mode. It is known that the number of guided modes is proportional to the value of V squared [2.32].

The V-parameter, also called normalised frequency, was introduced to analyse the relationship between number of guided modes and the structure. In a conventional fibre, the  $V$ -parameter depends on the core radius and the refractive index of core and cladding [2.32]. It is given by the equation [3.23]:

$$V_{\text{co-cl}} = 2\pi \frac{\Lambda}{\lambda} \sqrt{n_{\text{co}}^2(\lambda) - n_{\text{cl}}^2(\lambda)} \quad (2.10)$$

where  $V_{\text{co-cl}}$  is the V-parameter of the core-clad step index fibre.  $n_{\text{co}}(\lambda)$  and  $n_{\text{cl}}(\lambda)$  are the effective refractive index of the core and cladding regions, respectively.

$\Lambda$  is the radius of the effective core area. The conventional core-clad step index fibre

maintains single mode propagation when  $V_{\text{co-cl}} < 2.405$  [2.32]. However, as discussed above, in a PCF, there is no wavelength independent core and cladding refractive index which can be defined. It was analysed in [2.33] that the fibre will remain single-mode based on the formulation of V-parameter for a particular value of the pitch. Several formulations of the V-parameter for PCFs have been derived based on the standard step index fibre one. For example in [2.33]  $V_{\text{PCF}}$  is given as [2.32, 2.33].

$$V_{\text{PCF}} = 2\pi \frac{\Lambda}{\lambda} \sqrt{n_{\text{FM}}^2(\lambda) - n_{\text{FSM}}^2(\lambda)} \quad (2.11)$$

where  $n_{\text{FM}}(\lambda)$  is the effective refractive index of the fundamental mode depending on wavelength and  $n_{\text{FSM}}(\lambda)$  is denoted as the corresponding effective refractive index of the fundamental space filling mode of a PCF, which is defined as the mode with the largest modal index of the infinite two-dimensional photonic crystal that constitutes the PCF cladding. The effective core radius  $\rho$  is set at the value of  $\Lambda$ , which is the natural length scale of the period lattices and depends on the air-filling fraction, and so a relationship between  $\Lambda$  and the air-filling fraction dependant effective refractive index is built up. Another definition of  $V$  parameter is given by [2.34]:

$$V_{\text{PCF}} = 2\pi \frac{\rho}{\lambda} \sqrt{n_{\text{co}}^2(\lambda) - n_{\text{FSM}}^2(\lambda)} \quad (2.12)$$

where  $\rho$  is the effective core radius and  $n_{\text{co}}(\lambda)$  is the wavelength dependent effective refractive index of the fibre core. A value for  $\rho$  has been proposed by some authors in order to find the optimization of  $d/\Lambda$  with operating wavelength. The normalized cut-off frequency was achieved in each case for supplying the specification to choose the relative design parameters, which promise single mode transmission. For example, in a solid PCF with a 3 rod silica rod defect core reported in [2.35], Since the effective

refractive index of the cladding region approaches the refractive index of the pure material at short wavelengths, the refractive index contrast between core and cladding decreases with wavelength. This causes the  $V$ -parameter to approach a constant value.

PCFs can exhibit endlessly single mode propagation over an extremely large band region, power delivery with large mode, nonlinear optics with small mode area, specific dispersion engineering, and birefringence resulting in improved polarisation control, with the PCF parameters being designed with different specific requirements respectively. The following sub-section (section 2.3.4) will discuss the different specific applications [2.32].

## **2.3.4 Propagation mode of MOF**

### **2.3.4.1 Endlessly single mode**

The endlessly single mode propagation can be achieved by a proper design of the structure parameters. The limit of  $V$ -parameter can be obtained by numerical calculation when the mode index of the first higher mode exceeds the cladding region index as the function with the variable of  $d/\Lambda$ . In the study of [2.36] a choice of  $\rho = \Lambda$  was adapted, and  $V_{PCF} = \pi$  for single mode behaviour in this case, which is different from  $V \approx 2.405$  in conventional fibre [2.28]. It was quoted in [2.35] that the limit for single mode was achieved with  $d/\Lambda \approx 0.45$  in a 1 rod defect core version and  $\sim 0.25$  in a 3 rod defect core version. In the case of the 3 rod defect version, the

larger core relative to the pitch corresponds to increasing the normalized frequency, thus, causing the fibre to be multimode at a  $d/\Lambda$  of 0.45. In order to obtain a new limit for single mode behaviour, the value of  $d/\Lambda$  should be decreased. So it can be concluded that to achieve endlessly single mode applications, a relatively small value of  $d/\Lambda$  is wanted, which as will be shown in section 2.3.4.2, is the same requirement for achieving a large mode area fibre. In the case of a PCF with an infinite number of rings, the above design approach shows that the endlessly single mode is obtained regardless of wavelength. However, if the number of rings is finite, which leads to leakage in the fibres, the border between single mode and multimode operation is not clear. Thus, the value of  $d/\Lambda$  should be optimised by considering additional conditions such as confinement loss, because the study in [2.31] shows that the loss is inversely proportional to  $d/\Lambda$ .

#### 2.3.4.2 Large mode area

Large core fibres are used now for high power laser beam delivering, laser welding, polarisation maintaining fibres, highly birefringent PCF, fibre gyroscope, signal amplification and high power laser implementation [2.37]. Most of these applications require the core to be as large as possible, resistant to fibre micro-bends, and to deformation, while maintaining single mode operation. So, the large mode area PCF is a suitable method to realise some combinative application. In order to achieve the requirements of the above applications, the design for endlessly single mode and large mode area should be considered simultaneously. Also their combined attractions are

enabled to be achieved together with proper design. Generally, the requirement can be achieved by consideration of the two factors that mainly affect the effective mode area: core-cladding refractive index contrast and core diameter.

A combination of a large mode area PCF and the application of stress was adapted to make a polarization maintaining large mode core fibre [2.38]. Bending loss and leakage loss in large mode area fibres has been studied in previous literature [2.35, 2.37]. It reveals that the bending loss in the short wavelength region is introduced by micro-bends but that leakage loss is introduced at larger radius of curvature in the long wavelength region.

In the conventional core-clad fibre technology, in order to achieve a large mode area, the core dimension should be increased, or the numerical aperture should be reduced by lowering the concentration of doping material in silica in the core region [2.34]. In terms of microstructured fibre, particularly in triangular PCF, which has a triangular core suspended by ‘holey’ capillaries, the effective area can be significantly increased by decreasing the air-filling fraction, or by increasing the pitch with a fixed ratio of  $d/\Lambda$ . However, decreasing the air-filling fraction can lead to an increase of the leakage losses [2.39].

#### 2.3.4.3 High nonlinear with highly confined mode area

In contrast to the requirement of single mode operation and large mode guiding

discussed above, highly nonlinear applications require small effective core area. The nonlinear parameter, given by  $\gamma = 2\pi n_2 / (\lambda A_{\text{eff}})$ , where  $n_2$  is the nonlinear refractive index, and  $A_{\text{eff}}$  is the effective mode area, can be enhanced by decreasing the effective mode area, and, as discussed in section 2.3.4.2, the radius of the effective core ( $A_{\text{eff}}$ ) is dependent on the ratio of  $d / \Lambda$  and  $\lambda / \Lambda$ .

Many numerical investigations [2.11 - 2.15, 2.40] noted that small effective mode area can be obtained by reducing the core size in MOF, in which the fundamental mode is confined by air holes; this does not work in conventional fibre because the mode spreads more deeply into the cladding region. The effective core area of a MOF can be reduced and so a high nonlinear parameter can be achieved. The dispersion property of MOF is very attractive, due to the sensitive response of the design flexibility in the structure of MOF. For proper design of PCF,  $A_{\text{eff}}$  can be smaller than  $1 \mu\text{m}^2$  and  $\gamma$  can be enhanced by a factor of 50, or even more, when it is compared to conventional fibre [2.15]. It turned out that the effective mode area  $A_{\text{eff}}$  is nearly independent of the number of air rings number while the confinement loss is strongly dependent on it [2.39, 2.15].

The literature of [2.41] noted that the confinement loss becomes more severe as the fibre scale becomes relatively small. Thus, in order to approach high nonlinearity and low confinement loss spontaneously, a large air-filling fraction and pitch size larger than  $1 \mu\text{m}$  are suitable for the design.

Effective mode areas as small as  $1.3 \mu\text{m}^2$  in a silica PCF have been achieved at 1550 nm wavelength, corresponding to a  $\gamma$  of around  $70\text{W}^{-1}\text{km}^{-1}$ , more than 70 times than in the standard single-mode fibre [2.42].

Compared to the conventional fibre, MOFs offer many flexible design parameters with which the fibre dispersive properties could be tailored to fit any application. Many researchers indicate that the dispersion properties of MOF are strongly sensitive to the core size, the hole-diameter and pitch. The wavelength dependent dispersion parameter  $D = -(2\pi c / \lambda^2)\beta_2$  was analysed in [2.43] by varying the ratio of  $d / \Lambda$  with different pitch values, where  $\beta_2$ , named third order nonlinear parameter, is the second order differential term of the propagation constant  $\beta$ . It was shown that the PCF exhibits large nonlinear properties supplying large wavelength dependent dispersion (waveguide dispersion), which is of benefit for dispersion compensation. In this study, for a relative large pitch value of  $> 2 \mu\text{m}$ , a single zero dispersion point (a zero dispersion wavelength, ZDW) in the range from  $0.5 \mu\text{m}$  to  $1.8 \mu\text{m}$  shifts towards shorter wavelengths as the hole-diameter  $d$  is increasing. On the other hand, for relative short pitch value, two zero dispersion points appeared. These two points moved closer as pitch value and the ratio of  $d / \Lambda$  became smaller.

## **2.4 Supercontinuum (SC) mechanism and the benefit of SC with MOF**

Supercontinuum (SC) generation is a complex physical phenomenon which causes a significant spectral broadening of laser pulses propagating in a nonlinear medium [2.34].

A pulse launched into a highly nonlinear optical fibre can cause SC generation through a series of nonlinear phenomena, such as Self-phase Modulation (SPM), Cross-phase Modulation (XPM), Stimulated Raman Scattering (SRS), Self-steepening (SS), and Four-wave Mixing (FWM). The pump power, pulse length, pump wavelength, length of the fibre, the induced noise and the dispersion properties of fibres affect the pulses' spectral evolution to a large degree as well. Particularly, the pump wavelength related to the dispersion profile of the fibre determines which nonlinear mechanisms are active in the SC generation, and characterises the spectrum profile. Thus, many groups have researched on different combinations of the above factors, and some trends have been concluded.

SC was first reported in 1976 by launching Q-switched pulses of 10 ns width from a dye laser into a 20 metre long silica fibre with a 7  $\mu\text{m}$  core diameter; a 120 nm wide spectrum was achieved with an injected peak power of 1 kW [2.15]. A 200 nm spectral width was achieved in 1987, in which 830 fs pulse with peak power of 530 W was launched into a 1 kilometre long single mode fibre [2.40]. The birth of MOF made the situation dramatically change. In 2000, a broad band extending from 400 to 1550 nm was observed with 100 fs pulses at 790 nm launching into a 75 cm long MOF [2.40].

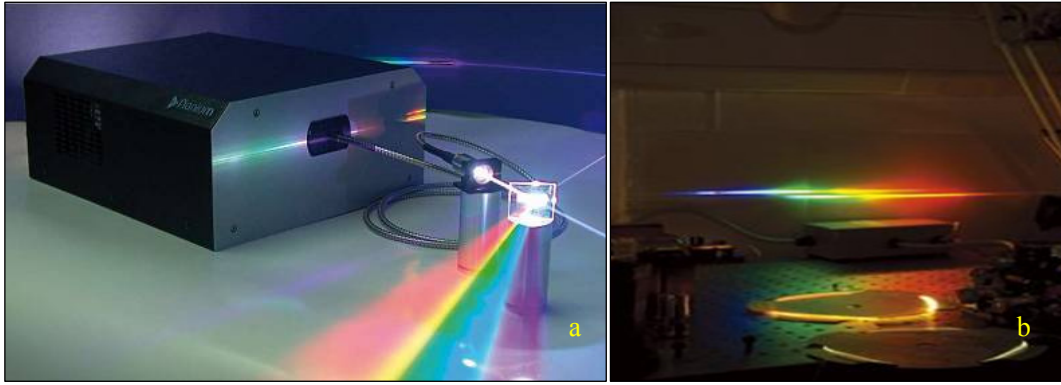


Figure 2.5 (a) SC400 fibre laser source developed by the Fianium company [2.44]; (b) blue band enhanced SC spectrum (top) and a traditional SC spectrum (bottom) in visible region [2.44].

Figure 2.5 (a) shows a supercontinuum fibre laser source covering the region from 400 nm to nearly 2400 nm with a power density of the order of  $mW / nm$ . This white light source adapts the highly nonlinear PCF designed by the University of Bath to enhance the propagation in the blue band [2.44]. The comparison between the blue band enhanced SC spectrum and a traditional SC spectrum is shown in figure 2.5(b) (the upper light spectrum in figure 2.5(b) is generated by guiding the light through a PCF). It shows how the use of a highly nonlinear PCF obtains spectrum expansion in the blue and violet regions.

### 2.4.1 Nonlinear phenomena in SC mechanism

The mechanism of supercontinuum generation is very complicated, and usually it is a combination of many nonlinear phenomena depending on many factors. The mechanism of each nonlinear phenomenon supplying a contribution to SC is presented below, and then, a summary of the complicated SC generation mechanism is made, where the formulas presented have been collected from several references [2.15, 2.45,

2.46].

(a) Self-phase modulation (SPM);

Here the phase shift given by:

$$\Phi = \int_0^L \beta_{NL} dz = \beta L + \gamma \mathcal{P}(t) L_{eff} = \beta L + \Phi_{SPM} \quad (2.13)$$

is raised while light is propagating through the nonlinear medium. Here  $\beta_{NL} = \beta - \gamma \mathcal{P}(t)$  is the propagation constant (section 2.3.4.3), due to power intensity dependent refractive index, and  $L_{eff} = (1 - \exp(-\alpha L)) / \alpha$  is the effective length of fibre with  $\alpha$  the loss coefficient of the fibre. The pulse power is modulated by the emergent wave with phase shift  $\Phi$ . From the formation of the output propagated, a Gaussian pulse given by [2.45]

$$E_{output} = E_0 \exp(-t^2 / \tau_0^2 + i(\omega_0 t - \beta L - \gamma \mathcal{P}(t) L_{eff})) \quad (2.14)$$

the instantaneous frequency of the propagated pulse is obtained as

$$\omega(t) = \frac{d}{dt} (\omega_0 t - \beta L - \gamma \mathcal{P}(t) L_{eff}) = \omega_0 - \gamma L_{eff} \frac{d\mathcal{P}(t)}{dt}. \quad (2.15)$$

Equation (2.15) reveals that the leading edge is downshifted and the trailing edge is upshifted in the frequency domain while the centre frequency is fixed. The spectral broadening combined with anomalous dispersion will compensate the pulse deformation forming a soliton, while with normal dispersion further increase of chirping is observed [2.15, 2.45].

(b) Cross-phase modulation (XPM);

When two different waves co-propagate in the fibre, the phase shift of one wave is given by:

$$\Phi = \beta L + \gamma \mathcal{P}(t) L_{eff} + 2\gamma \mathcal{P}'(t) L_{eff} = \beta L + \Phi_{SPM} + \Phi_{XPM} \quad (2.16)$$

in which  $P'(t)$  is the power of the second wave. So the instantaneous frequency of the light wave affected by SPM and XPM is given by:

$$\omega(t) = \omega_0 - \gamma_{eff} \frac{dP(t)}{dt} - 2\gamma_{eff} \frac{dP'(t)}{dt} \quad (2.17)$$

Thus each pulse is influenced by the other one, and the result is a downshift in the frequency domain at the overlap of leading edges and an upshift at the overlap of trailing edges [2.15, 2.45].

(c) Simulated Raman Scattering (SRS);

SRS, with high threshold, is due to the interaction between light and optical vibration modes. The pumped frequency is downshifted, so the power moves from shorter wavelengths and the longer wavelength signal is enhanced.

The investigation in [2.44] indicated that a proper design with the hole diameter to pitch ratio can maximize the Raman gain efficiency in a PCF. From this numerical simulation, a high  $d/\Lambda$  is required like that of a highly nonlinear PCF. It proved that PCFs can provide high Raman gain efficiency, 80 times higher than in a standard transmission fibre. Also, with the aim of reducing the threshold for SRS by two orders of magnitude, a hollow-core PCF filled with hydrogen has been designed [2.47].

(d) Self-Steepening (SS);

The light pulse can be steepened into an optical shock due to propagation in a medium with an intensity dependent index of refraction. The effect of self-steepening can narrow the lead trailing and end trailing shift the pulse centre frequency. Due to the

pumping wavelength, the SS effects in reverse trend and so can be controlled to maintain the soliton transmission.

#### (e) Four-wave Mixing

Four-wave Mixing (FWM) is a nonlinear recombination of light waves at different frequencies through the susceptibility [2.48]. With two photons at angle frequency  $\omega_p$  from the pump and one photon at  $\omega_s$  from the signal, the fourth wavelength component generated is referred to as the idler wave at  $\omega_i = 2\omega_p - \omega_s$ . The energy is transferred from the pump wave to the signal and idler wave by a coupled amplitude equation when the phase match condition is obtained [2.46].

### **2.4.2 Summary of SC mechanisms in specific experimental conditions**

A summary of experiment setup conditions, in which the mechanism of SC generation in PCF, is investigated in the following sub-section. The explanation of results in terms of the mechanisms will be done with some specific examples.

For simplification, the analysis of the various combinations of the nonlinear mechanisms described above does not include the factor of power peak. Obviously, an increase in peak power leads to further spectral broadening, but the noise intensity of the pulse is higher [2.45].

From a series of numerical investigations [2.50, 2.51], it is known that the spectral

broadening can be generally divided into three stages: (1) initial broadening in the spectrum and compression in the time domain; (2) a series of fundamental solitons are generated in soliton fission and (3) the subsequent propagation of these solitons to broaden further the spectrum.

#### 2.4.2.1 Pumped in normal and abnormal dispersion area

It can be concluded from the above that the creation of a SC always depends on dispersion properties. In addition to the structure of PCFs, the pumping wavelength relative to the zero dispersion wavelength is another crucial factor leading to SC. If the fibre is pumped in the normal dispersion region, which means the group index decreases while the wavelength is increasing, the Kerr effect and dispersion make the pulse dispersive simultaneously, so the peak power is decreased after propagating through a section of fibre. This tends to lower the SC generation. On the other hand, if the fibre is pumped in the anomalous dispersion range, the group velocity dispersion counteracts the Kerr effect to enable the pulse to transmit for a long distance in the form of a soliton. The maintenance of high peak power will lead to a further increase of the spectrum propagating and to result SC ultimately. With the adaption of a PCF, the zero group velocity dispersion point can be obtained and flexibly tuned within a large range. For example, for silica PCF anomalous dispersion is achieved at the usual operation pump wavelength (eg. 1064 nm and 800 nm), which is hard to achieve with a conventional fibre technique. The conclusion which can be generally induced is that pumping in an anomalous GVD region can increase the bandwidth compared with

pumping in a normal GVD region, but the spectrum is less smooth [2.49].

#### 2.4.2.2 SC of different pulse duration

The dependence of SC generation on the pulse width has been extensively researched [2.45, 2.50, 2.51]. The pumping pulses whose duration vary from the femtosecond regime, to the picosecond regime, to the nanosecond regime to coherent wavelength (CW) operation were investigated numerically and experimentally, and are described in order below.

In the femtosecond regime, an experiment and related numerical modelling have been reported in [2.50] where 100 fs pulses at 780 nm from a commercial Kerr-lens mode-locked Ti: sapphire laser in the nanosecond regime generated a spectrum from 450 nm to 1250 nm through a 1m length of PCF with a zero dispersion wavelength (ZDW) of 765 nm. This showed that the SPM, phase-matched FWM and soliton dynamic processes were the dominant operating mechanisms. A series of numerical investigations and experiments was done with different pump wavelengths in the femtosecond pulse regime. A comparison was made with experiment [2.51], in which 50 fs pulses of 10 kW were launched into a 15 cm silica glass fibre segment, and the pumping wavelength was varied from 600 nm to 900 nm. The comparison of the output spectrum and temporal output is shown in figure 2.6(a). The dashed line marks the ZDW of the PCF.

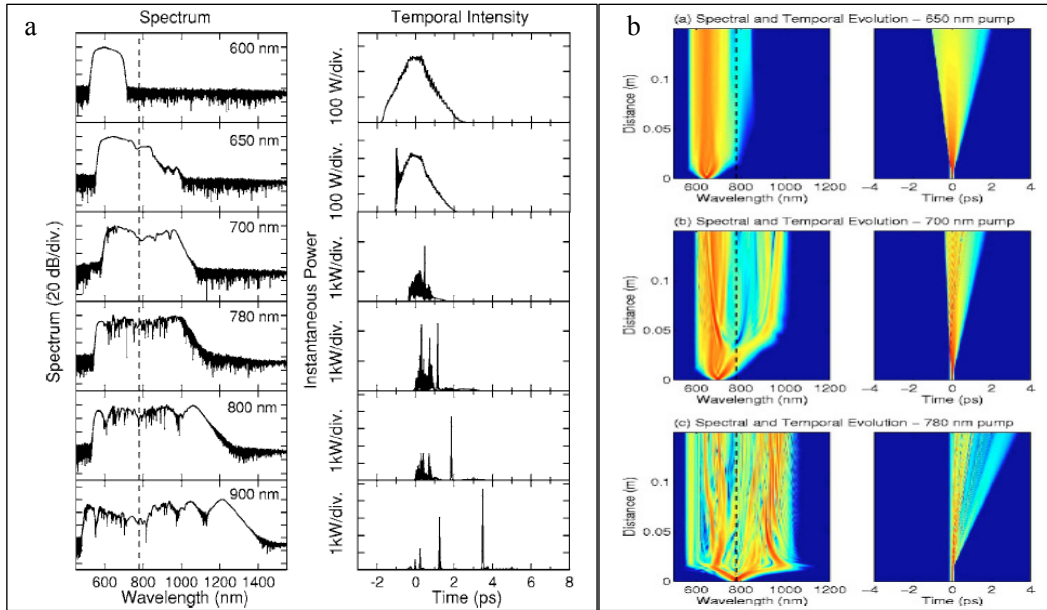


Figure 2.6(a) The comparison of SC with different pump wavelengths in spectral and temporal output [2.51]. (b) Spectral and temporal evolution of SC versus propagation distance [2.51]. This experiment is based on a solid core silica PCF with rings of holes of cladding arranged in hexagonal pattern.

The evolution of the pulse in the frequency and time domains with pulse centre wavelength from 600 nm to 900 nm in figure 2.6(a) shows that when pumping at the normal dispersion side of ZDW, the interaction of SPM and normal GVD affects the spectral and temporal output showing that the SPM is the dominant factor [2.52]. When the pumping point moves close to the ZDW, the initial spread spectrum transfers into the vicinity of the ZDW and even moves across the ZDW into the anomalous GVD region. In this process, Raman effects and the dispersion of nonlinearity are more active, so the temporal oscillations of the pulse envelope occur to modify the spectrum. The SPM broadening is accompanied by the Raman soliton in the anomalous GVD region, and perturbation in the short wavelength region appears. The XPM between soliton and nonsoliton components makes a contribution to the structure of the spectrum. The soliton dynamics dominate when deeply pumped within

the anomalous GVD region, because further spectral broadening and more distinct soliton peaks manifest themselves. When the pump point moves away from the ZDW into the anomalous GVD region, solitons are ejected from the spectrum constituent solitons, and being a role to contribute to spectral broadening even through the soliton order decreases. Also, the longer wavelengths are increasingly detuned from the ZDW leading to the position of the dispersive wave increasing correspondingly [2.51].

An analysis of different pulse durations varying from 20 fs to 500 fs, i.e. still within the femtosecond regime, with other conditions fixed, has also been made in [2.51]. The maintained peak power and longer pulse duration means more input energy and soliton number. However, a shorter pulse duration is associated with a reduced characteristic separation distance; thus, as shown in figure 2.7 (a) and (b) a shorter pulse results in a more distinct soliton structure.

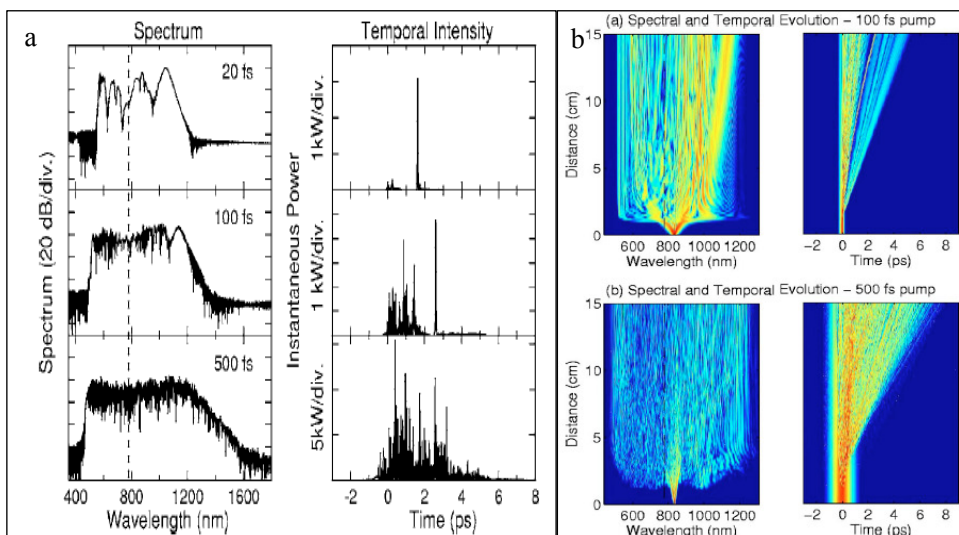


Figure 2.7 (a) Comparison of SC with different pulse duration in spectrum and temporal [2.51]. (b) SC in Spectral and temporal evolution of SC versus propagation distance [2.51]. This experiment is based on a solid core silica PCF with rings of holes of cladding arranged in hexagonal pattern.

It can be viewed from figure 2.7(b) that the spectral extension within the first several mm of PCF section is reduced with a longer pulse duration. The presence of a high order soliton contributes to the soliton fission process of the fundamental soliton by modulation instability.

In the picosecond longer pulse duration regime, mechanisms other than SPM and soliton fission are expected to be included in the SC generation process; FWM and Raman scattering also play especially important roles in propagating a long duration pulse. The SRS amplifies the spectrum on the long wavelength region as soon as the SPM broadens to a degree. In contrast to the asymmetric broadening supplied by SRS, the FWM offers symmetric broadening on both sides of the pumping wavelength, and the larger the power is, the further the sidebands of the FWM move from the pumping wavelength. Generally, the FWM-like coupling between Stokes and anti-Stokes bands, the FWM sidebands, the XPM and SRS through each band produce a flat SC [2.52]. Especially, the comparison of the SC spectra obtained pumping at different wavelength in the picosecond and femtosecond regime made in [2.51] is reproduced in figures 2.8(a) and (b). Employing a 2 m long PCF with a 20 ps pulse duration of energy of 500 W, Raman scattering took dominance in the spectral broadening process for longer pulses pumping at 650 nm and 700 nm in the normal GVD region. Rather, it can be viewed from figure 2.9 that the initial spectrum evolution had various Raman orders distinctly and then formed a continuous spectrum because of the effect of SPM and XPM. In figure 2.9(1.a), the sidebands of distinct Raman Stokes and anti-Stokes

peaks, which result from non-phase-matched parametric amplification, have been broadened and merged through the propagation along the fibre. When the pump point moves closer to the ZDW, figure 2.9(1.b), detuned spectral components appear in the normal and anomalous GVD regions except for the Raman structure around the pumping wavelength. These components are due to the high order dispersion phase-matched FWM. If the pump point is moved further towards longer wavelength and is deeply located in the anomalous region in figure 2.9(2), a more uniform spectrum is obtained, mainly characterised by phase-matched FWM.

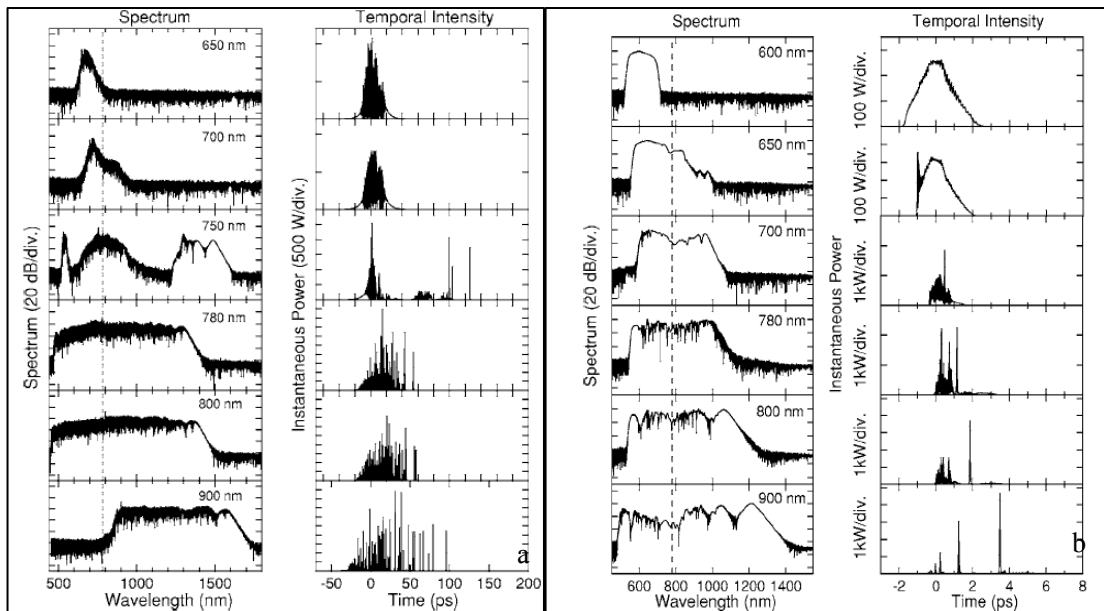


Figure 2.8 (a) The comparison of SC spectra pumping at different wavelength with picosecond regime (the ZDW is about 765 nm). (b) The comparison of SC spectrums pumping at different wavelength with femtosecond regime [2.51].

It can be seen that when pumping at 800 nm the greatest spectral bandwidth is obtained because the longer pumping wavelength generates less spectral bandwidth that can seed dispersive wave transfer into the normal GVD region.

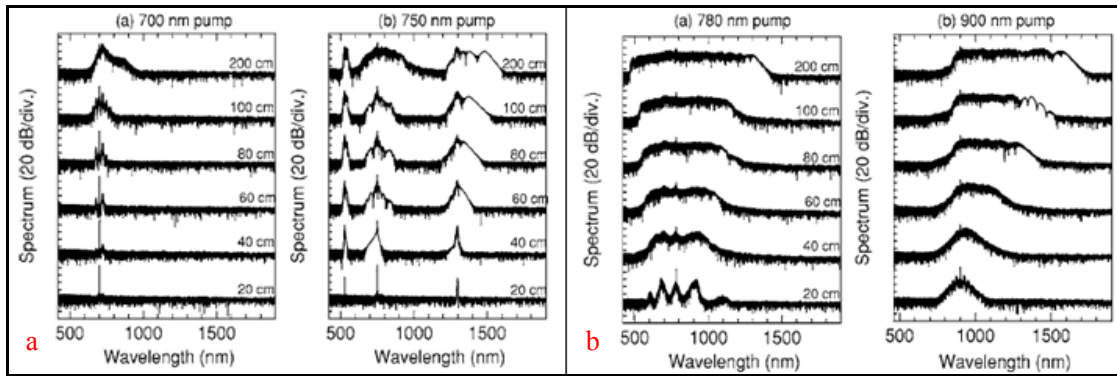


Figure 2.9 The spectral evolution raised from various pumping wavelengths with different propagation lengths[2.52].

SC in the nanosecond regime, even with continuous wave (CW) pumping from microstructured fibre was demonstrated as well [2.52]. It can be concluded that with the premise of a high power source, highly nonlinear fibre and a phase-matched suitable FWM process, SC generation is obtained. For the case of a CW source, FWM sidebands can be generated by modulation instability if the pump pulse experiences anomalous GVD. Then, the CW light is converted into a train of picosecond pulses by modulation instability. Thus, the SC mechanisms associated with the picosecond pulse regime take place in the subsequent broadening process [2.52].

## 2.5 Novel glass for SC generation

In this subsection, novel glass, as a cluster of candidates for SCG, is mentioned. SCG has been realised, as mid-infrared source, by using core-clad. chalcogenide glass fibre [2.83]. A summary of the SCG using novel glass is made in Table A.(ii), which is presented within Appendix II. Here some conclusions about novel glasses for SCG can be made, based on the literature which reports SCG with novel glasses to date (references 2.53 - 2.66). The important factor for achieving SCG can be concluded as

the types of waveguide used, the pumping scheme, kinds of novel glass and waveguide structure:

#### (1) Types of waveguide

As discussed in section 2.3, waveguides with high confinement are helpful for achieving SCG. Three types of waveguide (rib-waveguides, tapered fibres and MOFs) [2.24, 2.28] have been reported for obtaining SCG, because they can provide tight mode confinement to enable both dispersion management and high effective nonlinearity over extended interaction lengths.

#### (2) Pumping source

Based on the desired pumping wavelength and the equipment availability, different pumping schemes can be applied. For a seed in the visible window to 1.55  $\mu\text{m}$ , a Ti:Sapphire or an Er-fibre pump system is a good candidate. Seed wavelengths of 2.0 -2.25  $\mu\text{m}$  are readily accessible from commercially available optical parametric oscillator and amplifier (OPO/OPA) systems [2.24]. The desired ZDW (longer ZDW can help to get SCG at longer wavelengths and with wider bandwidth) of the fibre, which has been discussed in section 2.4, is also dependent on what pump wavelength is available.

#### (3) Material

There are five crucial facts to be considered in choosing the materials for achieving SCG application. These are chemical durability, thermal stability, transparent window

and bulk material dispersion curve and intrinsic loss. Here a comparison of the dispersion property only is discussed.

The ZDW of a glass shifts to longer wavelength with increasing linear refractive index (lead-silicate < bismuth-oxide < tellurite < GLS < As<sub>2</sub>S<sub>3</sub> < As<sub>2</sub>Se<sub>3</sub>). The material ZDWs of heavy metal oxide glasses (lead-silicate, bismuth-oxide, tellurite) are about 2~3 μm. The material ZDWs of chalcogenide glasses (GLS, As<sub>2</sub>S<sub>3</sub>) are larger than 4 μm [2.52].

The conclusion could be made that chalcogenide glass will help to obtain longer ZDWs than heavy metal oxide with the same waveguide structure, or in order to achieve the same ZDWs near the current pumping wavelength, smaller core size is allowed in chalcogenide MOF than that in heavy metal glass, because the smaller cross-section can supply higher waveguide dispersion.

#### (4) Waveguide structure and guiding wavelength

Fibres with small size of guiding area enable the ZDWs of the fibre to be tuned in a large range, because a small core supplies large waveguide dispersion to compensate the material dispersion to get zero dispersion at the desired wavelength, and give a flattened dispersion curve which leads to more intense and broader spectra. Small core and high NA MOF are good for SCG, but sometimes there is still a need to balance the demand on core size with power-handling capacity for large power SCG applications [2.45].

## **2.6 Advances in the fabrication of novel glass microstructured optical fibres (MOFs)**

In this section, the review of the fabrication of solid and holey novel glass MOFs is presented with the focus located on the aspects of glass preform shaping and the engineering of fibre-drawing.

### **2.6.1 Preform fabrication**

Generally, the fabrication techniques to achieve the preform of MOFs can be classified as follows: 1) a combination of rotational casting and stacking [2.67, 2.68, 2.69], 2) extrusion through a die [2.70], 3) casting material in mould [2.71, 2.72], 4) a combination of casting material and stacking [2.73, 2.74] and 5) ultrasonic drilling [2.75]. The selection of these techniques should be considered on the basis of the engineering flexibility, the quality of preform, the machine cost, and the quantity of human labour required to produce the specified fibre structure.

The stacking and drawing method is widely referenced as it is a flexible technique for preparing complete MOF structures with lots of ring of capillaries or canes, especially for preparing all-solid glass pair preform, [2.67 ~ 2.69]. However, it is tricky from the aspect of controlling the thermal process of preform shaping, hand stacking skill required, and the cost of significant human labour. Normally, it takes long time to set up the crystal pattern and it may be necessary to develop a mechanism to assist the stacking which was mainly by hand in our previous work [2.11]. Moreover, the

over-clad tube which could be fabricated by rotational casting has to be able to accommodate the stacking pattern.

The extrusion method is suitable to achieve monolithic, complicated MOF structures, especially those with small core and large air-filling fraction structure based on the design of the extrusion die [2.70]. However, this is at expense of surface quality and purity due to the physical and chemical contamination from the extrusion die. Obviously, it is a more straightforward approach to make a preform by an extrusion method than by the stack and draw method described above.

The method of casting material into a mould is a relatively new route to achieve monolithic, complicated structure MOF and as it allows flexibility in tube fabrication, it is a potential alternative candidate to rotational casting [2.67, 2.68]. This cast-tubing technique takes advantage of the relatively high precision in tube dimensions compared to rotational casting where it is tricky to control the enclosed space for the supposed tube volume. However experimental research [2.72] on avoiding preform cracking during the thermal processing is necessary due to the contrast of thermal expansion coefficient between chalcogenide glass and silica tubing. In the procedure described in [2.72, 2.81], the silica tube was dissolved by hydrofluoric acid, so that the investigation on how much the HF etching removes the silica mould is essential since it affects the surface quality of the preform. From our knowledge, it may be possible to adapt this cast-tubing method to fabricate the over-clad tube and so it could be a

potential alternate to the present rotational casting method for the fabrication of over-clad tube [2.72, 2.81].

The combination of the casting material into a mould and then stacking supplies a more flexible route of preform fabrication, for example the preform in the pattern of a hexagonal lattice. Also, a series of multistep stacking and over-clad method supplies the flexibility to obtain different aspect ratio of the MOFs [2.73, 2.74].

Drilling [2.75] is a more direct, immediate technique to achieve a holey microstructured preform compared to the multistep stacking and drawing process. However it needs a high cost mechanical machine for a precise drilling control on the position and dimension. Also, it is easy to induce tiny cracks because of mechanical vibration when working on a delicate glass structure. So this is mainly reserved for preforms with a small number of holes, thick wall thickness between holes and relatively short length. The appearance of ultrasonic drilling machine can improve the fabrication precision and reduce the labour cost by automatic control, but results in a higher facility cost. [2.82]

In conclusion, the above approaches all have their own advantage, which could be combined with flexibility based on the specific requirement.

## 2.6.2 Fibre drawing

The fabrication of MOFs from the preform is also a challenging procedure and it is mainly determined by the followed aspects. For the holey MOFs, the holes in cladding region are deformed due to the air pressure differentiation between inside and outside of the hole, the surface tension of the glass, the temperature gradient along the transverse direction of the preform during softening and the feeding speed of preform and fibre [2.83].

Some researchers have investigated the deformation process of a silica preform incorporating the temperature, feed speed and the collapse ratio [2.77, 2.78, and 2.79].

An equation that predicts how sensitive the collapse of the capillary is to the drawing parameters during fibre drawing is reported in [2.77] as:

$$C = \frac{\gamma L}{\mu v_{in} \ln(v_{out}/v_{in})} \left( \frac{d_{ID} + d_{OD}}{d_{ID} d_{OD}} \right), \quad (2.17)$$

where  $L$  denotes the hot zone length;  $v_{in}$  is the feed in speed of the preform;  $v_{out}$  is the feed out speed of fibre drawing;  $\gamma$  is the silica glass melt surface tension and  $\mu$  is the silica glass melt dynamic viscosity;  $d_{ID}$  and  $d_{OD}$  represent the internal and outer diameter of the capillary, respectively. The top end of the preform was left open to atmosphere, thus the ratio of gas pressure inside and outside the preform is a constant ratio in this experiment. Total collapse occurs when  $C = 1$ , whereas the dimension of the preform is perfectly preserved when  $C = 0$ . In this formula, the ratio of  $\gamma/\mu$  is dependant on the surface temperature of the glass melt. Study of the term of  $v_{in} \ln(v_{out}/v_{in})^{-1}$ , shows that the feed in speed,  $v_{in}$ , is more sensitive in determining the

collapse of the capillary. Also, the ratio of  $d_{ID}$  to  $d_{OD}$  is a measure of the collapse ratio of the capillary when it is being drawn down. An air-hole structured preform heats up faster than the corresponding solid preform due to the effect of the reduced thermal mass being greater than the effect of the thermal resistance of the air holes. However, there exists an air fraction below which the impact of greater thermal resistance of the air structure exceeds the impact of lower thermal mass and results in a slower heating of the preform centre [2.77 ~ 2.79].

Because the molar surface tension of a glass-forming melt decreases dramatically with the increase of the average field strength  $Z/r$ , in which  $Z$  is the valence of the atom, and  $r$  is the atomic radius, thus the chalcogenide glass type of fibre has a lower surface tension during fibre-drawing than the pure silica fibre by one or two orders of magnitude due to its large fraction of heavy, weakly bonded atoms [2.76]. Also, there ideas could be developed instead based on the structural approach of average coordination number (see section 2.1.2.1) and applied to chalcogenide glass fibre-drawing.

## **2.7 Summary**

The background of the MPhil project has been reviewed in the chapter. Firstly, the glass science and the properties of chalcogenide glasses were introduced. Chalcogenide glasses enable a variety of applications due to their high refractive index, high nonlinear optical properties and their transparency from near- to mid-infrared

region. Secondly, the Ge-Sb-Se glasses system was discussed to provide an alternative to the arsenic-containing glasses system in order to avoid the toxic element As in the glass forming system, for safety considerations. The principle of microstructured optical fibre (MOF) and the potential applications of chalcogenide glasses MOF were then described. The mechanism of supercontinuum generation (SCG) and the chalcogenide glasses fibre used to achieve SCG were reviewed. Finally, the fabrication methods of chalcogenide glasses MOF were reviewed. With fabrication techniques being refined in the future, more flexible design of the chalcogenide optical MOF can be realised to offer enormous potential applications. In the next chapter, the experimental techniques used in this project will be introduced.

## **Chapter 3 Experimental**

The whole procedure of microstructured optical fibre (MOF) fabrication includes glass synthesis and characterisation, glass preform shaping and fibre fabrication.

The techniques in the above procedure consist of glass preparation (ampoule: annealing, air baking and vacuum baking), element purification, batching, ampoule sealing, ampoule-holder-making, glass-melting, quenching, annealing, glass-cutting and polishing, glass characterisation, extrusion, rotational casting, stacking, and fibre drawing, which are all described in the chapter.

### **3.1 Chalcogenide glass preparation**

#### **3.1.1 Ampoule preparation**

The preparing of a glass preform is the initial task of MOF fabrication. Because the melting temperature of silica is much higher than for chalcogenide material, and also because the silica is usually not wetted by the chalcogenide glass melt [3.1], a fused silica ampoule (supplied by Multi-Lab, Global Quartz or QB Glass Ltd.) was used as the container in which to melt the chalcogenide glass. The size of the ampoule, especially the inner diameter (ID) and outer diameter (OD), used for each specific preform preparation was dependent on the subsequent usage of the melt, be it for tube making, extrusion or fibre drawing. Ampoules and tubes used in this work are depicted in figure 3.1.

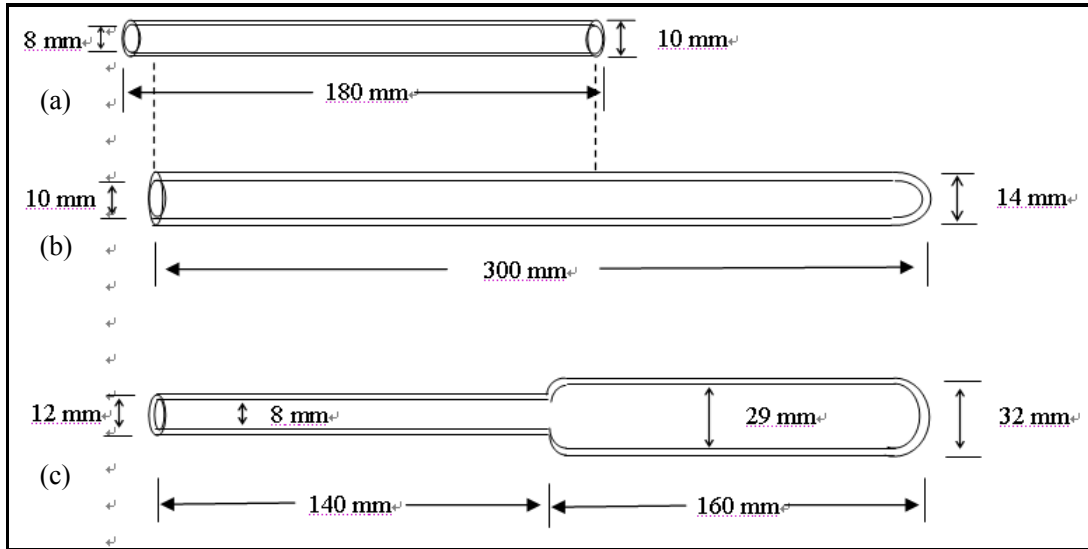


Figure 3.1 (a) The open silica tube with 8mm/10mm of ID/OD used inside a closed tube containing impure Se to collect impurity deposition during Se purification; (b) the silica ampoule (e.g. for  $\text{As}_{40}\text{Se}_{60}$ ) preform preparation and (c) the silica ampoule preparing a boule (e.g. for  $\text{Ge}_{10}\text{As}_{23.4}\text{Se}_{66.6}$ ) for subsequent extrusion.

The open tube (Figure 3.1 (a)) was used to collect impurity deposition during Se purification; the impure Se was held in a closed tube in which the open tube was placed. The ampoule with ID/OD 10 mm/14 mm (Figure 3.1 (b)) was used to prepare the unstructured fibre preform rod and the boule ampoule with 29 mm ID (Figure 3.1 (c)) was suitable for melting a larger glass boule to fit the extruder barrel for subsequent extrusion.

The orifice of the ampoules and tubes was heated gently with an oxy-propane flame torch to achieve a smooth edge. This operation avoided the rough cut edge leading to silica dust in the batched material and scratching of the inner surface of the ampoule.

HF etching was used in order to enhance the mechanical strength of the inside of the ampoule, prior to use. The ampoule was placed vertically for about 20 minutes inside a polythene beaker, which was filled with a solution of 0.4% of aqueous hydrofluoric acid. Ampoule annealing was carried out by Dr David Furness with the author in attendance to release the residual tension in the ampoule. The ampoule was horizontally placed into a furnace (Carbolite, STF 15/450) under argon (BOC) at 1160°C for 1.5 hours and cooled down to 900°C at 60°C / h and finally more quickly more quickly down to room temperature. Then, the ampoule (Figure 3.1 (b) or (c)) was rinsed three times with distilled water, and dried at 70°C in an oven (Heraeus Instruments/Lot1174) for 6 hours, in a class-10,000 cleanroom.

An air bake was next applied to remove any carbon-based deposits which might have been present on the inside surface of the ampoule [3.1]. The ampoule was placed vertically in a furnace (Instron, TF105/4.5/1ZF, tube ID 86mm, with a controller Eurotherm 2408), with its open end up, in the air atmosphere of the class10,000 cleanroom at 1000°C for 6 hours.

Next, a vacuum bake was applied, aimed at removing physisorbed and chemisorbed water from the internal ampoule surface. The ampoule was evacuated under a drawing vacuum ( $\sim 10^{-5}$  Pa) using a turbo pump (FIFA Turbo-drag Cube), and heated at 1000°C for 6 hours inside a furnace (Instron,

TF105/4.5/1ZF, tube ID 86mm, with a controller Eurotherm 2408) inside the class-10,000 cleanroom [3.1].

The ampoule, tube and the relative ring and attachment were selected in the consideration of a proper match in their ID and OD so that the tube fitted inside the ampoule with 0.5 mm to 1 mm radial clearance.

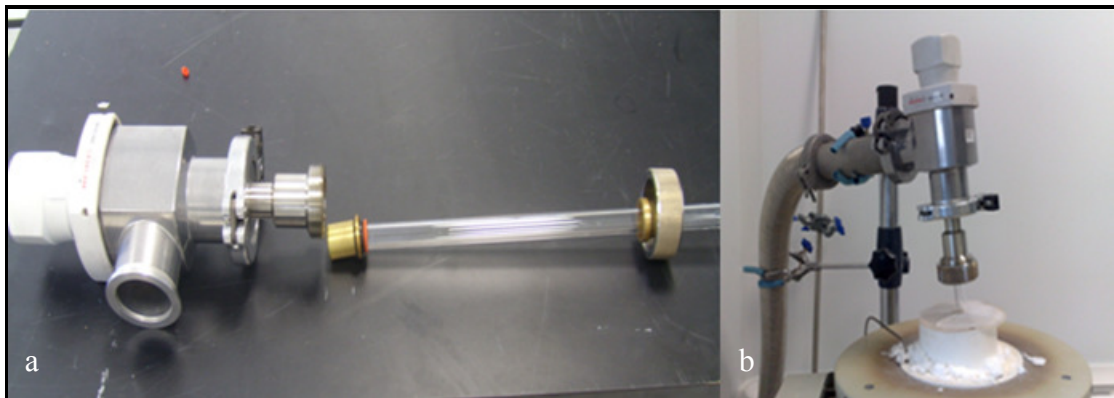


Figure 3.2 Vacuum baking to purify a silica glass ampoule: (a) The assembly of the valve, attachment, rings and ampoule and (b) the assembled vacuum system.

### 3.1.2 Purification of batch elements.

The precursor material purification, which ensured glass formability and limited extrinsic optical loss of the resulting preform by removing oxide and hydride impurities, was adopted [3.1]. Because the vapour pressure of the elemental As and Se is lower than the vapour pressure of their relative oxide in the relevant temperature range, the purification treatment was set by heating the precursor material inside a silica ampoule under evacuation to a temperature at which the oxide with higher vapour pressure vaporises out first and deposits onto the inside of a prepared ampoule (or, as in the case of Se, on the inside of an open tube). The

vapour pressure, melting point and boiling point (both at standard pressure) of some chalcogenide elements and their relative oxides have been collated by Rowe in [3.1] (see Table 3.1).

Table 3.1 Collation of the vapour pressures of the chalcogenide elements and their relative oxide compounds [3.1].

Formula	Thermal properties / °C		Vapour pressure / mm Hg	Density / kg m <sup>-3</sup>
	Melting point	Boiling point		
As	817 (3.70MPa)	603 sublimes	0.12 @ 300°C	5.75 x10 <sup>3</sup>
As <sub>2</sub> O <sub>3</sub> (arsenolite)	274	460	49.19 @ 300°C	3.86 x10 <sup>3</sup>
As <sub>2</sub> O <sub>3</sub> (claudetite)	313	460	49.19 @ 300°C	3.74 x10 <sup>3</sup>
As <sub>2</sub> O <sub>5</sub>	315 decomposes	-	-	4.75 x10 <sup>3</sup>
Ge	938	2833	-	5.3234 x10 <sup>3</sup>
GeO	700 decomposes	-	-	-
GeO <sub>2</sub>	1115	-	-	4.25 x10 <sup>3</sup>
Se	220.5	685	0.24 @ 300°C	4.81 x10 <sup>3</sup>
SeO <sub>2</sub>	340	315 sublimes	200.7 @ 300°C	3.95 x10 <sup>3</sup>
SeO <sub>3</sub>	118	Sublimes	-	3.44 x10 <sup>3</sup>
Te	449.51	988	-	6.24 x10 <sup>3</sup>
TeO <sub>2</sub>	733	1245	-	5.9 x10 <sup>3</sup>
TeO <sub>3</sub>	430	-	-	5.07 x10 <sup>3</sup>

KEY: - means not known.

It can be seen from Table 3.1 that the vapour pressure of As and Se is 0.12 mm Hg and 0.24 mm Hg at 300°C while their relative oxide's vapour pressure is 49.19

mm Hg and 200.7 mm Hg at 300°C, respectively. The large difference in vapour pressure of oxides and element in the temperature range below the boiling point and around the melting point of the chalcogenide element gives this purification treatment good feasibility.

The temperature scheme of the purification process is shown in Table 3.2.

Table 3.2 The temperature scheme used for the individual purification of Se and As and observations.

Stage	Schedule		Phenomenon		Pressure(Pa)
			Se	As	
1	25°C → 200°C @ 200°C/h		No	No	$2 \times 10^{-2}$
2	200°C → 250°C @ 100°C/ h	212 °C	Red deposit	No	$2 \times 10^{-2}$
		235 °C	Dark red deposit		
		250 °C	Black deposit		
3	Dwell at 250°C for 1 h	15 mins	-	White deposit appears near 250 °C	$2 \times 10^{-2}$
		30 mins	-		
		45 mins	-		
		1 h	-		
4	250°C → 300°C @ 100°C/h		-	Grey deposit appears	$2 \times 10^{-2}$
5	Dwell at 300°C for 1 h		-	Grey and black deposit appears	$2 \times 10^{-2}$

### 3.1.3 Batching.

The composition of the glass was calculated in atomic percentage using a Basic computer program written by Dr David Furniss. As discussed in section 2.6, the composition of  $\text{As}_{40}\text{Se}_{60}$  and  $\text{Ge}_{10}\text{As}_{23.4}\text{Se}_{66.6}$  were known to have good glass forming ability, however, glass forming ability is very sensitive to the material composition, so the batched amount of material should be very accurate. The glovebox (MBraun 150B-G) used for batching is shown in figure 3.3.

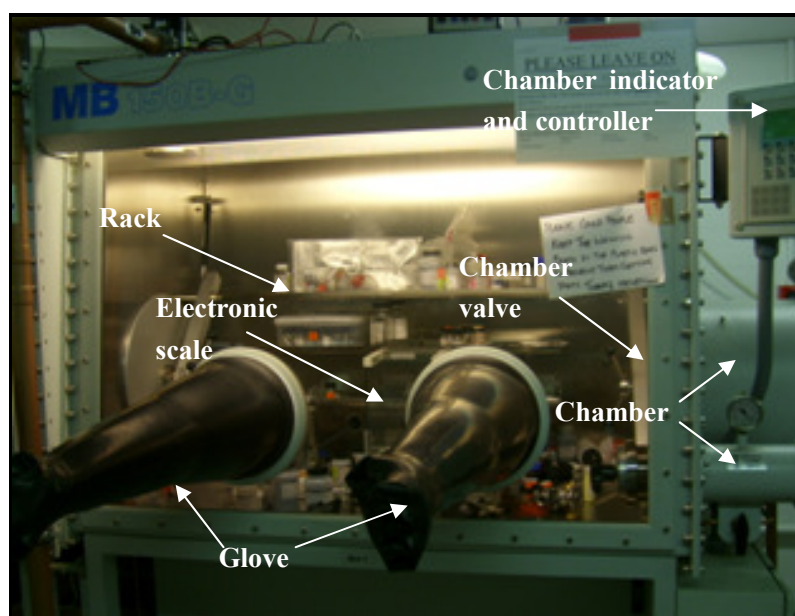


Figure 3.3 MBraun 150B-G glove box, in which elemental chalcogenide was stored and batched. The atmosphere of glovebox was kept  $< 0.1$  ppm  $\text{O}_2$  and  $< 0.1$  ppm  $\text{H}_2\text{O}$ .

The atmosphere inside of the glovebox was  $\text{N}_2$  (MBraun 150B-G,  $\leq 0.1$  ppm  $\text{O}_2$ ,  $\leq 0.1$  ppm  $\text{H}_2\text{O}$ ). Everything that went into the glovebox was first placed in the anti-chamber which was evacuated and refilled with  $\text{N}_2$  three times, before items were moved into the main body of the glovebox.

An electric balance inside the glovebox (Sartorius, model BP221S accurate to  $\pm 0.1\text{mg}$ ) was used to weigh the batch. The accuracy of the read-out value was nominally 4 decimal places. However, this varied because of static electricity build-up in the dry glovebox atmosphere. The batched material was weighed in a plastic boat (Fisher, rectangular with a sloped side for ease of pouring, 100ml, anti-static) shown in figure 3.4, with a new boat used respectively for each precursor, respectively.

From figures 3.4 (a) to (c), it can be seen that the surfaces of the as-received As and Se elements were not shiny. It is believed that the surfaces had reacted with oxygen to form the relevant oxide. It is difficult to isolate the elemental batch materials from contact with  $\text{O}_2$ , so precursor material purification was necessary.

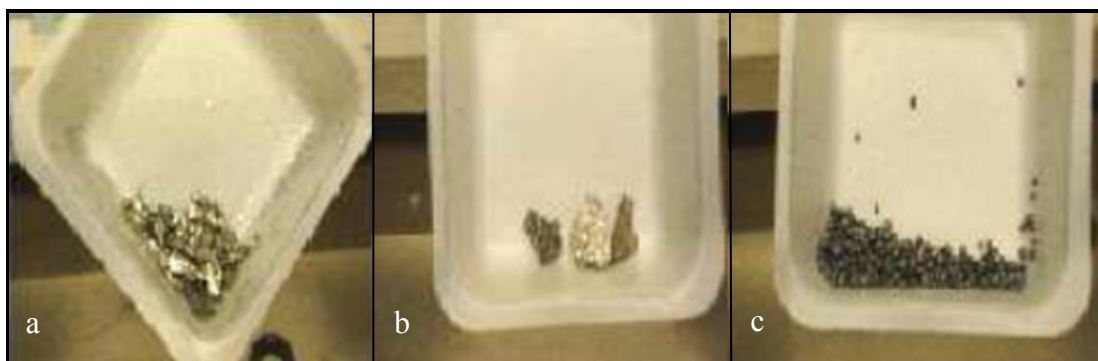


Figure 3.4 (a) Germanium (Cerac 99.999% purity, 3 ~ 6 mm pieces); (b) arsenic (Furukawa 99.99999% purity, 4 ~ 20 mm pieces); (c) selenium (Cerac 99.999% purity, ~ 3 mm pieces).

### **3.1.4 Operation of the vacuum system to seal the batch inside the silica glass ampoule under vacuum.**

The batched material inside the silica ampoule was isolated using a Saunder's

valve for transfer from the glovebox (figure 3.3, section 3.1.3) into the ambient air atmosphere and sealing. A vacuum system consisting of a roughing pump (VRC 200-7.0) and a diffusion pump (Edwards B30207240) was employed to evacuate the ampoule, as depicted in figure 3.5. This was the same vacuum system as was applied during material purification and the stages of operation were:

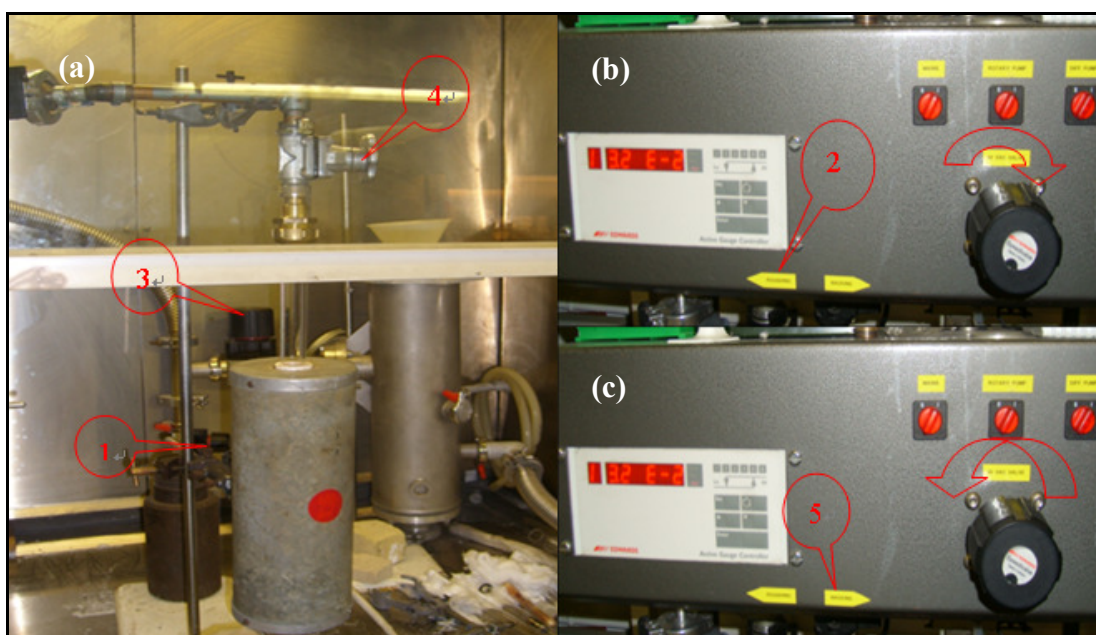


Figure 3.5 Shown is (a) the vacuum line, (b) the rotary pump and (c) the diffusion pump controllers. The order of operation is shown labelled 1-5 for the operation of each successive valve knob of the vacuum system. Please see the main text for a description of stages 1-5.

(1) The valve marked 1 (figure 3.5) was closed to isolate the vacuum system from the ambient atmosphere.

(2) The knob of the rotary pump (VRC 200-7.0) controller was turned clockwise and the knob marked 2 was flipped to “Roughing” to enable the rotary pump to work in the state of “Roughing”.

(3) The valve marked 3 was opened to link the rotary pump and the pipe to the ampoule.

(4) Valve 4 was opened to link the ampoule to the vacuum system, the pressure shown by the Pirani gauge first rose and then decreased again, the pressure normally decreased to nearly  $10\text{E-}2$  mbar (1 Pa).

(5) The knob of the diffusion pump controller was turned anti-clockwise and the knob marked 5 was flipped to the state of “backing” to enable the diffusion pump (Edwards B30207240) to reduce the pressure, shown by a Penning gauge decreased to less than  $10\text{E-}4$  mbar ( $10^{-2}$  Pa).

Before operating the vacuum system, two litres ( $\text{dm}^3$ ) of liquid  $\text{N}_2$  (BOC) were poured into the cold trap which was used to prevent impurities from going into the pumps.

### **3.1.5 Operation of sealing the ampoule.**

Evacuation of the ampoule was applied before sealing it in order to remove the glove box nitrogen containing trace oxygen which might subsequently react with the melt. As shown in figure 3.6(a), after batching, the ampoule was sealed with an oxy-propane (CALOR Gas) torch (Jensons, Junior Jet 7). The flame heated the ampoule evenly in a radial direction to encourage the silica glass to heat up evenly. The wall of the ampoule began to collapse inwards when the ampoule was heated up to its  $T_g$  under a low internal pressure ( $10^2$  Pa), and then a small load was applied to help the collapsed wall to form a seal, so the material was enclosed in vacuum. Then, as shown in figure 3.6(b) and (c) a section of wire (Kanthal, 0.65 mm gauge) and a band of thermal blanket (Superwool™ 607™ Blanket) were

used to make a holder to suspend the ampoule inside the melting furnace, and to wrap the ampoule to insulate it carefully from the sealed end of the ampoule to the level where the top of the material was in the ampoule. The ampoule was thus wedged into the rocking furnace (Instron, TF105/4.5/1ZF, tube ID 86mm, with a controller Eurotherm 2408) with the ampoule lying in the hot zone of the melting furnace as in figure 3.6 (d).

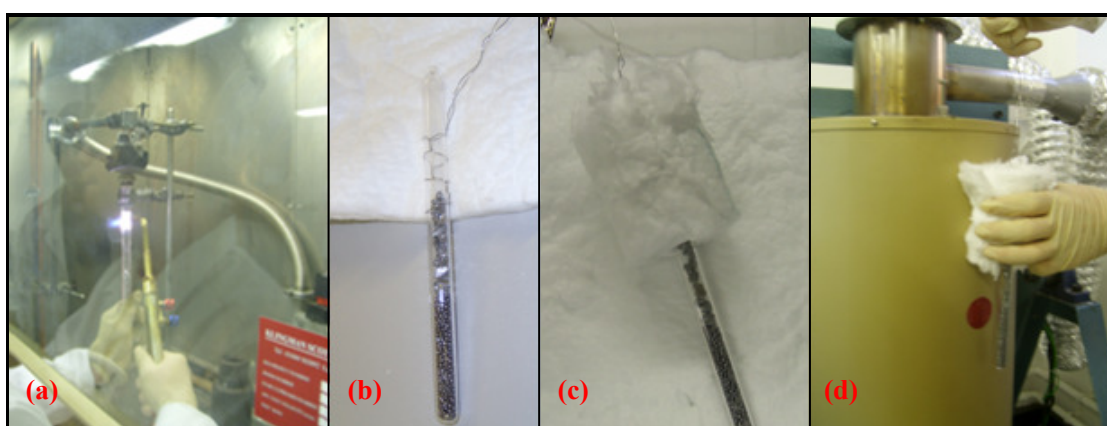


Figure 3.6 (a) Sealing of silica glass ampoule with batch inside; (b) attaching wire to ampoule; (c) attaching isolation blanket to ampoule and (d) loading prepared ampoule into melting furnace.

The temperature profile of the melting furnace was measured to decide the position in which to place the ampoule. From the result of the measurement, the real temperature at the centre of the furnace could be related to the nominal reading. This will be discussed further in section 3.1.7 (see figure 3.9).

### **3.1.6 Glass melting, quenching, and annealing.**

The melt schedule was dependent on chalcogenide glass composition due to the sensitive composition dependence of  $T_g$  and  $T_l$  on the glass composition. Because the molten melt is a viscous liquid above  $T_g$ , and even above  $T_l$ , thus, in order to

ensure the melting was carried out in a real thermodynamic equilibrium liquid state, the melting temperature should be higher than  $T_l$ . The temperature scheme of glass melting, quenching and annealing is shown in Table 3.3.

Table 3.3 Temperature schedule of chalcogenide glass melting, quenching and annealing. (Note: step 1 was an arbitrary dwell at RT to allow the manual quenching to be carried at a convenient time. RT is room temperature.)

Stage	Melting	
	Schedule( $\text{Ge}_{10}\text{As}_{23.4}\text{Se}_{66.6}$ )	Schedule ( $\text{As}_{40}\text{Se}_{60}$ )
1	RT dwell for the required h to start	RT dwell for required h to start
2	RT to 200°C @ 200°C/h	RT to 200°C @ 200°C/h
3	200 to 930°C @ 40°C/h (rocking on)	200 to 800°C @ 40°C/h (rocking on)
4	930°C for 12h	800°C for 12h
5	930 to 800°C @ 60°C/h(40°C/h)	800 to 650°C @ 60°C/h(40°C/h)
6	800°C until anneal for 2 h (rocking off)	650°C until anneal for 2 h (rocking off)
	Quenching	
	Air & liquid metal	air
	Annealing	
1	190°C for 5 min	Dwell @ 180°C for 1 h
2	190°C → 180°C @ 5°C/h	180°C → 140°C @ 5°C/h
3	Dwell @ 180°C for 1 h	140°C → 25°C @ 20°C/h
4	180°C → 140°C @ 5°C/h	
5	140°C → 25°C @ 20°C/h	

The melting furnace was set to rock  $\pm 30^\circ$  about the horizontal axial axis during the heating procedure to achieve better homogeneity of the molten components [figure 3.7(a)]. The hold time at the cycle extremes was about 20 seconds.

The quenching scheme was chosen to meet the demands of the cooling rate needed. As discussed before, the cooling rate should be large enough to prevent crystallisation and yet in consideration of the glass quality a relative slow cooling

process is needed. Because the As-Se glass is more stable than the Ge-As-Se ternary glass, air quenching, which was manipulated by holding the ampoule vertically and stable in air, was utilised for As-Se glass. A combination of air and liquid metal quenching was applied for Ge-As-Se. When the molten components became solid, the ampoule was reheated slightly within the annealing furnace around  $T_g$  to remove the thermal stress without glass crystallisation, and then cooled down slowly through the  $T_g$  region (see Table 3.3). The glass preform was formed after the complete melting, quenching and annealing schedule.



Figure 3.7 (a) Rocking furnace for chalcogenide glass melting; (b) furnace controller; (c) air quenching and (d) liquid metal quenching pot.

### 3.1.7 Annealing furnace temperature profile.

Before annealing could be properly carried out, the annealing furnace (annealing Furnace No.4) had to be characterised. The temperature varied along the length of

the furnace, and so the temperature profile of the furnace was measured. The annealing furnace (Instron, TF105/4.5/1ZF, tube ID 86mm, with a controller Eurotherm 2408) was set to nominal temperatures of 180°C and 245°C, respectively. A schematic presentation of the setup is shown in figure 3.8.

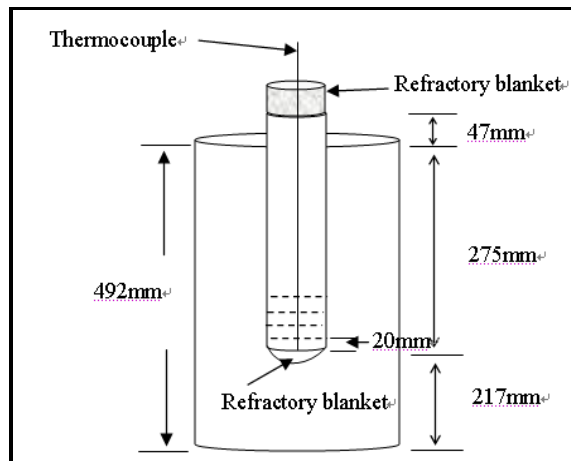


Figure 3.8 Schematic presentation of the set up for measuring the temperature profile of annealing furnace No.4 (TF 105/4.5/IZF, tube ID 86 mm).

The furnace temperature profile was measured by following the steps below: (1) the thermocouple was inserted into the tube furnace. The length of the furnace work tube was taken as a relative point position, taking the top surface of the furnace as the 0 mm point. The bottom of the furnace work tube had been filled with a refractory blanket to isolate the inner hot zone from the outside temperature condition. So the measurement was started at the point above the blanket. (2) The set temperature was adjusted to 180°C and then the furnace was left for four hours to reach thermal equilibrium. (3) The thermocouple was carefully withdrawn with each interval of 20 mm, and kept stationary for several minutes to reach thermal equilibrium, and the measured temperature recorded. The experiment was

repeated with a set temperature of 245°C. The temperature profile at 180°C and 245°C of annealing furnace No.4 are shown in figures 3.9(a) and (b), respectively.

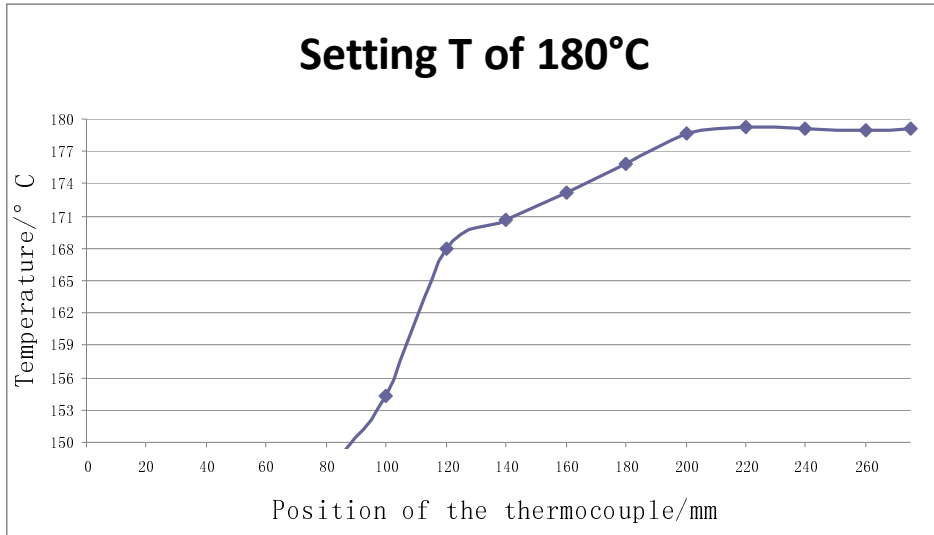


Figure 3.9 (a) Plot of the temperature profile of Furnace No.4 (Instron, TF105/4.5/1ZF, tube ID 86mm, with a controller Eurotherm 2408) at the set temperature of 180°C. Note zero position was at the top of the furnace.

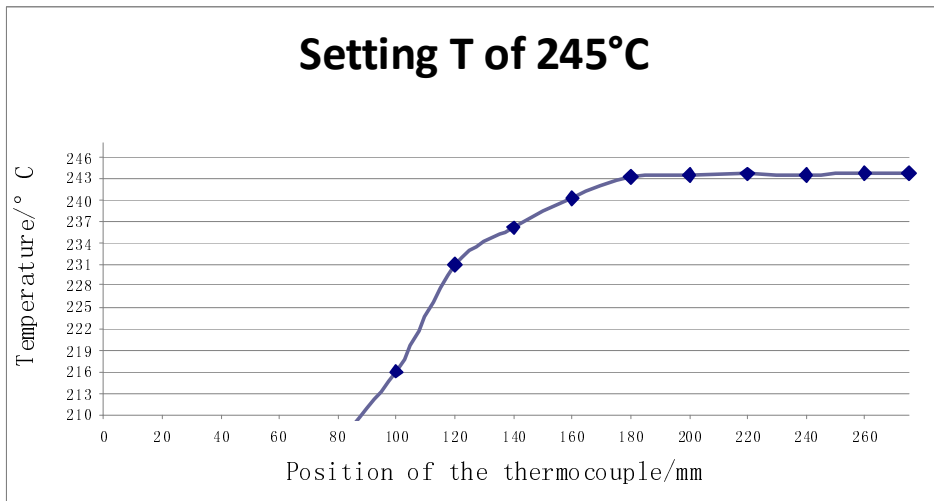


Figure 3.9 (b) Plot of the temperature profile of Furnace No.4 (Instron, TF105/4.5/1ZF, tube ID 86mm, with a controller Eurotherm 2408) at the set temperature of 245°C. Note that the zero position was at the top of the furnace.

For annealing a rotational casted tube (see section 3.3.4), a hot zone long enough in the furnace for the ampoule length to be at constant temperature is needed.

Thus, a section of aluminium cylinder of 30 mm / 83 mm ID /OD and 280 mm length was inserted into the furnace work tube of annealing furnace No.3, which is the same with annealing furnace No.4, to conduct heat through the length of the work tube homogeneously (see figure 3.10). Without the aluminium cylinder, the heat would not be conducted evenly. The temperature profile of modified Furnace No.3 is shown in figure 3.11.

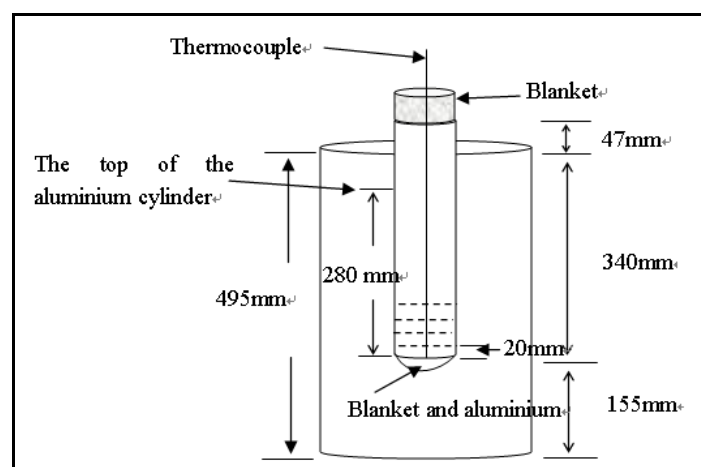


Figure 3.10 Schematic presentation of the set up for measuring the temperature profile of annealing furnace No.3 (TF 105/4.5/IZF, tube ID 86 mm) temperature measurement.

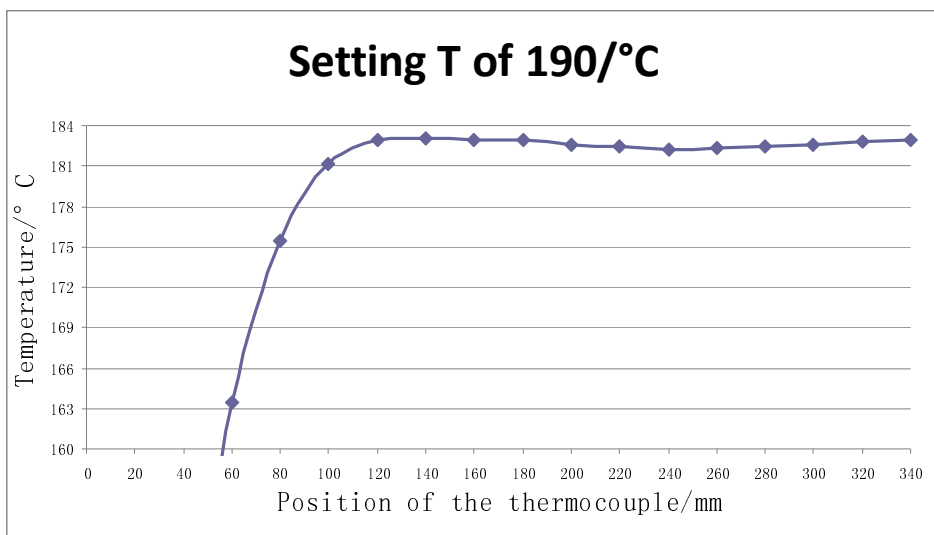


Figure 3.11 Plot of the temperature profile of Furnace No.3 (Instron, TF105/4.5/1ZF, tube ID 86mm, with a controller Eurotherm 2408) at a set temperature of 190°C. The nominal temperature was higher than the real temperature by 7°C across the hot zone.

The hot zoon is now uniformed to  $\pm 1^\circ\text{C}$  over a length of 220 mm which is long enough to anneal the rotationally casted tube.

### 3.1.8 Sample preparation: cutting, grinding and polishing.

A diamond coated copper circular cutting saw (Buehler Isomet: low speed saw and diamond coated wafering blade 15HC 100 mm OD, 0.35 mm thickness) was utilised to open the ampoule after the chalcogenide glass had been annealed, this was achieved by cutting several scores from the bottom of the ampoule through the length of the ampoule in even intervals in the ambient atmosphere. The preform was rinsed with acetone (Fisher Scientific, analytical reagent grade) air-dried and placed in a sample bag labelled with the samples' identification code. If the preform was to undergo glass characterisation or extrusion, it was then cut

into a disk with the required thickness and ground and polished to a 1  $\mu\text{m}$  finish.

## **3.2 Glass characterisation**

As discussed above, the transparent window (the transmission range),  $T_g$ , the composition of the chalcogenide glass, the quality and the mechanical properties of the chalcogenide glass must be analysed. A series of characterisation techniques has been utilised in glass characterisation as shall be discussed in sections 3.2.1 to 3.2.5 below.

### **3.2.1 X-ray diffraction (XRD)**

(1) Principle and methodology of XRD [3.1, 3.2, 3.4]

The aim of X-ray diffraction (XRD) is to judge whether there is crystalline substance in the glass samples. 0.154 nm wavelength X-rays were emitted from a copper source and cast on the rotated sample, then a diffraction pattern was collected using a Siemens Krystalloflex 810 diffractometer. The diffraction pattern of an amorphous glass lacks sharp peaks which appear for a crystal lattice corresponding to the crystal lattice parameters; in a long range periodic structure X-ray diffraction obeys Bragg's law and diffraction occurs at particular angles according to the X-ray wavelength and the interval between the atomic planes.

This relationship is given by the Bragg equation (3.1) [3.1, 3.2, 3.4]:

$$n\lambda = 2d \sin \theta \quad (3.1)$$

where  $n$  is an integer,  $\lambda$  is the wavelength of the X-ray,  $d$  is the interval of the

atom planes, and  $\theta$  is the angle of incidence of the X-ray with respect to the atomic plane.

## (2) XRD methodology

The chalcogenide glass sample was crushed to fine powder using agate mortar and a pestle fisher. Then, an aluminium sample holder was used to pack the sample powder, whose surface should be made flat by sliding a silicate glass microscope slide over the top of the powder to flatten the powder and make it smooth. The sample was scanned from  $5^{\circ}2\theta$  to  $80^{\circ}2\theta$ , with a step size of  $0.02^{\circ}2\theta$ , using a Philips, D 500 X-ray diffractometer at 40 kV voltage and 25 mA current [3.1, 3.2, 3.4].

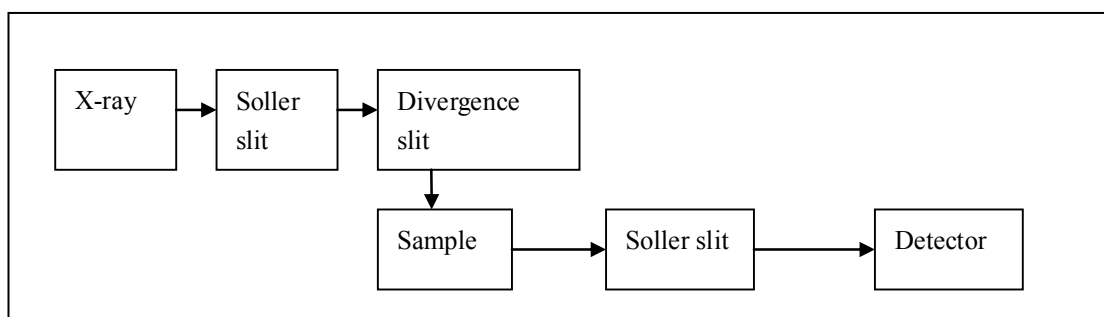


Figure 3.12 Schematic chart of X-ray diffractometer.

It is shown in figure 3.12 that the X-ray is gathered by the Soller slit and then goes through the divergence slit to be incident onto the sample. The diffracted beams were gathered by the Soller slit before being recorded by the detector.

### 3.2.2 Differential thermal analysis (DTA).

#### (1) Principle of DTA

Differential thermal analysis (DTA) is used to characterise the glass transition temperature of a glass. It measures the temperature difference ( $\Delta T$ ) between the sample ampoule and a reference ampoule when they are under the same temperature programme for an isothermal or an isochronal heating process.  $\Delta T$  is thus defined as:

$$\Delta T = T_{\text{sample}} - T_{\text{reference}} \quad (3.2)$$

where  $T_{\text{sample}}$  and  $T_{\text{reference}}$  are the temperatures of chalcogenide glass sample sealed under vacuum into a silica ampoule and the empty reference matched ampoule. A schematic diagram of DTA operation is shown in figure 3.13. The chalcogenide sample and reference, in their respective silica ampoule containment, were placed in their respective platinum holder side by side in a heating block which was heated at a constant rate; identical thermocouples were connected 'back to back' to the holders. As long as the sample and the reference were at a same temperature the thermocouple did not experience any net voltage. When a thermal event occurred in the sample, the  $\Delta T$ , would exist between sample and reference, which could be detected by the thermocouple.

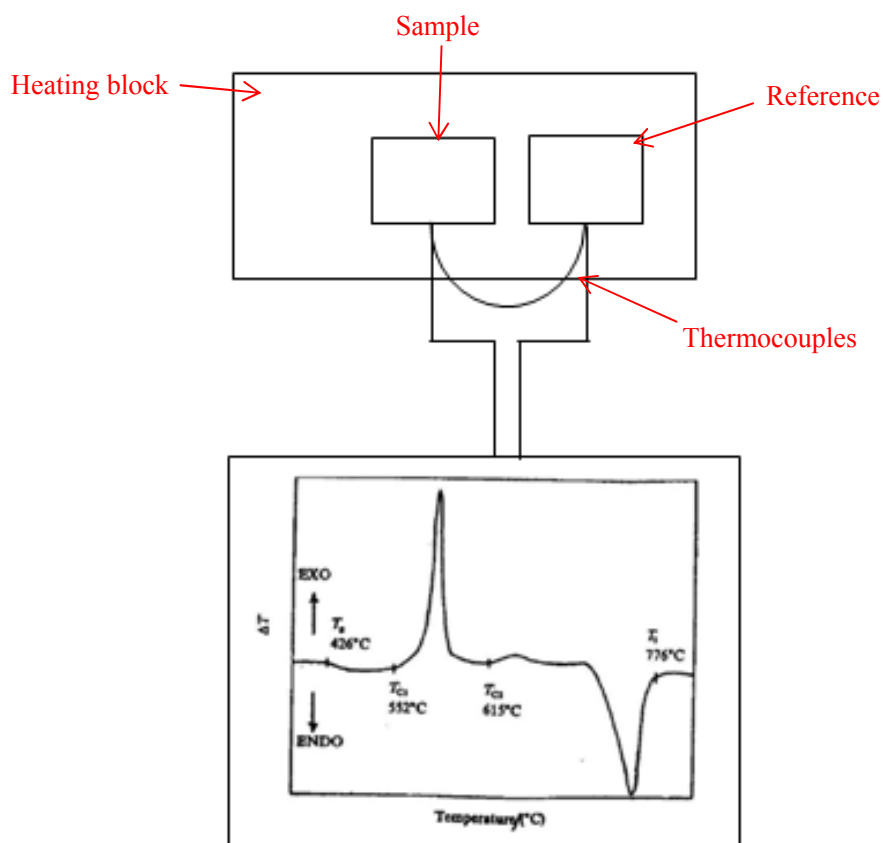


Figure 3.13 Schematic presentation of the principle of DTA.

## (2) Sample preparation and methodology of DTA

Small chunks of glass were broken from the rod of the glass by using a mortar and pestle (Agate, Fisher) and stainless steel tweezers. The sample was weighed, and sample weight was  $100 \text{ mg} \pm 1 \text{ mg}$ , with a balance (Sartorius, model BP221S accurate to  $\pm 0.1 \text{ mg}$ ) at ambient temperature. Then the chalcogenide glass samples were sealed inside a silica ampoule (Brambach, OD  $\varnothing \leq 4.7 \text{ mm}$ , ID  $\sim 3 \text{ mm}$ ) under vacuum operation (see section 3.1.5). An empty silica ampoule was sealed under vacuum as the reference sample and it ideally had the same mass (tolerance of  $\pm 20 \text{ mg}$ ) as the sealed ampoule for containing chalcogenide glass samples.

A Perkin Elmer DTA 7 analyser was applied to obtain the DTA curves. The characteristic temperatures are defined by the endothermic peaks ( $T_g$  and  $T_m$ ) and the exothermic peaks ( $T_c$ ) when the  $\Delta T$  was plotted versus temperature from room temperature to 800°C or 900°C (depended on composition) with the heating rate of 10 °C/min under a flowing helium (BOC) atmosphere. In order to compare different compositions with the same glass thermal history condition, a thermal history treatment was imposed and operated firstly by heating the chalcogenide sample at 10°C/min to ~20°C below  $T_g$  and then cooling it down to room temperature with a rate of 10 °C/min. The calibration of the DTA was done by using a pure element with a known melting point, Al, whose melting point is 660.32°C, is convenient for calibration over the temperature range of interest for chalcogenide glass. The DTA was calibrated when it had not been in use for over two months or when a different temperature range was required.

### **3.2.3 Thermomechanical analysis (TMA).**

The viscosity and thermal expansion coefficient of a chalcogenide glass is critical for glass shaping. The thermal mechanical analysis (TMA) was applied to do these two types of measurement.

#### 3.2.3.1 Viscosity / temperature relationship.

##### (1) Principle of viscosity measurement

Viscosity is defined as the parameter to measure the resistance of a fluid to being deformed by either shear stress or extensional stress [3.5]. The chalcogenide glass

is considered as an elastic solid below its  $T_g$ . In the  $T_g$  region, the chalcogenide glass behaves viscoelastically and the supercooled chalcogenide melt exhibits viscous flow above  $T_g$ .

The definition of viscosity can be drawn from the schematic diagram shown in figure 3.14.

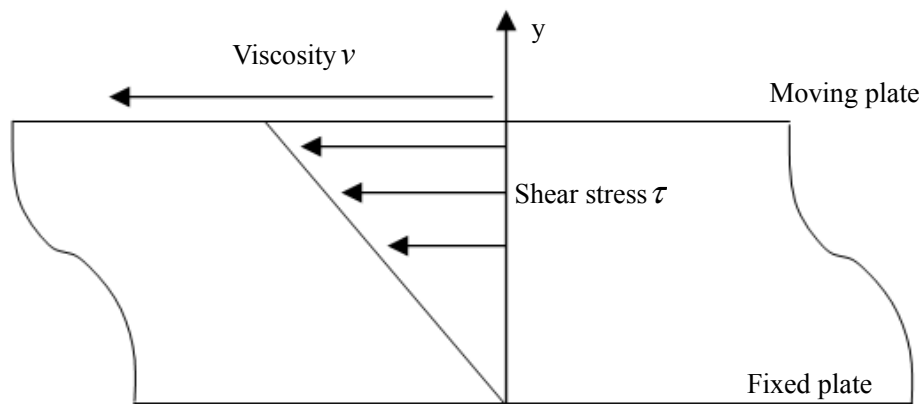


Figure 3.14 Schematic diagram of the relationship between shear stress and viscosity from which the equation (3.3) is drawn.

Newton postulated the equation of viscosity:

$$\tau = \eta \frac{dv}{dy} \quad (3.3)$$

where  $\eta$  (Pas) is the viscosity of the fluid,  $dv/dy$  is the velocity gradient ( $s^{-1}$ ), and  $\tau$  is the shear stress (Pa). It indicates that, for the straight, parallel and uniform flow, the shear stress  $\tau$  between two layers is in the direction perpendicular to the layers and proportional to the velocity gradient  $dv/dy$  [3.5], with the proportionality constant equal to the viscosity.

## (2) Sample preparation and methodology of viscosity measurement

The sample for viscosity measurement was prepared from a chalcogenide glass rod (4 mm OD), which was obtained by re-melting small chalcogenide glass chunks inside a silica ampoule (250 mm length, 4 mm / 7 mm of ID / OD) under vacuum, quenching and annealing. Then the chalcogenide glass rod (~ 50 to 60 mm length, 4 mm OD) was mounted onto an aluminium block with wax. Then two perpendicular cuts (using Isomet Low Speed Saw with a Beuhler diamond wafering blade) were applied along its length. It was critical to ensure that the two facets of the sample (4 mm OD, ~2.7 mm height) were parallel with each other and that the quality of the surface was as perfect as possible. In order to get parallel facets, perpendicular cuts were applied along the length of the rod in one go to get several discs.

The viscosity measurement was carried out using a Perkin Elmer TMA7 equipment, as shown in figure 3.15. The sample was clamped with a stainless steel polished foot and a bottom plate [see the schematic diagram in figure 3.16(a)]. The stainless steel polished foot was connected together with the silica pushrod of the TMA through which the load was applied to the top facet of the sample [see equipment setup figure 3.15 (a) and (b)]. The applied force was set to 50 mN for obtaining the data in the low viscosity range and ~400 to 500 mN for obtaining the data in the high viscosity range. The temperature was increased by 40°C / min to  $T_g$  and then the ramping rate was reduced to 10 °C / min while the

furnace was purged with helium (BOC). The programmed measurement was always stopped before the diameter of the sample expanded to 7 mm, because this was the size of the stainless plate in the equipment. The relationships of height variation versus temperature and time were recorded by means of the Perkin Elmer software.

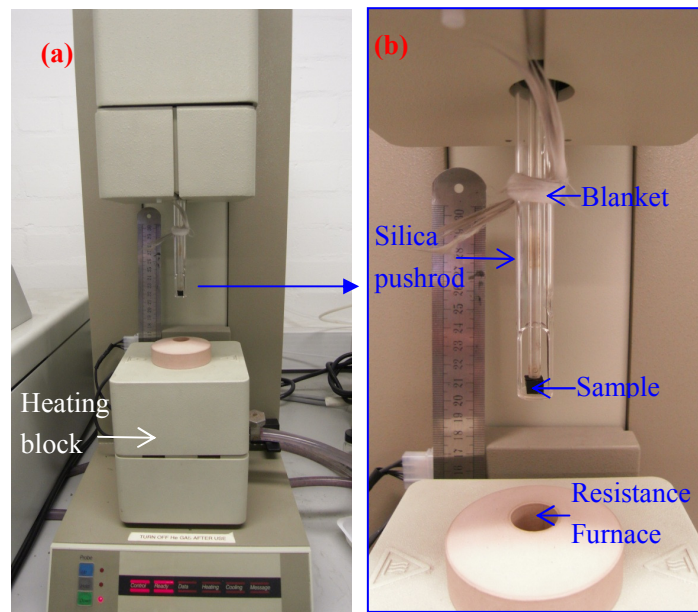


Figure 3.15 (a) Thermomechanical analyser (Perkin Elmer TMA7) and (b) a close view of the setup.

The measurement process is shown schematically in figures 3.16(a) and 3.16(b).

The viscosity was calculated using the equation 3.4 [3.7]:

$$\eta = \frac{2\pi F h^5(t)}{3V[2\pi h^3(t) + V] \frac{dh(t)}{dT}} \quad (3.4)$$

where  $\eta$  is viscosity in Pa,  $h(t)$  is the sample length at the particular time  $t$ ,  $F$  is the applied force,  $V$  is the volume of the sample and  $T$  is the temperature.

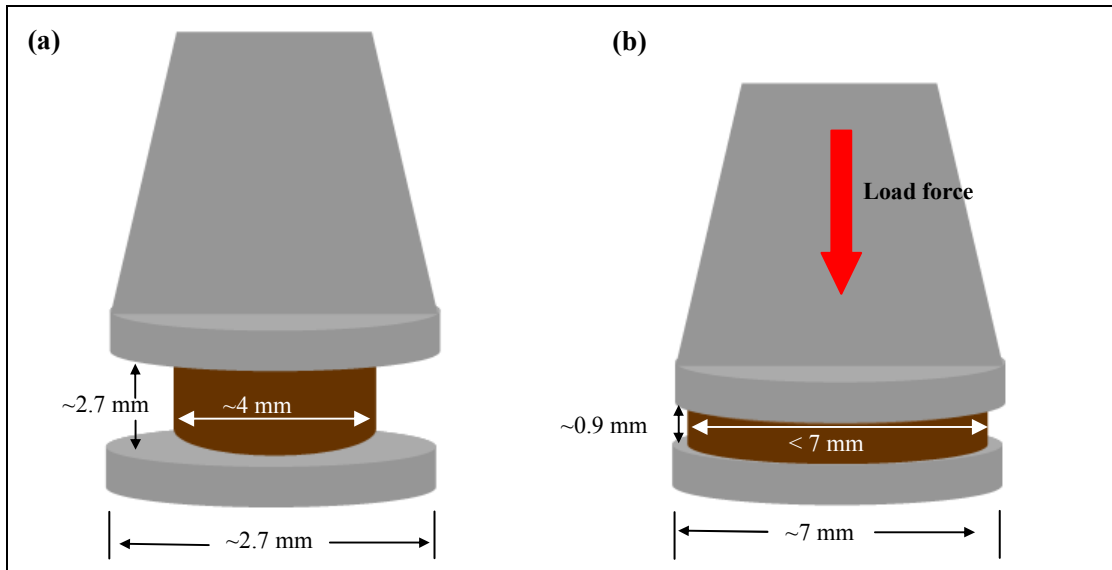


Figure 3.16 Schematic diagram of the state of the sample before and after the viscosity measurement. (a) A chalcogenide glass rod with ~ 4 mm OD and ~ 2.7 mm height was clamped by the 7 mm OD stainless plates; (b) the chalcogenide glass rod was deformed under heat treatment and load force.

### 3.2.3.2 Thermal expansion coefficient ( $\alpha$ ).

#### (1) Principle of thermal expansion coefficient measurement

The linear thermal expansion coefficient ( $\alpha$ ) is a parameter to measure how significant the material's linear dimension changes when it is under heat treatment.

Most glasses expand on heating and shrink on cooling. Knowledge of  $\alpha$  of a chalcogenide glass is essential for choosing the appropriate glass pairs to fabricate core-clad structure preforms and microstructured optical fibres, because the mismatch of the  $\alpha$  between the interface of the layers may lead to fibre cracks during the temperature variation below  $T_g$  where the residual tension cannot be released.

The  $\alpha$  in the  $T_g$  region may be defined as the equation [3.7]:

$$\alpha = \frac{1}{h_0} \frac{dh(t)}{dT} \quad (3.5)$$

where  $\alpha$  is the thermal expansion coefficient,  $h_0$  is the original length of the sample,  $h(t)$  is the sample's height at a particular time,  $T$  is the temperature and  $dh(t) / dT$  is the differential coefficient of sample's length versus temperature.

(2) Sample preparation and methodology of  $\alpha$  measurement

The sample for  $\alpha$  measurement was prepared from the chalcogenide rod (10 mm OD). The essential issue is that the two opposing facets of the sample, (a) and (b) on figure 3.17, have to be parallel and flat. The schematic figure 3.17 describes the procedure of preparing a sample for measurement of  $\alpha$ .

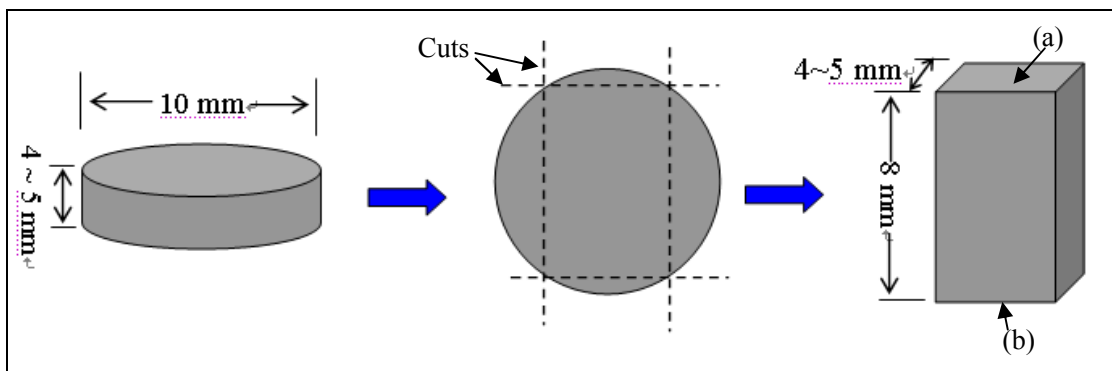


Figure 3.17 Schematic diagram of preparing a sample for measurement of linear thermal expansion coefficient  $\alpha$ .

As shown in figure 3.17, the cylinder disc (10 mm OD, 4~5 mm height) was cut from the chalcogenide rod and mounted onto an aluminium block with wax. With a Buehler Isomet low speed saw and diamond wafering blade (15HC 100 mm OD, thickness of 0.35 mm), four cuts were carried out to remove the round edges to leave the parallel and flat facets.

The  $\alpha$  measurement was carried out by employing a Perkin Elmer TMA7

equipment (see Figure 3.15). The setting up of the equipment and the operation procedure were similar to the viscosity measurement which has been described in section 3.2.3.1. The difference was that prior to the measurement of  $\alpha$  the sample was heated to close to  $T_g$ , but not exceeding it excessively, under the applied force of 50mN and then cooled to room temperature with the cooling rate of 10°C / min in order to get the same thermal history for all samples to aid comparison. Afterwards, the measurement of  $\alpha$  was undertaken. The sample was heated to the desired temperature with the ramping rate of 5 °C / min and the control program was stopped at the very moment when the sample was almost about to distort.

### **3.2.4 Optical microscopy.**

Optical microscopy (Nikon digital camera DXM1200F) was applied to observe the details of the sample surface down to  $> 1\mu\text{m}$  resolution. It can assist the judgement of the surface quality of a polished bulk glass or the cross-section of a fibre.

The optical microscope is constructed as follows. (a) Eyepiece – a cylinder containing two or more lenses to bring the image to the focus of the eye. (b) Objective lens – a cylinder containing one or more lenses to collect light from sample. The magnification values were 10x, 20x and 40x. (c) Stage – a platform below the objective lens which supports the object being viewed. A hole in the

centre of the stage allows light to pass through and illuminate the object. The stage has arms to hold slides where the object is mounted. (d) Light source – below the stage, light is provided and controlled by increasing or decreasing the resistance to change the brightness of the light.

The sample was mounted onto a microscope slide and placed on the item platform. The alignment of the sample relative to the objective lens was carried out in the sequence of applying the lens with low magnification first and then moving to higher magnification. A software package was employed to capture the picture digitally.

### **3.2.5 Environmental scanning electron microscope (ESEM) with energy dispersive X-ray spectroscopy (EDX).**

The environmental scanning electron microscope (ESEM) was applied to view the sample at a much higher resolution (accurate to 2 nm) than the optical microscope (accurate to  $\geq 1\mu\text{m}$ ) and the energy dispersive X-ray analysis (EDX) was used to determine the stoichiometry of the chalcogenide glass sample.

The scanning electron microscope (SEM) operated as shown in figure 3.18. The ESEM was operated at 1 atmosphere pressure under nitrogen.

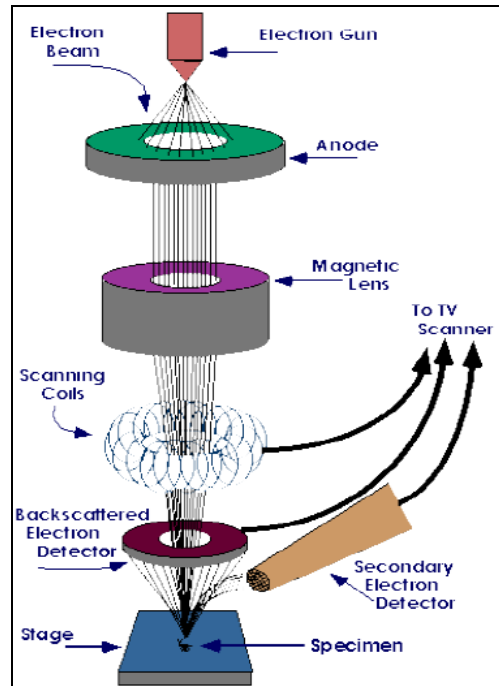


Figure 3.18 Schematic chart of the SEM. The electron beam emitted from the electron gun, which passed through a magnetic lens and scanning coils interacted with the sample producing different images. The types of images produced were secondary electron imaging (SEI), back-scattered electrons (BSE) and energy dispersive X-ray spectroscopy (EDS) analysis. [3.8]

The secondary electron imaging (SEI) mode back-scattered electron (BSE) imaging mode was applied to view the surface of the sample. The sample was hit by a primary electron beam, so the secondary electrons were released from the surface of the sample. The secondary electrons or back-scattered electrons were detected, amplified and image processed to build the image of the sample. The SEI mode is more dependent on the roughness of the sample and has better resolution than the BSE mode, thus, the SEI mode provides a better definition of the surface of the sample. The BSE mode has larger imaging area than SEI mode, also, it provides enough details of a sample with a smooth surface. Thus, BSE mode was used here.

For the EDX (energy X-ray dispersive analysis), a high energy electron beam was launched into the sample, raising a vacant energy level in the emitted electron shell, with a specific energy difference between the vacant and higher energy level. An X-ray, which characterises the energy difference between the two shells and the atomic structure of the element, is subsequently emitted due to the energy difference of the two shells. The identity of the element can be addressed with these X-rays [3.1, 3.2, 3.4].

## (2) Sample preparation and ESEM-EDX methodology

The ways of preparing the samples for different purposes are different. For viewing the surface of the sample, the chalcogenide glass sample was broken down to a few chunks and placed onto an aluminium stub with a carbon coated sticky tab. For viewing the cross-section of fibres, the samples were mounted on “blue tac” and mounted in epoxy. The procedures of cutting the epoxy, grinding and polishing to achieve a surface of 1  $\mu\text{m}$  finish were then followed. Afterwards, the epoxied sample was carbon coated (Edwards, Coating System E306A).

ESEM equipment (EDAX, CDUTM LEAPT<sup>TM</sup> detector, model: New XL-30 139-2.5) was employed. The sample holders were fitted under the electron beam in the ESEM chamber (Figure 3.19). The sample chamber was filled with N<sub>2</sub> gas (BOC) and the EDX analysis was operated at 15 kV and 10 mm working distance [3.1, 3.2, 3.4]. The ESEM imaging and EDX analysis were carried out in-house with the kind help of Dr. Nigel Neate (Technician in School of M3 in the

University of Nottingham).

### 3.2.6 Fourier transform infrared spectrometry (FTIR).

#### (1) Principle and methodology of FTIR

Fourier transform infrared spectrometry (FTIR) is applied to investigate the transparency of both bulk and fibre glass samples. When the IR radiation is incident on the sample, the bonds within the atomic structure absorb energy at their vibrational frequency (wavelength) by resonance. So the transparent window and what kinds of bonds exist in the sample can be investigated. The schematic presentation of a FTIR spectrometer is shown in figure 3.19.

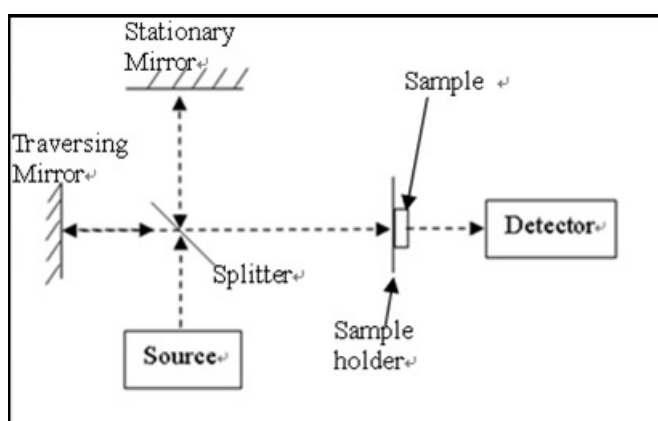


Figure 3.19 The schematic presentation of the FTIR spectrometer (Bruker IF 66 FTIR instrument) configuration.

The light emitted from the broadband source is split by the beam splitter into two paths, one is reflected by the stationary mirror and the other is reflected by the traversing mirror. The path difference between these two paths leads to constructive and destructive interference of the converged beams. Through a Fourier transform, an interference pattern is obtained, so the extrinsic or intrinsic absorption and scattering properties of a tested glass may be analysed from the

FTIR loss spectra [3.1, 3.2, 3.4]. The source, splitter and detector are chosen according to the light's wavelength range.

## (2) Sample preparation and FTIR methodology

The chalcogenide glass was cut to a disc of about 3mm thick and the two opposite circular faces polished to 1  $\mu\text{m}$  finish. The FTIR spectrometer (Bruker IF 66 FTIR instrument) was purged using dry air with  $\text{CO}_2$ ,  $\text{H}_2\text{O}$  removed (Parker Filtration, FT-IT purge gas generator, 75-52-12VDC) for 10 minutes to remove water and carbon dioxide from the spectrometer sample compartment and box, since these absorb light at wavelengths within the chalcogenide transparent window. Three circular apertures, with diameter of 1 mm, 3 mm and 5 mm were used depending to the size of the samples. A background spectrum without the sample present was collected. The tested sample was placed over the aperture of the holder, to be orthogonal to the light beam, as shown in figure 3.19. Then the sample chamber was purged the again. A computer was applied for data acquisition [3.1, 3.2, 3.4].

Depending on the wavelength range to be measured, different combination of light source, beam split and detector could be applied from Table 3.3 [3.1].

Table 3.3 Optical wavelength parameters of sources, beam splitters and detectors used in FTIR.

Item	Type	$\lambda$ range / ( $\mu\text{m}$ )	Spectrum	Manufacturer
Source	Tungsten lamp	0.3 – 3.3	Visible - NIR	Bruker
	Glow bar	3.3 – 100	NIR - IR	Bruker
Beam splitter	CaF <sub>2</sub> (broadband)	0.2 – 6	Visible - MIR	Bruker
	CaF <sub>2</sub> (NIR)	0.9 – 6	NIR - MIR	Bruker
	KBr	1.3 – 27	NIR - IR	Bruker
Detector	GaP	0.3 – 0.55	Visible	Bruker
	Si	0.4 – 1	Visible - NIR	Bruker
	InGaAs	0.8 – 1.7	NIR	Bruker
	InSb*	0.9 – 5.4	NIR - MIR	Judson
	DTGS	0.8 - 27	NIR - IR	Bruker
	MCT Photovoltaic*	2 – 11.7	MIR	Bruker

IR = Infrared, NIR = Near infrared, MIR = Mid infrared, \* = Liquid nitrogen cooled

### 3.2.7 Refractive index

(1) Principle of refractive index measurement.

Refractive index is a fundamental optical property of a material. Understanding the data of refractive index is necessary for selection of glass pairs for fibre fabrication and fibre design, because the propagation of optical signals can be controlled by controlling the refractive index profile of a fibre.

The measurement of refractive index was carried out by the method of minimum deviation. It is in Figure 3.20 shows the deviation angle  $\delta$  obtained when the incident laser beam is travelling through a prism sample with a certain incident angle. The minimum deviation can be obtained by turning the direction of the prism.

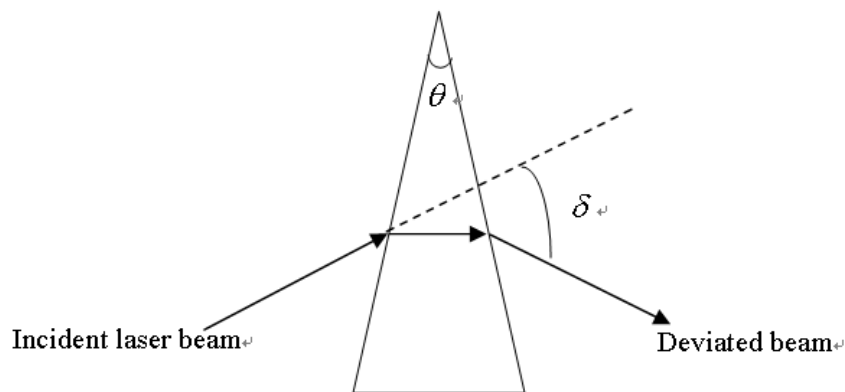


Figure 3.20 Schematic illustrated of the principle of the minimum deviation method. The apex angle  $\theta$  and the deviated angle  $\delta$  could be measured by recording the direction of the laser beam.

Equation (3.6) can be derived by applying the Snell's law and geometric optics [3.9].

$$n = \frac{\sin[(\theta + \delta)/2]}{\sin(\theta/2)} \quad (3.6)$$

where  $n$  is the refractive index of the glass,  $\theta$  is the apex angle of the prism and  $\delta$  is the minimum deviation angle.

(2) Sample preparation and methodology of the measurement.

A chalcogenide glass prism with the apex angle of 20 degree was prepared using the following procedures:

(a) a chalcogenide glass rod of ~10 mm was placed into a plastic holder, containing epoxy liquid, for 24 hours.

(b) The epoxy became solid after 24 hours and was mounted onto a brass jig whose top facet was inclined with a  $10^\circ$  angle with wax. The sample was mounted together with the jig onto the cutting machine (Buehler thin diamond blade size:  $5 \times 0.014 \times 1/2$ ) and the cutting was applied as the schematic presentation in figure 3.21(a). After cutting, a flat face was achieved for grinding and polishing (see figure 3.21 (b)). The sample was ground with 400 and 1000 grit silicon-carbide (SiC) grinding powder, then was polished in a sequence using  $6 \mu\text{m}$ ,  $3 \mu\text{m}$ , and  $1 \mu\text{m}$  Buehler Metadi II 200gm, diamond polishing compound. Then, the sample was turned around and mounted on with the polished facet on a brass jig with  $20^\circ$  angle. Another cut was applied (see figure 3.21 (c)) to obtain the  $20^\circ$  angle of the apex (see figure 3.21 (d)) and the cut surface was ground and polished with the same procedure as the first facet.

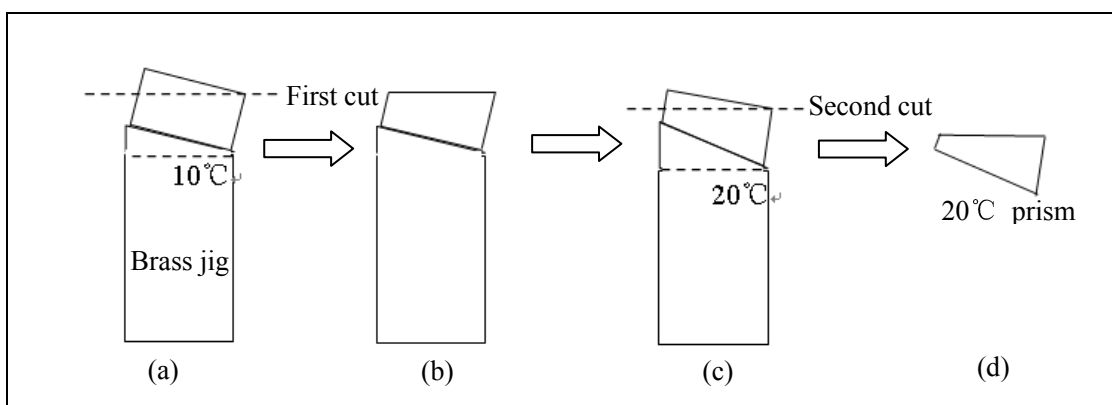


Figure 3.21 Schematic presentation of the procedure used for cutting the prism samples.

### **3.3 Preparation of chalcogenide glass preforms.**

The fabrication of the in-house designed microstructured fibres (MOF004, MOF005, MOF006, MOF007) comprised the following steps: (1) unstructured or core-clad structured preform extrusion; (2) over-clad tube rotational casting; (3) pre-fibre drawing; (4) stacking the designed structure preform and (5) final fibre drawing.

#### **3.3.1 Glass preparation prior to shaping.**

Refer to section 3.1.8. The molten glass was taken out of the ampoule. Because the glass shaping requires the preform to be a rod with high integrity in its shape, a relative lower speed of the cutting saw should be applied to avoid any vibration which may cause a crack on the chalcogenide rod.

Propylamine (Sigma-Aldrich 99.9 mol%) was applied to etch the preform in order to remove the oxide layer thought to grow on the surface of the preform in an ambient atmosphere. The etching rate should be traced each time because it was found to be variable for each individual preform, which had different composition, different surface quality and aging history.

#### **3.3.2 Extrusion of unstructured and core-clad chalcogenide glass rods.**

The technique of extrusion was employed to reduce the diameter of the preform. The extruder and its schematic diagram are depicted in figure 3.12 (a) and (b), respectively.

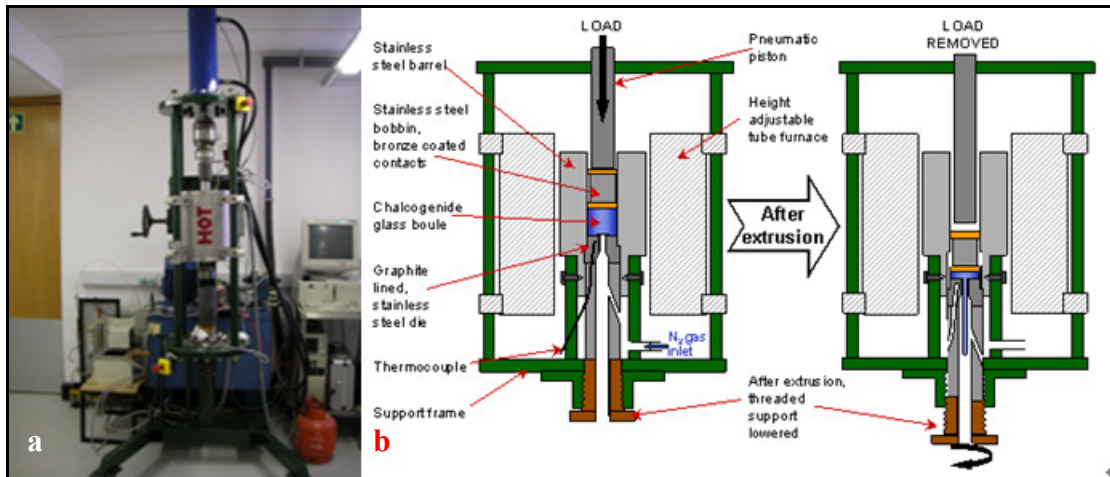


Figure 3.22 (a) Extruder designed and built by Dr. David Furniss of Novel Photonic Glasses Group, University of Nottingham, UK and (b) schematic diagram of the extruder cited from [3.1].

The glass boules (cylindrical, 29.5 mm diameter and  $\geq 15$  mm high see below) were horizontally loaded into the barrel of the extruder by rotating the extruder by  $90^\circ$  from its vertical position. A tube furnace surrounding the barrel, in which is filled with  $N_2$  (BOC) during the whole process, was heated to raise the temperature of the boule up to  $T_g$ . Then, the initial load was applied. The working times, temperature, applied load, which are dependent on composition, and the position of the bobbin were monitored by Pico Technology logging software. The actual extrusion took place at a viscosity of about  $10^8$  Pas where the corresponding temperature is above  $T_g$ , and then the extruded preform was cooled down to room temperature within the extruder.

To prepare the core-clad structured preform for MOF004 (made by Dr. Zhenggang Lian with the Author's assistance), the glass boules were cut to 15 mm height. The round end and contraction cone of each boule were cut away (see figure 3.23(a)).

Their interface surfaces were ground using 1000 grit SiC powder (Buehler) in oil (polishing oil, Buehler) then polished using diamond paste (Buehler) to a  $1\ \mu\text{m}$  finish. Acetone (Fisher Chemicals) was used to wash the surface of preform and a blue towel wiper was used to wipe and dry the surface.

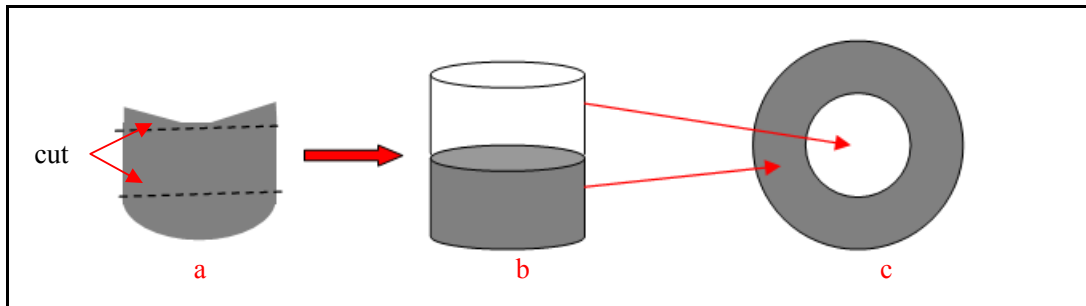


Figure 3.23 Schematic diagram of extrusion-prepared preform.

Two disks were stacked inside the extruder barrel with the polished surfaces together (as in figure 3.23(b)). As is shown in figure 3.23(c) the upper disk and the one below formed the core and cladding, respectively. An example extruded core-clad preform for making MOF004 is shown in figure 3.24.

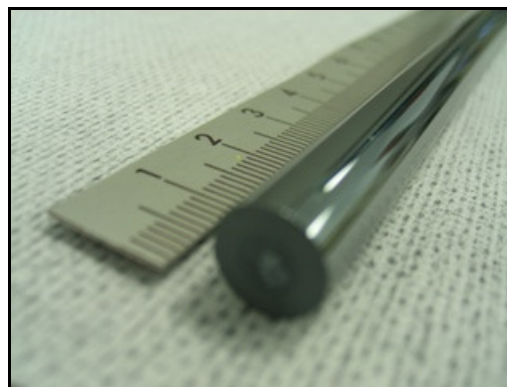


Figure 3.24 Core-clad preform (for MOF004) extruded by our group, cited from [3.3].

In this example, the surface of the extruded core-clad preform was shiny and the structure of the core-clad can be clearly observed in figure 3.24. This core-clad

fibre preform had an OD of 9 mm and a length of 300 mm. A 40 mm length of monolithic  $As_{40}Se_{60}$  was formed at the initial end to be extruded [3.3].

### **3.3.3 Cane-drawing**

The technique of chalcogenide cane-drawing is modified from the fibre-drawing (see section 3.3.5). Its purpose is to reduce the diameter of the chalcogenide rod from the order of 10 mm down to about 1 mm. Because the chalcogenide cane of about 1 mm diameter is too thick to be taken by the drum, a cane-puller driven by a motor (BBC Brown Boveri, FDFC12T, 24v, 200mA), modified by Dr. David Furniss, was used to clamp the bottom end of the cane during cane-drawing. The cane-puller was set up on the fibre-drawing tower (see figure 3.25). A 300 mm working distance was left between the diameter monitor and the cane-puller. The belt on the wheel takes and pulls the cane consistently. The relationship between the specific voltage of the motor and the desired diameter of the cane can be found out by pre-test. The principle of diameter control for cane-drawing is the same as fibre-drawing described in section 3.3.5. A constant feed out speed can be maintained by fixing the voltage being supplied to the motor during the fibre-drawing.

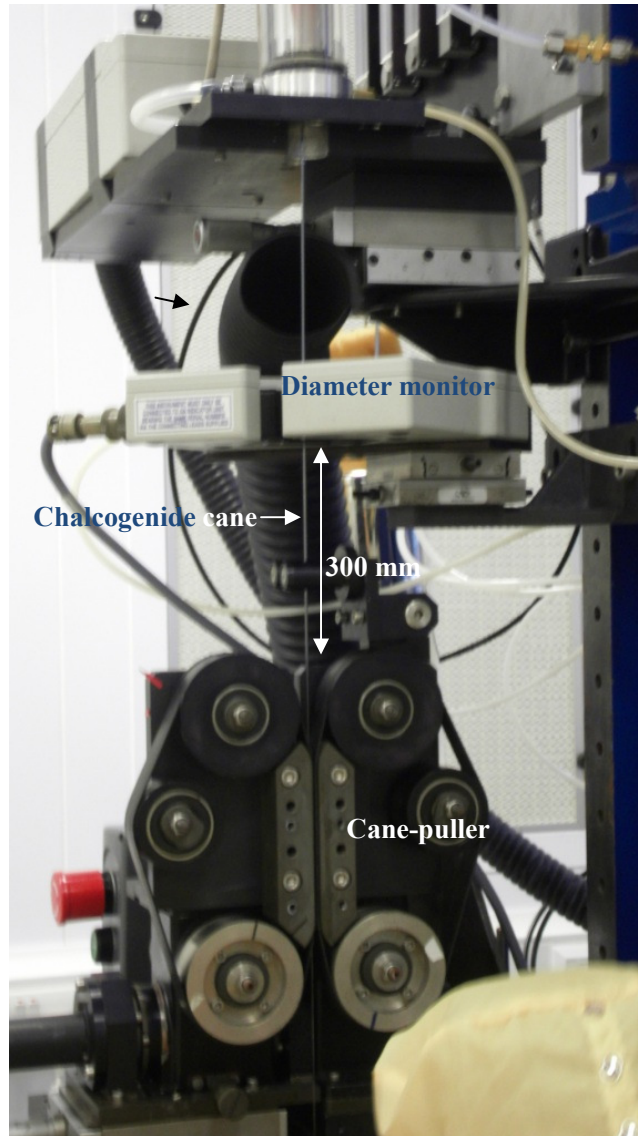


Figure 3.25 The cane-puller set up on the fibre-drawing tower.

### 3.3.4 Rotational casting of chalcogenide glass tubes.

The rotational casting (see a schematic diagram in figure 3.26) was applied to form an even chalcogenide glass tube in the radial direction along the length of the  $\text{As}_{40}\text{Se}_{60}$  tube. From the principle of the centrifugal effect,

$$mg = mr\omega^2 = mr(2\pi f^2), \quad (3.7)$$

where  $m$  is the mass of the material,  $r$  is the radius of the hole,  $g$  is the gravitation constant  $\sim 9.8 \text{ ms}^{-2}$ ,  $\omega$  is the angular velocity and  $f$  is the rotational frequency

(which can be related to the rotation speed of the equipment (rpm)). If the rotation rate is high enough than the rate in theory, an even walled tube may be achieved. In our experiment, the rotation rate was set to 2000 rpm and the time of rotation was 3 minutes and 30 seconds for all tubes. The tubes that have been prepared in this work are shown in figure 3.27.

Another point is how much space should be left inside of the pre-rotational cast ampoule above the glass melt. The OD of the over-clad tube (ie, the rotationally cast tube) was 10 mm which was the ID of the prepared ampoule. The ID required of the rotationally cast tube was dependant on the designed structure of the MOF. Thus the external diameter of the capillaries could be back-calculated with the aimed-tube's ID. Also, the external diameters of the capillaries were fixed at the first, then the tube's ID could be calculated. The tube's ID of MOF001 is 3.8 mm and MOF002 is 3 mm. the length of the ampoule to be sealed is calculated using equation 3.8:

$$\frac{m}{\rho} = V = \pi r_{ampoule}^2 l_1 = \pi (r_{ampoule}^2 - r_{tube}^2) l_2 \quad (3.8)$$

in which  $\rho$  is the density of the molten component,  $r_{tube}$  is the internal radius of the rotational casted tube.  $r_{ampoule}$  is the internal radius of the ampoule.  $l_1$  is the length of the batched material,  $l_2$  is the length of the rotational casted tube and the length of sealed ampoule.

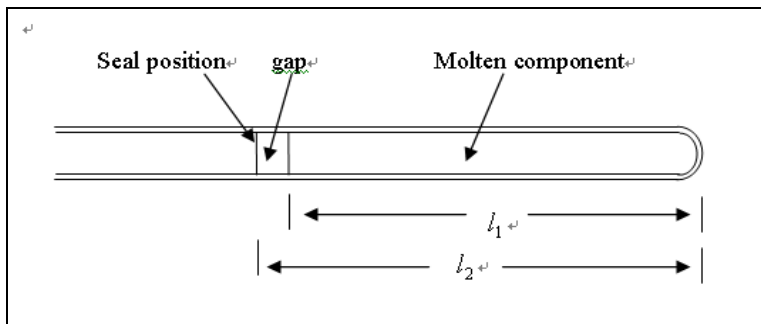


Figure 3.26 Schematic diagram of the sealed tube for rotational casting.

In figure 3.26, the seal position and the length of gap cannot be manipulated very precisely because of the contraction cone at the end of the glass and the sealing operation. The variation of the gap space leads directly to the variation of  $r_{tube}$ . This change in tube radius directly leads to unwanted modification of the MOF structure.

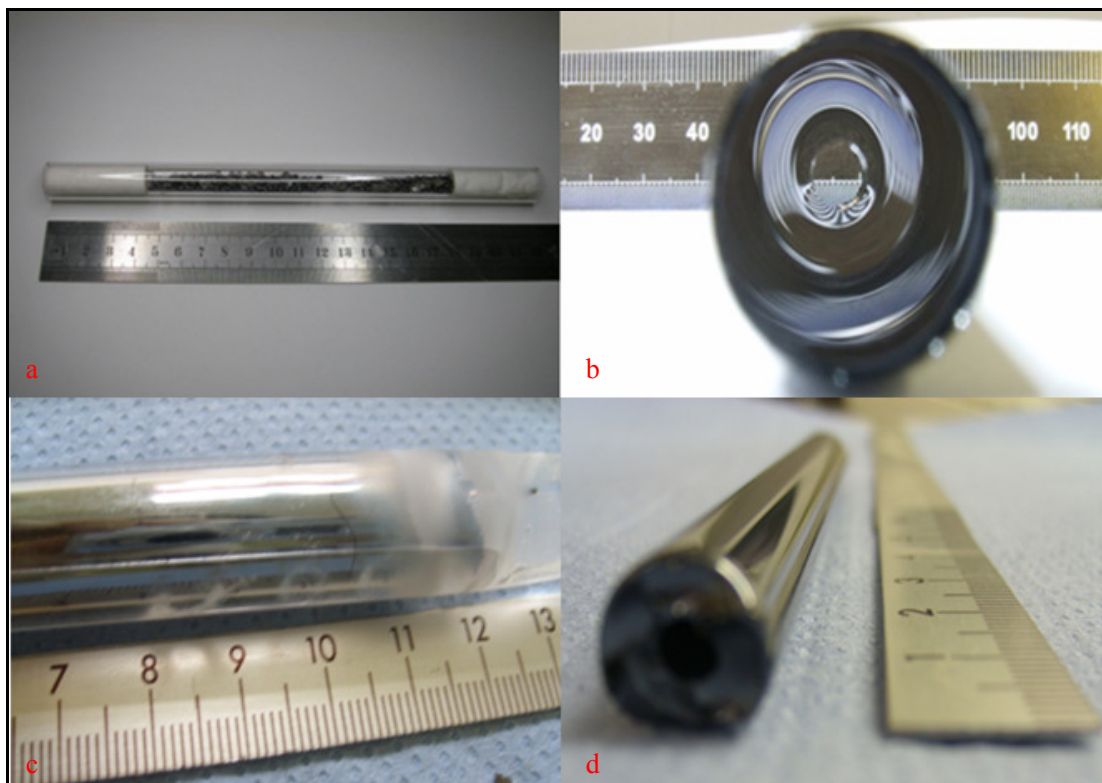


Figure 3.27(a) Prepared ampoule for the MOF001 tube rotational casting [3.3]; (b) rotationally cast tube ( $As_{40}Se_{60}$ ) used to construct the preform to draw to for MOF001 [3.3]; (c) prepared ampoule for MOF002; (d) rotationally cast tube ( $As_{40}Se_{60}$ ) for MOF002.

The rotationally cast tube for making MOF004 was shaped evenly in the radial direction through the length. However, during stacking of fibre inside the tube it was found necessary to add one extra core-clad fibre (drawn from fibre drawing tower) in order to fill the gap due to the diameter variation of the rotationally cast tube. Subsequently, rotationally cast tubes with a thicker wall have been made by using a double chamber ampoule (see section 5.1.3).

### **3.3.5 Chalcogenide glass preform assembly and fibre drawing.**

#### 3.3.5.1 Assembly of MOF preforms

Stacking is the step to hold the fibres within the rotational cast tube, through which the preform of the final MOF was built up.

Figure 3.28 shows the stacking of the preform for MOF004 (made by Dr. Zhenggang Lian with the assistance of the Author) as an example of preform assembly. The  $\text{As}_{40}\text{Se}_{60}$ -core preform drawn on the fibre-drawing tower was surrounded by stacking seven  $\text{Ge}_{10}\text{As}_{23.4}\text{Se}_{66.6}/\text{As}_{40}\text{Se}_{60}$  fibres drawn from an extruded core-clad preform. Figure 3.28 (a) shows the tube and the seven core-clad fibres and one unstructured fibre to form the core of the MOF004. Figure 3.28 (b) is the section view of the stacked fibre preform for MOF004. This work has now been published [3.2].

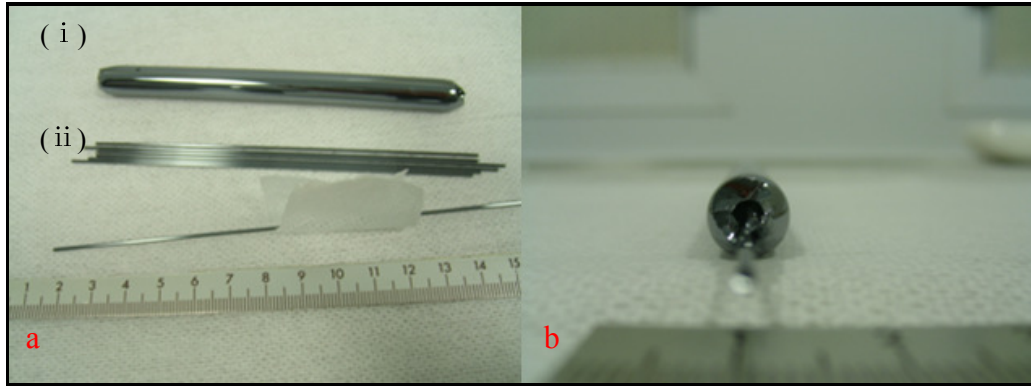


Figure 3.28 (a) (i) Rotationally cast tube, and (ii) seven core-clad fibres and one unstructured fibre to form the core of MOF001 before stacking prepared for stacking; (b) the section view of the stacked MOF preform using the components from (a) [3.2].

As already noted, because there was some variation existing during the fabrication of the rotationally cast tube and fibres, one extra core-clad fibre had to be inserted into the tube to ensure it was stacked tightly and so keep the structure scale ratio during the fibre drawing process.

### 3.3.5.2 MOF (microstructured optical fibre) drawing

The last step of MOF fibre fabrication was drawing the structured fibre preform to the final MOF. The modified fibre-drawing tower is shown in figure 3.29. The key points of structured fibre drawing are to keep the surface of the preform pristine and to keep the structure diameter ratio constant during the drawing process. The diameter of the drawn fibre was dependent on the temperature of drawing and the feed-in and feed-out speed of the fibre, controlled by the rotational speed of the take-up drum. The radio frequency (rf) power was raised in order to melt the preform which is thicker at the beginning, and then reduced to keep the thinned drawn fibre at its fibre drawing viscosity, for which a stable drawing process can

be kept. The rf power was modified manually according to the fibre tension visually observed. The fibres went through two tension wheels before feeding onto the fibre drum. The fibre drum rotated and moved transversely, therefore preventing successive fibre sticking together as it was wound around a polystyrene drum (circumference of 1 m). The drum was designed and built in-house by Dr. David Furniss.

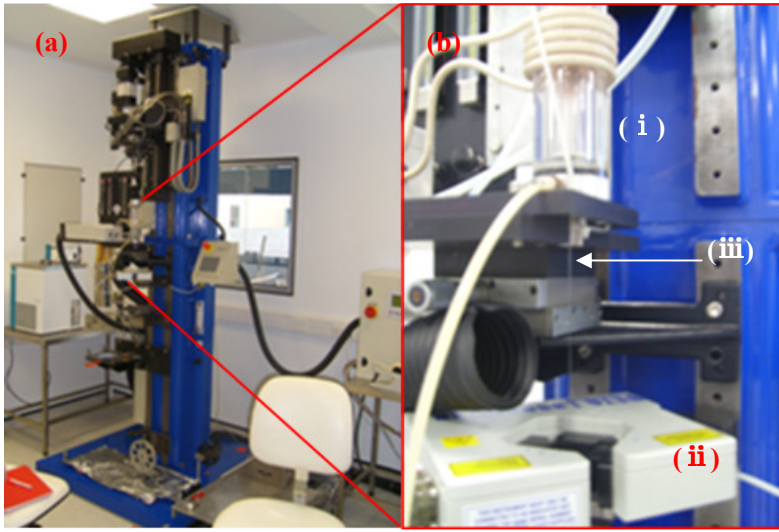


Figure 3.29 (a) The fibre-drawing tower; (b) (i) radio frequency fibre drawing furnace (Severn Furnaces Ltd), together with (ii) the laser diameter monitor and (iii) the drawn fibre.

In figure 3.29, the rf fibre-drawing furnace is shown, in which the copper coil radiates the rf waves to heat the graphite rings which transfer heat to the loaded chalcogenide glass preform evenly. The fibre was fed onto a fibre drum at a calculated speed, dependent on the diameter ratio of the feed-out fibre to feed-in preform, as decided by the equation 3.9:

$$\frac{V_{feedout}}{V_{feedin}} = \frac{A_{preform}}{A_{fibre}} = \frac{\pi r_{preform}^2}{\pi r_{fibre}^2} \quad (3.9)$$

where the  $A_{preform}$  and  $A_{fibre}$  are the cross section of the preform and drawn fibre, respectively. The feed-speeds at the input and the output ends are inversely

proportional to the square of the preform's diameter at each end.

The core-clad ( $\text{Ge}_{10}\text{As}_{23.4}\text{Se}_{66.6}$  /  $\text{As}_{40}\text{Se}_{60}$ ) preform was drawn to fibre using an rf power setting of 29% at first which was then reduced to 25% and then returned back to 29%. The core ( $\text{As}_{40}\text{Se}_{60}$ ) was drawn using an rf power setting of 23%; because the viscosity at any temperature  $> T_g$  of  $\text{Ge}_{10}\text{As}_{23.4}\text{Se}_{66.6}$  glass was higher than that of  $\text{As}_{40}\text{Se}_{60}$ .

### **3.4 Conclusions.**

The experiment procedures used in this work have been described in this chapter. They are the techniques and schedule of glass synthesis: ampoule processing, raw chemical element purification, the chalcogenide glass melting, quenching, annealing and polishing; the methods used to characterise glass: X-ray Diffraction (XRD) for examining the amorphicity of glass, Differential Thermal Analysis (DTA) for testing the glass  $T_g$ , Thermomechanical Analysis (TMA) for measuring the thermal expansion coefficient ( $\alpha$ ) and viscosity of glass, Environmental Scanning Electron Microscopy (ESEM) for viewing and imaging the sample at micro-scale and Fourier Transform Infrared Spectroscopy (FTIR) for finding the transparent window and absorption properties of certain glasses.

The procedures for the fabrication of MOF have also been described. They are the techniques of precursor purification and glass preparation; the rotational casting method for making the over-clad tube, the extrusion of chalcogenide rods, microstructure pattern assembly and fibre drawing.

## **Chapter 4 Thermal and optical characterisation of a glass pair in the Ge-Sb-Se chalcogenide glass family**

In this chapter, the ternary Ge-Sb-Se glass system is studied to find a glass pair for the fabrication of single mode and multimode core-clad, step-index structured optical fibres and a microstructured optical fibre for application in the near- and mid-infrared regions. The glass forming region and the glass forming ability are reviewed and checked. Glass transition temperatures, viscosity / temperature relations, thermal expansion coefficients, refractive indices at 1.5  $\mu\text{m}$  wavelength and also their resistance to crystallisation during fibre shaping are reported and analysed with respect to glass structure in terms of the average coordination number.

The author helped to supervise Final Year Undergraduate Project students Harriet Jackson [4.1] and Woraphat Aphisawetkarn [4.2] who contributed to measuring some of the data presented here.

### **4.1 Background and motivation**

As introduced in sections 2.1 and 2.2, chalcogenide glasses have attracted broad interest in recent years. Their high linear and nonlinear refractive indices and low photon energies are attractive for the requirements of all-optical signal processing which is critical for high-bit-rate optical communication in the near infrared. Also, their wide infrared transmission window, flexibly tailorable composition and

durable chemical properties and acceptable mechanical properties make them a versatile platform to fabricate compact optical devices using both fibre and other waveguide formats for the near- and mid- infrared spectral regions. Here there is interest in fabrication of optical fibres for passive and active use in the mid-infrared. The application of rare earth-doped chalcogenide fiber for mid- and long-wave IR lasers, highly nonlinear chalcogenide fiber and photonic crystal fiber for wavelength conversion in the mid- and long-wave IR has been discussed by Naval Research Laboratory [4.3, 4.4]. Also, supercontinuum generation investigation based on the fibre of  $\text{As}_{40}\text{Se}_{60}$  has been achieved [4.5].

Glass formation in the Ge-Sb-Se system was chosen here as an alternative to the more common Ge-As-Se glasses for the near and mid-infrared range because of their relatively lower vapour pressure [4.6] and lower toxicity. Previously, investigations [4.7, 4.8] on the glass synthesis and physical properties of the Ge-Sb-Se glasses shows this glass system is appropriate for mid-infrared application and glass shaping in terms of its optical transmission, thermal properties and glass forming ability. The glass forming phase diagram shown in figure 4.1 has been reported some time ago in 1978 [4.7], which indicates the glass forming ability and glass transition temperature ( $T_g$ ) isotherm of 160°C, 220°C and 280°C by empirical fitting. These  $T_g$  isotherms extend in the direction, along which the variation of concentration of Ge and Sb would be expected to change the refractive index in an analogous tendency. Although the reliability of

the  $T_g$  fitting is questionable, the curves indicate the trend to modify the composition for desired thermal and optical properties. In order to modify the glass composition to achieve similar glass transition temperature ( $T_g$ ), and to choose the compositions with the moderate  $T_g$  and stable glass forming ability, nine Ge-Sb-Se compositions (see Table 4.1) have been chosen around the  $T_g$  isotherm of 220°C suggested by [4.7].

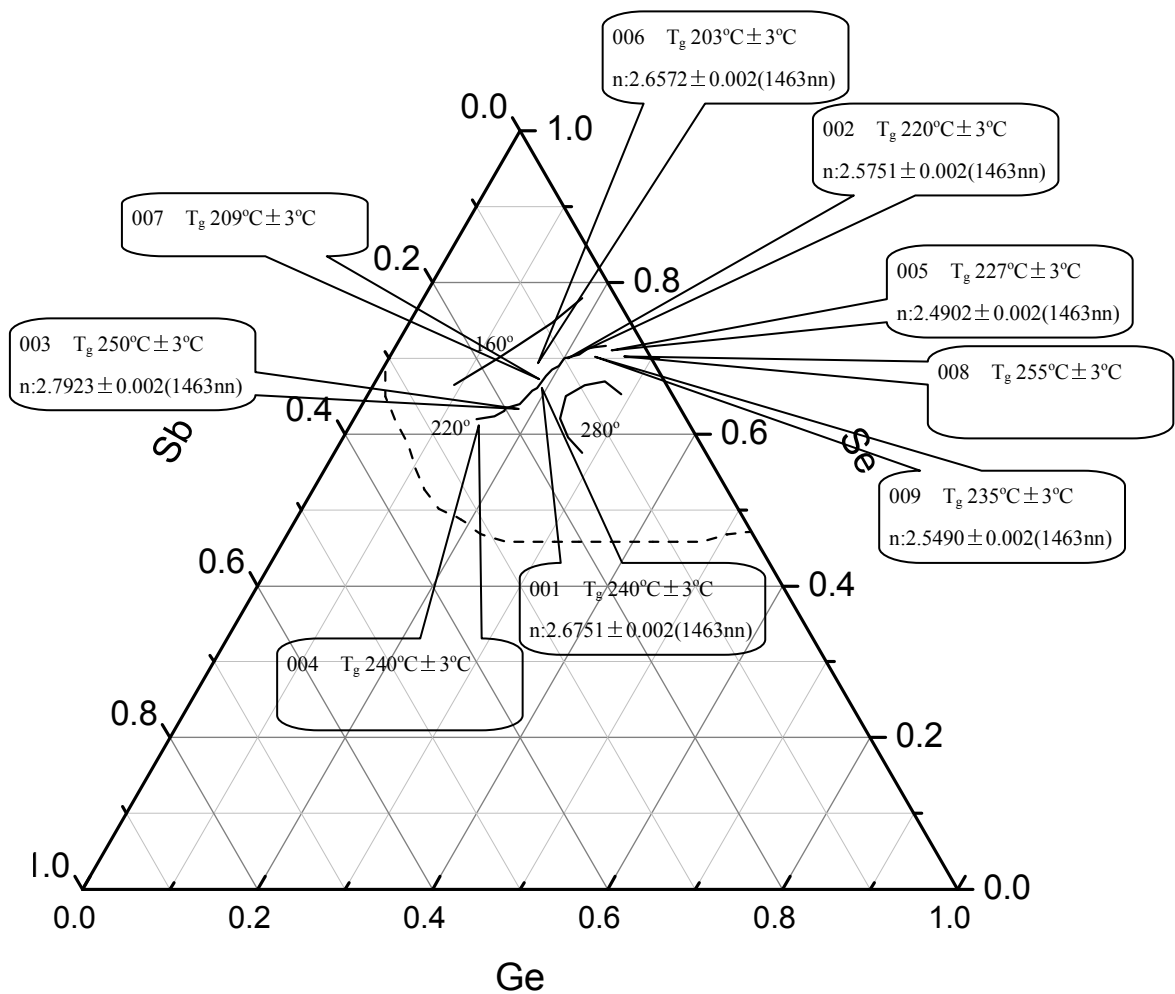


Figure 4.1 Ternary phase diagram of Ge-Sb-Se shows the glass forming region as determined by Hilton in 1978 according to [4.7]. The solid curve is the original data of Hilton according to [4.8] and was reported as isothermal of  $T_g = 160^\circ\text{C}$ ,  $T_g = 220^\circ\text{C}$  and  $T_g = 280^\circ\text{C}$ , respectively. The dashed curve is the extent of the Ge-Sb-Se glass-forming region according to [4.7].

Note, nine compositions (001 ~ 009) were chosen to be characterised in this project. Values of  $T_g$  measured here are shown as well as refractive index at 1463 nm. The refractive index of the compositions of 004, 007, 008 were not measured.

Glass structure in this ternary system has been reported in terms of their physical properties versus average coordination number in order to reveal the relationship between the glass structure and their thermal properties [4.9- 4.13]. Analysis of the constituent binary systems of  $\text{GeSe}_2\text{-Sb}_2\text{Se}_3$  in the Ge-Sb-Se glass system

revealed that the maximum temperatures of  $T_g$  and most stable thermal properties could be achieved when the glass is compounded only by the cross-link network of  $\text{GeSe}_2$  and  $\text{Sb}_2\text{Se}_3$  [4.11, 4.12]. The mid-infrared absorption spectroscopy analysis on the sub-series of  $\text{Ge}_x\text{Sb}_{15}\text{Se}_{85-x}$  confirmed the chain-crossing model, where Ge and Sb crosslink the chains of Se [4.14]. Their optical transparency has been investigated in [4.14- 4.17], showing a transparency window from around 0.9  $\mu\text{m}$  to 16  $\mu\text{m}$  and this can be extended into the visible range with the addition of alkali metal halide compounds [4.18], in which the high photon energy transparency edge of  $\text{Ga}_5\text{Ge}_{25}\text{Sb}_{10}\text{Se}_{60}$  has been extended from about 820 nm to 750 nm by adding 10 wt.% of CsI.

With the addition of a limited amount of Ga, the Ge-Sb-Se glass system has been explored as a good host glass for rare earth doping [4.19, 4.20], in which  $\text{Pr}^{3+}$  and  $\text{Dy}^{3+}$  have been doped into the Ga-Ge-Sb-Se glasses to obtain a amplifier for 1.34  $\mu\text{m}$  and 1.64  $\mu\text{m}$ . It is also mentioned in [4.20] that the change of refractive index in Ge-Sb-Se glass system is larger than that of Ge-As-Se glass system with the substitution of Se by S. This infers a glass pair with more close thermal properties at the desired refractive index contrast, which is desired in this project, might be achieved by applying the former glass system. A glass pair in Ge-As-Se glass system, used for making microstructured optical fibre (MOF), will be introduced in section 5.2.1. The study of the compositional dependence of the nonlinear optical properties in this glass system has been reported in [4.17, 4.21], in which

the nonlinear refractive index ( $n_2$ ) is concluded to increase with higher lone electron pair concentration and larger photonic band gap energy. This conclusion indicates the inclusion of Sb increases  $n_2$  and the  $n_2$  of Ge-Sb-Se glass system provides higher  $n_2$  than that of Ge-As-Se glass system. A high  $n_2$  is helpful for supercontinuum generation.

The fabrication of “holey” microstructured optical fibres (MOF) comprising Ge-Sb-S has been reported in [4.22]. A stack and draw method was applied to make a single material, three rings of holey cladding solid core MOF. Single-mode propagation was proved in the core area of the fibre. A single mode core-clad fibre of different composition Ga-Ge-Sb-S glasses has been reported [4.23], in which  $\text{Ga}_5\text{Ge}_{20}\text{Sb}_{10}\text{S}_{65}$  and  $\text{Ga}_4\text{Ge}_{21}\text{Sb}_{10}\text{S}_{65}$  were selected from the sub-series of  $\text{Ga}_x\text{Ge}_{25-x}\text{Sb}_{10}\text{S}_{65}$  as the glass pair for core and clad. Single-mode propagation was demonstrated at 1550 nm.

All solid chalcogenide microstructured fibre based on As-Se and Ge-As-Se glasses has also been demonstrated in our laboratory in [4.24], because it is easier to maintain the designed aspect ratio and with more flexibility in designing the index profile and mechanically more robust compared to the air/glass MOF.  $\text{Ge}_{10}\text{As}_{23.4}\text{Se}_{66.6}$  and  $\text{As}_{40}\text{Se}_{60}$  were chosen as the glass pair for the reverse refractive index core-clad preform due to their similar thermal properties. These preforms were intended for forming the structured cladding of an all-solid

chalcogenide MOF as described in [4.24] and in section 5.2. The glasses for both of the core and clad were shaped into 29 mm diameter / 15 mm height bulk and the glass for core region was stacked on top of the one for clad. The stacked glass pair was extruded at their viscosity point of  $\sim 10^8$  Pas.

It was reported in 1987 [4.25] that a core-clad structure fibre in Ge-Sb-Se system has been made by the extrusion and rod-in-tube method. Both of the rod and tube were made by means of extrusion. In detail the work achieved in [4.25] is as follows. The composition of  $\text{Ge}_{28}\text{Sb}_{12}\text{Se}_{60}$  (TI 1173 glass) was taken as a representative of this glass system to investigate its transparency window (0.8 to  $15\mu\text{m}$ ). Combinations of  $\text{Ge}_{28}\text{Sb}_{12}\text{Se}_{60}$  (TI 1173 glass),  $\text{Ge}_{25}\text{Sb}_{15}\text{Se}_{60}$  and  $\text{Ge}_{32}\text{Sb}_8\text{Se}_{60}$  were selected to make cylindrical and square fibres, however the tendency to determine the glass pair was not explained. Thus, it is helpful to reveal how the thermal and optical properties of the glass can be modified by adjusting their compositions. The refractive index of  $\text{Ge}_{28}\text{Sb}_{12}\text{Se}_{60}$  (TI 1173 glass) has been obtained in [4.26] by the minimum-deviation method using a prism of the material and curve-fitting. Comparisons of refractive index versus composition have been made using interference fringe spacing of the transmission from thin, flat and polished samples. It was concluded that there is a trend of higher refractive index with decreasing Ge : Sb ratio, with fixed Se. The wavelength of zero material dispersion of Ge-Sb-Se glass system increases with decreasing Ge : Sb atomic ratio.

In this chapter, measuring the optical and thermal properties of Ge-Sb-Se glass system to identify suitable glass pairs with a view to fabricating MOF and single and multi-mode core-clad fibre, step-index optical fibres is reported.

## 4.2 Glass synthesising.

The compositions of ternary Ge-Sb-Se chalcogenide glasses (see table 4.1) have been selected according to the glass forming diagram shown in figure 4.1 along the 220°C T<sub>g</sub> isotherm.

Table 4.1. Glass compositions synthesised and tested here in the Ge-Sb-Se glass system, along the 220°C T<sub>g</sub> isotherm of figure 4.1.

Glass code	Batch composition / at%
001	Ge <sub>18.90</sub> Sb <sub>15.00</sub> Se <sub>66.10</sub>
002	Ge <sub>20.00</sub> Sb <sub>10.00</sub> Se <sub>70.00</sub>
003	Ge <sub>16.60</sub> Sb <sub>20.00</sub> Se <sub>63.40</sub>
004	Ge <sub>13.50</sub> Sb <sub>24.87</sub> Se <sub>61.63</sub>
005	Ge <sub>24.00</sub> Sb <sub>4.36</sub> Se <sub>71.64</sub>
006	Ge <sub>16.70</sub> Sb <sub>13.30</sub> Se <sub>70.00</sub>
007	Ge <sub>17.67</sub> Sb <sub>14.03</sub> Se <sub>68.30</sub>
008	Ge <sub>25.56</sub> Sb <sub>4.64</sub> Se <sub>69.80</sub>
009	Ge <sub>22.50</sub> Sb <sub>7.50</sub> Se <sub>70.00</sub>

The glasses have been prepared as discussed in section 3.1 starting with the high purity elements of Ge (5n Cerac), Sb (6n Cerac) and Se (5n Cerac). The chemical elements were batched into silica ampoules (Global Quartz) which had been processed by hydrofluoric acid etching (0.3% hydrofluoric acid etching the inside

of the ampoule for 20 minutes at room temperature), ampoule annealing (the ampoules were annealed at 1160°C for 1.5 hours to release the tension then cooled to 900°C at 60°C / h and finally cooled down to room temperature by switching off the furnace) and baking (the ampoules were baked at 1000°C for 6 hours under an air atmosphere to remove any carbonaceous impurity and then baked at 1000°C for 6 hours under vacuum of  $10^{-5}$  Pa in an attempt to remove physical and chemical bonded water). In a nitrogen-recirculated glovebox (MBraun, < 0.1 ppm O<sub>2</sub> and 0.1 < ppm H<sub>2</sub>O), 13 g total of the above elements for each composition were batched. 13 g was selected as this was sufficient to carry out the required thermal and optical analysis. The ampoule was then sealed under vacuum ( $\sim 10^{-2}$  Pa) and placed into a rocking furnace (Instron, TF105/4.5/1ZF, tube ID 86 mm, modified in house) and set to rock  $\pm 30^\circ$  about the horizontal axial axis.

The temperature of the rocking furnace was programmed to start rocking at a temperature where some of the raw material (Se) was liquid to protect the ampoule from scratching by the element solid chunks. Thus the temperature of about 450°C was selected. The temperature was gradually increased to 850°C at 40°C / h and kept rocking at 850°C for 12 hours before being cooled at 40°C / h down to a refining temperature, which is about 150°C ~ 200°C higher than the estimated liquidus of each glass. The furnace was placed vertically and kept stable for two hours' refining to allow oxide particulate impurities, if present, to rise to the surface. The liquidus was estimated using the two thirds law [4.39] expressed

as  $T_1 = \frac{3}{2} T_g - 273$ ; where  $T_1$  is the liquidus of the glass and all temperatures are in Kelvin. Thus a temperature of about 700°C was applied for each melting. Air quenching, starting from the refining point, has been chosen for this glass system to prevent crystallisation and too large temperature gradient along the radial direction of the molten glass which leads to a deep contraction cone [4.40]. All of the glasses on quenching exhibited shiny glassy surfaces. Each melt-schedule is shown in section 4.2; a well-controlled melting schedule was obtained by accumulating the experience gain from melting samples 001 to 009.

Compared to the Ge-As-Se glass system, the supercooled liquids of the glass system of Ge-Sb-Se have a higher viscosity at any particular temperature and any particular composition because of replacing As by Sb. Thus, the melting temperature was set to 900°C and the refining temperature was set to 700 °C for 001Ge<sub>18.9</sub>Sb<sub>15</sub>Se<sub>66.1</sub>. An over-quenching schedule using a liquid metal alloy (see section 3.1.6), was applied to obtain a stable glass for this first melt trial. The  $T_g$  of Ge<sub>18.9</sub>Sb<sub>15</sub>Se<sub>66.1</sub> was estimated as 220 °C according to the figure 4.1, [4.7], so the sealed silica ampoule, containing the molten chalcogenide glass, was inserted into the liquid metal alloy pot with the metal liquid of 180 °C for ~4.5 min. The quenching time was chosen to be up to the moment when the temperature of the liquid metal alloy started to increase to the peak value and then started to drop to 182°C. The silica glass ampoule containing the chalcogenide glass melt was then removed from the liquid metal alloy pot and placed in the annealing furnace,

which had been preheated to 180°C. Thus, the annealing schedule was started at 180°C for 15 min then the temperature of the furnace was raised to 220°C at 20°C / h. 1.5 h was allowed for the annealing to take place and then the temperature was decreased to 150°C at 5°C / h temperature. After that the rate of 20°C / h was applied to cool the glass to room temperature. As-produced 001Ge<sub>18.9</sub>Sb<sub>15</sub>Se<sub>66.1</sub> exhibited a shiny glassy surface, with a 10 mm long contraction cone in the 10 mm diameter and 30 mm long monolithic rod.

Exactly the same melting, quenching and annealing procedure was applied to the first melting of 002Ge<sub>20</sub>Sb<sub>10</sub>Se<sub>70</sub> because it was supposed to have the same T<sub>g</sub> as 001 (220°C according to the isotherm in figure 4.1 [4.7, 4.8]). However, the rod suffered a thermal shock during quenching or annealing. Thus, an air quenching (see section 3.1.6) was applied to the subsequently melted compositions of Ge<sub>18.9</sub>Sb<sub>15</sub>Se<sub>66.1</sub> and Ge<sub>20</sub>Sb<sub>10</sub>Se<sub>70</sub> and an non-cracked, monolithic glass rods with shiny surface were obtained.

The same melting schedule for the compositions of Ge<sub>18.9</sub>Sb<sub>15</sub>Se<sub>66.1</sub> and Ge<sub>20</sub>Sb<sub>10</sub>Se<sub>70</sub> was applied to the melting of 003Ge<sub>16.6</sub>Sb<sub>20</sub>Se<sub>63.4</sub>, 004Ge<sub>13.5</sub>Sb<sub>24.87</sub>Se<sub>61.63</sub> and 005Ge<sub>24</sub>Sb<sub>4.36</sub>Se<sub>71.64</sub> because their estimated T<sub>g</sub> were again the same at 220°C (figure 4.1 [4.7, 4.8]) and their compositions are located in the narrow region of the glass forming diagram (figure 4.1). The liquid metal alloy quenching and annealing schedule, which were used for the composition of

$\text{Ge}_{10}\text{As}_{23.4}\text{Se}_{66.6}$ , was applied to these melts 003 to 005, inclusive, because the experimental results of melts 001 and 002 demonstrated that this glass system has stable glass forming ability and an air quenching is fast enough to prevent the glass from crystallising during quenching for the chosen composition in Ge-Sb-Se glasses system. However, in order to make sure a good amorphous glass was achieved, a liquid metal quenching with a liquid metal alloy pot (Seba developments Ltd. Series No. 1530) was applied for the subsequent melting. The only temperature points that need to be adjusted were the temperature of the liquid metal alloy at the beginning of the quenching and the temperature of the annealing furnace setting, according to the exact  $T_g$  of each composition.

From the results of melts 003, 004 and 005 (see table 4.2 in section 4.4.1), a difference between their  $T_g$  as measured here and the isotherm determined in [4.7, 4.8] in figure 4.1 exists. Thus, the  $T_g$  for more compositions needs to be obtained to adjust the reported isotherm of  $220^\circ\text{C}$  which does not fit the  $T_g$  results obtained here and in order that the true tendency of adjusting the  $T_g$  by varying the composition could be found. Based on the results of the first five compositions and the glass forming diagram, the composition of 006  $\text{Ge}_{16.7}\text{Sb}_{13.3}\text{Se}_{70}$ , 007  $\text{Ge}_{17.67}\text{Sb}_{14.03}\text{Se}_{68.3}$ , 008  $\text{Ge}_{25.56}\text{Sb}_{4.64}\text{Se}_{69.8}$  and 009  $\text{Ge}_{22.5}\text{Sb}_{7.5}\text{Se}_{70}$  were chosen for melting. The same melting schedule, liquid metal alloy quenching and annealing schedule of the procedure for the melts 001 to 009 were applied by only changing the temperature of liquid metal alloy at the beginning of quenching and the

temperature of annealing furnace setting according to the exact  $T_g$  of each composition (see table 4.2 in section 4.4.1).

All of the chalcogenide glasses prepared as above are called henceforward in the text “as-prepared glasses”. All of the as-prepared glasses (see section 4.2.1) appeared glassy judging from their shiny surface. The powder XRD pattern of all the as-prepared glasses exhibited broad diffraction humps. The  $T_g$  of the experimental as-prepared compositions (see table 4.1) and the previous data from [4.7, 4.8] are plotted together in figure 4.1. It is found that the experimental compositions 001 to 005 melted here were located according to their composition on the 220°C isotherm of [4.7] but data found here of  $T_g$  do not show a good fit with the data of [4.7, 4.8], except the point for sample 002  $\text{Ge}_{20}\text{Sb}_{10}\text{Se}_{70}$  with an agreed  $T_g$  of 220°C.

### **4.3 Re-melting of glasses to obtain correctly sized samples for TMA measurement of viscosity / temperature behaviour**

The samples for re-heating to measure viscosity / temperature behaviour have been obtained by using the technique and procedure introduced in section 3.2.3.1. 3.5 g of chalcogenide glass (prepared as in section 4.2) was crushed into small chunks by using a agate mortar and pestle and batched into a silica glass ampoule (250 mm length, 4 mm / 7 mm ID / OD) and sealed under vacuum ( $\sim 10^{-1}$  Pa) for re-melting. The schedule for re-melting, quenching, and annealing was kept the

same as in section 4.2. The Se glass samples are referred to in the text henceforward as “re-melted glasses”. The re-melted glass rod (~ 35 mm long, 4 mm diameter) was mounted onto an aluminium block with wax. Perpendicular cuts were applied along the length of the rod to get several discs (~ 2.7 mm thickness, ~ 4 mm diameter,  $\pm 0.005$  mm tolerance). The diameter and thickness of each sample were measured with a micrometer each of four times on different areas of the sample to check the degree of roundness and that the saw-cuts were orthogonal to the axial direction of the sample. The heat treatment procedures of the samples have been completed synchronously with the procedures of viscosity measurement by applying Thermomechanical Analysis (Perkin Elmer TMA7) as described in section 3.2.3.1. The sawn samples were heated, under 50 mN load, which is suitable for measuring the viscosity of the interested compositions at their fibre-drawing temperature (300°C ~ 400°C). Samples were heated from room temperature to 10°C below their  $T_g$  at 40°C / min under helium flow (20 ml / min, BOC), then the temperature was increased at 10°C / min, which was slow enough to provide sufficient observation details, until achieving  $\geq$  the viscosity of  $10^{4.5}$  Pas (nominal fibre-drawing viscosity). These samples are referred to in the text henceforward as “re-heat-treated samples”.

## **4.4 Results of glass characterisation**

### **4.4.1 DTA**

The differential thermal analysis of the glasses was carried out as the technique

and operational procedure described in section 3.2.2. The glass transition temperature ( $T_g$ ) of each composition has been measured by using a Perkin Elmer DTA 7 analyser. The equipment was calibrated with appropriate temperature material standards (In, Zn and Al melt at 156.6°C, 419.4°C and 660.2°C, respectively). The reference DTA samples, whose mass was to be the same as the sample's ampoule with tolerance of  $\pm 20$  mg, were made by sealing an empty silica ampoule under vacuum ( $10^{-1}$  Pa). Baseline runs, in which both ampoules were empty, were carried as required and subtracted from the traces to remove the effect of any artefacts unrelated to the specimen. In order to give every sample the same thermal heat history, each sample was heated to about 5°C above their  $T_g$  and then cooled to room temperature at 10°C / min. For the  $T_g$  measurement itself, the sample was re-heated at a heating rate of 10°C / min from room temperature to 750°C. 101 mg glass from the as-annealed glass rod of each composition was batched into a silica ampoule with 3 mm ID, which is sealed under vacuum ( $10^{-1}$  Pa). The measured  $T_g$ , with error of  $\pm 3^\circ\text{C}$ , has been measured by taking the intersection of the tangential lines around the onset of the curve of endotherms ( $\Delta T$ ) against temperature. The measurements were repeated several times adjusting the intersection. The DTA curves obtained are shown in figure 4.2.

As an initial indication, the stability of each as-prepared glass composition to reheating may be observed from the differential thermal analysis curves (figure 4.2). The crystallisation temperature ( $T_c$ ) was measured by drawing the

intersection of the tangential lines around the onset of the crystallisation peak and the gap of  $T_g$  and  $T_c$  supplies a measure of glass stability (see table 4.2). The as-prepared glass composition of 001, 002, 008 and 009 with a relatively larger contrast of  $T_g$  and  $T_c$  than the others probably have a more stable glass forming ability.

The height and area of the crystallisation peak in figure 4.2 also indicate the tendency of a composition to crystallise. The compositions of 001, 002, 008 and 009 do not exhibit an obvious exothermic peak above  $T_g$ . Whilst the compositions of 003, 005, 006 and 007 do not show a sharp exothermic peak, multiple exothermic peaks exist which indicate that these glasses are not stable enough for thermal treating and glass shaping. The composition of 004 exhibits a high exothermic peak height and area which indicates an obvious tendency to crystallise. The glass compositions yielding DTA curves without crystallisation tendency are the potential candidates for making optical fibre preforms. The composition's glassy stability could be confirmed from the glass forming diagram (figure 4.1). The results obtained suggest that the closer to the centre of the glass forming region of Figure 4.1 a particular composition lies, the more stable the composition is.

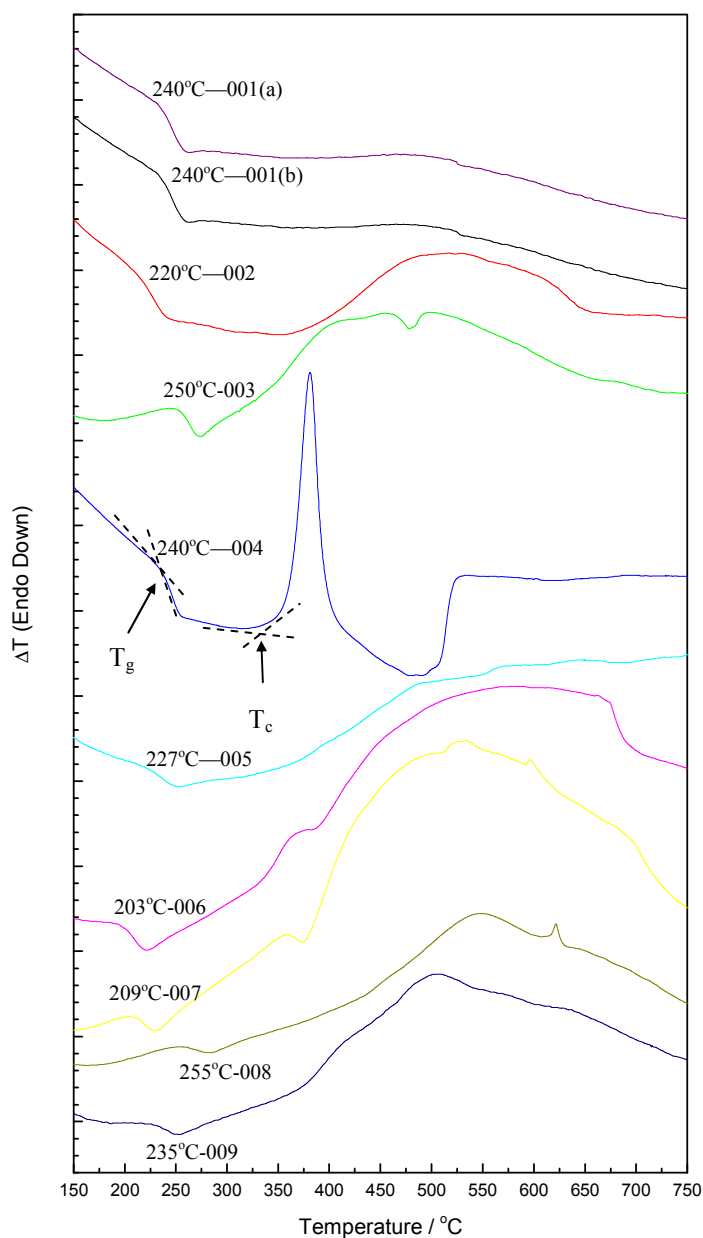


Figure 4.2. Differential thermal analysis curves of Ge-Sb-Se as-prepared glasses showing  $T_g$  values in  $^{\circ}\text{C}$ : 001(a)  $\text{Ge}_{18.90}\text{Sb}_{15.00}\text{Se}_{66.10}$ ; 001(b)  $\text{Ge}_{18.90}\text{Sb}_{15.00}\text{Se}_{66.10}$ ; 002  $\text{Ge}_{20.00}\text{Sb}_{10.00}\text{Se}_{70.00}$ ; 003  $\text{Ge}_{16.60}\text{Sb}_{20.00}\text{Se}_{63.40}$ ; 004  $\text{Ge}_{13.50}\text{Sb}_{24.87}\text{Se}_{61.63}$ ; 005  $\text{Ge}_{24.00}\text{Sb}_{4.36}\text{Se}_{71.64}$ ; 006  $\text{Ge}_{16.70}\text{Sb}_{13.30}\text{Se}_{70.00}$ ; 007  $\text{Ge}_{17.67}\text{Sb}_{14.03}\text{Se}_{68.30}$ ; 008  $\text{Ge}_{25.56}\text{Sb}_{4.64}\text{Se}_{69.80}$  and 009  $\text{Ge}_{22.50}\text{Sb}_{7.50}\text{Se}_{70.00}$  ( $T$  is temperature). See table 4.2 for  $T_g$  (glass transition) and  $T_c$  (onset crystallisation) temperatures.

Note: The samples 001 (a) and 001(b) come from different glass melting but with the same composition and same glass synthesis schedule.

Table 4.2. Glass transition temperature ( $T_g$ ) and crystallisation temperature ( $T_c$ ) of the Ge-Sb-Se glasses.

Glass code	Batch composition / at%	Mean $T_g$ and maximum error / °C	Mean $T_c$ and maximum error / °C	$\Delta T$ ( $=T_c-T_g$ ) / °C
001(a)	Ge <sub>18.90</sub> Sb <sub>15.00</sub> Se <sub>66.10</sub>	240 ± 3	435 ± 5	195
001(b)	Ge <sub>18.90</sub> Sb <sub>15.00</sub> Se <sub>66.10</sub>	240 ± 3	435 ± 5	195
002	Ge <sub>20.00</sub> Sb <sub>10.00</sub> Se <sub>70.00</sub>	220 ± 3	395 ± 5	175
003	Ge <sub>16.60</sub> Sb <sub>20.00</sub> Se <sub>63.40</sub>	250 ± 3	360 ± 5	110
004	Ge <sub>13.50</sub> Sb <sub>24.87</sub> Se <sub>61.63</sub>	240 ± 3	355 ± 2	115
005	Ge <sub>24.00</sub> Sb <sub>4.36</sub> Se <sub>71.64</sub>	227 ± 3	380 ± 5	153
006	Ge <sub>16.70</sub> Sb <sub>13.30</sub> Se <sub>70.00</sub>	203 ± 3	340 ± 5	137
007	Ge <sub>17.67</sub> Sb <sub>14.03</sub> Se <sub>68.30</sub>	209 ± 3	330 ± 5	121
008	Ge <sub>25.56</sub> Sb <sub>4.64</sub> Se <sub>69.80</sub>	255 ± 3	430 ± 5	175
009	Ge <sub>22.50</sub> Sb <sub>7.50</sub> Se <sub>70.00</sub>	235 ± 3	390 ± 5	155

#### 4.4.2 X-ray diffraction

The glassy state of the as-prepared samples (as section 4.2) and the re-melted products after the test of their viscosity / temperature behaviour, in which the samples were heated from room temperature to 10°C below their  $T_g$  at 40°C / min and then the temperature was increased at 10°C / min until achieving  $\geq$  the viscosity of  $10^{4.5}$  Pas, called “remelted-heat-treated samples” were supplied (as section 4.3). These samples were investigated with X-ray diffraction in power and disc form. The heating schedule of the heat treatment which took place is given in detail for each glass melt in section 4.3. The sample was scanned from 5°2 $\theta$  to 80°2 $\theta$  at a step size of 0.02°2 $\theta$  by using a Philips, D 500 X-ray diffractometer at 40 kV voltage and 25 mA current.

X-ray diffraction analysis (see section 3.2.1) on all of the firstly melted, quenched and annealed samples of 001 to 009 (see section 4.2) proved that an amorphous glass sample was obtained by means of the glass synthesising technique described in section 4.2.

In order to investigate the stability of the glass around fibre-drawing temperature, re-melted samples were prepared (see section 4.3) and have gone through the “remelted-heat-treated” heating process (see section 4.3). X-ray diffraction analysis on all of the remelted-heat-treated samples, which could be used to determine the suitability of a glass composition for glass shaping, was carried out. The compositions of 003, 004 and 008 exhibited obvious peaks in the remelted-heat-treated disc XRD pattern, which indicated that crystal phases exist. For the compositions of 001, 002, 005, 006, 007 and 009, their re-heat-treated disc XRD patterns showed broad diffraction humps.

In figure 4.3 (a), the X-ray diffraction pattern of sample 001, represents the glassy profile of the XRD curve for the Ge-Sb-Se glass system. Also, it is the representative of a composition without crystallisation after re-heating in this glass system. The curves of 003, 004, which were crystallised during the heat treatment for investigating the viscosity / temperature behaviour (see section 4.3), have been plotted for comparison. Additionally, the theoretical intensity phase of  $\text{Sb}_2\text{Se}_3$  has been plotted for the usage of identification. It can be seen from figure

4.3 that the pattern of 001 appears smooth at each angle; this profile represents a typical amorphous pattern of a Ge-Sb-Se glass without crystallisation. From figure 4.3, and table 4.3 the crystal pattern of 003 and 004 fit the theoretical X-ray intensity phase of  $\text{Sb}_2\text{Se}_3$  (00-015-0861) [4.43] very well. So the crystal phase can confidently be identified as  $\text{Sb}_2\text{Se}_3$ .

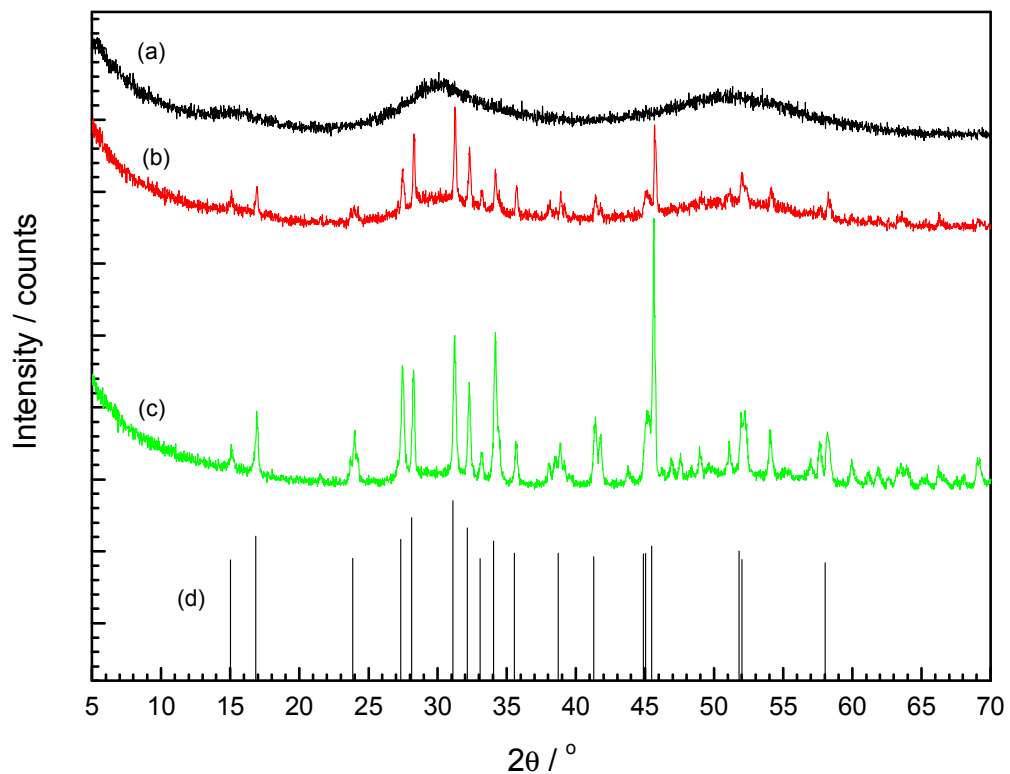


Figure 4.3 X-ray diffraction pattern of Ge-Sb-Se glasses: (a) (001)  $\text{Ge}_{18.90}\text{Sb}_{15.00}\text{Se}_{66.10}$ ; (b) (003)  $\text{Ge}_{16.60}\text{Sb}_{20.00}\text{Se}_{63.40}$ ; (c) (004)  $\text{Ge}_{13.50}\text{Sb}_{24.87}\text{Se}_{61.63}$  and (d) the theoretical intensity phase for  $\text{Sb}_2\text{Se}_3$  (00-015-0861)[4.43].

Table 4.3 the value of  $2\theta / ^\circ$  versus intensity / counts in figure 4.3.

(003) $\text{Ge}_{16.60}\text{Sb}_{20.00}\text{Se}_{63.40}$		(004) $\text{Ge}_{13.50}\text{Sb}_{24.87}\text{Se}_{61.63}$		$\text{Sb}_2\text{Se}_3$	
$2\theta / ^\circ$	I / %	$2\theta / ^\circ$	I / %	$2\theta / ^\circ$	I / %
-	-	-	-	10.676	8
15.036	19.7	15.072	7.1	15.029	25
-	-	-	-	15.211	6
16.863	21	16.885	20.1	16.874	55
-	-	21.471	3.3	21.446	10
23.665	9.6	23.66	9.3	23.643	12

23.92	11.4	23.919	16.7	23.901	<b>30</b>
24.179	14.4	24.145	10.3	24.152	<b>16</b>
27.076	7.8	-	-	27.023	<b>12</b>
27.408	37.1	27.411	37.8	27.395	<b>70</b>
28.236	63.6	28.202	36.9	28.2	<b>75</b>
-	-	-	-	30.326	<b>2</b>
-	-	-	-	30.699	<b>4</b>
31.212	88.2	31.166	49.5	31.16	<b>100</b>
32.258	51.6	32.226	33.7	32.22	<b>60</b>
-	-	-	-	32.424	<b>10</b>
33.17	16.6	33.135	10.9	33.115	<b>20</b>
34.128	39.3	34.11	49.1	34.075	<b>60</b>
34.397	16.8	34.402	15.8	34.358	<b>20</b>
35.658	28.6	35.627	15.3	35.7	<b>30</b>
38.067	11.6	38.005	8.5	37.984	<b>25</b>
-	-	-	-	38.354	<b>14</b>
38.513	12.1	38.463	9.8	38.49	<b>14</b>
38.856	25.8	38.805	16	38.801	<b>35</b>
39.128	15.5	39.096	8.3	39.081	<b>12</b>
-	-	39.449	4.8	39.456	<b>8</b>
-	-	39.714	3.5	39.71	<b>8</b>
41.368	23.3	41.351	21.4	41.305	<b>35</b>
41.736	17.7	41.707	15.4	41.705	<b>20</b>
-	-	43.716	6.7	43.694	<b>10</b>
44.999	21.4	45.048	21.2	44.95	<b>35</b>
-	-	-	-	45.068	<b>30</b>
-	-	-	-	45.258	<b>30</b>
-	-	-	-	45.354	<b>25</b>
45.678	100	45.582	100	45.571	<b>25</b>
-	-	46.166	6.8	46.209	<b>8</b>
-	-	46.859	10.3	46.84	<b>8</b>
-	-	-	-	46.892	<b>8</b>
47.459	9.5	47.515	11.3	47.49	<b>8</b>
48.964	10.2	48.928	15.2	48.902	<b>8</b>
-	-	-	-	49.469	<b>4</b>
-	-	-	-	49.584	<b>4</b>
-	-	-	-	49.903	<b>4</b>
-	-	-	-	50.765	<b>8</b>
51.092	13.1	51.068	15.7	51.039	<b>16</b>
51.949	31.5	51.92	26.8	51.879	<b>45</b>
52.244	18.2	52.195	26.2	52.166	<b>20</b>
54.072	22.6	54.012	21.1	53.956	<b>14</b>
-	-	-	-	54.865	<b>6</b>

-	-	-	-	55.807	6
-	-	-	-	56.328	1
-	-	-	-	56.479	1
-	-	-	-	56.821	6
-	-	56.925	9.1	56.898	8
-	-	57.58	17.7	57.559	12
58.216	29.6	58.136	20.4	58.115	18
-	-	-	-	58.276	10
-	-	59.908	9.5	59.854	8
-	-	-	-	60.155	6

#### **4.4.3 Field emission gun environmental scanning electron microscope-energy dispersive X-ray analysis (FEG-ESEM-EDS)**

The stoichiometry of the chalcogenide samples, which had been re-heat-treated with the same thermal process of glass shaping, has been determined by means of energy dispersive X-ray analysis (EDS) of the sample (see section 3.2.5). The crystal phase has been confirmed using the back-scattered electrons mode of a field emission gun environmental scanning electron microscope (FEG-ESEM, XL 30 Philips). The samples for atomic concentration determination were prepared by mounting an FTIR sample (see section 3.2.6), which had a flat and polished surface, onto a SEM copper stub. The samples for crystal phase imaging using XRD were obtained by cracking the disc after “re-heat-treatment” (see in section 4.3) and mounting the sample onto a stub with sticky carbon with its fractured internal surface up. Because the compositions of 003 and 004 appeared to be crystallised after the “remelted-heat-treatment”, these latter samples were picked out for crystal phase characterisation.

Figure 4.4 shows the image of a crystalline phase observed on the fractured interior surface of the composition 003 ( $\text{Ge}_{16.60}\text{Sb}_{20.00}\text{Se}_{63.40}$ ), which was “re-melted” and then “re-heat-treated” in the TMA, using the backscattered electron beam mode (FEG-ESEM, XL 30 Philips, see section 3.2.5). This sample is representative of the glasses of 003, 004 and 008 that had also crystallised after being re-melted (section 4.3) and then heating to the fibre-drawing temperature. The detailed remelted-heat-treated schedule for sample 003 is given in table 4.4 for completeness. Images obtained similarly for the crystal phases of re-melted samples of 004 ( $\text{Ge}_{13.50}\text{Sb}_{24.87}\text{Se}_{61.63}$ ) and 008 ( $\text{Ge}_{25.56}\text{Sb}_{4.64}\text{Se}_{69.80}$ ) showed similar crystal features.

Table 4.4 The heating schedule applied to “remelted” sample of 003 ( $\text{Ge}_{16.60}\text{Sb}_{20.00}\text{Se}_{63.40}$ ) for investigating the viscosity / temperature behaviour. After this the sample was called “remelted-heat-treated”.

step	schedule
1	Dwell at RT for 5 min
2	RT to 240°C @ 40°C / min
3	Dwell at 240°C for 5 min
4	240°C to 362°C @ 10°C / min
5	Switch off the furnace for cooling

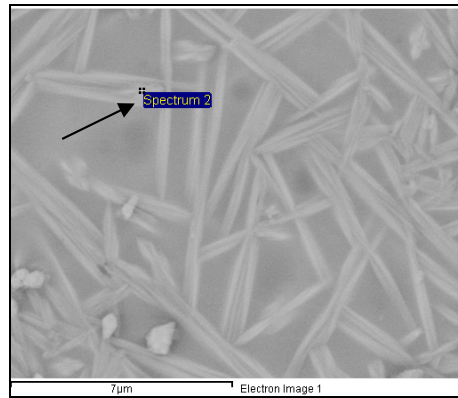


Figure 4.4 Back scattered scanning electron micrographic image of the composition 003 ( $\text{Ge}_{16.60}\text{Sb}_{20.00}\text{Se}_{63.40}$ ) “re-melted” and then heated in TMA (see table 4.4). Note: the bright needles are crystals which have been defined as the phase  $\text{Sb}_2\text{Se}_3$  according to XRD (see figure 4.3 and table 4.3). The arrow indicates where the EDS spectrum was collected (see table 4.5).

Figure 4.4 shows the back scattered scanning electron micrographic image of the composition 003 “re-melted” and then heated in TMA. The bright needles are crystals and the arrow indicates where the EDS spectrum was collected. The brighter area of 003 shows the experimental atomic % of  $\text{Ge}_{12.97}\text{Sb}_{24.31}\text{Se}_{62.71}$  (see table 4.5), which has slightly higher Sb concentration than the batched composition 003 ( $\text{Ge}_{16.60}\text{Sb}_{20.00}\text{Se}_{63.40}$ ). Note that the approximate length of the needle shaped crystals is  $\sim 5 - 7 \mu\text{m}$  from figure 4.4. This crystalline phase can be identified as  $\text{Sb}_2\text{Se}_3$  with the assistance of XRD result (see figure 4.3 and table 4.3). This indicates that obvious crystallisation appeared when the sample was heated around its fibre-drawing temperature range.

Table 4.5. EDS quantification results of the arrow pointed crystal phase inside sample after heat treatment (see figure 4.3). The error on is  $\pm 0.5$  at%. XRD of  $\text{Sb}_2\text{Se}_3$  is shown in figure 4.3 and table 4.3.

Observed			Batch composition	XRD phase observed
Element	Weight wt %	Atomic at%	/ at%	$\text{Sb}_2\text{Se}_3$ / at%
Ge	10.63	12.97	16.6	0
Se	55.93	62.71	63.4	60
Sb	33.44	24.32	20	40

#### 4.4.4 Thermal properties: viscosity / temperature relations

The viscosity / temperature relation of each glass melt (001 to 009) was measured by means of a Perkin Elmer TMA7 equipment and the procedure was synchronous with the heating treatment and cooling for analysing glass stability (see table 4.6). These glasses sample were re-melted and the samples preparation and temperature schedule is described in section 4.3. A good agreement was obtained between results obtained for different samples with the same composition. Three samples were measured for each composition and the curves of viscosity against temperature showed a good overlap (with a standard deviation of viscosity data versus temperature of  $\pm 10^{0.02}$  Pas).

The viscosity / temperature curves of compositions 001 to 009 are plotted in figure 4.5. The viscosity / temperature relationships of these compositions are studied in further detail in section 4.5. Three compositions were chosen as the candidates of the chalcogenide glass pair for subsequent fibre fabrication: (a) (002)  $\text{Ge}_{20.00}\text{Sb}_{10.00}\text{Se}_{70.00}$  (red); (b) (001)  $\text{Ge}_{18.90}\text{Sb}_{15.00}\text{Se}_{66.10}$  (black) and (c) (009)

$\text{Ge}_{22.50}\text{Sb}_{7.50}\text{Se}_{70.00}$  (dark blue).

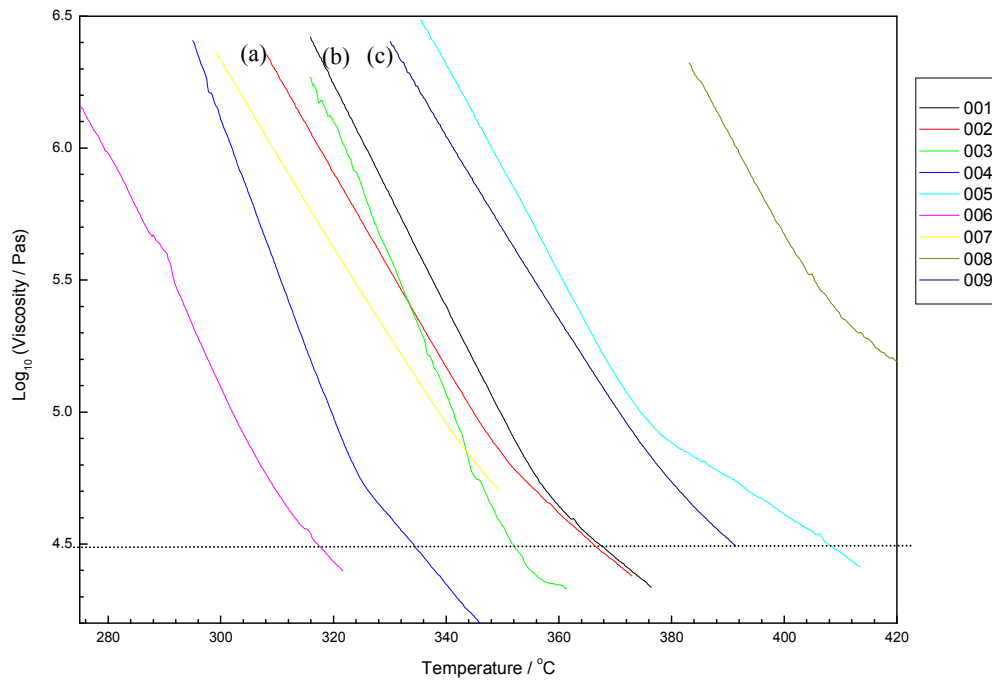


Figure 4.5 Log (viscosity / Pas) versus temperature /  $^\circ\text{C}$  for the glasses of composition 001 to 009 (plot in nine different colours). Three compositions were chosen as the candidates of the chalcogenide glass pair: (a) (002)  $\text{Ge}_{20.00}\text{Sb}_{10.00}\text{Se}_{70.00}$  (red); (b) (001)  $\text{Ge}_{18.90}\text{Sb}_{15.00}\text{Se}_{66.10}$  (black) and (c) (009)  $\text{Ge}_{22.50}\text{Sb}_{7.50}\text{Se}_{70.00}$  (dark blue).

Table 4.6 Heating and cooling schedule of re-melted glasses (see section 4.3) during the TMA viscosity / temperature measurement

Glass code	Batch composition	Heat schedule	Cooling schedule
001	Ge <sub>18.90</sub> Sb <sub>15.00</sub> Se <sub>66.10</sub>	RT to 230°C @ 40°C / min Dwell at 230°C for 5 min 230°C to 377°C @ 10°C / min	Switch off the furnace
002	Ge <sub>20.00</sub> Sb <sub>10.00</sub> Se <sub>70.00</sub>	RT to 210°C @ 40°C / min Dwell at 210°C for 5 min 210°C to 374°C @ 10°C / min	Switch off the furnace
003	Ge <sub>16.60</sub> Sb <sub>10.00</sub> Se <sub>63.40</sub>	RT to 240°C @ 40°C / min Dwell at 240°C for 5 min 240°C to 362°C @ 10°C / min	Switch off the furnace
004	Ge <sub>13.50</sub> Sb <sub>24.87</sub> Se <sub>61.63</sub>	RT to 230°C @ 40°C / min Dwell at 230°C for 5 min 230°C to 346°C @ 10°C / min	Switch off the furnace
005	Ge <sub>24.00</sub> Sb <sub>4.36</sub> Se <sub>71.64</sub>	RT to 217°C @ 40°C / min Dwell at 217°C for 5 min 217°C to 413°C @ 10°C / min	Switch off the furnace
006	Ge <sub>16.70</sub> Sb <sub>13.30</sub> Se <sub>70.00</sub>	RT to 193°C @ 40°C / min Dwell at 193°C for 5 min 193°C to 322°C @ 10°C / min	Switch off the furnace
007	Ge <sub>17.67</sub> Sb <sub>14.03</sub> Se <sub>68.30</sub>	RT to 199°C @ 40°C / min Dwell at 199°C for 5 min 199°C to 350°C @ 10°C / min	Switch off the furnace
008	Ge <sub>25.56</sub> Sb <sub>4.64</sub> Se <sub>69.80</sub>	RT to 245°C @ 40°C / min Dwell at 245°C for 5 min 245°C to 430°C @ 10°C / min	Switch off the furnace
009	Ge <sub>22.50</sub> Sb <sub>7.50</sub> Se <sub>70.00</sub>	RT to 225°C @ 40°C / min Dwell at 225°C for 5 min 225°C to 392°C @ 10°C / min	Switch off the furnace

#### 4.4.5 Thermal properties: thermal expansion coefficient

Thermal expansion coefficient ( $\alpha$ ) has been obtained by measuring the expansion of a 7 mm high chalcogenide piece of the re-melted (see section 4.3) (not further heat treated) material with parallel and flat opposite faces. The as-annealed glass cylinder (see in section 4.2.1, ~ 5 mm height, 10 mm diameter) was mounted onto

a aluminium block with wax and two parallel cuts were applied with  $\sim 7$  mm intervals along the cylinder's surface to obtain the opposite faces (no polishing). All of the thermal expansion coefficient measurements were based on a uniform sample thermal history in which the samples were heated to about  $5^\circ\text{C}$  above  $T_g$  at  $10^\circ\text{C} / \text{min}$ , allowed to equilibrate at this temperature by holding isothermally for 3 minutes before cooling back to room temperature at  $10^\circ\text{C} / \text{min}$ . Then, in situ, for the actual  $\alpha$  measurement, the sample was reheated using a heating rate of  $5^\circ\text{C} / \text{min}$  under a constant load of 50 mN. The thermal expansion coefficient (TEC) of all the compositions is shown in table 4.7.

Table 4.7 Thermal expansion coefficient ( $\alpha$ ) of Ge-Sb-Se glasses.

Glass code	Batch composition	TEC / $10^{-6}\text{K}^{-1}$				Error / $10^{-6}\text{K}^{-1}$	Error / %
		40-180°C	40-80 °C	80-120 °C	120-180 °C		
001	Ge <sub>18.90</sub> Sb <sub>15.00</sub> Se <sub>66.10</sub>	17.7	16.9	17.2	18.5	$\pm 0.2$	1.1%
002	Ge <sub>20.00</sub> Sb <sub>10.00</sub> Se <sub>70.00</sub>	20.3	18.8	20.0	21.7	$\pm 0.2$	0.8%
003	Ge <sub>16.60</sub> Sb <sub>20.00</sub> Se <sub>63.40</sub>	16.7	16.4	16.4	17.0	$\pm 0.2$	1.2%
004	Ge <sub>13.50</sub> Sb <sub>24.87</sub> Se <sub>61.63</sub>	15.6	15.5	15.7	15.8	$\pm 0.2$	1.3%
005	Ge <sub>24.00</sub> Sb <sub>4.36</sub> Se <sub>71.64</sub>	21.0	19.2	19.6	23.1	$\pm 0.2$	1.0%
006	Ge <sub>16.70</sub> Sb <sub>13.30</sub> Se <sub>70.00</sub>	22.5	21.6	21.9	23.3	$\pm 0.2$	0.8%
007	Ge <sub>17.67</sub> Sb <sub>14.03</sub> Se <sub>68.30</sub>	22.0	21.0	21.3	22.3	$\pm 0.2$	0.9%
008	Ge <sub>25.56</sub> Sb <sub>4.64</sub> Se <sub>69.80</sub>	16.2	16.0	16.0	16.6	$\pm 0.2$	1.2%
009	Ge <sub>22.50</sub> Sb <sub>7.50</sub> Se <sub>70.00</sub>	19.9	18.4	18.9	21.5	$\pm 0.2$	0.8%

Three times of measurement were done for each composition to achieve a good agreement on the value of TEC. Three thermomechanical analysis (TMA) dilatometric response (thermal expansion) versus temperature curves obtained from different measurements on the same sample of the compositions 001 are compared in Figure 4.6.

The thermomechanical analysis (TMA) dilatometric response (thermal expansion) versus temperature curves of the compositions 001 to 009 are compared in figure 4.7.

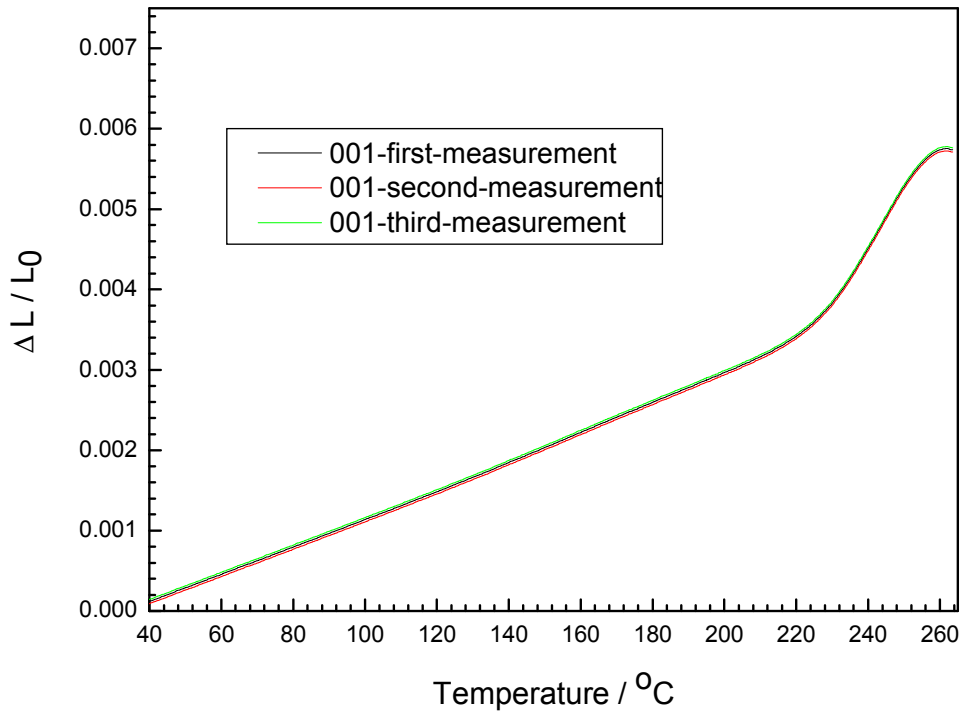


Figure 4.6 Thermomechanical analysis (TMA) dilatometric response (thermal expansion) versus temperature / °C for the glasses composition of 001. Three times of measurements were applied to the same sample. The curve in black, red and green are the curves for the first, second and third time's measurement, respectively. A good agreement was achieved between different measurements to provide an error of  $\pm 0.2 \times 10^{-6} \text{K}^{-1}$  for the value of thermal expansion coefficient ( $\alpha$ ), (see Table 4.7).

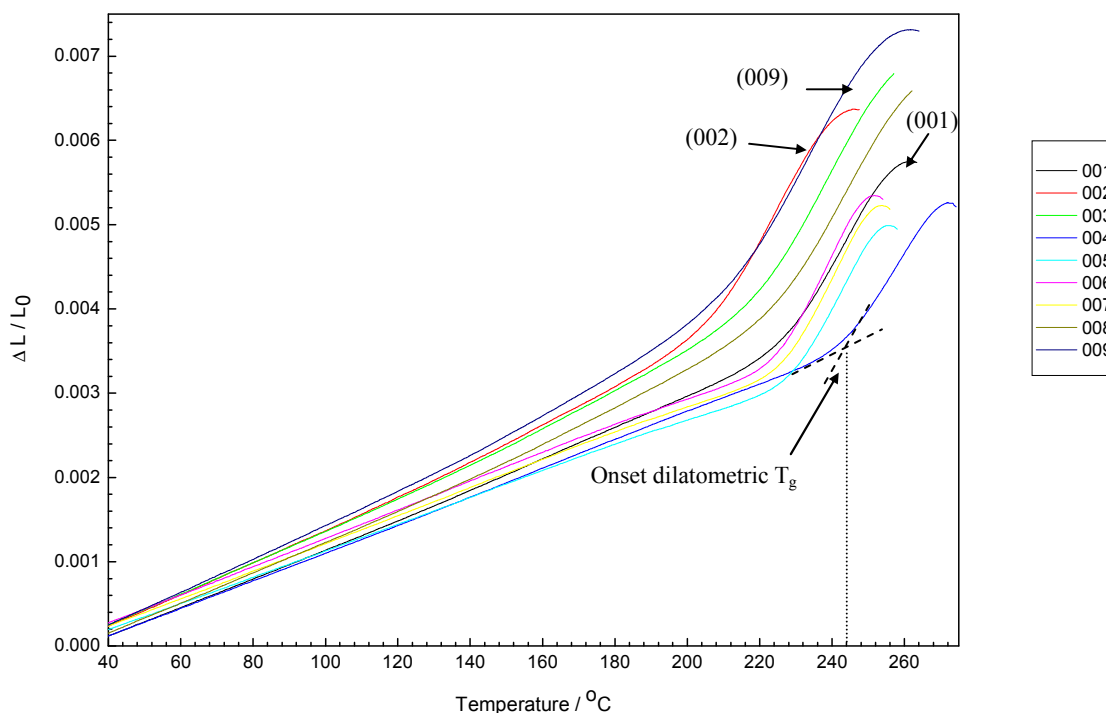


Figure 4.7 Thermomechanical analysis (TMA) dilatometric response (thermal expansion) versus temperature / °C for the glasses composition of 001 to 009 (in different colours). Three composition were chosen as the candidate of glass pair: (001)  $\text{Ge}_{18.90}\text{Sb}_{15.00}\text{Se}_{66.10}$  (black); (002)  $\text{Ge}_{20.00}\text{Sb}_{10.00}\text{Se}_{70.00}$  (red), and (009)  $\text{Ge}_{22.50}\text{Sb}_{7.50}\text{Se}_{70.00}$  (dark blue). ( $\Delta L$  is change in length of the sample and  $L_0$  is the original sample length.)

From the figure 4.7, it can be found that the rate of  $\Delta L / L_0$  begins to increase faster at about 15°C below the DTA  $T_g$  of each composition. Then the rate of  $\Delta L / L_0$  begins to decrease at about 10 to 15°C above the DTA  $T_g$  of each composition. The onset dilatometric  $T_g$ s are given in table 4.9 and are defined as the temperature at which there is a change in slope. The dilatometric  $T_g$ s do not follow the same trend as the DTA  $T_g$ s (section 4.4.1), but this may be due to the problem of estimating the dilatometric  $T_g$ s. The dilatometric  $T_g$ s lie within  $\pm 20^\circ\text{C}$  of the DTA  $T_g$ s.

Table 4.8 Onset dilatometric  $T_g$  of the glass composition of 001 to 009 as shown in figure 4.6.

Glass code	Batch composition	Onset dilatometric $T_g$ / °C
001	Ge <sub>18.90</sub> Sb <sub>15.00</sub> Se <sub>66.10</sub>	224 ± 10
002	Ge <sub>20.00</sub> Sb <sub>10.00</sub> Se <sub>70.00</sub>	208 ± 10
003	Ge <sub>16.60</sub> Sb <sub>20.00</sub> Se <sub>63.40</sub>	220 ± 10
004	Ge <sub>13.50</sub> Sb <sub>24.87</sub> Se <sub>61.63</sub>	244 ± 10
005	Ge <sub>24.00</sub> Sb <sub>4.36</sub> Se <sub>71.64</sub>	225 ± 10
006	Ge <sub>16.70</sub> Sb <sub>13.30</sub> Se <sub>70.00</sub>	220 ± 10
007	Ge <sub>17.67</sub> Sb <sub>14.03</sub> Se <sub>68.30</sub>	225 ± 10
008	Ge <sub>25.56</sub> Sb <sub>4.64</sub> Se <sub>69.80</sub>	230 ± 10
009	Ge <sub>22.50</sub> Sb <sub>7.50</sub> Se <sub>70.00</sub>	218 ± 10

#### 4.4.6 Optical properties: Fourier transform infrared spectroscopy

The absorption spectra of the Ge-Sb-Se 001 – 009 glasses have been investigated by means of a Bruker IF 66 FTIR from ~ 0.9  $\mu\text{m}$  to 16  $\mu\text{m}$ . The samples have been prepared by cutting a ~2.7 mm thick disc from the 10 mm diameter glass rod of each as-prepared chalcogenide glass (see section 4.2.1). The opposite large faces of the discs were then ground parallel and polished to a 1 $\mu\text{m}$  finish. The absorption spectra of all the compositions have been compared to check the agreement of the position of the absorption bands. Three combinations of light source, beam splitter and detector have been chosen for different spectral ranges:

1) tungsten lamp (Bruker), CaF<sub>2</sub> beam splitter (broadband, Bruker) and InGaAs detector (Bruker) were applied for the range of < 1.2 μm; 2) tungsten lamp (Bruker), CaF<sub>2</sub> beam splitter (broadband, Bruker) and DTGS detector (Bruker) were assigned for the range from 1.2 μm to 3.4 μm; 3) Globar (Bruker), KBr beam splitter (Bruker) and DTGS detector (Bruker) were used for the range from 3.4 μm to ~17 μm. The height of impurity absorbance bands was presented in a comparable unit / cm<sup>-1</sup>, obtained by dividing the intensity of the absorbance by the sample thickness, so different absorbance spectrum could be closely compared.

The FTIR result (see operation in section 3.2.6 and section 4.3.6) shows that, for the Ge-Sb-Se glass system, the height of the absorption band, taken as the maximum height of the band minus the height at the base of the band, varies with different atomic concentration of glass composition but their wavelength positions exhibit a good overlap for the different Ge-Sb-Se glass compositions. Thus, the absorption spectrum of the composition 001 (Ge<sub>18.9</sub>Sb<sub>15</sub>Se<sub>66.1</sub>) has been chosen for the plot in figure 4.8 to identify typical absorption bands of the Ge-Sb-Se glass system. The bands due to Ge-O exist at 7.8 μm and 11.8 μm [4.26, 4.21, 4.29, 4.30, 4.31 and 4.32]. The Se-H vibrational absorption band appears at the wavelength of 4.6 μm [4.27, 4.28] and the bands of Sb-O exist at 12.7 μm and 16 μm [4.26]. The O-H stretch and H<sub>2</sub>O vibrational bending absorption bands are indentified in reference [4.26] at the wavelengths of 2.8 μm and 6.3 μm, respectively. The C-H band appears at the wavelength of 3.4 μm and the Si-O

absorption appears at 8.9  $\mu\text{m}$ . The broadness of the absorption bands provides further evidence, with the XRD results, to confirm that no obvious crystallisation appears in the glass. It should be noted that all of the observed FTIR absorption bands are due to unwanted chemical impurities.

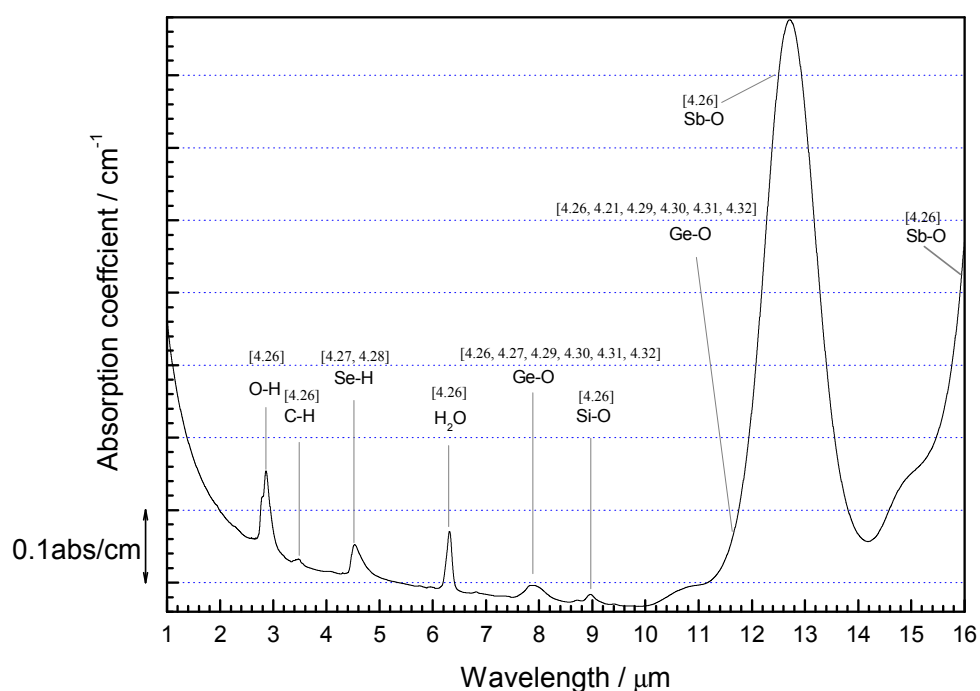


Figure 4.8 FTIR spectrum of as prepared bulk  $\text{Ge}_{18.90}\text{Sb}_{15.00}\text{Se}_{66.10}$  (code 001). Note that there is a Ge-O contribution expected at a wavelength of 11.5  $\mu\text{m}$  but it is dominated by the Sb-O band 11.3  $\mu\text{m}$  - 14 $\mu\text{m}$ .

#### 4.4.7 Optical properties: refractive indices at 1.463 $\mu\text{m}$ wavelength

The refractive index of the following Ge-Sb-Se glass compositions: 001  $\text{Ge}_{18.90}\text{Sb}_{7.50}\text{Se}_{70.00}$ , 002  $\text{Ge}_{20.00}\text{Sb}_{10.00}\text{Se}_{70.00}$ , 003  $\text{Ge}_{16.60}\text{Sb}_{20.00}\text{Se}_{63.40}$ , 005  $\text{Ge}_{24.00}\text{Sb}_{4.36}\text{Se}_{71.64}$ , 009  $\text{Ge}_{22.50}\text{Sb}_{7.50}\text{Se}_{70.00}$ , was measured using the standard minimum deviation method (see section 3.2.7) at a wavelength of 1463 nm. The

prisms with 20° apex have been made for the measurement in the following procedure. A 10 mm diameter and ~ 9 mm height chalcogenide glass rod from the as-prepared glass rod (see section 4.2.1) was mounted using epoxy resin (Struers) and mounted onto a 10°C brass jig with wax. A perpendicular cut was applied to the free end to render a 10°C inclined surface, then that surface was ground and polished to a 1 μm finish. Afterwards, the sample was mounted onto a 20°C brass jig on its polished surface and the unpolished surface was cut perpendicularly to obtain an apex angle of 20°C. That surface was also finely ground and polished to a 1 μm finish. A retroreflection technique, in which the laser beam was instant normally to the surface of the sample and went back to its original instant position with least scattering, was applied to measure the exact prism apex angle. The refractive index data were obtained from the measurement for the surface which scattered the beam the least. Measurements were repeated four times for each prism to achieve an error limit; the standard deviation was  $\pm 0.003$  and so the precision of the refractive index obtained from this system is  $3 \times 10^{-3}$ .

The refractive indices of the experimental compositions are presented in table 4.9 and are also plotted in figure 4.1. The refractive index of the glasses decreases from the Sb rich side to Sb poor side, and also decreases from the Ge poor side to Ge rich side (refer to figure 4.1).

Table 4.9 Refractive index of Ge-Sb-Se glasses measured at 1460 nm wavelength.

Glass code	Batch composition	Refractive index (1463 nm)					Error
		1	2	3	4	mean	
001	Ge <sub>18.90</sub> Sb <sub>15.00</sub> Se <sub>66.10</sub>	2.675	2.677	2.674	2.678	2.676	± 0.003
002	Ge <sub>20.00</sub> Sb <sub>10.00</sub> Se <sub>70.00</sub>	2.575	2.577	2.578	2.573	2.576	± 0.003
003	Ge <sub>16.60</sub> Sb <sub>20.00</sub> Se <sub>63.40</sub>	2.792	2.795	2.790	2.792	2.792	± 0.003
005	Ge <sub>24.00</sub> Sb <sub>4.36</sub> Se <sub>71.64</sub>	2.490	2.491	2.493	2.489	2.491	± 0.003
009	Ge <sub>22.50</sub> Sb <sub>7.50</sub> Se <sub>70.00</sub>	2.549	2.547	2.550	2.549	2.549	± 0.002

A quantitative refractive index contrast comparison can be made with the compositions of Ge<sub>16.7</sub>Sb<sub>13.30</sub>Se<sub>70.00</sub>, Ge<sub>20.00</sub>Sb<sub>10.00</sub>Se<sub>70.00</sub> and Ge<sub>22.50</sub>Sb<sub>7.50</sub>Se<sub>70.00</sub>. Their refractive indices at 1463 nm are 2.657, 2.575 and 2.549, respectively. The contrast of refractive index is 0.082 and 0.026 when the Ge / Sb atomic ratio increases from 1.26 to 2 and for Ge / Sb = 3 the contrast can be 0.026 or 0.108, all with a fixed concentration of Se. However the variation of refractive index versus composition is not linear with Ge / Sb ratio from the data observed.

#### **4.5 Development of a glass pair with matched thermal properties and disparate refractive indices**

If the glassy state was preserved without crystallization after heating to the temperature of fibre drawing and cooling back to room temperature as in during the TMA measurement of viscosity versus temperature (see section 4.3, table 4.6), then these glass compositions are the candidates to make fibre. Furthermore, the requirement of a chalcogenide glass pair for a core-clad preform is that the selected pair has the aimed refractive index contrast for the desired numerical aperture (NA) and similar thermal properties, which are close enough to ensure success in fabrication. Additionally, a compressive clad will be ideal to make the

fibre robust. This would be achieved if the cladding glass TEC is slightly smaller than the core glass TEC. Due to the above reasons, it is critical to further analyse the results presented in section 4.4 in order to understand how the modified composition varies  $T_g$  and then varies their thermal properties. This is done in the sub-sections 4.5.1, 4.5.2 and 4.5.3.

#### **4.5.1 Glass $T_g$ stability and properties in comparison with the previous literature**

It has been shown in figure 4.1 that the glass transition temperatures of our experimental compositions, chosen from Hilton's 220°C  $T_g$  empirical isotherm, do not agree with the reported isotherm. Note,  $T_g$  here was measured using DTA (see section 4.3, table 4.2). From the data presented here, the compositions close to the Ge rich corner exhibit higher  $T_g$  because the increased Ge concentration will increase  $T_g$ . This tendency is also confirmed in the investigation of sub-series of glasses  $(\text{Ge}_x\text{Sb}_{(30-x)})_{30}\text{Se}_{70}$  and  $(\text{Ge}_x\text{Sb}_{(35-x)})_{35}\text{Se}_{65}$  shown in figure 4.9 in which the  $T_g$  exhibits a monotonic increase with increase in Ge concentration, for a fixed atomic percentage of Se. It can be found that  $T_g$  will increase by reducing the Se concentration with the same atomic ratio of Ge to Sb.

In order to analyse how the  $T_g$  is affected by adjusting the Ge-Sb-Se glass's composition, the  $T_g$  against each composition's Ge / Sb atomic % and average coordination number are listed in table 4.10.

Table 4.10 Glass transition temperature ( $T_g$ ) of the Ge-Sb-Se glasses together with the average coordination number  $\langle r \rangle$ .

Glass code	Batch composition / at%	Ge/Sb Atomic %	$\langle r \rangle$	Mean $T_g$ and maximum error / °C
001(a)	Ge <sub>18.90</sub> Sb <sub>15.00</sub> Se <sub>66.10</sub>	1.26	2.528	240 ± 1.2
001(b)	Ge <sub>18.90</sub> Sb <sub>15.00</sub> Se <sub>66.10</sub>	1.26	2.528	240 ± 1.7
002	Ge <sub>20.00</sub> Sb <sub>10.00</sub> Se <sub>70.00</sub>	2.00	2.500	220 ± 1.4
003	Ge <sub>16.60</sub> Sb <sub>20.00</sub> Se <sub>63.40</sub>	0.83	2.532	250 ± 2.5
004	Ge <sub>13.50</sub> Sb <sub>24.87</sub> Se <sub>61.63</sub>	0.54	2.519	240 ± 1.6
005	Ge <sub>24.00</sub> Sb <sub>4.36</sub> Se <sub>71.64</sub>	5.50	2.524	227 ± 1.5
006	Ge <sub>16.70</sub> Sb <sub>13.30</sub> Se <sub>70.00</sub>	1.26	2.467	203 ± 1.5
007	Ge <sub>17.67</sub> Sb <sub>14.03</sub> Se <sub>68.30</sub>	1.26	2.494	209 ± 1.4
008	Ge <sub>25.56</sub> Sb <sub>4.64</sub> Se <sub>69.80</sub>	5.50	2.558	255 ± 1.8
009	Ge <sub>22.50</sub> Sb <sub>7.50</sub> Se <sub>70.00</sub>	3.00	2.525	235 ± 1.0

The relationship of  $T_g$  versus the atomic ratio of (Ge / Sb) in the sub-series of  $(Ge_xSb_{(30-x)})_{30}Se_{70}$  and  $(Ge_xSb_{(35-x)})_{35}Se_{65}$  has been plotted in figure 4.9.

It also can be confirmed from the  $T_g$  data for samples 001, 006, 007, 005 and 008 presented in table 4.11, which have the same ratio of Ge to Sb, that the incorporation of Se decreases the  $T_g$ .

The relationship between  $T_g$  and average coordination number has been plotted in figure 4.10.

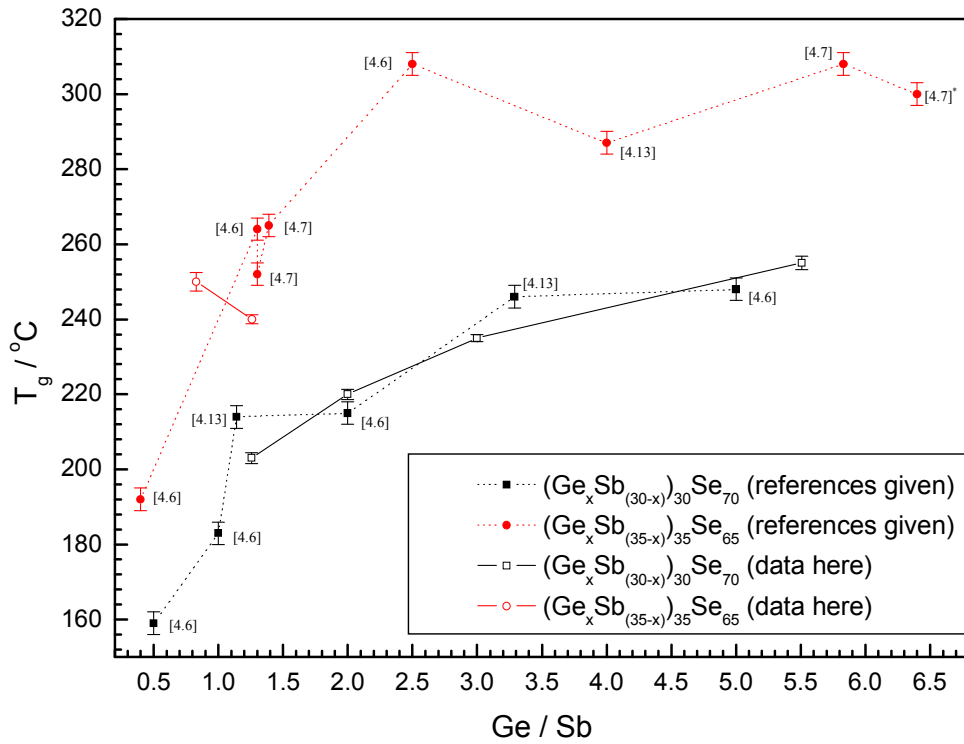


Figure 4.9 Glass transition temperature ( $T_g$ ) from DTA (see section 4.3, table 4.2) versus (Ge / Se) (atomic % ratio) for the sub-series of glasses  $(\text{Ge}_x\text{Sb}_{(30-x)})_{30}\text{Se}_{70}$  and  $(\text{Ge}_x\text{Sb}_{(35-x)})_{35}\text{Se}_{65}$  for data acquired here and by others (see reference number in brackets against data point, note: \* is  $\text{Ge}_{32}\text{Sb}_5\text{Se}_{63}$  [4.7]).

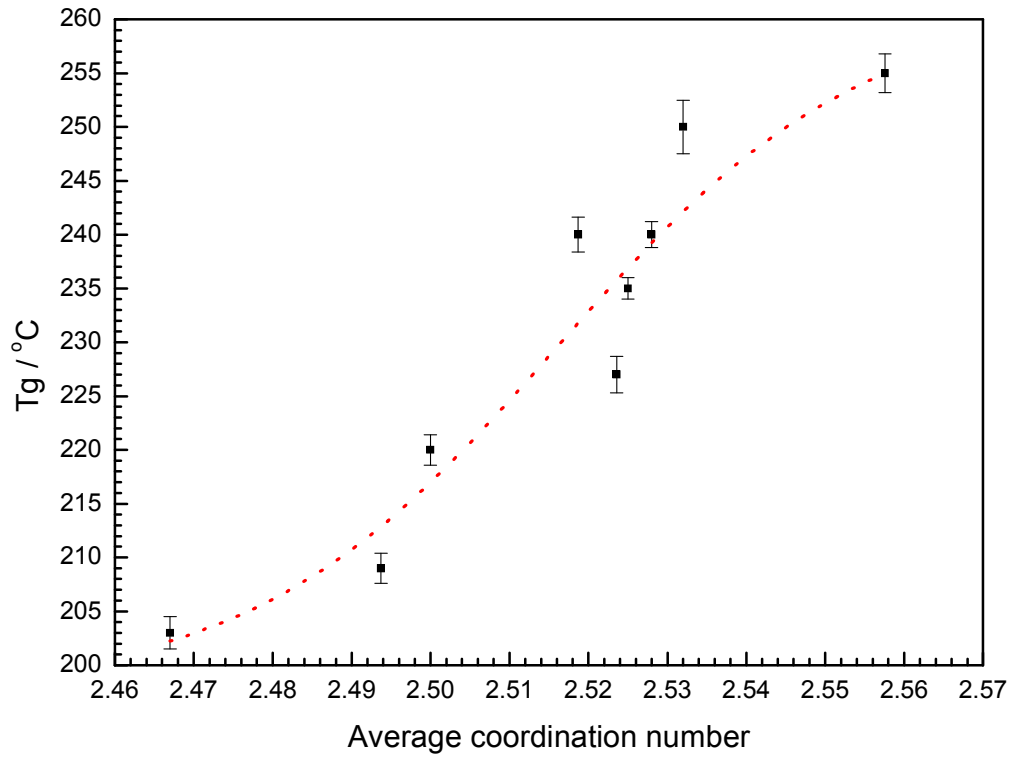


Figure 4.10 Glass transition temperature ( $T_g$ ) determined by DTA (section 4.3, table 4.2) versus average coordination number of Ge-Sb-Se glasses (curve is drawn as a visual aid only). The curve is drawn as a visual aid only.

TEC versus the glass transition temperature ( $T_g$ ), and the average coordination number  $\langle r \rangle$ , are shown in figures 4.11 and 4.12, respectively.

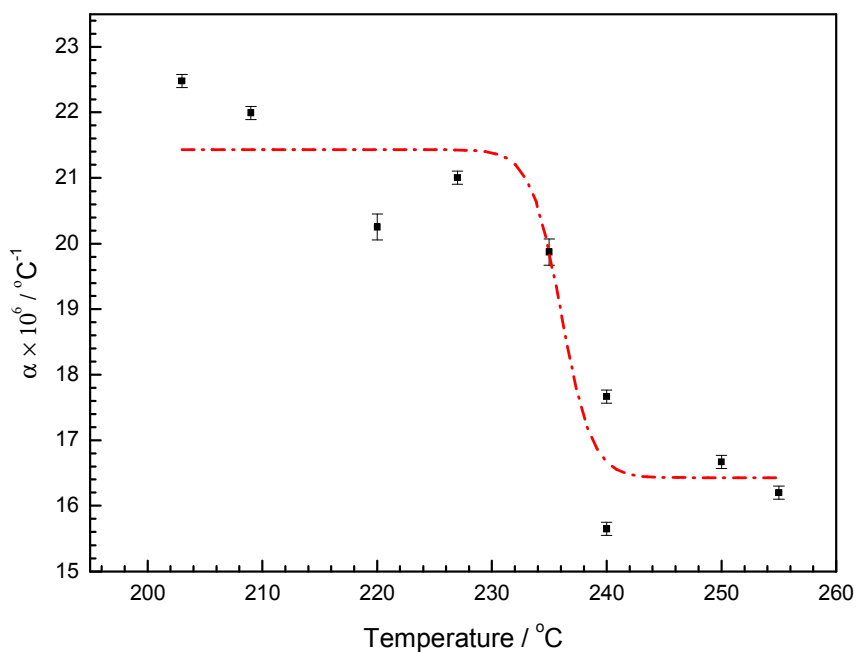


Figure 4.11.  $\alpha$  (TEC) versus glass transition temperature ( $T_g$ ) for Ge-Sb-Se glasses. The error bar indicates the largest contrast between the mean and an individual measurement. The line is drawn as a visual aid only.

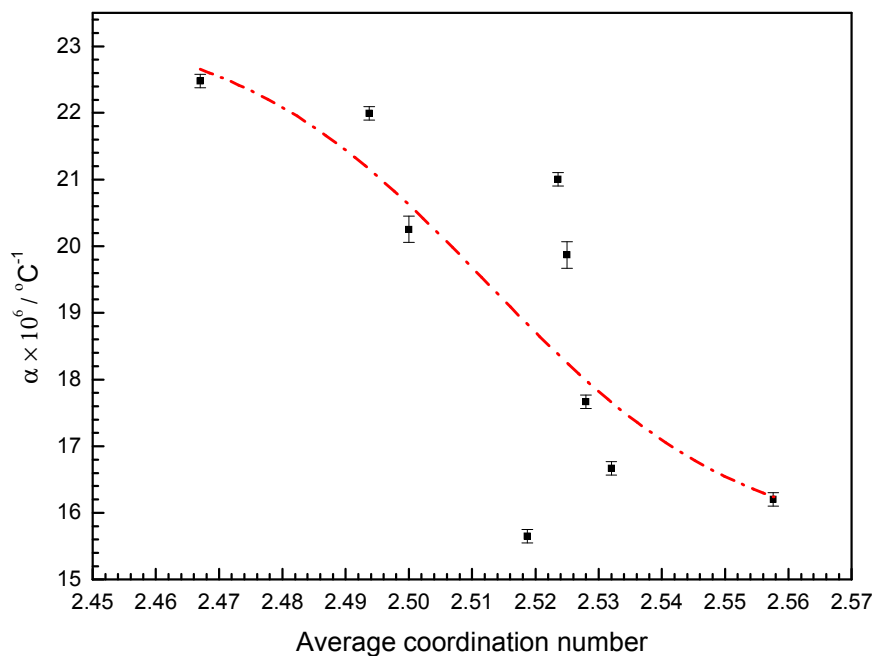


Figure 4.12.  $\alpha$  versus average coordination number. The error bar indicates the largest contrast between the mean and an individual measurement. The line is drawn as a visual aid only.

Others have claimed that for a similar glass series the produced  $(TEC \times T_g)$  is approximately constant [4.39]. Thus, the  $(TEC \times T_g)$  of the composition 001 to 009 was tabulated in table 4.11 for verification. However the results here do not support that supposition.

Table 4.11 The value of  $(TEC \times T_g)$  of compositions 001 to 009.

Glass code	Batch composition / at%	$T_g$ / °C	$T_g$ / K	TEC / $10^{-6}K^{-1}$	$T_g$ °C $\times$ TEC	$T_g$ /K $\times$ TEC
001	Ge <sub>18.90</sub> Sb <sub>15.00</sub> Se <sub>66.10</sub>	240	513	17.2	4.13	8.82
002	Ge <sub>20.00</sub> Sb <sub>10.00</sub> Se <sub>70.00</sub>	220	493	19.5	4.29	9.61
003	Ge <sub>16.60</sub> Sb <sub>20.00</sub> Se <sub>63.40</sub>	250	523	16.4	4.1	8.58
004	Ge <sub>13.50</sub> Sb <sub>24.87</sub> Se <sub>61.63</sub>	240	513	15.7	3.76	8.05
005	Ge <sub>24.00</sub> Sb <sub>4.36</sub> Se <sub>71.64</sub>	227	500	19.6	4.45	9.80
006	Ge <sub>16.70</sub> Sb <sub>13.30</sub> Se <sub>70.00</sub>	203	476	22.0	4.47	10.5
007	Ge <sub>17.67</sub> Sb <sub>14.03</sub> Se <sub>68.30</sub>	209	482	21.3	4.45	10.3
008	Ge <sub>25.56</sub> Sb <sub>4.64</sub> Se <sub>69.80</sub>	255	528	16.0	4.08	8.45
009	Ge <sub>22.50</sub> Sb <sub>7.50</sub> Se <sub>70.00</sub>	235	508	18.9	4.44	9.60

The thermal expansion coefficient versus the atomic ratio has been plotted for

sub-series of glasses  $(\text{Ge}_x\text{Sb}_{(30-x)})_{30}\text{Se}_{70}$  in figure 4.13. Average  $(\text{TEC} \times T_g)$  for this sub-series is  $4.3 \pm 0.2$ , showing that small sub-series do show reasonable correlation.

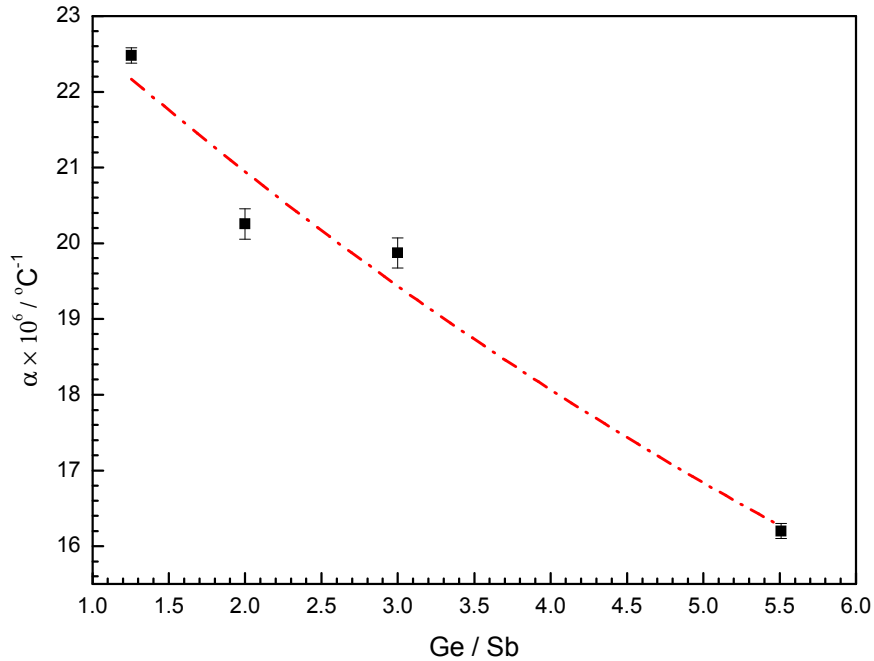


Figure 4.13.  $\alpha$  (TEC) versus (Ge / Sb) (atomic % ratio) for the sub-series of glasses  $(\text{Ge}_x\text{Sb}_{(30-x)})_{30}\text{Se}_{70}$ .

#### 4.5.2 In view of the average coordination number

The investigation here into the relationship between thermal properties and the average coordination number of this glass system helps to reveal the glass structure and find the trend to modify the glass properties. It can be seen that understanding the structure of the Ge-Sb-Se glass is helped by considering the glasses to comprise of  $\text{GeSe}_2$  and  $\text{Sb}_2\text{Se}_3$ . Because the Ge-Se bond is stronger than the Sb-Se bond, then the  $T_g$  of a Ge-Sb-Se glass increases and the thermal expansion coefficient decreases with an increasing atomic ratio of Ge/Sb. This

trend has also been confirmed from the research here on the sub-series of glasses  $(\text{Ge}_x\text{Sb}_{(35-x)})_{35}\text{Se}_{65}$  and  $(\text{Ge}_x\text{Sb}_{(30-x)})_{30}\text{Se}_{70}$  shown in figures 4.9 and 4.13. The extreme of  $T_g$  appears when a glass just consists of the network of  $\text{GeSe}_2$  and  $\text{Sb}_2\text{Se}_3$  [4.6-4.8], which is also confirmed in figure 4.9 from the data point for  $\text{Ge}_{25}\text{Sb}_{10}\text{Se}_{65}$  ( $25\text{GeSe}_2 + 5\text{Sb}_2\text{Se}_3 = \text{Ge}_{25}\text{Sb}_{10}\text{Se}_{65}$ ) in [4.7], so excess Se or Ge atomic makes the structure weaker and so decreases  $T_g$  which is confirmed from the data here shown in table 4.10.

The way of modifying the thermal properties of Ge-Sb-Se glass has also been analysed from the view of average coordination number  $\langle r \rangle$ . Some previous investigations reported in the literature attempt to predict the physical properties versus  $\langle r \rangle$  and two topological thresholds have been raised. The one at  $\langle r \rangle = 2.4$  is according to Phillips' constraint theory [4.34]. Glasses could be optimised at  $\langle r \rangle = 2.4$ , where the structure of the glasses transfers from an underconstrained or a 'floppy' network ( $\langle r \rangle > 2.4$ ) to overconstrained or 'rigid' network ( $\langle r \rangle < 2.4$ ), implying a maximum glass forming tendency. However, controversy exists in applying the constraint theory because some research results [4.9, 4.10] show an anomalous distribution of the extreme of the physical properties. Another threshold at  $\langle r \rangle = 2.67$ , based on dimensionality considerations [4.36] and a chemically ordered covalent network model [4.6, 4.37], indicates the structure transformation from a layered structure to a three dimensional network at  $\langle r \rangle = 2.67$ . The  $\langle r \rangle$  of compositions synthesised here are all between 2.46 and 2.56

(see table 4.10). The anomalous distribution and questionable importance of the significance of the threshold at  $\langle r \rangle = 2.4$  is also confirmed from the data here shown in figure 4.2 and table 4.3, in which moving the compositions closer to the threshold of  $\langle r \rangle = 2.4$  does not imply a stronger glass forming tendency. This is also confirmed from figure 4.1, in which the glass forming ability varies along the  $T_g$  isotherm and of  $\langle r \rangle$ . The thermal expansion coefficient exhibits an approximate monotonic decrease with the increase of  $\langle r \rangle$  and DTA extrapolated onset  $T_g$  (see figure 4.11 and figure 4.12). This result has an agreement with the data in [4.9] indicating that the physical extreme may not exist in the glassy state or may be a glass which tends to crystallise. It can be seen from figure 4.11 that increasing the Ge concentration and decreasing the Sb concentration may lead to a reduction of the thermal expansion coefficient.

#### **4.5.3 Adjusting the optical properties**

From previous investigation in our laboratory of the ternary Ge-As-Se glass systems [4.40 - 4.42], it can be found that the incorporation of Ge will decrease the refractive index. It is well known that the introduction of Sb can increase the refractive index of Ge-Sb-Se glasses because Sb is a heavier atom than the others in the system. The isothermals of  $T_g$  in the glass-forming region of the Ge-Sb-Se ternary phase diagram (see figure 4.1) extend to the direction, in which the atomic percentage of Ge varies a lot. Thus, these trends indicate that it may be possible to find two compositions with relatively large refractive index contrast and similar

$T_g$ , although the contrast of thermal properties may exist in the glass pair which have close  $T_g$ . The data of refractive index in table 4.9 shows that enough refractive index contrast could be achieved when considering the trade-off between optical properties contrast and thermal properties matching.

#### **4.6 Selecting a chalcogenide Ge-Sb-Se glass pair with matched thermal properties and disparate refractive indices**

The candidates for a chalcogenide Ge-Sb-Se glass pair for the core-clad structure fibre should have moderate  $T_g$ , stable glass forming ability and be reluctant to undergo crystallisation when being heated to the fibre drawing temperature. The compositions for core and clad. region should have relatively close  $T_g$ , thermal expansion coefficient and viscosity regarding to the same fibre drawing temperature. Ideally, the fibre has a compressive clad by applying a composition with lower TEC than its core's composition.

The core glass refractive index should be higher than that of the cladding glass and for PCF the contrast should be as high as possible. The refractive index contrast may be modified based on the required numerical aperture (NA) of the core-clad fibre. For the application of supercontinuum generation, a single mode chalcogenide fibre is competitive but a multimode chalcogenide fibre also has its advantage. This can be seen from the single mode propagation condition for a conventional core-clad fibre shown in equations (4.1) and (4.2) [4.33] in which

the diameter of the core and NA is a trade-off in the same working wavelength.

$$\frac{2\pi a NA}{\lambda} \leq 2.405 \quad (4.1)$$

$$NA = \sqrt{n_{co}^2 - n_{cl}^2} \quad (4.2)$$

where  $a$  is the diameter of the core, NA is numerical aperture,  $n_{co}$  is the refractive index of the core,  $n_{cl}$  is the refractive index of the clad and  $\lambda$  is the working wavelength. This condition restraint requires extremely small diameter of the core with a recognisable refractive index contrast for short wavelength guiding. It is tricky for fabrication and also optical assessment. Also, the strong laser power focused into such a small core may cause the damage of the chalcogenide glass propagating medium due to the high power intensity. In order to avoid the above issues, multimode chalcogenide fibre, which has high nonlinear optical properties, with a relatively large core diameter and large NA simultaneously helps to realise supercontinuum generation which has been obtained in multimode fibre [4.4, 4.5].

Based on the discussion above, the candidates could be modified from the centre of the glass forming region, along the direction parallel to the isothermal of  $T_g$  and between the iso- $\langle r \rangle$  of 2.4 and 2.6 (see figure 4.1). The glass compositions of 001  $\text{Ge}_{18.90}\text{Sb}_{15.00}\text{Se}_{66.10}$  and 002  $\text{Ge}_{20.00}\text{Sb}_{10.00}\text{Se}_{70.00}$  show a temperature contrast of  $\sim 8^\circ\text{C}$  when they both reach the viscosity of  $10^{4.5}$  Pas which is close enough for fibre drawing (see figure 4.5). A  $20^\circ\text{C}$  contrast of  $T_g$  exists between these two compositions. Whilst this may be a bit large, their TEC values shown in table 4.7 indicate a contrast of  $2.6 \times 10^{-6} \text{K}^{-1}$  (12.8% - 14.7%) and it indicates the possibility

of making a core-clad fibre. Thus,  $\text{Ge}_{18.9}\text{Sb}_{15}\text{Se}_{66.1}$  has been recommended for the core and  $\text{Ge}_{20}\text{Sb}_{10}\text{Se}_{70}$  for the cladding region. This glass pair offered a core-clad fibre with a NA of 0.72 at a working wavelength of 1460 nm.

A glass pair with reversed step index profile (lower index in core region) is required for making the cladding region of chalcogenide microstructured fibre (MOF) reported in [4.19], which has the higher index in the core and the over clad regions. The MOF's clad region consists of rings of index-reversed core-clad preform whose clad is made with the same composition of the core of MOF. The requirement for choosing this glass pair is the same with that for core-clad fibre. However the composition with lower refractive index should be applied to the core region. The glass compositions of (001)  $\text{Ge}_{18.90}\text{Sb}_{15.00}\text{Se}_{66.10}$  and (009)  $\text{Ge}_{22.50}\text{Sb}_{7.50}\text{Se}_{70.00}$  show a temperature contrast of  $\sim 20^\circ\text{C}$  when they both reach the viscosity of  $10^{4.5}$  Pas which is experience in the group suggest is suitable for fibre drawing (see figure 4.5). It remains for further investigation to verify if this temperature contrast will allow successful fibre drawing practice. A  $5^\circ\text{C}$  contrast of  $T_g$  between these two compositions is helpful and their TEC value shown in table 4.7 indicates a contrast of  $2.2 \times 10^{-6}\text{K}^{-1}$ . Thus,  $\text{Ge}_{18.90}\text{Sb}_{15.00}\text{Se}_{66.10}$  has been recommended for the clad and  $\text{Ge}_{22.5}\text{Sb}_{7.5}\text{Se}_{70}$  for the core region of the MOF core-clad preform. This glass pair offers a refractive index contrast of 0.129. Furthermore, better glass pair could be found by modifying the composition to the desired thermal and optical properties based on the discussion in this chapter.

## 4.7 Conclusions

In order to find the glass pairs, which do not show crystallisation after the same heat treatment condition of preform shaping and fibre drawing, with similar thermal properties and relatively large refractive index contrast, the ternary Ge-Sb-Se glass system has been investigated here. The glass forming ability of these glasses is strong and reluctant to crystallization, which makes them competitive candidates to make preforms for fibre drawing. Two compositions could be found by modifying the glass's composition roughly along the isothermal of  $T_g$  with the assistance of the view of glass's cross-linking structure and average coordination number. A glass pair of negative refractive index contrast and compressive clad can be applied to make MOF. Also, a glass pair with positive index step and a relatively large NA is suggested suitable for a core-clad fibre design with potential application in supercontinuum generation.

The compositions 001 ( $\text{Ge}_{18.90}\text{Sb}_{15.00}\text{Se}_{66.10}$ ) and 002 ( $\text{Ge}_{20.00}\text{Sb}_{10.00}\text{Se}_{70.00}$ ) were selected to be the candidate glass pair for a core-cladding fibre. The compositions of 009 ( $\text{Ge}_{22.50}\text{Sb}_{7.50}\text{Se}_{70.00}$ ) and 001 ( $\text{Ge}_{18.90}\text{Sb}_{15.00}\text{Se}_{66.10}$ ) have been selected as the candidate glass pair with reverse refractive index for making the MOF (see 5.2, figure 5.5). Their  $T_g$  contrast, thermal expansion coefficient contrast, the contrast in temperature when achieving the fibre-drawing temperature and refractive contrast of these glass pairs have been summarised in table 4.12.

Table 4.12 The selected chalcogenide Ge-Sb-Se glass pairs. Their  $T_g$  contrast, thermal expansion coefficient contrast, the contrast in temperature when achieving the fibre-drawing temperature and refractive contrast. Note: the negative “-” indicates the parameter of core is less than that of cladding.

<b>Glass pair (Core / cladding)</b>	$\Delta T_g$ /°C	$\Delta \text{TEC}$ / $10^{-6}\text{K}^{-1}$	$\Delta T$ at fibre-drawing temperature /°C	$\Delta n$ at 1463 nm
001 / 002	20	-2.6	9	0.100
009 / 001	-5	2.2	20	-0.126

## **Chapter 5 Improvement on the fabrication of chalcogenide microstructured optical fibres (MOFs) and MOFs fabrication**

This chapter reports the fabrication of all solid MOFs with the glass pair of  $\text{As}_{40}\text{Se}_{60}$  and  $\text{Ge}_{10}\text{As}_{23.3}\text{Se}_{66.6}$ . The technology of preform shaping, assembling, and fibre drawing have been refined based on the previous route in our group [5.1 - 5.3]. The method of fabricating a rotationally cast tube is discussed in section 5.1. The initial trial fabrication of an all-solid suspended microstructured fibre (MOF) is detailed in section 5.2. The solution of improvement of chalcogenide cane shaping and MOF preform assembling procedures is developed in section 5.3. Finally, the successful fabrication of an all-solid suspended MOF is described in section 5.4.

### **5.1 Research on the fabrication of rotationally casted tube**

The over-clad tube, also called jacket tube is one of the precursors to make up the MOF preform [5.3]. In order to achieve a tube with a uniform, smooth and clean surface of controlled and various internal diameters, the technique of rotational casting [5.1 ~ 5.4], which is based on the principle of centrifugation, was applied here. Several approaches are analysed in this section and comparisons made between the theoretical calculation of dimensions and the experimental process. The extrusion technique [5.5] and the ‘cast-tubing’ method presented in [5.6] are not applied in preparing the over-clad tubes here because of the consideration of

surface contamination and defects. However, they are still potential alternatives to the current approach. From the experimental results, each approach has its own advantages and shortcomings, so the final decision of approach should be made based on the target tube ID, the equipment cost, the fabrication period and the time to achieve it. The theory of the method to carry out rotational casting has been described in section 3.3.4. Note that for the work presented in sections 5.1.1 and 5.1.2, the silica glass ampoules were pre-purified (see section 3.1.1) and the arsenic and selenium were also pre-purified (see section 3.1.2).

#### **5.1.1 Straightforward rotational casting of tube ID $\geq 4.5$ mm**

The so called ‘standard ampoule’ method is aimed at achieving a rotationally cast chalcogenide glass tube in a straightforward approach, through which the repeated heating of ampoule and the special ampoule design can be avoided. The principal ideal is enclosing the supposed “empty” volume for the hole of the consequent chalcogenide glass tube as well as the actual chalcogenide glass comprising the tube solid volume, inside the silica ampoule. This situation was analysed by a series of calculations based on engineering principles and practical processing. If the chalcogenide glass tube internal diameter (ID) aimed for is relatively large (larger than 4.5 mm for the composition of  $\text{As}_{40}\text{Se}_{60}$ ), the tube can be obtained by one melting using a silica ampoule with 10 mm ID and 300 mm length, and finally a straightforward rotational casting (seen in figure 5.1). The time and temperature schedule have been detailed in section 3.3.4.

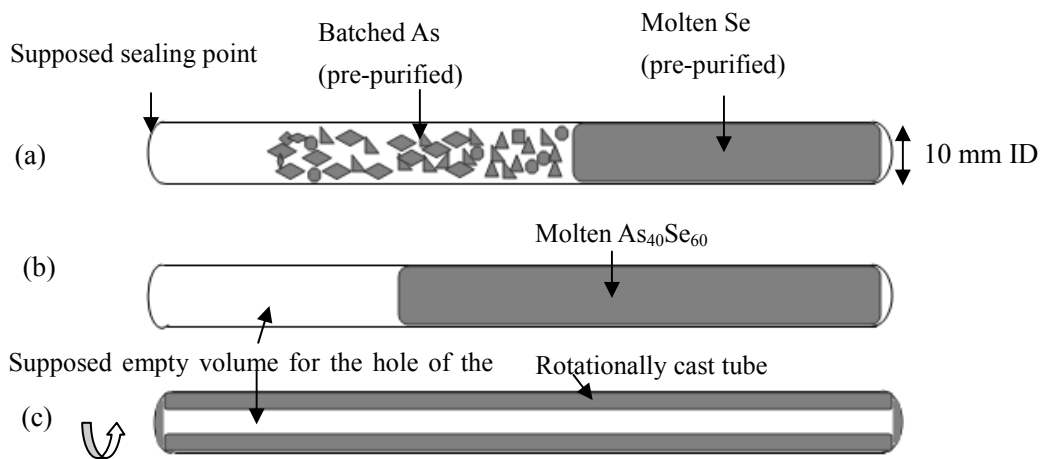


Figure 5.1 Schematic presentation of the method of tube making by straightforward melting in a standard ampoule. Se was purified in the molten state and then pre-purified As pieces were batched. After, the As pieces were batched and the ampoule was sealed at the supposed point (a), at the place to enclose the correct empty volume (b) calculated under the consideration of glass density, tube ID and tube length to give the correct tube ID, in (c) the finished rotationally cast tube.

Note: the silica glass ampoule was pre-purified as in section 3.1.1.

### 5.1.2 Rotational casting of tube ID < 4.5 mm

On the other hand, if the required ID of the tube is relatively small (less than 4.5 mm), this means more material is batched in the silica glass ampoule. A re-melting is needed with an inserted silica glass rod to fix the enclosed empty volume. This is the re-melting and rotational casting approach shown schematically in figure 5.2. In the previous section 5.1.1, the straightforward experiment of tube casting was discussed and successfully demonstrated. This latter route of tube making could ensure a minimum tube diameter of  $\geq 4.5$  mm. If < 4.5 mm tube ID is needed, this means more material must be batched into the initial silica glass melting ampoule. However, it has been found in this project that the empty space in the enclosed ampoule will not be enough to allow the

increment of the chalcogenide material's volume during its expansion in the liquid state. Thus, the silica glass ampoule may undertake the risk of cracking when it is pressurised by the expanded liquid. The rod inserted into the ampoule was 9 mm OD. Its length depends on the length of the empty part of the silica ampoule. The main thing is that the rod can come out of the silica ampoule by 10 mm. Four axial surface cuts along the length of the silica rod with 2 mm depth were applied, with the method detailed in section 3.1.8 [see figure 5.2(d)]. The silica rod was sealed to the ampoule under vacuum (see section 3.1.4 and 3.1.5). The time and temperature schedule was described in section 3.3.4.

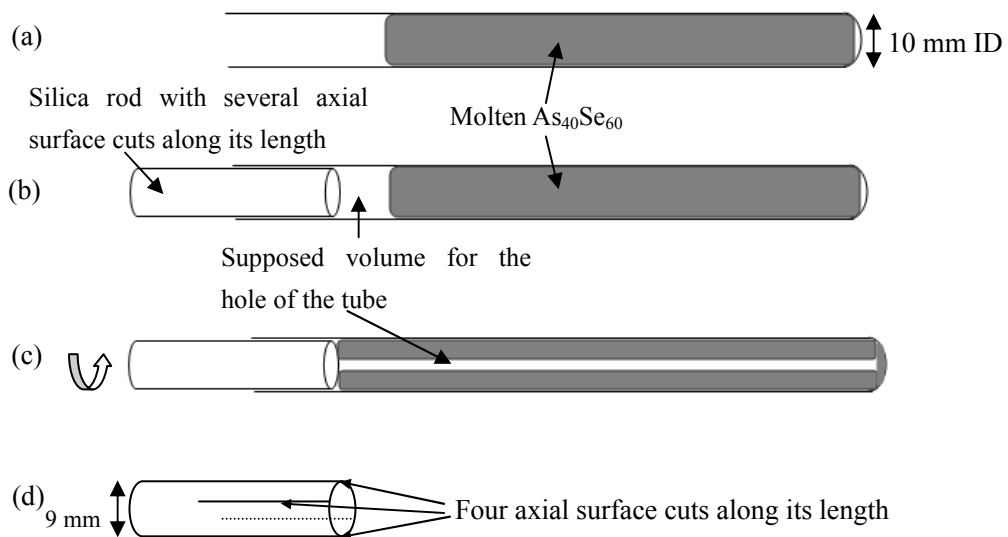


Figure 5.2 Schematic presentation of the re-melt and inserted silica glass rod approach for chalcogenide glass tubes with ID < 4.5 mm. (a) Glass was synthesised first in the silica glass ampoule. (b) Ampoule was opened inside the glove box (MBraun 150B-G, the atmosphere of glovebox was kept < 0.1 ppm  $O_2$  and 0.1 ppm  $H_2O$ ) and a silica glass rod with several axial surface cuts was inserted into the supposed sealing point to maintain the expected empty volume for the hole of the tube, (c) Rotational casting was implemented after the re-melt. (d) The rod with four axial surface cuts.

### 5.1.3 ‘Two chamber silica glass ampoule’ method for tube ID < 4.5 mm

As described above, the ratio of material to the empty space in the enclosed ampoule determines how thick the walls of the rotational casting tube will be. Thus the sealing point is critical for the method above (see section 5.1.2), which makes the ‘rod-in and re-melt’ approach tricky in practice for small ID tubes. So, an alternative was proposed by means of synthesizing the chalcogenide glass in a two-chamber-ampoule (customised from OH silica-glass-tubing, Multilab), re-melting and spinning. The narrow neck design was insensitive to the sealing point; it is shown schematically in figure 5.3.

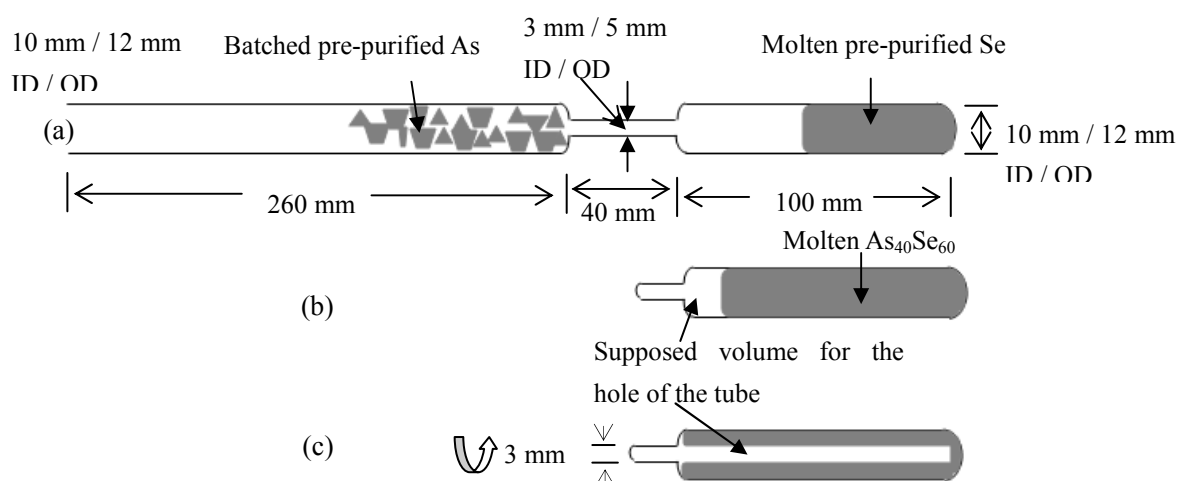


Figure 5.3 Schematic presentation of the ‘two chambers ampoule’ approach for making chalcogenide glass tubes < 4.5 mm ID. (a) Pre-purified Se was batched then melted down to the bottom chamber and pre-purified As was batched and enclosed in the double chambers ampoule which had the neck section with the same diameter as that of the desired tube ID; (b) molten  $As_{40}Se_{60}$ ; (c) re-melting and rotational casting.

The Se element first pre-purified (see section 3.1.2), then batched and melted down (see section 5.4.1) through the narrow neck region to the bottom chamber

by a modified Se purification temperature schedule in order to leave enough space in the upper chamber for As element batching and ampoule sealing. The As was pre-purified prior to batching (see section 3.1.2). Also, the temperature schedule of the  $\text{As}_{40}\text{Se}_{60}$  glass synthesis was adjusted, by setting the rocking furnace to start to rock after the elemental selenium had softened, in order to avoid the ampoule being scraped by the raw arsenic pieces and mixing of the molten glass to the bottom chamber. After melting, the chalcogenide glass was re-sealed into the lower part of the ampoule at the narrow neck region as shown in figure 5.3, which was the key feature of the scheme. It made the sealing work feasible whilst keeping very small space in the enclosed ampoule. Also, it provides enough space for the increment of the volume of the liquid material due to thermal expansion. The sealed ampoule was then placed inside a silica jacket tube for the re-melting and rotational casting stages. After a specific spinning time in the air and annealing schedule (see section 5.2.1.2), a chalcogenide glass tube was obtained (see section 5.2.1.2).

#### **5.1.4 Suggested additional method for tube making by casting**

From the indication of preform fabrication in the literature [5.4] and [5.6], a further proposal for utilising the so called ‘cast-tubing’ approach for preparing the over-clad tube is presented.

A mould for making a chalcogenide glass tube can be achieved by fusing a silica

glass capillary between two slices of silica glass tube whose ID fits the capillary's OD. The mould is then placed into a silica tube and fused together with the silica tube (see figure 5.4), afterwards, one end of the silica tube will be enclosed (see figure 5.4). The synthesised  $As_{40}Se_{60}$  glass is batched and sealed with the mould and then taken through re-melting, quenching and annealing processes. HF with the concentration of about 40% by volume is applied to etch off the silica mould afterwards. The schematic presentation is shown in figure 5.4. In this method, the empty volume, which is the volume which would have to be taken by chalcogenide glass, located between the two silica slices and outside the silica capillary must be calculated.

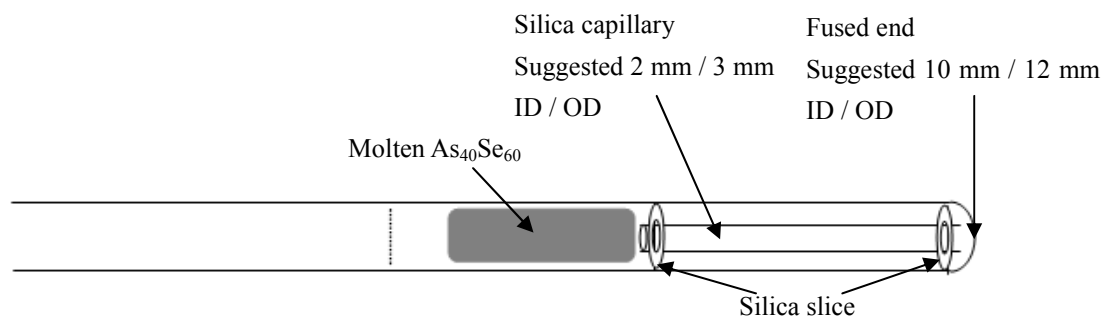


Figure 5.4 Schematic presentation of cast-tubing approach, a proposed method which was not carried out experimentally.

The length and the wall thickness of the capillary should be investigated, considering the mechanical strength during glass forming because of the contrasting thermal properties of chalcogenide glass and silica. A good starting point would be a capillary OD of 3 mm and then to make this OD successively smaller. Because this approach is migrated from the method of preform preparing [5.4 and 5.6], it needs to be further investigated experimentally, it is anticipated

that a comparison between the above methods (see section 5.1 to 5.4) should be concluded based on the specific requirements for the ID and OD of the chalcogenide glass tube.

## **5.2 Fabrication and characterisation of all-solid MOF005**

The all-solid microstructured optical fibre MOF005 with a small core has been designed in this project for the potential applications of single mode propagation and supercontinuum generation. An all-solid chalcogenide microstructured fibre (MOF) has been fabricated successfully here by Dr. Zhenggang Lian [5.3]. The structure of MOF004 can be seen from figure 5.5, which is the optical micrograph of the cross-section of the finished fibre. A  $\text{Ge}_{10}\text{As}_{23.4}\text{Se}_{66.6}$  /  $\text{As}_{40}\text{Se}_{60}$  core / clad rod (300 mm length and 9 mm diameter) and an  $\text{As}_{40}\text{Se}_{60}$  rod (40 mm length and 9 mm diameter) were extruded [5.3]. A rotationally cast  $\text{As}_{40}\text{Se}_{60}$  tube (140 mm length and 3.8 mm / 9.95 mm ID / OD) was made as the preform of over-clad tube [5.3].

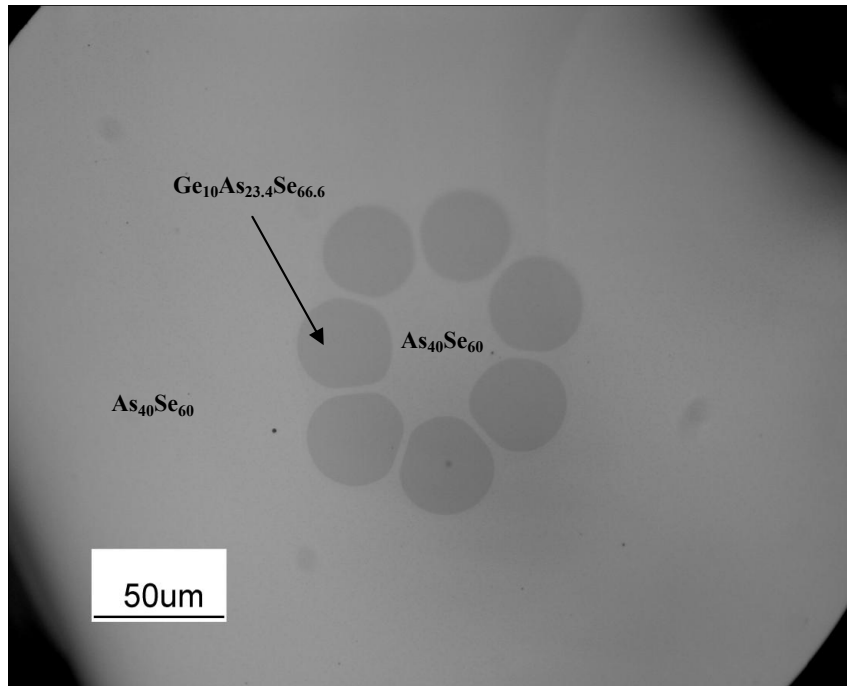


Figure 5.5 The optical micrograph of MOF004 made from a  $As_{40}Se_{60}$  rod, a  $As_{40}Se_{60}$  rotationally cast tube and a  $Ge_{10}As_{23.4}Se_{66.6} / As_{40}Se_{60}$  core / clad extruded rod. The fibre-drawing gives a ring formed by seven circles ( $Ge_{10}As_{23.4}Se_{66.6}$ ) surrounding a core ( $As_{40}Se_{60}$ ). The largest diameter of MOF004 was  $377 \mu m$  and the core diameter was  $52.6 \mu m$  [5.3]. The smallest core diameter fabricated was  $12.5 \mu m$  [5.3].

The aspect ratio of the cross-section of MOF004 was maintained during the micro-structuring. Multi-mode propagation in a sample of MOF004 ( $85 \mu m$  OD and  $12.5 \mu m$  core) was demonstrated at a wavelength of  $1.55 \mu m$  [5.3].

## 5.2.1 Fabrication of all-solid MOF005.

### 5.2.1.1 Glass pair of $As_{40}Se_{60}$ and $Ge_{10}As_{23.4}Se_{66.6}$ .

The glass pair of  $As_{40}Se_{60}$  and  $Ge_{10}As_{23.4}Se_{66.6}$  were chosen due to their relatively close  $T_g$ , thermal expansion coefficient ( $\alpha$ ) and viscosity at the same fibre drawing temperature (see table 5.1). The characterisation of this glass pair has been done by W.J. Pan [5.7] and Z.G. Lian [5.2] in our group previously. Figure

5.6 explains how the glass pair was used to comprise the core, cladding region and over-cladding region of a new, small core MOF. The chalcogenide composition with lower viscosity at a particular temperature is preferred in the core and the over-clad tube, because the cladding, which is the outer-layer of the core-clad rod, with higher viscosity at any particular temperature could maintain its shape while the over-cladding flows more readily and contacts more tightly with the three  $\text{Ge}_{10}\text{As}_{23.4}\text{Se}_{66.6}$  cladding canes during fibre-drawing of the stacked MOF preform.

Table 5.1 The thermal and optical properties of the chalcogenide glass pair [5.2, 5.7] selected for MOF005.

Glass / at%	$T_g$ / °C	$\alpha / (10^{-6}\text{K}^{-1})$	Viscosity / Pas	Refractive index at 1560 nm	Application in MOF
$\text{As}_{40}\text{Se}_{60}$	180	$19.1 \pm 0.5$	$10^{7.4}$ at 230°C	$2.823 \pm 0.001$	Core, over-clad tube
$\text{Ge}_{10}\text{As}_{23.4}\text{Se}_{66.6}$	190	$21.5 \pm 0.5$	$10^{7.8}$ at 230°C	$2.634 \pm 0.001$	Three cane's cladding region

The amorphous nature of these two compositions:  $\text{As}_{40}\text{Se}_{60}$  and  $\text{Ge}_{10}\text{As}_{23.4}\text{Se}_{66.6}$  (at%) has been demonstrated [5.2 and 5.7] and work on MOF fibre drawing reported in [5.3].

#### 5.2.1.2 Preparation of preform for MOF005.

The preform of the MOF005 is composed of an  $\text{As}_{40}\text{Se}_{60}$  core fibre, three  $\text{Ge}_{10}\text{As}_{23.4}\text{Se}_{66.6}$  canes and an  $\text{As}_{40}\text{Se}_{60}$  over-clad tube. The calculated dimensions of the preform are shown in figure 5.6.

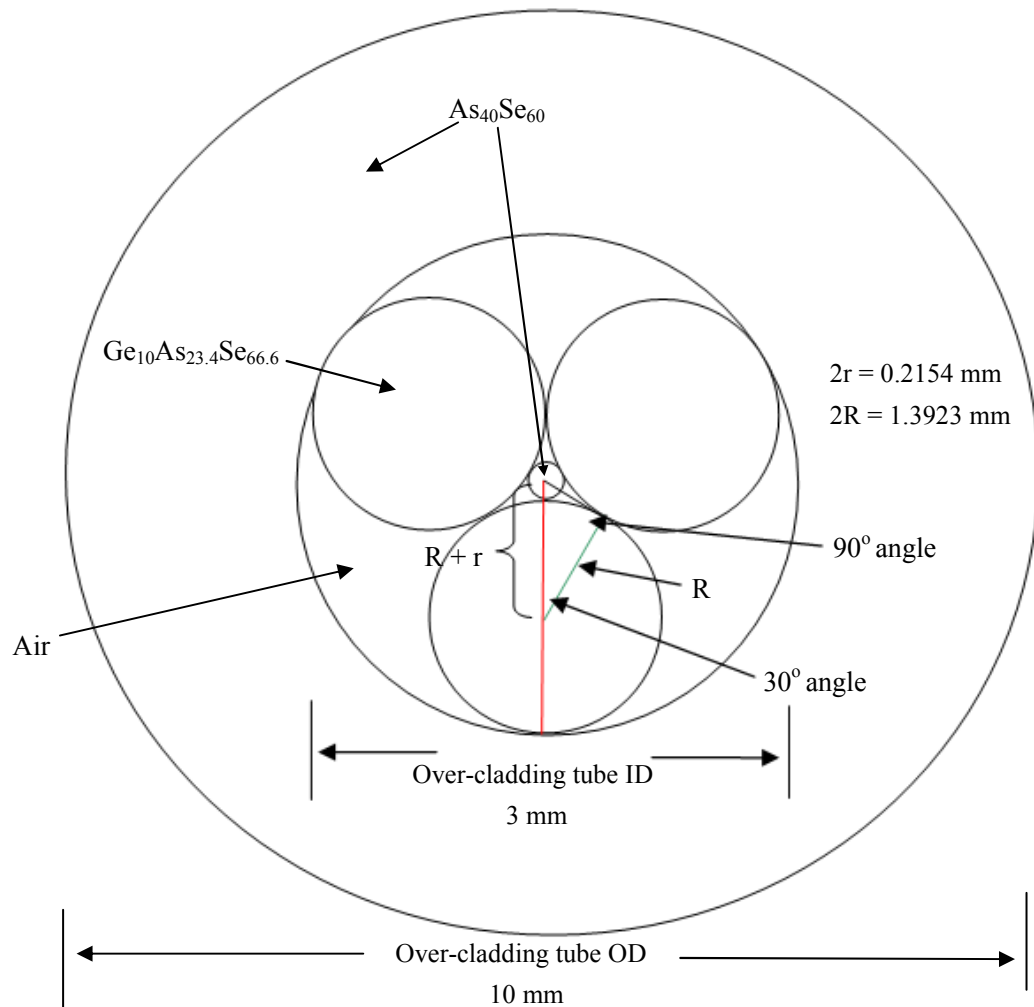


Figure 5.6 Structure presentation of the preform MOF005. The dimensions of the assembly of all the preform is given in this diagram. The diameter of the core was  $215.4\mu\text{m}$  and the diameter of the  $\text{Ge}_{10}\text{As}_{23.4}\text{Se}_{66.6}$  cane in the cladding region was  $1.3923\text{ mm}$  and the outside diameter of the cladding area, which is the internal diameter of the over-cladding tube, was  $3\text{ mm}$ . However, a small clearance of about  $0.1\text{ mm}$  to  $0.2\text{ mm}$  was left between the cladding region and the inner surface of over-clad tube, in order to stack the pattern into the tube. So, the aimed diameter of the canes can be around  $1.25 \pm 0.05\text{ mm}$ .

The over-clad tube was prepared by means of the so called two chambers ampoule approach see section 5.1.2 and figure 5.3(a). The aim was to produce an  $\text{As}_{40}\text{Se}_{60}$  tube of  $100\text{ mm}$  length,  $3\text{ mm} / 10\text{ mm}$  ID / OD. The volume of the enclosed

ampoule was calculated. The bottom chamber was fixed at length 100 mm ( $\pm 2$  mm) and the ID of the neck region was fixed at about  $3 \pm 0.05$  mm. The desired batched quantity of material was calculated based on the density of  $\text{As}_{40}\text{Se}_{60}$  ( $4.61 \times 10^{-3}$  /  $\text{kg m}^{-3}$  at  $25^\circ\text{C}$ ). The volume taken up by the molten glass was controlled to be, and worked out from, the known value of silica glass chamber volume and the volume of the hole of the aimed chalcogenide glass tube. Because the desired inner dimension of the aimed chalcogenide tube is the premise, the volume taken by the hole (see figure 5.3(c)) is fixed. The volume of the bottom silica glass chamber was measured by the means of measuring the mass of water which takes the same volume of the ampoule chamber. The empty two chambers silica glass ampoule and the same ampoule with its bottom chamber filled with water were weighed with a balance (Sartorius, model BP221S accurate to  $\pm 0.1$  mg), respectively. The weight of these two is the mass of the water which filled the bottom chamber of the two chamber silica ampoule. The water's volume was its mass divided by its density at the temperature of  $24^\circ\text{C}$ . Thus, the volume of the bottom chamber, which is the same as the weighed water, can be found out.

There was residual permanent strain left in the customised silica glass two chambers' ampoule after its manufacture, which was customised (supplied by Multi-Lab). Two polarisers, which were placed in their vertical polarisation direction, and a light box (Whatman, EAV00024) was used to incident through them. Several colourful rings appeared when the silica glass ampoule was placed

between the polarisers, which indicated the silica ampoule was not homogeneous and it was due to the strain left. Therefore an annealing process was applied to the silica glass ampoule to release the strain. A furnace (CARBOLITE, 78 mm ID tube, 880 mm long) was used to heat the silica ampoule at 200°C / h to 1160°C, which is the  $T_g$  of silica glass [5.1], for 1.5 h and then it was cooled down to 950 °C with the cooling rate of 60°C / h, afterwards decreased to room temperature rapidly (see table 5.2). The silica ampoule was suspended by an iron holder inside the tube furnace and argon gas (BOC) was applied during the process.

Table 5.2 The schedule of silica glass ampoule annealing.

Stage	Schedule
1	RT to 1160°C @ 200°C / h
2	Dwell at 1160°C for 1.5 h
3	1160°C to 950°C @ 60°C / h
4	950°C to RT @ 200°C / h

The elemental As (Furukawa 99.99999% purity, 4 ~ 8 mm in pieces size) and Se (Cerac 99.999% purity, about 3 mm in pieces size) were weighed (Sartorius balance, model BP221S accurate to  $\pm 0.1$ mg), batched and sealed, and then went through the process of melting, air quenching, annealing, re-sealing, re-melting, rotational casting and annealing (see section 3.1.5 and 3.1.6).

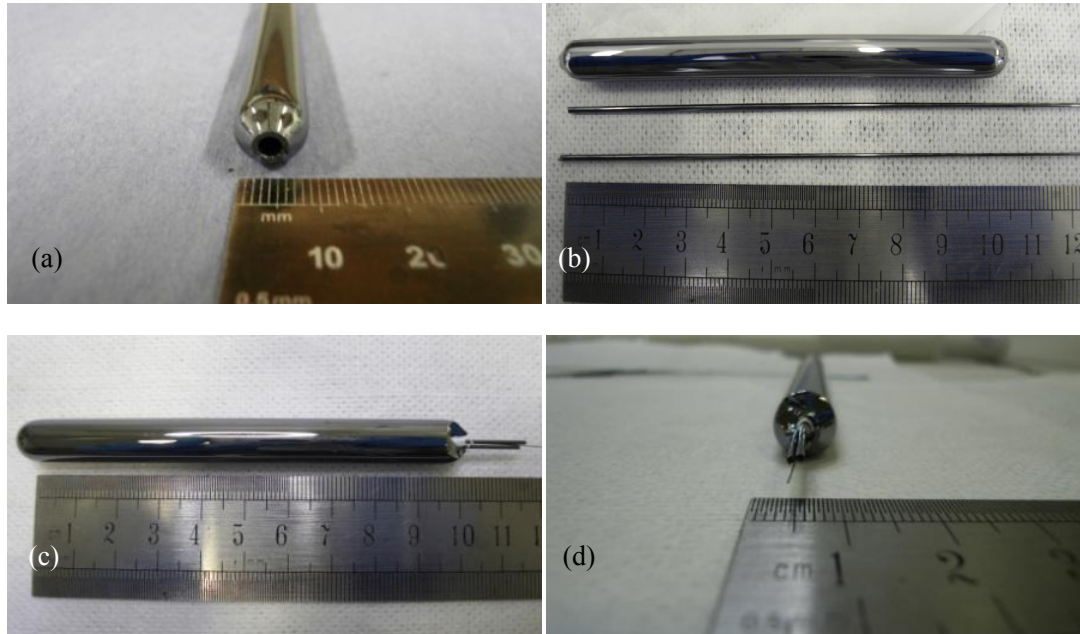


Figure 5.7 (a) Rotationally cast  $\text{As}_{40}\text{Se}_{60}$  (at%) over-clad tube with ID 2.95 mm; (b) over-clad tube and  $\text{As}_{40}\text{Se}_{60}$  canes to be stacked; (c) stacked preform for MOF; (d) cross-section of the stacked MOF005 preform.

The ID of the rotationally cast tube (2.95 mm) had a small error from the target (3 mm). Furthermore, the  $\text{Ge}_{10}\text{As}_{23.4}\text{Se}_{66.6}$  canes prepared, which were drawn from the extruded  $\text{Ge}_{10}\text{As}_{23.4}\text{Se}_{66.6}$  rod (130 mm length, 9 mm OD), did not correspond perfectly with the calculated geometry. The feed out end of the  $\text{Ge}_{10}\text{As}_{23.4}\text{Se}_{66.6}$  cane was taken by hand, thus there was not a good control on the diameter of the cane. They had a variation in diameter ( $1.25 \pm 0.25$  mm) along their length. A cane with 1.5 mm diameter, which is 0.25 mm larger than the ideal dimension, would make it hard to insert required canes into the tube. In contrast, a cane with smaller dimension ( $< 1.2$  mm) may let the core fibre escape from the centre through the gaps between the canes. Three 10 mm length of canes with diameter of 1.5 mm, 1.2 mm and 1 mm were chosen, respectively, because the uniform of diameter was not achieved for this first trial. An  $\text{As}_{40}\text{Se}_{60}$  core fibre with a diameter of

$\sim 210\mu\text{m} \pm 10\mu\text{m}$  (see the assembly's dimension in figure 5.6) was placed in the centre as the core.

The  $\text{As}_{40}\text{Se}_{60}$  core fibre,  $\text{Ge}_{10}\text{As}_{23.4}\text{Se}_{66.6}$  canes had been etched in 99% propylamine (Sigma-Aldrich) at room temperature for 30 minutes and 12 hours, respectively, which is considered to remove the surface oxide [5.8, 5.9, 5.10]. The stacking procedure was done by hand. The core was placed onto the joint area of two canes and the third cane was stacked on (see figure 5.6). The assembly of core and cladding was inserted into the jacket tube horizontally. It was found necessary to leave a little clearance ( $\sim 0.1$  mm) between the assembly and the ID of the jacket tube because of frictional resistance of the chalcogenide glass which resists movement. The position of the core fibre should be located exactly at the middle, where all three canes meet, and these canes should be tightly fitted to prevent the core fibre escaping from the centre before, or during fibre-drawing.

#### 5.2.1.3 Fibre drawing for MOF005.

The designed MOF (see figure 5.6) was to support single mode propagation at a wavelength of  $4\mu\text{m}$ , if its core diameter less than  $3.12\mu\text{m}$  and its OD less than  $145\mu\text{m}$  (see section 2.3.3 and equation 2.10) with the known refractive index contrast between  $\text{Ge}_{10}\text{As}_{23.4}\text{Se}_{66.6}$  ( $n=2.62$  at  $1.55\mu\text{m}$ ) and  $\text{As}_{40}\text{Se}_{60}$  ( $n=2.82$  at  $1.55\mu\text{m}$ ) [5.2 and 5.7] (see table 5.1). With its ability to constrain the light into the very small core, this fibre can be applied to the potential applications on nonlinear

optics, say, around  $4\mu\text{m}$ . Thus, the diameter of the core should be smaller than  $3.12\mu\text{m}$  from the single mode propagation condition for step index fibre [5.11]. Thus, the corresponding maximum diameters of the cladding region and the whole fibre are  $43.45\mu\text{m}$  and  $144.82\mu\text{m}$ , respectively.

The stacked preform was drawn down to the fibre with a series of outer diameters of  $135\mu\text{m}$ ,  $115\mu\text{m}$ ,  $150\mu\text{m}$ ,  $200\mu\text{m}$ , and  $215\mu\text{m}$  on the fibre-drawing tower (see section 3.3.5) in sequence. The feed-in speed of the preform was fixed at around  $3\text{ mm / min}$  and the drawn speed was varied from  $16.46\text{ m / min}$  to  $22.68\text{ m / min}$ , and then subsequently decreased to  $13.33\text{ m / min}$ ,  $7.5\text{ m / min}$  and  $6.49\text{ m / min}$ . These draw speeds were calculated from the draw down ratio of the preform and final fibre, to achieve the above desired diameters. The preform was heated at 10% power of a radio frequency fibre drawing furnace (Severn Furnaces Ltd) with a  $3\text{ mm}$  carbon graphite receptor around the fibre, and was drawn under a  $\text{N}_2$  atmosphere (BOC). The fibre drawing process was nominally successful and a length of about  $150\text{ m}$  of fibre, visually with a smooth, shiny surface and no defects, was achieved.

### **5.2.2 Characterisation of all-solid MOF005.**

The fabricated MOF005 was examined under the optical microscope and scanning electron microscope (SEM). The physical structure and chemical composition were verified, respectively, as follows.

#### 5.2.2.1 Optical microscopy.

The fibre sample for optical microscope imaging was prepared by cleaving using a diamond pen. The tip of the diamond pen was pressed on the fibre surface and oriented orthogonally to the perpendicular axis of the straight fibre, gently sliding the cleaver to the right, and then pushing the fibre above the cleave on the pressed side so that the cleaved portion toppled off and could be examined. This was done several times. Afterwards, the fibre samples were mounted on “blue tac” with the cleaved face up for optical microscope characterisation. A Nikon Digital Camera (DXM1200F) was used for this observation.

Figure 5.8 shows the cross section of the MOF005. From figure 5.8 (a) it is suggested that the core fibre resides at the joining edge of only two of the three canes, and not as expected at the centre of the three canes. Also the three canes' clad region was not symmetrical due to the variation of diameter between the canes. In figure 5.8 (b), the joining edge of the same two canes is shown at higher magnification to identify the core fibre. The scratch in figure 5.8 (b) was a defect present on the sample and the bright light was the light reflected in the optical microscope.

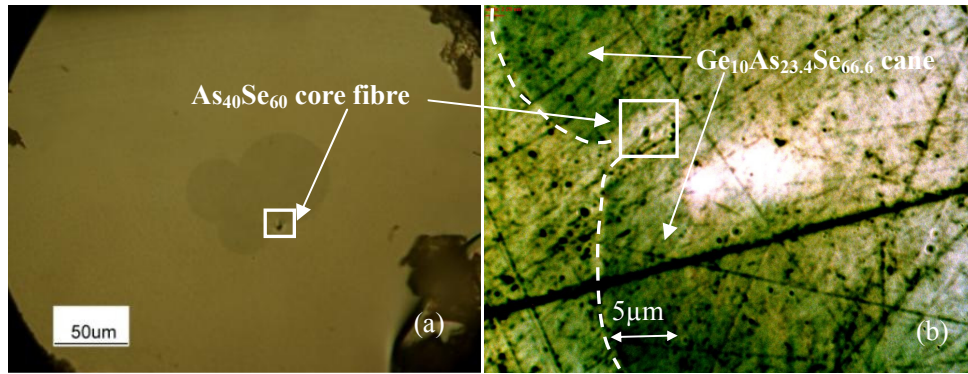


Figure 5.8 Optical reflection micrographs of the MOF MOF005 fabricated. Here the outer diameter & central region diameter are respectively: 325  $\mu\text{m}$  and  $\sim 70$  to 97  $\mu\text{m}$ . (a) the view of the whole cross-section of MOF005; (b) the view of the core fibre at the joining edge of two canes.

#### 5.2.2.2 SEM.

Samples chosen from different positions of the drawn fibre were mounted vertically on “blue tac” then the “blue tac” fibre assembly was mounted in epoxy. The procedures of cutting the epoxy, grinding and polishing to achieve a surface of 1 $\mu\text{m}$  finish were then followed (see section 3.2.5). Afterwards, the epoxied sample was carbon coated (Edwards, Coating System E306A) and a scanning electron microscope (SEM Philips XL30) was used to investigate the sample.

In the figure 5.9 (a), the back-scattered image was zoomed in to observe the three canes’ cladding region. In (b) the As content inside the spots clearly shows a cladding ring with lower As content than the jacket tube region (and what would be expected in the core region), as expected. (c) Ge only occurred in the spots arranged as a ring, as expected from the arrangement in the MOF preform before drawing down, surrounding the central fibre. (d) Se exhibited a close-to-uniform

distribution across the whole fibre cross-section as expected.

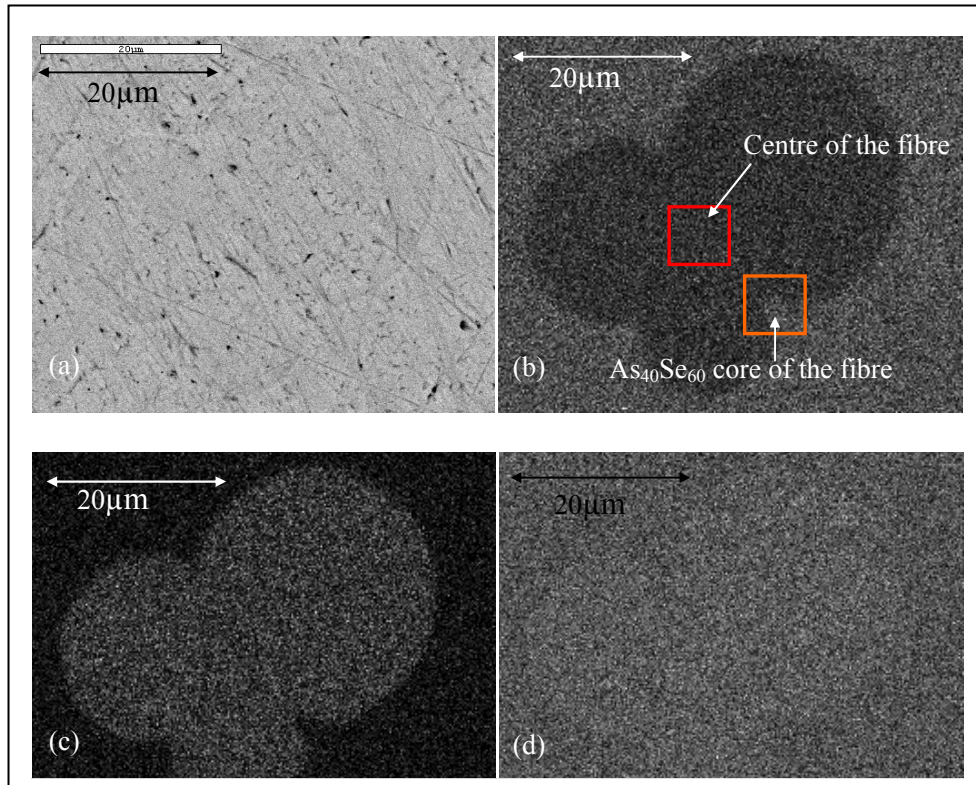


Figure 5.9 Scanning electron microscope, back-scattered electron elemental mapping of the all-solid, chalcogenide glass MOF005 fabricated here: (a) back scattered image, (b) As, (c) Ge and (d) Se. Note: the canes selected were not even because the uniform of cane diameter could not be obtained in this first trial (see section 5.2.1.2).

Note: the area enclosed by the squares in (b) are the physical centre of MOF005 and the actual position of the As<sub>40</sub>Se<sub>60</sub> core which should be in the centre.

### 5.2.3 Summary regarding MOF005

It can be concluded that it could be feasible to fabricate all solid chalcogenide microstructured fibre with the route discussed above. Overall the fabrication of the MOF005 design was not successful since the structure of the preform was not preserved during the stacking and fibre shaping process, principally because the stacked Ge<sub>10</sub>As<sub>23.4</sub>Se<sub>66.6</sub> canes' diameters were not equal. Overall, the glass synthesis and fibre-drawing for MOF005 was successful, but a more precise

control of dimensions and a better engineering of the stacking process was needed, as follows in section 5.3.

### **5.3 Improvement in fabrication of MOF preforms.**

Solutions are proposed here: (i) to minimise the uneven diameter of the  $\text{Ge}_{10}\text{As}_{23.4}\text{Se}_{66.6}$  canes which formed the optical cladding for MOF005 (see section 5.3.1) and (ii) to facilitate the preform assemblage (see section 5.3.2).

#### **5.3.1 Diameter monitor for cane drawing and cane-drawer system for cane > 0.5 mm diameter and < 3.00 mm diameter.**

In order to draw cane of consistent diameter and with a diameter above 0.5 mm, a real-time and non-contact diameter monitor, and a mechanism to clamp the cane and control the feed speed of the drawn down cane are essential. In this section, the system solution and the development of the associated software will be discussed.

##### 5.3.1.1 Explanation of system solution

The block diagram of the system solution is shown in figure 5.10. The drawing cane was imaged by a USB (Universal Serial Bus) camera and fed into a computer installed with Labview software. The script realising the image processing and sample measurement was created in Vision Builder of Labview. Also, a script of PID (proportional, integral, differential) control, which could loop control the motor of the fibre drawer to make the actual diameter of cane approaching the

target, is under construction, but this work was beyond the scope of this thesis.

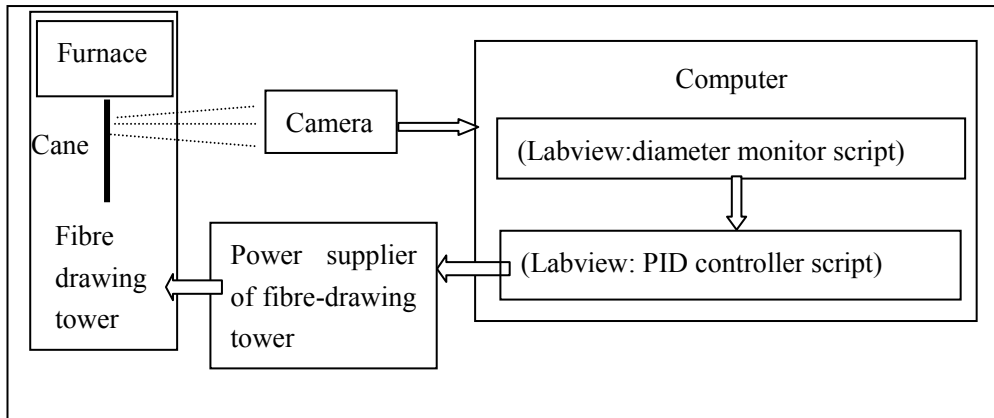


Figure 5.10 Block diagram of real-time and non-contact cane diameter monitor. The image of the cane is obtained by the camera and fed into the computer, processed by the diameter monitor script to give the diameter of the cane in real-time. The different between the on-going cane's diameter and the aimed cane's diameter is worked out by PID (proportional, integral, differential) controller script and the PID controller script can give a feedback to control the power supplier of fibre-drawing tower to turn up or down the power for fibre-drawing.

Note diameter of drawn chalcogenide cane is  $x$  and  $0.5 \text{ mm} < x < 3 \text{ mm}$ .

The imaging system included in the block diagram (figure 5.10) consisted of the chalcogenide glass drawn cane sample whose diameter was to be monitored, a camera and the image processing software. The operation of the imaging system considered the factors of the field of view, working distance, contrast, resolution and depth of field. The concept of the image processing is shown in figure 5.11.

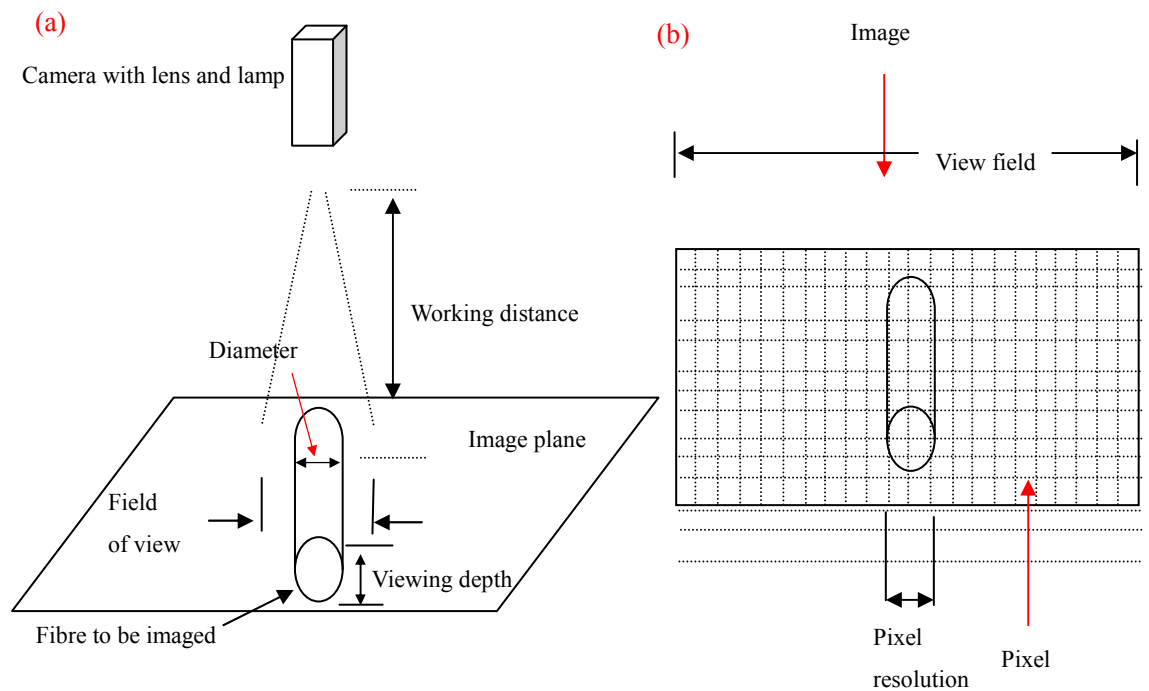


Figure 5.11 Concept of the imaging system: (a) the relative position of the camera, chalcogenide cane and the image plane; (b) the principle of the image resolution.

From figure 5.11, the camera was placed at the side of the vertical chalcogenide glass cane just below the furnace where the rod had softened to form the cane sample with a working distance of 17mm which was the focal length of the lens used in this project. A sheet of white paper was placed 100 mm behind the chalcogenide cane to supply enough contrast to enable the object to be distinguished from the background. When setting the lens focus, the imaging viewing depth was considered because the image quality may change when the sample moves closer to or further from the camera lens. The image on the screen is represented on the camera by a pixel matrix. The field of view can be zoomed in by adjusting the working distance and lens focus to increase the pixel resolution, which is defined as the minimum number of pixels needed to represent the object

under inspection. In consideration of the depth of view, the vibration of the drawing cane and the dimension of the fibre tower platform, a compromise between pixel resolution and working distance had to be made.

The image system was set up on the fibre-drawing tower. The arrangement of the imaging system, and the cane-puller on the fibre drawing tower is shown in figure 5.12.

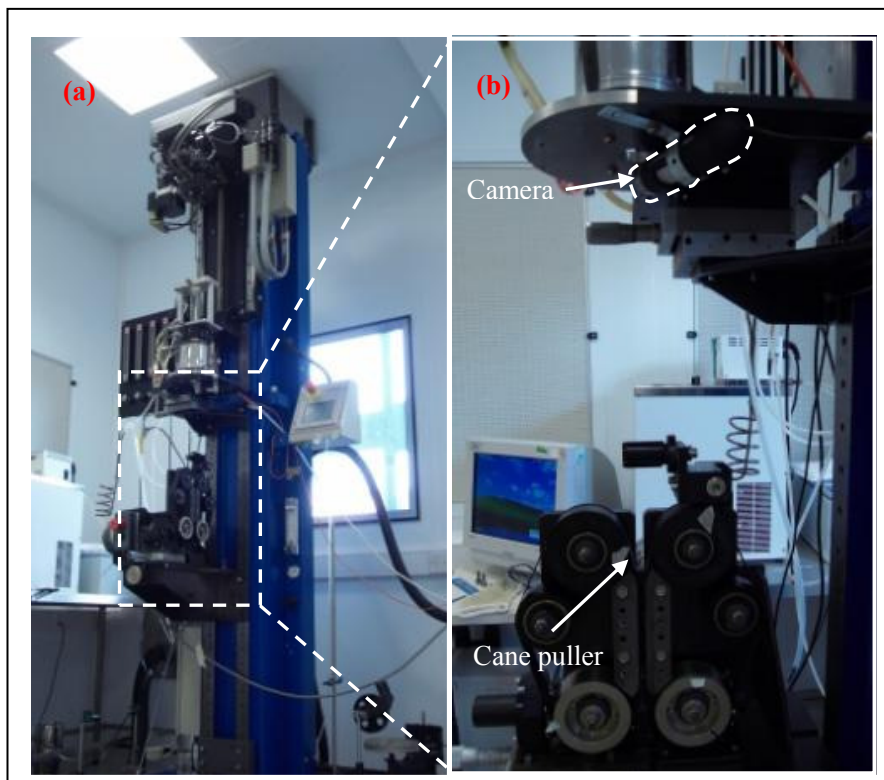


Figure 5.12 (a) The 3 m fibre drawing tower with the setup for cane drawing; (b) the real-time diameter monitor and the cane puller aligned on. The USB camera was applied and the motor was used to drive the roller.

The figure 5.12 shows the fixing and alignment of the camera (Veho VMS-001 Camera) and cane puller driven by a motor (BBC Brown Boveri, FDFC12T, 24v, 200 mA) on the fibre-drawing tower. The rollers of the cane puller, which clamp canes (see section 3.3.3), could be adjusted transversely to clamp canes with

different diameter (0.5 mm ~ 3 mm). The speed of the rolling was controlled by tuning the power of the tachometer manually. If the feed-in speed of a 10 mm chalcogenide rod was selected, the speed of rolling in the range between 1200 mm / min and 33.3 mm / min can be obtained in theory; a rolling speed of 192 mm / min was desired for drawing a 1.25 mm OD chalcogenide cane.

### 5.3.1.2 Development of LabView software solution

The LabView script with the function of image acquisition, image processing and diameter monitoring was created by the author with Vision Builder of Labview. The algorithm of the real-time monitor was composed of the functions illustrated in figure 5.13, which are: image acquisition, image format transformation and colour inspection, threshold image, image calibration, edge detection and clamper measurement.

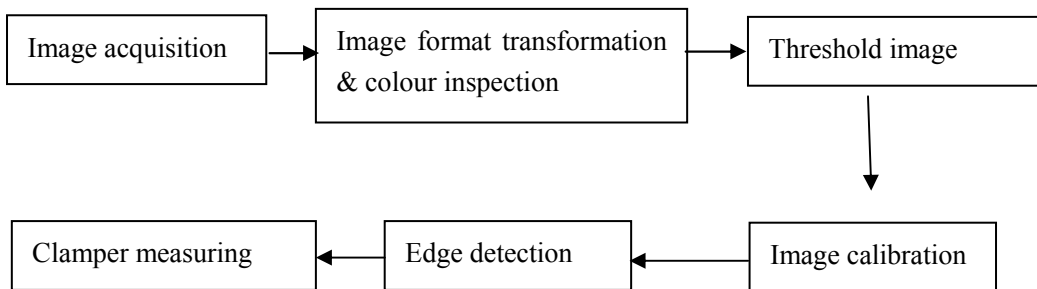


Figure 5.13 The logic block of the real-time diameter monitor algorithm to measure the diameter of the chalcogenide cane with no touching during cane-drawing.

The image acquisition function was set to capture the image of the chalcogenide cane and fed the data to the USB camera; the image of the chalcogenide cane was transferred to digital format, colour inspected in RGB (red, green, blue) colour

space, then transferred into 256 grey scales in order to map the natural colour to binary data format. A threshold was set, which enabled the image to be represented by two grey values representing the object and the background, so enabling the object to be clearly distinguished from the background. The calibration function was used as follows to convert the dimensions on the screen, which was in the unit of pixels, to the true size. Afterwards, the edge detection function was applied to detect the edges of the cane. The reading of the diameter in  $\mu\text{m}$  was then given by the clamper measurement function.

It can be seen from the figure 5.14 that the wirelike object, chalcogenide glass cane, being imaged was represented as white in the grey-scale when the script was running. The nominal diameter reading was shown on the screen and the feeding speed could be adjusted to let the nominal diameter approach the target diameter. The diameter monitor system was tested on soda-lime-silica glass cane drawing with manual adjustment of the drawing speed. The accuracy of the diameter measurement was found to reach about  $\pm 20 \mu\text{m}$  when applying a focal lens (focal length of 17 mm) with 40 times magnification (see section 5.3.1.1). This accuracy was acceptable for the canes of diameter  $\sim 1.25\text{mm}$ . In future work the more testing is required on different working dimensions and materials leading to better cane diameter control.

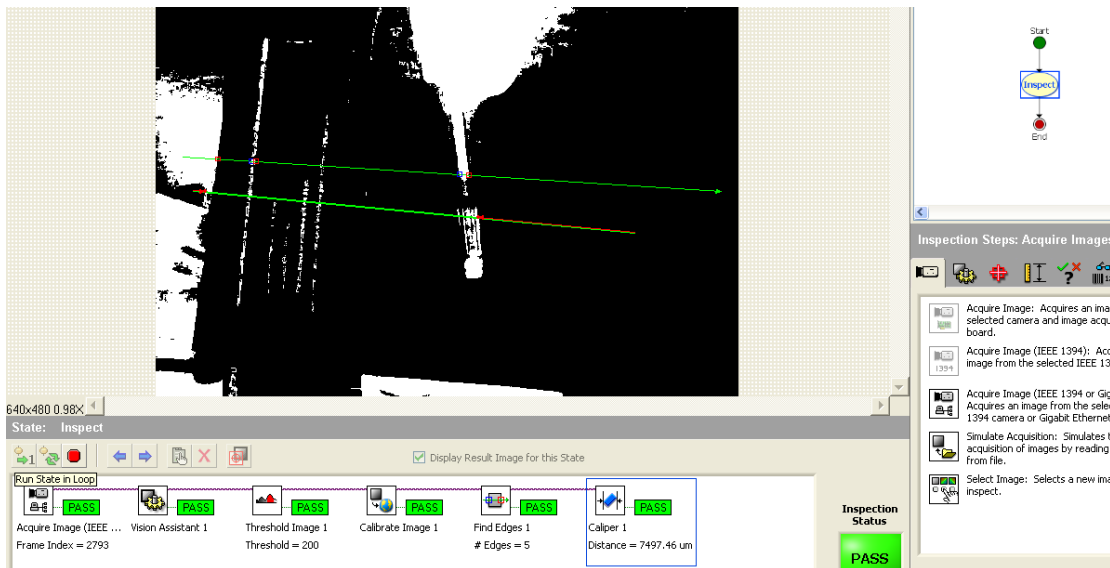


Figure 5.14 The screen shot from the graphical interface of the LabView software and the working state of diameter monitoring of the chalcogenide cane.

### 5.3.2 Stacking mechanism design for assembly of the microstructure.

A stacking mechanism was designed for stacking the hexagonal pattern of MOF. A tuneable V-groove with adjustable width of  $> 6.5$  mm and depth of 5.6 mm, which was used to hold the canes into the required 2 dimensional pattern, was shaped and fastened onto two micrometers (Newport) to adjust the horizontal place of each cane. Also, two vacuum holders (diffusion pump, Edwards B30207240) were designed to take the cane and positioned  $\pm 14$  mm vertically and  $\pm 30$  mm horizontally using the two micrometers.

The stacking holder design was undertaken in collaboration with PhD student George Athanasiou, undergraduate student Koh Haoyan and Dr. David Furniss. It was fabricated in the University of Nottingham Mechanical Engineering Workshop. A schematic representation of the stacking holder design is shown in figure 5.15.

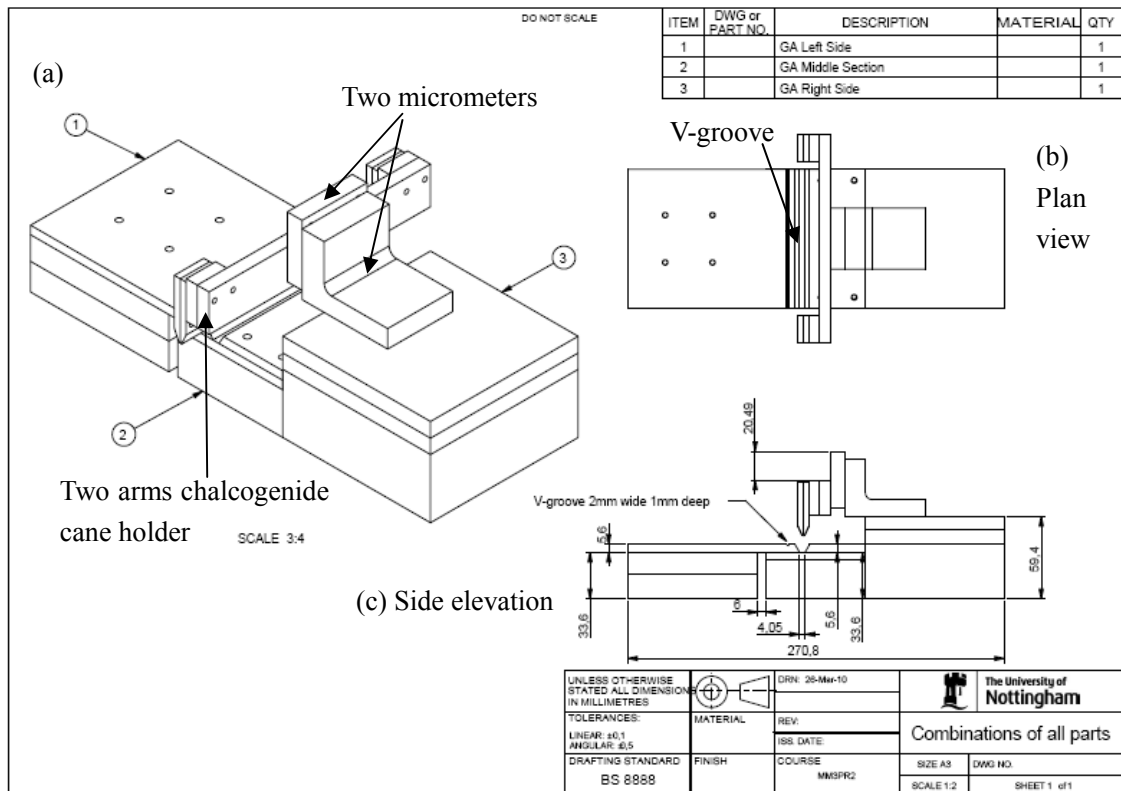


Figure 5.15 Schematic presentation of stacking mechanism to stack the chalcogenide canes in a 2 dimensional pattern. (a) the over view of the stacking mechanism: two micrometers are moved vertically and horizontally to control the position of the holder which locate the chalcogenide cane into the V-groove to form the 2 dimensional pattern; (b) Plan view: the relative position of the V-groove and the two-arm chalcogenide cane holder; (c) side elevation: the dimensions of the assembly.

The V-groove was made of three nylon plates, one plate is underneath the other two, whose ends had been shaped to an angle of  $60^\circ$ , and which were placed on the opposite side of each other and used to place the chalcogenide glass canes into the desired pattern. The width of the V-groove could be tuned using a horizontal micrometer (by  $> 6.5$  mm), which had been screwed into the nylon plate. Two vacuum holders, which held the cane by means of suction, could be moved in both vertical and horizontal directions by tuning a vertical micrometer and a horizontal micrometer, respectively. So, the cane could be placed precisely into the desired

position.

The dimensions of the mechanism and the clearance of each part were then verified with the actual product. The stacking-rig is shown in figures 5.16 (a) and 5.16 (b).

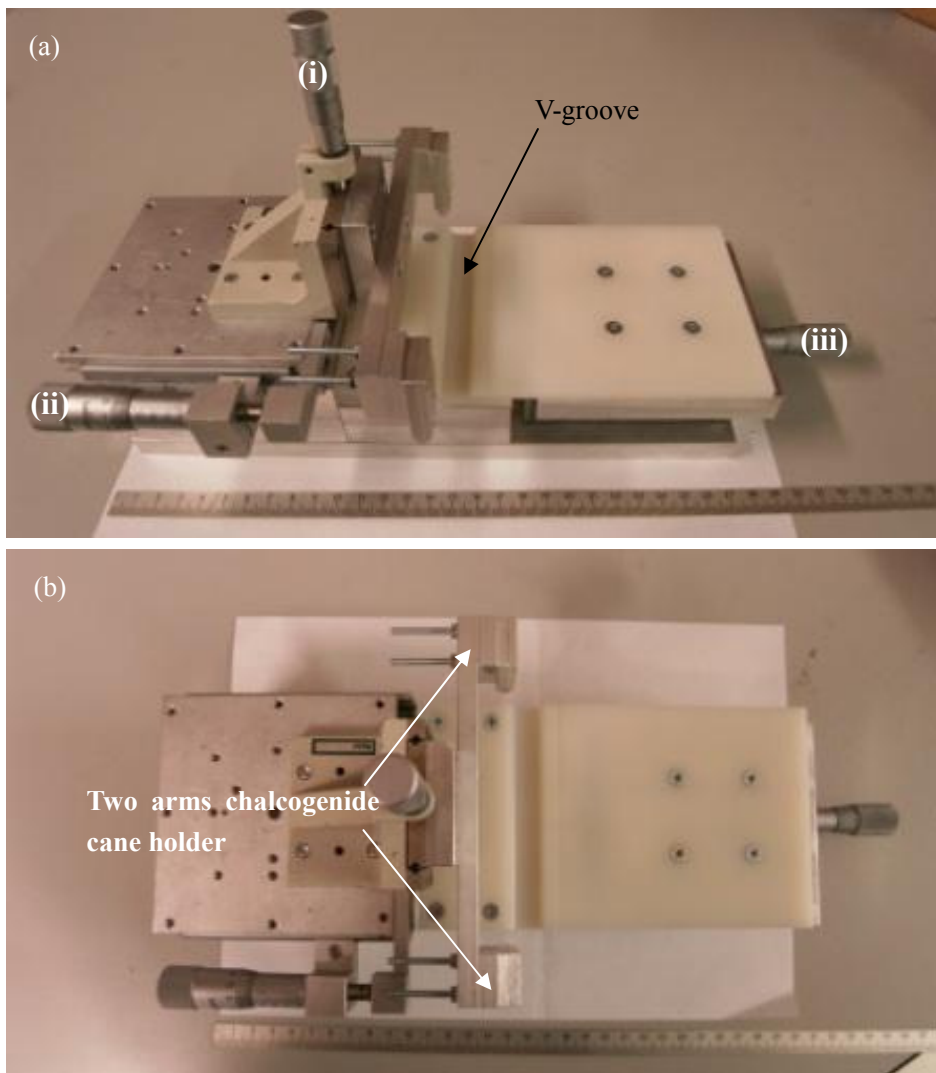


Figure 5.16 (a) over and top view of the stacking-rig to assemble the 2 dimensional pattern. The chalcogenide cane would be held by the two-arm chalcogenide cane holder. The cane holder can move vertically  $\pm 14$  mm by turning the knob (i) and horizontally  $\pm 30$  mm by turning the knob (ii). The width of the V-groove could be adjusted by  $> 6.5$  mm by turning a third knob (iii).

The stacking holder is undergoing testing by PhD student George Athanasiou of the date of completion of this thesis.

## **5.4 Fabrication and characterisation of all-solid MOF006.**

The fibre MOF006 is the second time trial to fabricate the structure shown in figure 5.6, with the improvements described in section 5.3.1.

### **5.4.1 Fabrication of all-solid MOF006.**

#### 5.4.1.1 Preparation of preform for MOF006.

##### (i) Fabrication of $As_{40}Se_{60}$ jacket-tube.

A two-chamber ampoule (see figure 5.17), with the dimensions described in section 5.3, was made from a 400 mm length and ID / OD of 8 mm / 10 mm silica glass tube (GlobalQuartz) to prepare the jacket tube for MOF006. The silica ampoule was a customised ampoule prepared from a 800mm tube with a sealed end (supplied by GlobalQuartz) which underwent the following clean and strengthen process: (i) hydrofluoric acid etching (0.3% by volume hydrofluoric (aq. HF) acid of the inside of the ampoule for 20 minutes), (ii) rinsing of the two chamber ampoule in deionised water 3 times then oven dried at 70°C and cooled to room temperature, (iii) annealing of the ampoule (see section 5.2.1.2 and table 5.2) by heating at 1160°C for 1.5 hours to release the potentially permanent strain then cooled to 950°C at 60°C / min. (iv) finally cooling down to ambient. Next the two chamber ampoule was baked at 1000°C / 6 hours under atmosphere (class

10,000 cleanroom) to remove any carbonaceous impurity and baked at 1000°C / 6 hours under vacuum of  $10^{-5}$  Pa in an attempt to minimise physically and chemically bonded water.

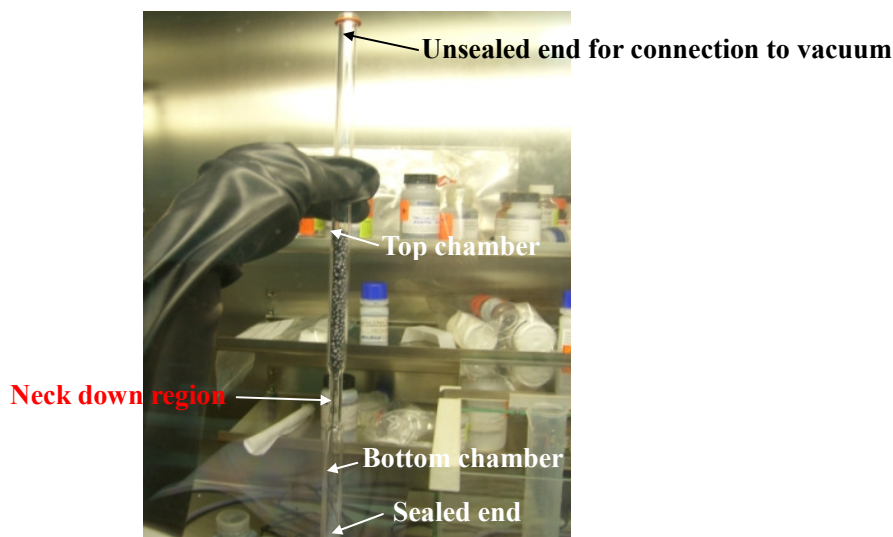


Figure 5.17 The two-chamber ampoule (customised from a 800 mm length Global Quartz silica tube) applied to fabricate the jacket-tube.

Based on the discussion in section 5.2.1.2, the quantity of Se required to be batched was 19.2960 g. The Se element (Cerac 99.999% purity, about 3 mm in pieces size) was batched in a  $N_2$ -recirculated glovebox (MBraun,  $< 0.1$  ppm  $O_2$  and  $0.1 < \text{ppm } H_2O$ ) and weighed by a balance (Sartorius, model BP221S accurate to  $\pm 0.1$  mg).

The hot zone of a resistance furnace (Instron, TF1005/4.5/1ZF) was set at the narrow neck section of the ampoule (see the position of hot zone and top of the furnace in figure 5.18 (a)) in order to melt the Se pieces from the top chamber down to the bottom chamber of the two chamber silica glass ampoule. This heating procedure was not for the purpose of a standard Se purification but to

leave enough engineering space for the top chamber by moving the material down to the bottom through the neck. However, the Se could be purified as well during the process if required, thus, for MOF006 an inner SiO<sub>2</sub> glass tube was used to collect the impurity of the Se. The temperature schedule was set the same as for a Se purification (see section 3.1.2) only the top temperature was raised from 250°C to 270°C to let the Se liquid achieve a low enough viscosity (see figure 5.18 (b)) so it could get through the narrow neck.

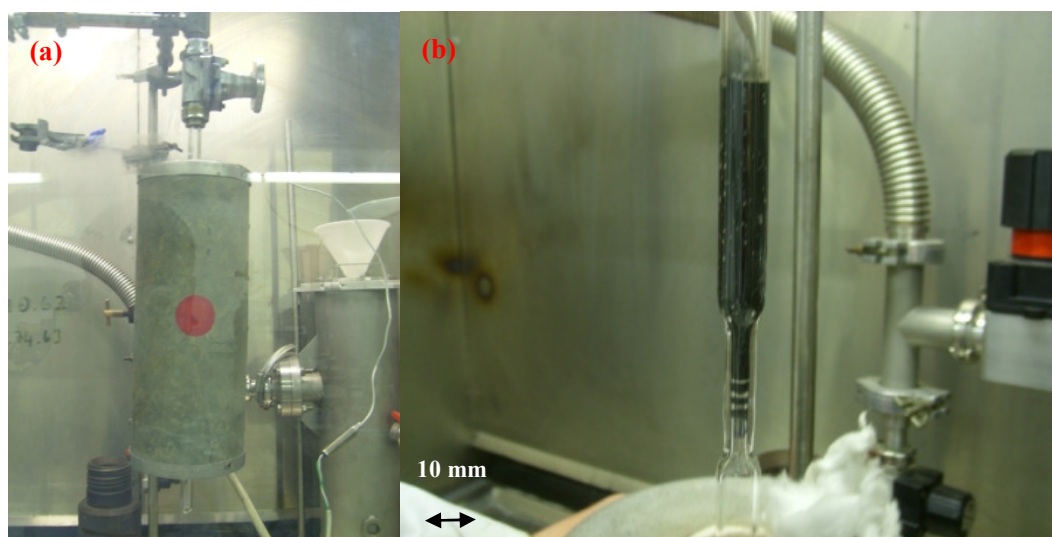


Figure 5.18 Photographs of an adjusted Se process for the preparation of the jacket tube for preform of MOF006: (a) the hot zone of furnace was placed at the narrow neck of the top chamber ampoule; (b) the Se was heated to the liquid state and is about to flow through the neck.

12.2061 g of As (Furukawa 99.99999% purity, ~ 4 - 8 mm in piece size) was then batched into the ampoule and it was placed in the top chamber of the ampoule (see figure 5.19 (a)). The space left in the top ampoule (because the Se had been moved down to the lower ampoule) was enough to proceed with the oxy-propane flame sealing off of the top of the two-chamber ampoule. The ampoule with the batched material is shown in figure 5.19 (b).

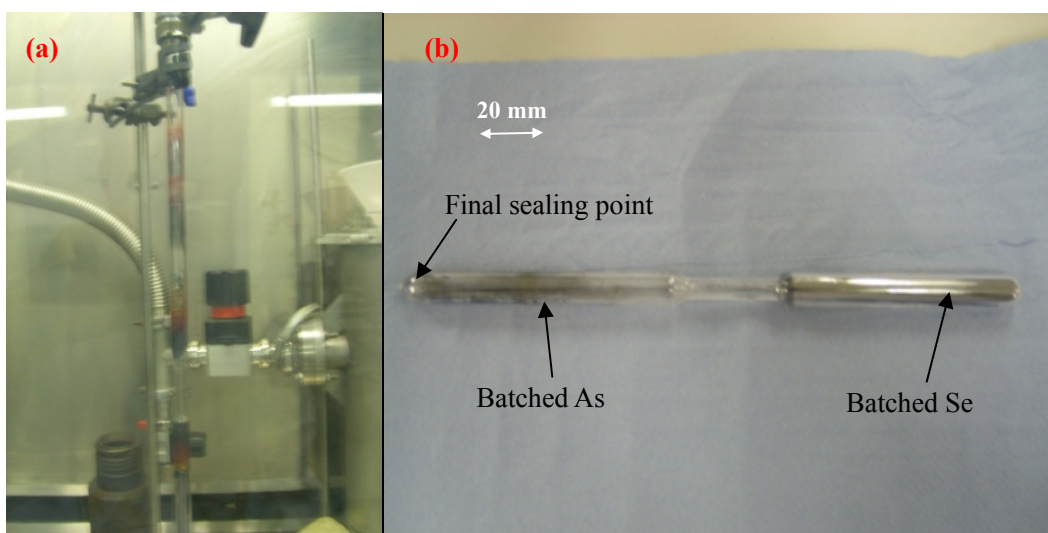


Figure 5.19 (a) The two-chamber ampoule used to prepare MOF006 was set up ready for sealing; (b) the sealed ampoule with enclosed material.

The melting schedule for the batched elements in the two-chamber ampoule was adjusted from the melting of  $\text{As}_{40}\text{Se}_{60}$  in a standard ampoule described in section 3.1.6. The furnace was set stable at  $45^\circ$  to the horizontal with the molten Se end up whilst the temperature was raised to  $280^\circ\text{C}$  at  $80^\circ\text{C} / \text{h}$  when the Se became fluid enough to flow down to the As end of the two-chamber ampoule. This had the purpose to mix the As chunks with the Se viscous fluid to avoid scratching the internal walls of the silica glass ampoule with the As chunks. Then, the temperature was raised to  $800^\circ\text{C}$  at  $40^\circ\text{C} / \text{h}$ . The furnace was set to start rocking at a temperature of  $400^\circ\text{C}$  (section 3.1.6). Then, at  $800^\circ\text{C}$ , there was an isothermal hold for 12 hours and the furnace remained rocking to allow homogeneous melting. After that, the temperature was reduced from  $800^\circ\text{C}$  to  $650^\circ\text{C}$  at  $60^\circ\text{C} / \text{h}$ . The furnace was placed stably and vertically for two hours at  $650^\circ\text{C}$  to let the molten material drop down to the bottom chamber at  $650^\circ\text{C}$ , which is high enough above its liquidus so the viscosity was low enough to get through the narrow neck

thoroughly. After that, the temperature was taken down to 570°C, which is about 100°C above the liquidus of the  $As_{40}Se_{60}$  but not too far away from it in order to avoid thermal shock during quenching. This had the purpose to reduce the temperature gap relative to the liquidus for the quenching procedure to avoid the silica ampoule suffering any thermal shock. A double air quenching was applied to ensure no cracking appeared in the silica glass ampoule during the quenching process. The ampoule was placed in the open air for 2 minutes and then placed into an annealing furnace, which was pre-set to the temperature of annealing (180°C for  $As_{40}Se_{60}$ ), and held there for 30 s and then placed in the open air for another 30 s. An annealing schedule (see section 5.2.1.2) was subsequently applied to the ampoule with the chalcogenide glass supercooled melt inside.

The ampoule was sealed at the neck and it can be seen in figure 5.20 (a) that the outer ampoule had survived after this first melting and the raw material had melted. The sealed ampoule was located into a buffer tube to go through a re-melt process, in which the temperature of the ampoule was heated to 650°C at 40°C / h and rocking started at 650°C and continued for 6 h with temperature held isothermally at 650°C. Then a rotational casting process was applied to replace a standard air quenching. It can be seen in figure 5.20 (b) that the assembly was located in the centre of in-house built (by Dr D. Furniss) rotational casting equipment (based on a Metalworker variable speed lathe). Starting the rotation of the assembly had to be fast, once the assembly had been clamped and fastened in

the rotational equipment. A rotational speed of 2000 rpm was applied to the assembly for 2.5 min. The location of the buffer tube had to be checked before the buffer tube was placed into the melting furnace to ensure it subsequently rotated symmetrically.



Figure 5.20 Preparation of MOF006 preform: making the  $\text{As}_{40}\text{Se}_{60}$  jacket tube: (a) The sealed ampoule and quenched and annealed first melt before the re-melt for the rotational casting; (b) the assembly of the ampoule and buffer tube and the rotational casting equipment.

A standard preform annealing procedure (see in section 3.1.6) was applied to the assembly afterwards. The over-clad tube made for MOF006 can be seen in figure 5.21 (a) and (b).

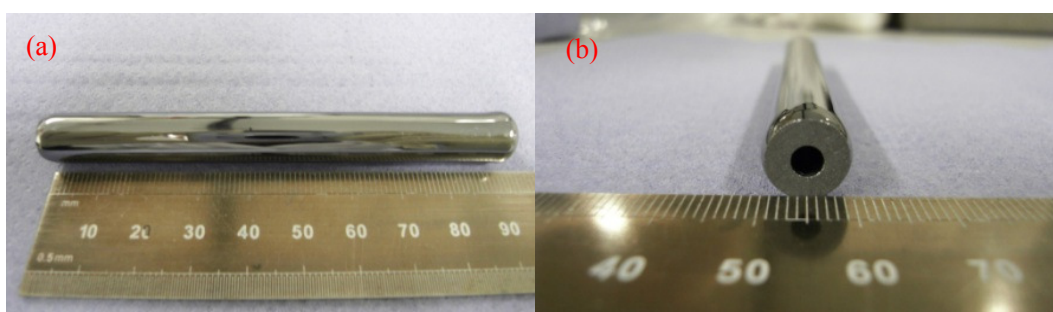


Figure 5.21 (a) The surface of the jacket tube; (b) the cross section of the jacket tube with ID / OD of 3 mm / 10 mm.

#### (ii) Fabrication of $\text{Ge}_{10}\text{As}_{23.4}\text{Se}_{66.6}$ for stacking inside $\text{As}_{40}\text{Se}_{60}$ jacket tube

An  $\text{Ge}_{10}\text{As}_{23.3}\text{Se}_{66.6}$  rod of 9 mm diameter and 130 mm length was made by using the extrusion technique (see section 3.3.2). 7 days of etching in 99% propylamine

(Sigma-Aldrich) was applied to the rod in an effort to clear up its oxide surface and remove surface defects. It can be seen from figure 5.22(a) that the chalcogenide rod was immersed into the propylamine and its surface was shiny after this etching (figure 5.22 (b)).

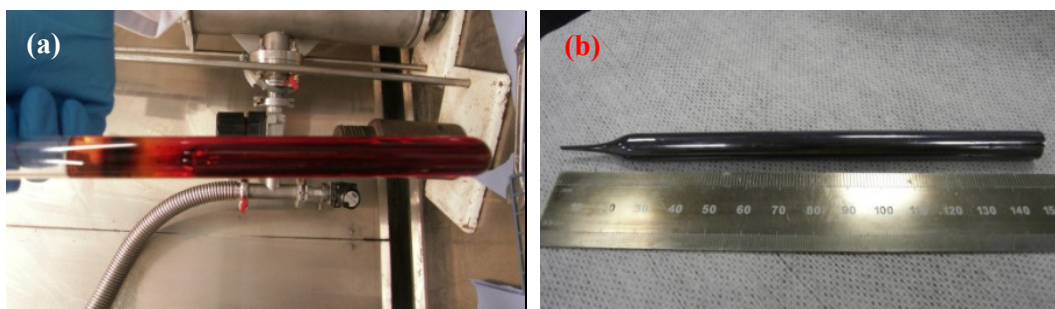


Figure 5.22 Fabrication of MOF 006: (a) Propylamine etching for the  $\text{Ge}_{10}\text{As}_{23.4}\text{Se}_{66.6}$  rod; (b) the extruded  $\text{Ge}_{10}\text{As}_{23.4}\text{Se}_{66.6}$  rod after propylamine etching.

The  $\text{Ge}_{10}\text{As}_{23.4}\text{Se}_{66.6}$  rod was shaped into many canes with diameter of 1.25 mm and length of 100 mm using the improved cane drawing and diameter monitor techniques (described in section 5.3.1). For this specific design, the feed-in speed of the rod and the drawing speed of the cane puller were set to 3 mm / min and 150.35 mm / min, respectively. A radio frequency fibre drawing furnace (Severn Furnace Ltd.) was applied to heat the chalcogenide rod and 8% setting of the power was used. The diameter of the cane was very thin at the very beginning but became thicker, approaching the aimed-at value, when it was being taken by the puller stably. After 33 mm of rod had been fed into the hot zone of the furnace, the aimed-for diameter of 1.26 mm for the cane was obtained, and the diameter was monitored by the real-time diameter monitor with the error of  $\pm 100\mu\text{m}$ . It can be seen from figure 5.23 (a) and (b) that three  $\sim 10$  mm length and 1.26 mm OD

chalcogenide canes were fabricated successfully. The improvement of this work was that the canes' diameters were more even along their length compared to the work for MOF005 described in section 5.2.1.

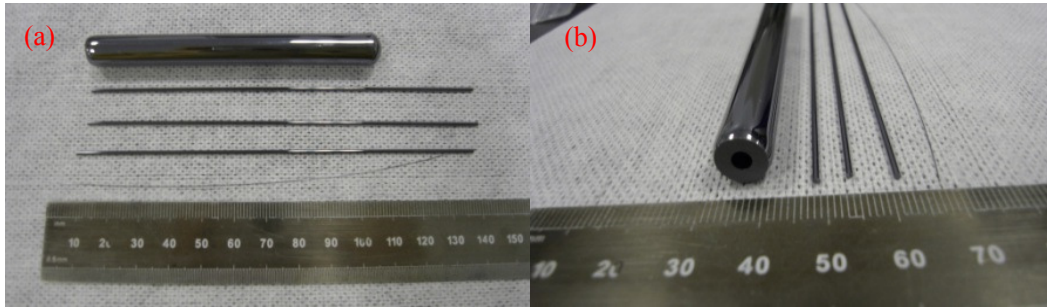


Figure 5.23 Fabrication of MOF006 preform: (a) the  $\text{As}_{40}\text{Se}_{60}$  over-clad tube, three  $\text{Ge}_{10}\text{As}_{23.4}\text{Se}_{66.6}$  canes and a  $\text{As}_{40}\text{Se}_{60}$  fibre ready for preform stacking; (b) the cross-section of the components.

The stacking of the components is tricky for this three cane structure (see section 5.2.1.2, figure 5.6), because it requires a perfect match of each component's diameter but a suitable clearance between the three canes' assembly and the over-clad tube. Also, the chalcogenide material is too "sticky" for the canes to be slide against each other. Thus, a stacking process was planned as follows. Two  $\text{Ge}_{10}\text{As}_{23.4}\text{Se}_{66.6}$  canes were placed together tightly enough and stuck using twin adhesive masking tape and PTFE tape. A  $\sim 200\mu\text{m}$  OD  $\text{As}_{40}\text{Se}_{60}$  fibre was then placed as the MOF006 core along the interface of these two canes. The fibre had to be longer than the canes so it could drop by its own weight and lie straight. This is to ensure the fibre fitted into the gap along all the length of canes (see figure 5.24 (a)). The third  $\text{Ge}_{10}\text{As}_{23.4}\text{Se}_{66.6}$  cane was placed to enclose the core fibre (see figure 5.24 (b)).

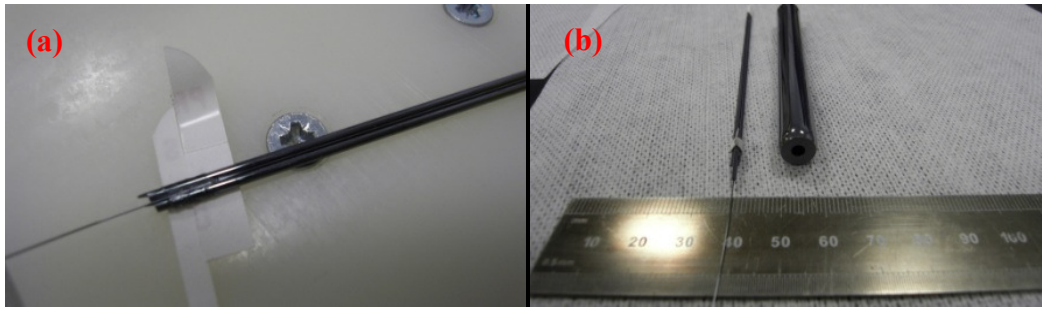


Figure 5.24 Fabrication MOF006: (a) the  $\text{As}_{40}\text{Se}_{60}$  core fibre seated into the gap between the first two  $\text{Ge}_{10}\text{As}_{23.4}\text{Se}_{66.6}$  canes; (b) the assembly of the  $\text{As}_{40}\text{Se}_{60}$  core fibre and three  $\text{Ge}_{10}\text{As}_{23.4}\text{Se}_{66.6}$  canes.

The whole assembly was fixed by PTFE tape and slowly inserted into the  $\text{As}_{40}\text{Se}_{60}$  jacket tube. The stacking assembly equipment was not used for this fibre because the  $200\mu\text{m}$  OD  $\text{As}_{40}\text{Se}_{60}$  fibre had to be fastened with the two  $\text{Ge}_{10}\text{As}_{23.4}\text{Se}_{66.6}$  canes before the third cane was placed. The stacking equipment is suitable for stacking the pattern with only chalcogenide canes.

#### 5.4.1.2 Fibre drawing for MOF006.

The assembly was then located onto the fibre drawing tower (see section 3.3.5.2) and a vacuum of 3 kPa was applied to remove the air when the  $\text{As}_{40}\text{Se}_{60}$  jacket tube was heated to its softening point to let the tube touch the assembly properly. This was to make sure no gap or bubbles exist between the jacket tube and the assembly of 3 canes and 1 core fibre. The ratio of feed in and feed out speed was changed to obtain MOF006 fibre diameters of  $115\mu\text{m}$ ,  $135\mu\text{m}$ ,  $145\mu\text{m}$ ,  $155\mu\text{m}$ ,  $200\mu\text{m}$ , respectively.

### 5.4.2 Characterisation of all-solid MOF006.

#### 5.4.2.1 Reflection optical microscopy.

It can be seen in figure 5.25 (a) that the jacket tube was about to be collapsed down onto the three cane assembly and the core fibre was located in the area between the three canes. The gap in the preform was fulfilled by the material and the core was located at the centre of the MOF006 (see figure 5.25 (b)).

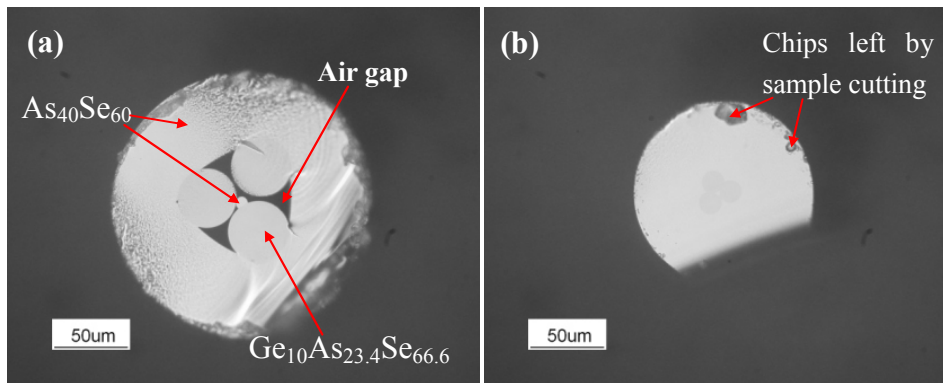


Figure 5.25 MOF006 fibre: (a) the cross-section of the beginning section of the fibre (155µm OD), the shape of the  $As_{40}Se_{60}$  core fibre,  $As_{40}Se_{60}$  jacket tube and three  $Ge_{10}As_{23.4}Se_{66.6}$  canes before MOF006 collapsed down. The  $As_{40}Se_{60}$  jacket tube was about to collapsed down and gap still existed between three  $Ge_{10}As_{23.4}Se_{66.6}$  canes; (b) the cross-section of fibre (115µm OD) when the fibre drawing was getting stable. The images were acquired using reflection optical microscopy (see section 3.2.4).

Reflection optical microscopy of higher magnification was applied to investigate the central area of the MOF's cross-section. In figure 5.26, the same sample shown in figure 5.25(b) was enlarged. The diameter of its triangular core is 2.2µm and the diameter of the cane is 14.2 µm, so it proved the aspect ratio of the cross-section (see section 5.2.1.2) has been roughly kept during the fibre drawing process.

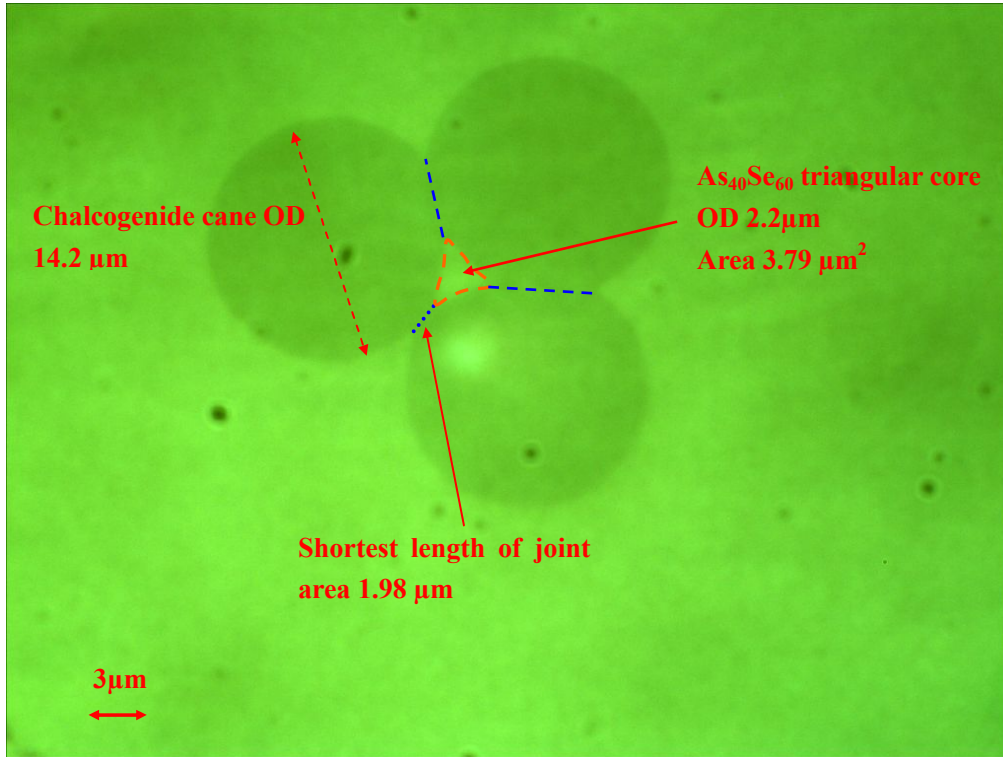


Figure 5.26 Optical reflection micrographs of the MOF MOF006 fabricated. Here the outer diameter and central region diameter are respectively:  $\sim 115\mu\text{m}$  and  $\sim 2.5\mu\text{m}$ . It proves that the core fibre has been located at the centre of three canes. The diameter of the triangle core area is  $2.4 \pm 0.2\mu\text{m}$  and the diameter of the  $\text{Ge}_{10}\text{As}_{23.4}\text{Se}_{66.6}$  cladding canes are  $14.2 \pm 0.2\mu\text{m}$ . Note: the blue lines indicate the joint ends of three  $\text{Ge}_{10}\text{As}_{23.4}\text{Se}_{66.6}$  canes which isolate the triangular  $\text{As}_{40}\text{Se}_{60}$  core from the  $\text{As}_{40}\text{Se}_{60}$  jacket tube.

It can be seen from figure 5.26 above that the  $\text{As}_{40}\text{Se}_{60}$  core fibre has been enclosed by the three  $\text{Ge}_{10}\text{As}_{23.4}\text{Se}_{66.6}$  canes. The triangular core appeared to be successfully isolated from the jacket  $\text{As}_{40}\text{Se}_{60}$  tube by the touching end of three canes. The thinnest joint end is just about  $1.98\mu\text{m}$  (see figure 5.26) which is half of the other two joint ends and this defect affected the symmetry of the fibre.

#### 5.4.2.2 SEM characterisation.

It figure 5.27 (a), the As content inside the spots clearly shows a cladding ring of canes of  $\text{Ge}_{10}\text{As}_{23.4}\text{Se}_{66.6}$  (as batched) lower As content than that expected in the

central region, and jacket region for  $\text{As}_{40}\text{Se}_{60}$  (as batched). The triangular core area can be found at the centre but it is not clear due to the contrast of the image not being that large; (b) Ge only occurred in spots arranged as a ring, as expected from the stacking arrangement achieved in the MOF006 preform before drawing down (see section 5.4.1.1(ii)). The triangular core could be found clearly located at the centre from this image; (c) Se exhibited a close-to-uniform distribution across whole fibre cross-section.

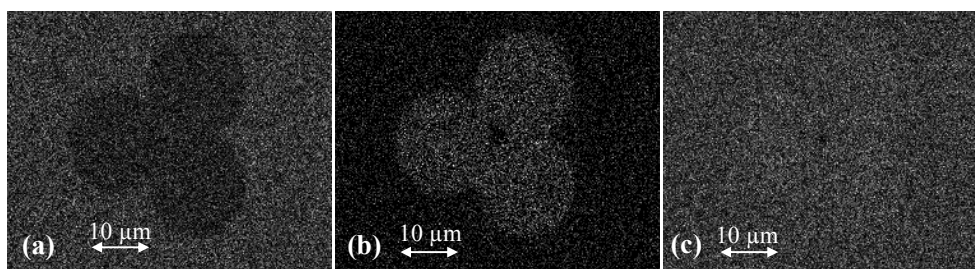


Figure 5.27 Scanning electron microscopy, back-scattered electron elemental mapping of the all-solid, chalcogenide glass MOF fabricated here: (a) As, where the brighter area has higher As concentration; (b) Ge, where the three canes cladding area has higher Ge concentration and (c) Se, the concentration of Se is very close in the core, three canes cladding and jacket tube area because the concentration discrepancy of Se is just 6.6 at% between the composition of  $\text{As}_{40}\text{Se}_{60}$  and  $\text{Ge}_{10}\text{As}_{23.4}\text{Se}_{66.6}$ .

The fabrication of MOF006 demonstrated again that the route of fabricating all solid chalcogenide microstructured fibre discussed above is stable. Also, the structure of the preform could be preserved during the stacking and fibre shaping process based on the more controllable technique of tube making and cane-drawing (see the solution in section 5.3.1) to obtain the diameter of the preform precisely. Overall, the glass synthesis and fibre shaping for MOF006 was successful, however, a more precise control of chalcogenide preform's dimensions

is still needed because a tiny defect will affect the symmetry of the fibre which may change the guiding properties of the design. Furthermore, a more feasible stacking engineering and a way to fix the stacked preform is still needed in the future work. The stacking equipment described in section 5.3.2 is able to stack the pattern with the tolerance of about 100  $\mu\text{m}$  but does not work if there is a fibre with a diameter of about 200  $\mu\text{m}$  in the pattern.

#### 5.4.2.3 Light guiding characterisation of MOF006.

The samples from the section of as-drawn MOF006 with OD of 115  $\mu\text{m}$ , 135  $\mu\text{m}$ , 145  $\mu\text{m}$  and 200  $\mu\text{m}$ , respectively, were cut from the drawn fibre for optical assessment. A tapered silica glass optical fibre (9  $\mu\text{m}$  OD) was used to couple the 1.463 $\mu\text{m}$  to 1.55  $\mu\text{m}$  wavelength laser beam (supplied by Agilent, model 81980A) into one end of the MOF006 sample. The transmitted light from the input end of MOF006 was guided through to the its other end and then collected using a  $\times 10$  or a  $\times 25$  silicate glass microscope objective and focused onto an infrared sensitive camera (Siemens XQ1112). A television monitor and computer were connected to the near-infrared camera as a direct image output. The light guiding test of MOF006 was carried out and a test bench was constructed as in figure 5.28.

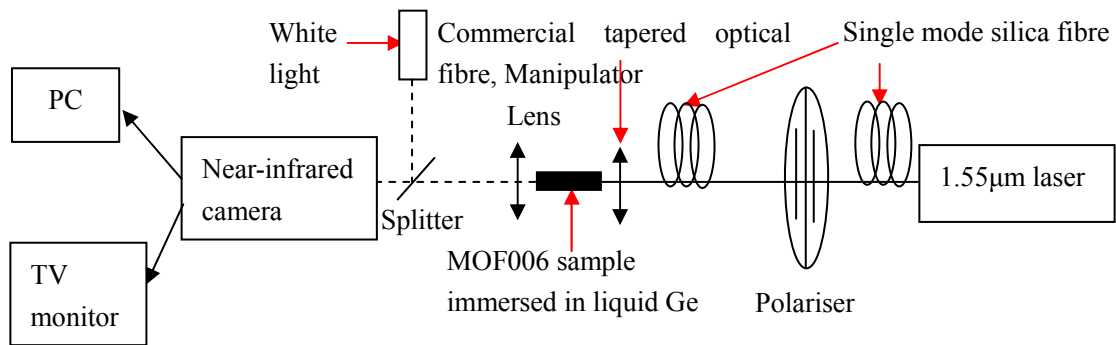


Figure 5.28 Light guiding test bench constructed by Pan (of the Novel Photonic Glasses Group, University of Nottingham) and cited from [5.7].

All of the samples of MOF006 exhibited a guiding in the three  $\text{Ge}_{10}\text{As}_{23.4}\text{Se}_{66.6}$  canes area which is the clad of the MOF. The expected guiding in the triangle core area did not appear (see figure 5.29 (a) with a  $\times 10$  microscope objective and figure 5.29 (b) with a  $\times 25$  microscope objective).

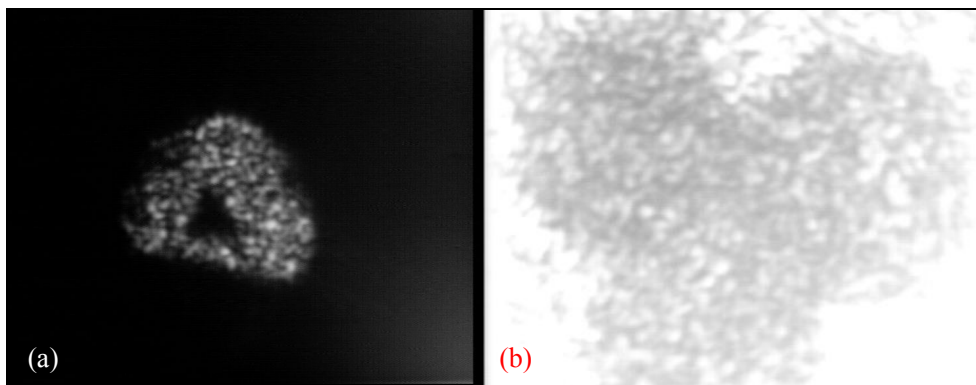


Figure 5.29 MOF006 (a)  $1.55\mu\text{m}$  light guiding profile with a  $\times 10$  microscope objective and (b)  $1.55\mu\text{m}$  light guiding profile with a  $\times 25$  microscope objective in which the core and clad area has been zoomed in on.

In order to strip the cladding mode from the cladding area which may suppress the guiding in the triangular core, 300 mm length of sample was immersed into a 150 mm length aluminium groove filled with liquid Ge for 20 minutes and the light guiding test afterwards. The light launched into cladding was saturated gradually but there is still no light guiding in the core. However the  $\text{As}_{40}\text{Se}_{60}$  core was only

2.2  $\mu\text{m}$  diameter and the silica glass input fibre was 9  $\mu\text{m}$  diameter hence it was impossible to launch light into the  $\text{As}_{40}\text{Se}_{60}$  core only. This will be the subject of future work.

## **5.6 Conclusion.**

It can be concluded that the technique of MOF fabrication with the glass pair of  $\text{As}_{40}\text{Se}_{60}$  and  $\text{Ge}_{10}\text{As}_{23.4}\text{Se}_{66.6}$  is mature to achieve a complete MOF structure. The glass pair is a mature candidate for all-solid MOF. The rotational cast technique with two chamber ampoules could obtain a very thick wall tube which is needed for the small core MOF. A cane puller with a real-time diameter monitor enabled a more precise control of chalcogenide glass cane shaping. The stacking technique of the preform still needs to be investigated to make the pattern preserved perfectly during the handling of preform and fibre drawing. The work of MOF006 also demonstrated the perfectness of the symmetry of the fibre's cross section is essential for MOF and a tiny defect may disorder the designed light guiding property. Also, a more delicate optical device and more advanced alignment technique of light guiding bench may needed due to the fibre's core area is in micro-scale.

## **Chapter 6 Conclusion and Future Work**

During this MPhil, the glass synthesis, thermal properties and optical refractive index of the Ge-Sb-Se glass system have been investigated in depth. The modification of the glasses' properties by adjusting the glass composition was obtained to link to the discovery of a glass pair for MOF fabrication.

### **6.1 Properties of Ge-Sb-Se glass and fibre fabrication**

In the project, glass pairs were successfully identified for the fabrication of found chalcogenide MOF and core-clad. fibre. Fabrication of a core-clad fibre with this non-arsenic-containing glass, which may link to an application with mono-mode or multimode guiding, is worth exploring in the future. As it has been discussed in chapter 4, based on the potential glass pair's index contrast and single mode guiding condition, a multimode core-clad fibre with relatively close dimension of core and clad might be easier in the aspect of engineering. Also, because the replacing of Sb for As, the purification procedure of Ge-Sb-Se glasses system and how does the transparent window affected by the impurities should be investigated based on the purification technique of As-containing glasses. The nonlinear optical properties of Ge-Sb-Se glasses could be studied to find the proper light guiding solution for the applications which rely on high optical nonlinearities such as SCG.

## **6.2 The technique of MOF fabrication and the solution for application**

In the project, a suspended core, all-solid chalcogenide MOF was fabricated successfully. The technique of fabrication of a fibre preform jacket tube has been investigated in depth. Different procedures to make a tube with a wall thickness of 1.5 mm to 3.5 mm have been explained and demonstrated in chapter 5. An initial investigation of improving the precision of dimension control during preform shaping has been done. A more advanced real time contactless dimension monitoring solution and electronic auto-control system, which can report dimension measurement and provide real time feedback to adjust power supplied in the preform shaping, is necessary to achieve higher dimension accuracy, since it is critical to realise the desired optical properties of the MOF. This is enabled with a more precise control on the dimensions of the chalcogenide preform.

The stacking and assembly in tube methods have been studied. This procedure has been demonstrated to be a mature way for the fabrication of all-solid chalcogenide MOF. The fabrication of “holey” MOF is more complicated than that of all-solid chalcogenide MOF, because of the internal air holes. Further numerical modelling of the collapse of tube shaping process, to reveal the pattern flow information, will help the further understanding of the process of holey MOF fibre-drawing.

Supercontinuum generation (SCG) using chalcogenide glasses core-clad fibre and

MOF has a bright application prospect in the future. An literature study of SCG based on the silica fibre has been done in chapter 2. Thus, at the next stage, SCG experiments could be implemented starting with unstructured chalcogenide glass fibre and then move to core-clad fibre and MOF. In order to obtain the loss information of the core-clad fibre and MOF, an advanced system solution is needed to build at the next step. A new optical bench should be developed to develop to ensure all of the light can be collected into the measured small core fibre and with a more precise alignment between the light and the fibre. It may include selecting a suitable pump source for SCG, choosing a more dedicate and tighter light confining solution and building a setup to fasten the sample to prevent even tiny vibration during an on-going light guiding experiment and finally to analyse the output.

## References:

- [1.1] A.Zakery, S.R.Elliott, 'Optical nonlinearities in chalcogenide glasses and their applications', Springer-Verlag Berlin Heidelberg (2007).
- [1.2] A.R. Hilton, C.E. Jones and M. Brau, 'Nonoxide chalcogenide glasses as infrared optical materials', *Physics and Chemistry of Glasses*, 7, 105, (1966).
- [1.3] Z.G. Lian, Q.Q. Li, D. Furniss, T.M.Benson, A.B.Seddon, 'Solid microstructured chalcogenide glass optical fibers for the near- and mid-infrared spectral regions', *Photonics Technology Letters, IEEE*, 21, (24), 1804-1806, (2009).
- [1.4] P.St.J.Russell, 'Photonic-crystal fibers', *IEEE Journal of Lightwave Technology*, 24, (12), December (2006).
- [1.5] Z.G. Lian, 'Planar and fibre optical waveguides in chalcogenide glasses', University of Nottingham: PhD Thesis, Nottingham, (2009).
- [2.1] H.Rawson, 'Properties and applications of glass', Elsevier Scientific Publishing Company, 3, (1980).
- [2.2] J.E. Shelby, 'Introduction to glass science and technology', The Royal Society of Chemistry, Turpin Distribution Service Ltd, (1997).
- [2.3] A.Zakery, S.R.Elliott, 'Optical Nonlinearities in Chalcogenide Glasses and their Applications', Springer-Verlag Berlin Heidelberg (2007).
- [2.4] A.K. Varshneya, A.N. Sreeram and D.R. Swiler, 'A review of the average coordination-number concept in multicomponent chalcogenide glass systems', *Physics and Chemistry of Glasses* 34, 179-193 (1993).
- [2.5] P. Kumar and R. Thangaraj, 'Glassy state and structure of Sn–Sb–Se chalcogenide alloy', *Journal of Non-Crystalline Solids* 352, 2288-2291 (2006).
- [2.6] Z.P. Lu and C.T. Liu, 'Glass formation criterion for various glass-forming systems', *Physical Review Letters*, 91, (2003), 115505.
- [2.7] Z.G. Lian, 'Planar and fibre optical waveguides in chalcogenide glasses', University of Nottingham: PhD Thesis, Nottingham, (2009).
- [2.8] W.J. Pan, 'Development of hot embossing for fabricating optical waveguides based on chalcogenide glasses', University of Nottingham: PhD Thesis, Nottingham, (2008).

- [2.9] J.M. Harbold, F.O. Ilday, F.W. Wise, J.S. Sanghera, V.Q. Nguyen, L.B. Shaw, and I.D. Aggarwal, 'Highly nonlinear As-S-Se glasses for all-optical switching.' *Optics Letters*, 27(2), 119-121, (2002).
- [2.10] Ho, K.S., S.H. Liu, and G.S. He, *Physics of nonlinear optics*. 2000, London: World Scientific.
- [2.11] Z.G. Lian, Q.Q. Li, D. Furniss, T.M. Benson and A.B. Seddon, 'Solid microstructured chalcogenide glass optical fibers for the near- and mid-infrared spectral regions', *Photonics Technology Letters*, 21, (24), 1804-1806, (2009).
- [2.12] A.R. Hilton, C.E. Jones and M. Brau, 'Nonoxide chalcogenide glasses as infrared optical materials', *Physics and Chemistry of Glasses* 7, 105, (1966).
- [2.13] J.A. Savage, *Infrared Optical Materials and their Antireflection Coatings*, Adam Hilger, Bristol, (1985).
- [2.14] J. Wasylak, 'New glasses of shifted absorption edge in infrared as materials for optics and light fiber technique', *Optical Engineering*, 36, (6), 1652-1656, (1997).
- [2.15] Z.Y. Wang, C.J. Tu, Y.M. Li and Q.Q. Chen, 'The effects of Sn and Bi additions on properties and structure in Ge-Se-Te chalcogenide glass', *Journal of Non-Crystalline Solids*, 191, 132-137, (1995).
- [2.16] H.L. Ma, Y. Guimond, X.H. Zhang and J. Lucas, 'Ga-Ge-Sb-Se based glasses and influence of alkaline halide addition', *Journal of Non-Crystalline Solids*, 256&257, 165-169, (1999).
- [2.17] X.H. Zhang, H.L. Ma, Jean-Luc Adam, J. Lucas, G.R. Chen and D.H. Zhao, 'Thermal and optical properties of the Ga-Ge-Sb-Se glasses', *Materials Research Bulletin*, Vol. 40, Issue 10, 1816-1821, (2005).
- [2.18] J.A. Savage, P.J. Webber and A.M. Pitt, 'An assessment of Ge-Sb-Se glasses as 8 to 12  $\mu\text{m}$  infrared optical materials', *J.Mat.Sci.*, 13, 859, (1978).
- [2.19] P.S.L. Narasimham, A. Giridhar and Sudha Mahadevan, 'Electrical conductivity studies on families of glasses of the Ge-Sb-Se system', *Journal of Non-Crystalline Solids* 43, 365-378, (1981).
- [2.20] X.H. Zhang, H.L. Ma, J. Lucas, 'Evaluation of glass fibres from the Ga-Ge-Sb-Se system for infrared applications', *Optical Materials*, Volume 25, Issue 1, February 2004,

Pages 85-89.

- [2.21] W. Chung, H. Seo, B. Park, J. Ahn, and Y. Choi, 'Selenide glass optical fiber doped with  $\text{Pr}^{3+}$  for U-band optical amplifier', Electronics and Telecommunication Research Institute Journal 27, 411-417, (2005).
- [2.22] L. petit, N. Carlie, H. Chen, S. Gaylord, J. Massera, G. Boudebs, J. Hu, A. Agarwal, L. Kimerling, K. Richardson, 'Compositional dependence of the nonlinear refractive index of new germanium-based chalcogenide glasses', Journal of Solid State Chemistry, 182, 2756-2761, (2009).
- [2.23] P.St.J.Russell, 'Photonic-crystal fibers', IEEE Journal of Lightwave Technology, 24, (12), December (2006).
- [2.24] R.Buczynski, 'Photonic crystal fibers', ACTA Physica Polonica Series A, 106, (2), 141-167, (2004).
- [2.25] J.C.Knight, T.A.Birks, P.St.J.Russell, and D.M.Atkin, 'All-silica single-mode optical fiber with photonic crystal cladding', Optics Letters, 21, 1547-1549, (1996).
- [2.26] R.F. Cregan, B.J. Mangan, J.C. Knight, T.A. Birks, P.S. Russell, P.J. Roberts, D.C. Allan, 'Single-mode photonic band gap guidance of light in air', Science 285, (5433), 1537-1539, (1999).
- [2.27] M.D. Nielsen, N.A. Mortensen, J.R. Folkenberg, A. Petersson and A. Bjarklev, 'Improved all-silica endlessly single-mode photonic crystal fiber', Optical Society of America (2003).
- [2.28] H.Kogelnik, 'Theory of optical waveguides in guided-wave optoelectronics', T.Tamir, ed., Springer Verlag (1998).
- [2.29] G. Pearce, J. Pottage, D. Bird, P. Roberts, J.C. Knight, and P.J. Russell, 'Hollow-core PCF for guidance in the mid to far infra-red', Optics Express, 13, (18), 6937-6946, (2005).
- [2.30] J.M. Pottage, D.M. Bird, T.D. Hedley, T.A. Birks, J.C. Knight, P.J. Russell, and P.J.Roberts, 'Robust photonic band gaps for hollow core guidance in PCF made from high index glass', Optics Express, 11, 2854-2861, (2003).
- [2.31] P. Blattnig, V. Romano, W. Luthy and T. Feurer, 'Numerical analysis of hexagonal solid-core photonic crystal fibers', Optical Society of America, (2006).
- [2.32] G.P. Agrawal, 'Applications of nonlinear fibre optics', Elsevier Inc (2008).

- [2.33] M.D. Nielsen, N.A. Mortensen, J.R. Folkenberg, and A. Bjarklev, 'Mode-field radius of photonic crystal fibers expressed by the V parameter', *Optics Letters*, 28, (23), 2309-2311, (2003).
- [2.34] F. Poli, A. Cucinotta, S. Selleri, 'Photonic crystal fibers', Published by Springer, P.O.Box 17,3300 AA Dordrecht, The Netherlands, (2007).
- [2.35] M.D. Nielsen, N.A. Mortensen, J.R. Folkenberg, A. Petersson and A. Bjarklev, 'Improved all-silica endlessly single-mode photonic crystal fiber', *Optical Society of America* (2003).
- [2.36] M.D. Nielsen, N.A. Mortensen, 'Photonic crystal fiber design based on the V-parameter', *Optics Express*, 11, (21), 2762-2768, (2003).
- [2.37] V.P. Minkovich, A.V. Kir'yanov, A.B. Sotsky, L.I. Sotskaya, 'Large core holey fibers with a few air channels in cladding - modeling and experimental investigation of the modal properties', *Journal of the Optical Society of America B, OSA*, 21, (6), 1161-1169, (2004).
- [2.38] J.R. Folkenberg, M.D. Nielsen, N.A. Mortensen, C. Jakobsen, and H.R. Simonsen, 'Polarization maintaining large mode area photonic crystal fiber', *Optics Express*, 12, (5), 956-960, (2004).
- [2.39] M.G. Franczyk, J.C. Knight, T.A. Birks, P.J. Russell, and A. Ferrando, 'Birefringent photonic crystal fibre with square lattice,' in *light guides and their Applications II*, J.Wojcik and W.Wojcik, Eds. *Proc SPIE*, 5576, 25-28, (2004).
- [2.40] J.K. Ranka, R.S. Windeler and A.J. Stentz, 'Visible continuum generation in air-silica microstructure optical fibers with anomalous dispersion at 800 nm', *Optics Letters*, 25, (1), 25-27, (2000).
- [2.41] V.M. Finazzi, T.M. Richardson, D. James, 'The role of confinement loss in highly nonlinear silica holey fibers' *Photonics Technology Letters*, 15, (9), 1246, (2003).
- [2.42] J.H. Lee, W. Belardi, K. Furusawa, P. Petropoulos, Z. Yusoff, T.M. Monro, and D.J. Richardson, 'Four-wave mixing based 10-Gb/s tunable wavelength conversion using a holey fiber with a high SBS threshold', *Photonics Technology Letters*, 15, 440-442, (2003).
- [2.43] K. Saitoh and M. Koshiba, 'Numerical modeling of photonic crystal fibers', *Journal of Lightwave Technology*, 23, 3580, (2005).
- [2.44] [http://www.physics.usyd.edu.au/current/tsp/Martijn\\_deSterke.pdf](http://www.physics.usyd.edu.au/current/tsp/Martijn_deSterke.pdf), (August 2009).

- [2.45] G.P. Agrawal, 'Nonlinear fiber optics', 3rd ed. Aca Academic, San Diego (2001).
- [2.46] A. Zakety, Y. Ruan, A.V. Rode, M. Samoc, B.L. Davies, 'Low-loss waveguides in ultrafast laser-deposited As<sub>2</sub>S<sub>3</sub> chalcogenide films', *Journal of the Optical Society of America B* 20, 1844, (2003).
- [2.47] N.G.R. Broderick, T.M. Monro, P.J. Bennett, and D.J. Richardson, 'Nonlinearity in holey optical fibers: measurement and future opportunities,' *Optics Letters*, 24, 1395–1397, (1999).
- [2.48] X.Z. Sang, and C.X. Yu, 'Applications of nonlinear effects in highly nonlinear photonic crystal fiber to optical communications', *Optical and Quantum Electronics*, 37, (2005), 965–994.
- [2.49] J.M. Dudley, G. Genty, and S. Coen, 'Supercontinuum generation in photonic crystal fiber', *Reviews of Modern Physics*, 78, 1135, (2006).
- [2.50] J.M. Dudley, L. Provino, N. Grossard, and H. Maillotte, 'Supercontinuum generation in air–silica microstructured fibers with nanosecond and femtosecond pulse pumping', *Journal of the Optical Society of America B*, 19, (4), 765-771, (2004).
- [2.51] J.M. Dudley, G. Genty, S. Coen, 'Supercontinuum generation in photonic crystal fiber', *Reviews of Modern Physics*, 78, 1135, (2006).
- [2.52] B. Ung and M. Skorobogatiy, 'Chalcogenide microporous fibers for linear and nonlinear applications in the mid-infrared', *Optics Express*, 18, 8, 8647-8659, (2010).
- [2.53] M.S. Liao, C. Chaudhari, G.S. Qin, X. Yan and T. Suzuki, Yasutake Ohishi, 'Tellurite microstructure fibers with small hexagonal core for supercontinuum generation', *Optics Express*, 17, (14), 12174-12182, (2009).
- [2.54] M.S. Liaoa, X. Yan, G.S. Qin, C. Chaudhari, T. Suzuki, Yasutake Ohishib 'A highly non-linear tellurite microstructure fiber with multi-ring holes for supercontinuum generation', *Optics Express*, 17, (18), 15481-15490, (2009).
- [2.55] P. Domachuk, N.A. Wolchover, M.C. Golomb, A. Wang, A.K. George, C.M.B. Cordeiro, J.C. Knight, F.G. Omenetto, 'Over 4000 nm bandwidth of mid-IR supercontinuum generation in sub-centimeter segments of highly nonlinear tellurite PCFs', *Optics Express*, 16, 7161-7168, (2008).
- [2.56] X. Feng, W.H. Loh, J.C. Flanagan, A. Camerlingo, S. Dasgupta, P. Petropoulos, P.

- Horak, K.E. Frampton, N.M. White, J.H.V. Price, H.N. Rutt, and D.J. Richardson, 'Single-mode tellurite glass holey fiber with extremely large mode area for infrared nonlinear applications', *Optics Express*, 16, 13651-13656, (2008).
- [2.57] T. Delmonte, M.A. Watson, E.J.O. Driscoll, X. Feng, T.M. Monro, V. Finazzi, P. Petropoulos, J. Price, J. Baggett, W. Loh, D.J. Richardson, D.P. Hand, 'Generation of mid-IR continuum using tellurite microstructured fiber', *Conference on Lasers, Optical Society of America* (2006).
- [2.58] M.R. Wehner, M. Ross, A. Efimov, and A.J. Taylor, V.V.R.K. Kumar, A.K. George, and J.C. Knight, N.Y. Joly, and P.J. Russell, 'Spectrally smooth supercontinuum from 350 nm to 3000 nm in sub-centimeter lengths of soft-glass photonic crystal fibers', *Optics Express*, 14, 4928-4934, (2006).
- [2.59] J.T. Gopinath, H.F.M. Shen, H. Sotobayashi, and E.P. Ippen, 'Highly nonlinear bismuth-oxide fiber for smooth supercontinuum generation at 1.5  $\mu\text{m}$ ', *Journal of Lightwave Technology*, 23, 3591, (2005).
- [2.60] P. Petropoulos, H.E. Heidepriem, T. Kogure K. Furusawa, V. Finazzi, T.M. Monro, D.J. Richardson, 'A spliced and connectorized highly nonlinear and anomalously dispersive bismuth-oxide glass holey fiber', in *Conference on Lasers and Electro-Optics* (2004).
- [2.61] M.R.E. Lamont, B.L. Davies, D.Y. Choi, S. Madden, and B.J. Eggleton, 'Supercontinuum generation in dispersion engineered highly nonlinear ( $\gamma = 10 \text{ /W/m}$ )  $\text{As}_2\text{S}_3$  chalcogenide planar waveguide', *Optics Express*, 16, 14938-14944, (2008).
- [2.62] J. Hu, C.R. Menyuk, L.B. Shaw, J.S. Sanghera, and I.D. Aggarwal, 'Raman response function and supercontinuum generation in chalcogenide fiber', in *Conference on Lasers and Electro-Optics/Quantum Electronics and Laser Science Conference and Photonic Applications Systems Technologies*, OSA Technical Digest (CD), Optical Society of America, (2008), paper CMDD2.
- [2.63] D. Yeom, E.C. Mägi, M.R.E. Lamont, M.A.F. Roelens, L. Fu, and B.J. Eggleton, 'Low-threshold supercontinuum generation in highly nonlinear chalcogenide nanowires', *Optics Letters*, 33, 660-662, (2008).

- [2.64] F. Désévéday, G. Renversez, J. Troles, L. Brilland, P. Houizot, Q. Coulombier, F. Smektala, N. Traynor, and J.L. Adam, 'Te-As-Se glass microstructured optical fiber for the middle infrared', *Applied Optics*, 48, 3860-3865, (2009).
- [2.65] M. Hughes, W.J. Yang, and D. Hewak, 'Spectral broadening in femtosecond laser written waveguides in chalcogenide glass', *Journal of the Optical Society of America B*, 1370-1378, (2009).
- [2.66] J. Fatome, C. Fortier, T.N. Nguyen, T. Chartier, F. Smektala, K. Messaad, B. Kibler, S. Pitois, G. Gadret, C. Finot, J. Troles, F. Desevedavy, P. Houizot, G. Renversez, L. Brilland, and N. Traynor, 'Linear and nonlinear characterizations of chalcogenide photonic crystal fibers', *Journal of Lightwave Technology*, 27, 1707-1715, (2009).
- [2.67] D.J. Richardson, F. Poletti, J.Y.Y. Leong, X. Feng, H. Ebendorff Heidepreim, V. Finazzi, K.E. Frampton, S. Asimakis, R.C. Moore, J.C. Baggett, J.R. Hayes, M.N. Petrovich, M.L. Tse, R. Amezcua, J.H.V. Price, N.G.R. Broderick, P. Petropoulos and T.M. Monro, 'Advances in Microstructured Fiber Technology', *Proc. IEEE Fibres and Optical Passive Components*, 1-9, (2005).
- [2.68] E.F. Chillece, C.M.B. Cordeiro, L.C. Barbosa and C.H. Brito Cruz, 'Tellurite photonic crystal fiber made by a stack-and-draw technique', *Journal of Non-Crystalline Solids*, Vol. 352, Issues 32-35, 3423-3428, (2006).
- [2.69] L. Brilland, F. Smektala, G. Renversez, T. Chartier, J. Troles, T.N. Nguyen, N. Traynor and A. Monteville, 'Fabrication of complex structures of holey fibers in chalcogenide glass', *Optics Express*, Vol. 14, Issue 3, 1280-1285, (2006).
- [2.70] A. Wang, V. V. Ravi Kanth Kumar, Alan K. George, J. C. Knight and P.J. Russell, 'Extruded tellurite photonic crystal fibre', *Optics Express*, Vol. 11, No. 20, 2645, (2003).
- [2.71] Y.N. Zhang, K. Li, L.L. Wang, L.Y. Ren, W. Zhao, and R.C. Miao, 'Casting preforms for microstructured polymer optical fibre fabrication', *Optics Express*, Vol. 14, Issue 12, 5541-5547, (2006).
- [2.72] Q. Coulombier, L. Brilland, P. Houizot, T. Chartier, T.N. Nguyen, F. Smektala, G. Renversez, A. Monteville, D. Méchin, T. Pain, H. Orain, J.C. Sangleboeuf and J. Trolès, 'Casting method for producing low-loss chalcogenide microstructured optical fibers', *Optics Express*, Vol. 18, Issue 9, 9107-9112, (2010).

- [2.73] M.S. Liao, Xi. Yan, G.S. Qin, C. Chaudhari, T. Suzuki and Y. Ohishi, 'A highly non-linear tellurite microstructure fiber with multi-ring holes for supercontinuum generation', *Optics Express*, Vol. 17, Issue 18, 15481-15490, (2009).
- [2.74] M.S. Liao, C. Chaudhari, G.S. Qin, X. Yan, T. Suzuki and Y. Ohishi, 'Tellurite microstructure fibers with small hexagonal core for supercontinuum generation', *Optics Express*, Vol. 17, Issue 14, 12174-12182, (2009).
- [2.75] A. S. Webb, F. Poletti, D. J. Richardson, and J. K. Sahu, 'Suspended-core holey fiber for evanescent-field sensing', *Optical Engineering*, Vol. 46, 010503, (2007).
- [2.76] X. Feng, A.K. Mairaj, D.W. Hewak, and T.M. Monro, 'Nonsilica glasses for holey fibers', *Journal of Lightwave Technology*, Vol. 23, Issue 6, 2046 – 2054, (2005).
- [2.77] S.Q. Lou, H. Fang, T.Y. Guo and S.S. Jian, 'Investigation on the fabrication of photonic crystal fibre', *Chinese Physics Letters*, Vol.23, No.3, 860, (2006).
- [2.78] C. J. Voyce, A. D. Fitt, T. M. Monro, 'The mathematical modelling of rotating capillary tubes for holey-fibre manufacture', *Journal of Engineering Mathematics*, Vol. 60, No. 1, 69-87, (2008).
- [2.79] I. M. Griffiths and P. D. Howell, 'Mathematical modelling of non-axisymmetric capillary tube drawing', *Journal of Fluid Mechanics*, 605:181-206, (2008).
- [2.80] A. Zakery and S.R. Elliott, 'Optical nonlinearities in chalcogenide glasses and their applications', Springer-Verlag Berlin Heidelberg (2007).
- [2.81] J. Troles, Q. Coulombier, G. Canat, M. Duhant, W. Renard, P. Toupin, L. Calvez, G. Renversez, F. Smektala, M. El Amraoui, J. L. Adam, T. Chartier, D. Mechin, and L. Brilland, 'Low loss microstructured chalcogenide fibers for large non linear effects at 1995 nm', *Optics Express*, 18, 25, 26647-26654, (2010).
- [2.82] D.J. Richardson, F. Poletti, J.Y.Y. Leong, X. Feng, H. Ebendorff Heidepreim, V. Finazzi, K.E. Frampton, S. Asimakis, R.C. Moore, J.C. Baggett, J.R. Hayes, M.N. Petrovich, M.L. Tse, R. Amezcua, J.H.V. Price, N.G.R. Broderick, P. Petropoulos and T.M. Monro, 'Advances in microstructured fiber technology', *Proc. IEEE Fibres and Optical Passive Components*, 1-9, (2005).
- [2.83] J.S. Sanghera, L.B. Shaw, and I.D. Aggarwal, 'Chalcogenide glass-fiber-based mid-IR sources and applications', *IEEE Journal of Quantum Electronics*, Volume 15, Issue 1 114 –

119, (2009).

[3.1] H.L. Rowe, 'Infra-red transmitting optical fibres with potential use in medical diagnosis and treatment', PhD Thesis, (June 2008), University of Nottingham, UK.

[3.2] Z.G. Lian, 'Planar and fibre optical waveguides in chalcogenide glasses', PhD Thesis, (2009), University of Nottingham, UK.

[3.3] Z.G. Lian, Q.Q. Li, D. Furniss, T.M. Benson, A.B. Seddon, 'Solid microstructured chalcogenide glass optical fibers for the near- and mid-infrared spectral regions', *Photonics Technology Letters, IEEE*, 21, (24), 1804-1806, (2009).

[3.4] N. Prasad, 'Microwave assisted synthesis of chalcogenide glasses', PhD Thesis, (March 2009), University of Nottingham, UK.

[3.5] Rawson, H., *Glass science and technology, properties and applications of glass 3*. 1980: Elsevier Scientific publishing company.

[3.6] F. P. Incropera and Dewitt D. P., *Fundamentals of heat and mass transfer*, John Wiley & Sons, (2001).

[3.7] D. Furniss and A. B. Seddon, chapter 10: "Thermal analysis of inorganic compound glasses and glass-ceramics" in *principles and Applications of Thermal Analysis* Editor Paul Gabbott, Blackwells (2007).

[3.8] Undergraduate Individual Project Report, Faculty of Engineering, University of Nottingham UK, "Characterisation of microstructured infrared transmitting glass optical fibres", Hao Yan, Koh, Supervisor: Prof Angela Seddon (2009/11).

[4.1] Undergraduate Individual Project Report, Faculty of Engineering, University of Nottingham UK, "Mid-infrared glasses based on antimony-germanium-selenium: optical properties", Harriet Jackson, Supervisor: Prof Angela Seddon Seddon (2010/11).

[4.2] Undergraduate Individual Project Report, Faculty of Engineering, University of Nottingham UK, "Mid-infrared glasses on germanium-antimony-selenium: thermal properties", Woraphat Aphisawetkarn Supervisor: Prof Angela Seddon Seddon (2010/11).

[4.3] J.S. Sanghera, L.B. Shaw and I.D. Aggarwal, 'Applications of chalcogenide glass optical fibers', *Comptes Rendus Chimie*, Volume 5, Issue 12, Pages 873-883, (2003).

[4.4] J.S. Sanghera, L.B. Shaw, and I.D. Aggarwal, 'Chalcogenide glass-fiber-based mid-IR sources and applications', *IEEE Journal of Quantum Electronics*, Volume 15, Issue 1 114 –

119, (2009).

[4.5] J. Hu, C.R. Menyuk, L.B. Shaw, J.S. Sanghera, and I.D. Aggarwal, 'Maximizing the bandwidth of supercontinuum generation in  $\text{As}_2\text{Se}_3$  chalcogenide fibers', *Optics Express*, Vol. 18, Issue 7, 6722-6739, (2010).

[4.6] B.T. Kolomiets, 'Vitreous semiconductors', *Physica Status Solidi*, 7, 359, (1964).

[4.7] J.A. Savage, P.J. Webber and A.M. Pitt, 'An assessment of Ge-Sb-Se glasses as 8 to  $12\mu\text{m}$  infrared optical materials', *Journal of Materials Science*, 13, 859, (1978).

[4.8] A.R. Hilton, C.E. Jones and M. Brau, 'Nonoxide chalcogenide glasses as infrared optical materials', *Physics and Chemistry of Glasses* 7, 105, (1966).

[4.9] A. Giridhar, P.S.L. Narasimham and Sudha Mahadevan, 'Electrical properties of Ge-Sb-Se glasses', *Journal of Non-Crystalline Solids*, 37, 165-179, (1980).

[4.10] P.S.L. Narasimham, A. Giridhar and Sudha Mahadevan, 'Electrical conductivity studies on families of glasses of the Ge-Sb-Se system', *Journal of Non-Crystalline Solids*, 43, 365-378, (1981).

[4.11] A.N. Sreeram, A.K. Varshneya and D.R. Swiler, 'Molar volume and elastic properties of multicomponent chalcogenide glasses', *Journal of Non-Crystalline Solids*, 128, 294-306, (1991).

[4.12] U. Senapati and A. K. Varshneya, 'Configurational arrangements in chalcogenide glasses: a new perspective on Phillips' Constraint Theory', *Journal of Non-Crystalline Solids*, 185, 289-296, (1995).

[4.13] U. Senapati and A. K. Varshneya, 'Viscosity of chalcogenide glass-forming liquids: an anomaly in the 'Strong' and 'Fragile' classification', *Journal of Non-Crystalline Solids*, 197, 210-218, (1996).

[4.14] D.R. Goyal and A.S. Maan, 'Far-infrared absorption in amorphous  $\text{Sb}_{15}\text{Ge}_x\text{Se}_{85-x}$  glasses', *Journal of Non-Crystalline Solids*, 183, 182-185, (1994).

[4.15] A.R. Hilton, D.J. Hayes and M.D. Rechten, 'Infrared absorption of some high-purity chalcogenide glasses', *Journal of Non-Crystalline Solids*, 17, 319-338, (1975).

[4.16] R. A. Nyquist and R. O. Kagel, 'Hand book of infrared and raman spectra of inorganic compounds and organic salts', by Academic Press, Inc., 4, (1997).

[4.17] L. Petit, N. Carlie, H. Chen, S. Gaylord, J. Massera, G. Boudebs, J. Hu, A. Agarwal, L.

Kimerling and K. Richardson, 'Compositional dependence of the nonlinear refractive index of new germanium-based chalcogenide glasses', *Journal of Solid State Chemistry*, 182, 2756-2761, (2009).

[4.18] H.L. Ma, Y. Guimond, X.H. Zhang and J. Lucas, 'Ga-Ge-Sb-Se based glasses and influence of alkaline halide addition', *Journal of Non-Crystalline Solids*, 256&257, 165-169 (1999).

[4.19] Z.Y. Yang, W. Chen and L. Luo, 'Dy<sup>3+</sup>-doped Ge-Ga-Sb-Se glasses for 1.3 μm optical fiber amplifiers', *Journal of Non-Crystalline Solids*, Volume 351, Issues 30-32, 1, 2513-2518, (2005).

[4.20] W. Chung, H.S. Seo, B.J. Park, J.T. Ahn, and Y.G. Choi, 'Selenide optical fibre doped with Pr<sup>3+</sup> for U-band optical amplifier' *Electronics and Telecommunication Research Institute journal*, 27, 4, 411-417 (2005).

[4.21] L. Petit, N. Carlie, K. Richardson, A. Humeau, S. Cherukulappurath and G. Boudebs, 'Nonlinear optical properties of glasses in the system Ge/Ga-Sb-S/Se', *Optics Letters*, 31, 10, 1495 (2006).

[4.22] J. Fatome, C. Fortier, T.N. Nguyen, T. Chartier, F. Smektala, K. Messaad, B. Kibler, S. Pitois, G. Gadret, C. Finot, J. Troles, F. Desevedavy, P. Houizot, G. Renversez, L. Brilland and N. Traynor, 'Linear and nonlinear characterizations of chalcogenide photonic crystal fibres', *Journal of Lightwave Technology*, 27, 11, 1707 (2009).

[4.23] J. Troles, Y. Niu, C. Duverger-Arfulso, F. Smektala, L. Brilland, V. Nazabal, V. Moizan, F. Desevedavy and P. Houizot, 'Synthesis and characterization of chalcogenide glasses from the system Ga-Ge-Sb-S and preparation of a single-mode fiber at 1.55μm', *Materials Research Bulletin*, 43, 976-982 (2008).

[4.24] Z.G. Lian, Q.Q. Li, D. Furniss, T.M. Benson and A.B. Seddon, 'Solid microstructured chalcogenide glass optical fibers for the near- and mid-infrared spectral regions', *Photonics Technology Letters, IEEE*, 21, (24), 1804-1806 (2009).

[4.25] P. Klocek, M. Roth and R.D. Rock, 'Chalcogenide glass optical fibers and image bundles: Properties and Application', *Optical Engineering* 26 (2), 088-095 (1987).

[4.26] P. Klocek and L. Colombo, 'Index of refraction, dispersion, bandgap and light scattering in GeSe and GeSbSe glasses', *Journal of Non-Crystalline Solids*, 93, 1-16 (1987).

- [4.27] W. Chen, J. J. Cheng and G. R. Chen, 'Formation and properties of chalcogenide glasses in the  $\text{As}_2\text{Se}_3\text{-GeTe-CuI}$  system', *Journal of Non-Crystalline Solids* 221, 274 (1997).
- [4.28] W.A. King, A.G. Clare and W.C. Lacourse, 'Laboratory preparation of highly pure  $\text{As}_2\text{Se}_3$  glass', *Journal of Non-Crystalline Solids* 181, 231-237 (1995).
- [4.29] M. F. Churbanov, 'High-purity chalcogenide glasses as materials for fiber optics', *Journal of Non-Crystalline Solids* 184, 25 (1995).
- [4.30] A.M. Reitter, A.N. Sreeram, A.K. Varshneya and D.R. Swiler, 'Modified preparation procedure for laboratory melting of multicomponent chalcogenide glasses', *Journal of Non-Crystalline Solids* 139, 121-128 (1992).
- [4.31] D.S. Ma, P.S. Danielson and C.T. Moynihan, 'Bulk and impurity infrared-absorption in  $0.5\text{As}_2\text{Se}_3 - 0.5\text{GeSe}_2$  glass', *Journal of Non-Crystalline Solids* 37, 181-190 (1980).
- [4.32] P.J. Webber and J.A. Savage, 'Some physical properties of Ge-As-Se infrared optical glasses', *Journal of Non-Crystalline Solids* 20, 271-283 (1976).
- [4.33] Virendra N. Mahajan, 'Handbook of optics', New York : McGraw-Hill, (2010).
- [4.34] J.C. Phillips, 'Topology of covalent non-crystalline solids II: Medium-range order in chalcogenide alloys and A Si(Ge)', *Journal of Non-Crystalline Solids*, 44, 17 (1981).
- [4.35] M.F. Thorpe, 'Continuous deformations in random networks', *Journal of Non-Crystalline Solids*, 57, 335 (1983).
- [4.36] K. Tanaka, 'Layer structures in chalcogenide glasses', *Journal of Non-Crystalline Solids*, 103, 149 (1988).
- [4.37] A.K. Varshneya, A.N. Sreeram and D.R. Swiler, 'Configurational arrangements in chalcogenide glasses: A new perspective on Phillips' constraint theory', *Physics and Chemistry of Glasses* 34, 179 (1993).
- [4.38] R.A. Nyquist and R.O. Kagel, 'Hand book of infrared and raman spectra of inorganic compounds and organic Salts', Academic Press, Inc. (1997).
- [4.39] D. Furniss and A. B. Seddon, chapter 10: "Thermal analysis of inorganic compound glasses and glass-ceramics" in principles and Applications of Thermal Analysis Editor Paul Gabbott, Blackwells (2007).
- [4.40] H.L. Rowe, 'Infrared transmitting optical fibres with potential use in medical diagnosis and treatment', PhD Thesis, (June 2008), University of Nottingham, UK.

- [4.41] W.J. Pan, 'Development of hot embossing for fabricating optical waveguides based on chalcogenide glasses', in *Electrical and Electronic Engineering*. 2008, University of Nottingham: Thesis, Nottingham.
- [4.42] Z.G. Lian, 'Planar and fibre optical waveguides in chalcogenide glasses', PhD Thesis, (2009), University of Nottingham, UK.
- [4.43] H.E. Swanson, 'Standard X-ray diffraction powder patterns', *Natl. Bur. Stand. (U.S.) Monogr.* 25, volume 3, page 7 (1964)
- [5.1] H.L. Rowe, 'Infrared transmitting optical fibres with potential use in medical diagnosis and treatment', PhD Thesis, (June 2008), University of Nottingham, UK.
- [5.2] Z.G. Lian, 'Planar and fibre optical waveguides in chalcogenide glasses', PhD Thesis, (2009), University of Nottingham, UK.
- [5.3] Z.G. Lian, Q.Q. Li, D. Furniss, T.M. Benson, A.B. Seddon, 'Solid microstructured chalcogenide glass optical fibers for the near- and mid-infrared spectral regions', *Photonics Technology Letters, IEEE*, 21, (24), 1804-1806, (2009).
- [5.4] Y.N. Zhang, K. Li, L.L. Wang, L.Y. Ren, W. Zhao, and R.C. Miao, 'Casting preforms for microstructured polymer optical fibre fabrication', *Optics Express*, Vol. 14, Issue 12, 5541-5547, (2006).
- [5.5] A. Wang, V. V. Ravi K. Kumar, A.K. George, J.C. Knight and P. St. J. Russell, 'Extruded tellurite photonic crystal fibre', *Optics Express*, Vol. 11, No. 20, 2645, (2003).
- [5.6] Q. Coulombier, L. Brilland, P. Houizot, T. Chartier, T.N.N'Guyen, F. Smektala, G. Renversez, A. Monteville, D. Méchin, T. Pain, H. Orain, J.C. Sangleboeuf and J. Trolès, 'Casting method for producing low-loss chalcogenide microstructured optical fibers', *Optics Express*, Vol. 18, Issue 9, 9107-9112, (2010).
- [5.7] W.J. Pan, 'Development of hot embossing for fabricating optical waveguides based on chalcogenide glasses', in *Electrical and Electronic Engineering*. 2008, University of Nottingham: PhD Thesis, Nottingham.
- [5.8] Undergraduate Individual Project Report, Faculty of Engineering, University of Nottingham UK, "Etching infrared-transmitting fibreoptic preforms", Cassandra Woodhouse, Supervisor: Prof Angela Seddon (2009/10)
- [5.9] Summer Research Placement Report, Faculty of Engineering, University of Nottingham

UK, “The development of a fibre optical sensor functioning in the mid-infrared region: propylamine etching”, Johanna Ernst, Supervisor: Prof Angela Seddon (2011).

[5.10] P. Lucas, A.A. Wilhelm, M. Videa and C.B. Plédel, B. Bureau, ‘Chemical stability of chalcogenide infrared glass fibers’, Corrosion Science, 50, 7, 2047 – 2052 (2008).

## Appendix I

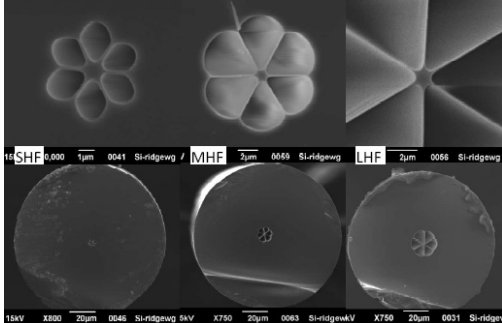
**Table A (i) Ge-Sb-Se glass system**

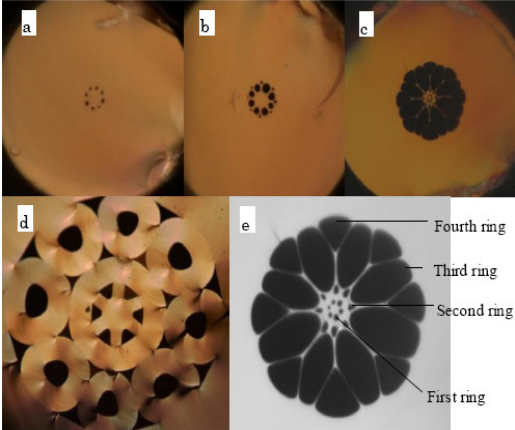
Ge	Sb	Se	Addition		T <sub>g</sub> (°C)	T <sub>x</sub> (°C)	T <sub>x</sub> - T <sub>g</sub> (°C)	n (wavelength / μm)	Softening point °C	Thermal expansion coefficient $\frac{\Delta L}{L C} \times 10^{-6}$	Density (kg m <sup>-3</sup> x 10 <sup>-3</sup> )	Reference
			Ga	CsI (Wt.%)								
5	25	65	5		186	315	129					[2.16]
10	10	80			121	285	164			28.2	4.61	[2.18]
10	15	75			143							[2.19]
10	20	70			159	286	127			20.5	4.90	[2.18]
10	25	65			192	312	120			18.4	5.04	[2.18]
12	10	70	8		186	316	130					[2.16]
13	7	80			151			2.64 (1.064)			4.37	[2.22]
15	5	80			138	-				26.5	4.48	[2.18]
15	10	75			159	459	300			19.2	4.62	[2.18]
15	15	60	10		274	383	109					[2.16]
15	15	70			183	466	283			20.1		[2.18]
15	15	70			182							[2.19]
15	20	60	5		253							[2.16]
15	25	60			232	336	104				5.04	[2.18]
16	14	70			214			2.68(1.064)			4.69	[2.22]
20	5	65	10		316	440	124					[2.16]
20	5	75			186					24.91	4.5	[2.18]
20	5	75			190							[2.19]
20	10	70			215	521	306			20.2	4.6	[2.18]
20	15	65			264	425	161			16.8	4.7	[2.18]
20	15	65			252							[2.19]
20	20	60			248	383	135			15.4	4.9	[2.18]
20.84	15	64.16			265							[2.19]
23	7	70			246			2.62(1.064)			4.55	[2.22]
25	5	65	5		331	483	152					[2.16]
25	5	65	5	5	319	490	171					[2.16]

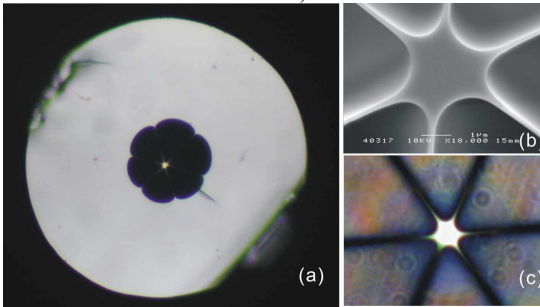
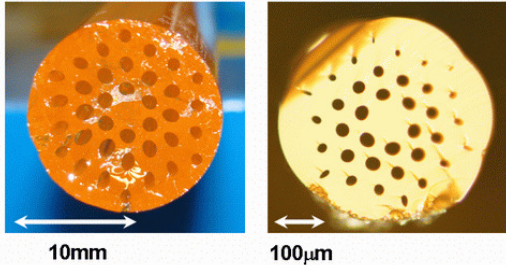
Ge	Sb	Se	Addition		T <sub>g</sub> (°C)	T <sub>x</sub> (°C)	T <sub>x</sub> - T <sub>g</sub> (°C)	n (wavelength / μm)	Softening point °C	Thermal expansion coefficient $\frac{\Delta L}{L^\circ C} \times 10^{-6}$	Density (kg m <sup>-3</sup> x 10 <sup>-3</sup> )	Reference
			Ga	CsI (Wt.%)								
25	5	65	5	10	316	478	162					[2.16]
25	5	65	5	20	292	460	168					[2.16]
25	5	65	5	30	271	395	124					[2.16]
25	5	70			248					18.5	4.46	[2.18]
25	8	62	5		301	461	160					[2.16]
25	5	70			242							[2.19]
25	10	60	5		283			2.6709 ± 0.0001(2) 2.6198 ± 0.00025 (12) 2.628(10.6)		155 ± 5 × 10 <sup>-7</sup> ( K <sup>-7</sup> )		[2.16,2.20]
25	10	65			308	415	107			15.55	4.51	[2.18]
25	12	55	8		275	387	112					[2.16]
25	15	60			268	521	253			14.7	4.75	[2.18]
25	15	60			242							[2.19]
28	5	60	7		288	459	171					[2.16]
28	7	60	5		288	448	160					[2.16]
28	7	65			287			2.59 (1.064)			4.61	[2.22]
28	12	60			277	522	245			13.79	4.68	[2.18]
28	12	60						2.62 (5) 2.6163 (3)	326	15		[2.12,2.13]
28	15	57			223							[2.19]
29.17	5	65.83			308							[2.19]
30	8	60	2		290	477	187	2.615 (1.5) 2.61(1.6)				[2.21]
30	8	55	2	5(S)	294	478	184	2.587 (1.5) 2.58(1.6)				[2.21]
30	10	60			287	410	123			14.7	4.62	[2.18]
32	5	63			300							[2.19]
35	5	60			311	432	121			12.6	4.51	[2.18]
35	5	60			293							[2.19]
35	7	58			299			2.58 (1.064)			5.00	[2.22]

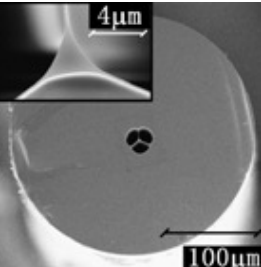
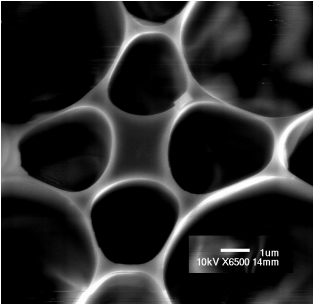
## Appendix II

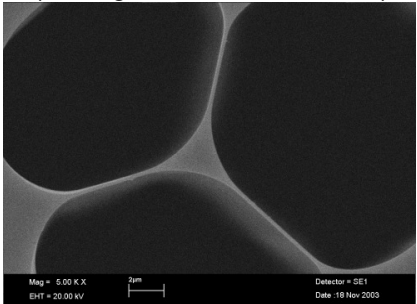
**Table A(ii) Supercontinuum Generation in Novel Glasses**

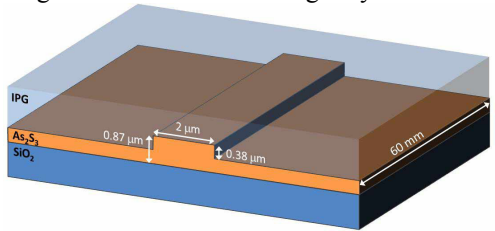
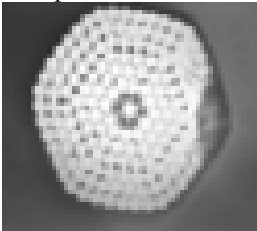
	Material of PCF	Structure of PCF	Range of SC / $\mu\text{m}$	ZDW of PCF/ $\mu\text{m}$	Pumping $\lambda$ / $\mu\text{m}$	Pump pulse duration /fs	Laser used	Length of PCF /mm	reference
1	76.5TeO <sub>2</sub> -6Bi <sub>2</sub> O <sub>3</sub> -6ZnO-11.5Li <sub>2</sub> O	<p>1<math>\mu\text{m}</math> hexagonal core, 120<math>\mu\text{m}</math> of OD, three types of MOF with different diameter ratio of hole region to core are 3.5, 10 and 20 (pump pressures were 1.6 kPa, 4.3 kPa and 7.8 kPa respectively)</p> 	0.519 to 2.4 (LHF)	0.876 and 1.606 (LHF)	1.557	400	femtosecond fiber laser, 573 pJ pulse	60	[2.53] 2009

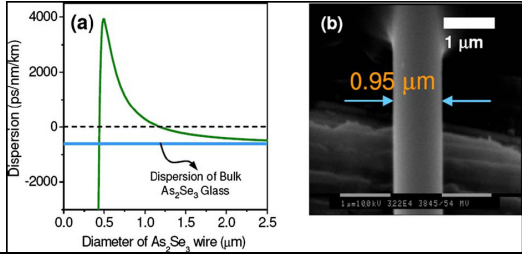
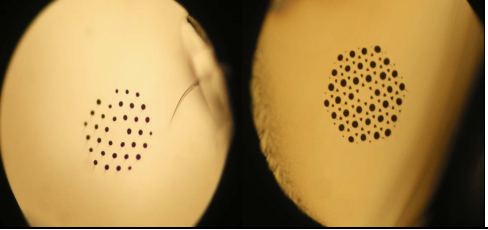
	Material of PCF	Structure of PCF	Range of SC / $\mu\text{m}$	ZDW of PCF/ $\mu\text{m}$	Pumping $\lambda$ / $\mu\text{m}$	Pump pulse duration /fs	Laser used	Length of PCF /mm	reference
2	76.5TeO <sub>2</sub> -6Bi <sub>2</sub> O <sub>3</sub> -6ZnO-11.5Li <sub>2</sub> O	<p>1.8<math>\mu\text{m}</math> core surrounded by four ring holes</p>  <p>Fig. 1. The cross-sections of the fibers drawn under different pump pressures and the final cane: a. 2.8 kPa, b. 3.6 kPa, c. 8.5 kPa; d. final cane, e. 8.5 kPa. Inset a-d were taken by an optical microscope. Inset e was taken by a scanning electron microscope.</p>	0.9 to 2.4	1.39	1.557	400	femtosecond fiber laser, 394 pJ pulse	300	[2.54] 2009

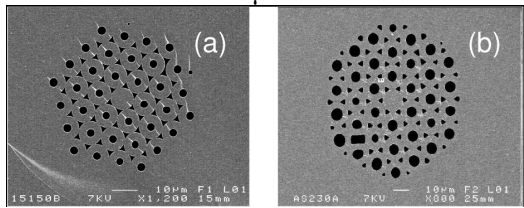
	Material of PCF	Structure of PCF	Range of SC / $\mu\text{m}$	ZDW of PCF/ $\mu\text{m}$	Pumping $\lambda$ / $\mu\text{m}$	Pump pulse duration /fs	Laser used	Length of PCF /mm	reference
3	75 TeO <sub>2</sub> -12ZnO- 5PbO-3PbF <sub>2</sub> - 5Nb <sub>2</sub> O <sub>5</sub>	<p>120<math>\mu\text{m}</math> OD, six fine filaments 16<math>\mu\text{m}</math> long and 120 nm wide, 2.5 <math>\mu\text{m}</math> diameter core, effective mode area is 1.7<math>\mu\text{m}^2</math> (preform is fabricated using extrusion process from a bulk Te glass billet, jacketed in an extruded tube made in the same fashion)</p> 	789 nm to 4870 nm (power of 90 mW)	1380 nm	1.55 $\mu\text{m}$	100fs	Ti:sapphire laser, pulse power 1.9 nJ	8 mm	[2.55] Knight 2008
4	75 TeO <sub>2</sub> -20ZnO- 5Na <sub>2</sub> O (n of 2.0 at 1.55 $\mu\text{m}$ )	<p>410<math>\mu\text{m}</math> OD, 80<math>\mu\text{m}</math> core diameter, mode area of 3000<math>\mu\text{m}^2</math>, hole spacing <math>\Lambda</math> of 53<math>\mu\text{m}</math>, d1=28.1<math>\mu\text{m}</math>, d2=23.3<math>\mu\text{m}</math>, to d3=13.8<math>\mu\text{m}</math></p> 	0.9 $\mu\text{m}$ to 2.5 $\mu\text{m}$ (power of 6 mW)	2.15 $\mu\text{m}$	2.15 $\mu\text{m}$	120 fs	Power of 15.2 mW, i.e., 15.2 $\mu\text{J}$ per pulse	9 cm	[2.56] Richardson 2008

	Material of PCF	Structure of PCF	Range of SC / $\mu\text{m}$	ZDW of PCF/ $\mu\text{m}$	Pumping $\lambda$ / $\mu\text{m}$	Pump pulse duration /fs	Laser used	Length of PCF /mm	reference
5	75 TeO <sub>2</sub> -20ZnO-5 Na <sub>2</sub> O	<p>250<math>\mu\text{m}</math> of OD, triangular core diameter of 2.7<math>\mu\text{m}</math>, held by three struts 7.4 <math>\pm</math> 0.2<math>\mu\text{m}</math> long and 180 <math>\pm</math> 20 nm thick</p> 	1.4 $\mu\text{m}$ to 2.5 $\mu\text{m}$ (Power of 30mW)	1.4 $\mu\text{m}$	1.56 $\mu\text{m}$		An OPO, pumped using a tunable Coherent Mira femto-second laser (~800 nm), Power 160 mW (2.1 nJ perpulse)		[2.57] 2006
6	Schott SF6 PCF	<p>by extrusion of a glass rod through a suitably shaped perform die, 2.6 micron core diameter</p> 	350 nm to beyond 3000 nm (power of 70 mW)	1300 nm	1550 nm	110 fs	optical parametric oscillator (OPO) laser source, power 1nJ,	5.7 mm	[2.58] 2006
7	Bismuth-oxide	<p>a core diameter of 1.7 <math>\mu\text{m}</math> and an effective area of 3.3 <math>\mu\text{m}^2</math> ( index of the core is 2.22, and that of the cladding 2.13 at 1550 nm)</p>	1200 nm to 1800 nm	> 1540 nm	1540 nm	150 fs	sub-0.5 nJ pulse energies	2 cm	[2.59] 2004

	Material of PCF	Structure of PCF	Range of SC / $\mu\text{m}$	ZDW of PCF/ $\mu\text{m}$	Pumping $\lambda$ / $\mu\text{m}$	Pump pulse duration /fs	Laser used	Length of PCF /mm	reference
8	Bismuth-oxide based glass	<p>small core is supported by three fine struts, each <math>\sim 5 \mu\text{m}</math> long, a core diameter of <math>2.0 \mu\text{m}</math></p> 		$< 1558 \text{ nm}$	1558 nm	$\sim 2.5 \text{ ps}$	a mode-locked erbium-fiber laser (300mW)	1.4 m	[2.60] 2003

	Material of PCF	Structure of PCF	Range of SC / $\mu\text{m}$	ZDW of PCF/ $\mu\text{m}$	Pumping $\lambda$ / $\mu\text{m}$	Pump pulse duration /fs	Laser used	Length of PCF /mm	reference
9	As <sub>2</sub> S <sub>3</sub>	<p>60 mm long with a cross-section of 2<math>\mu\text{m}</math> by 870 nm, A<sub>eff</sub> of 1.23<math>\mu\text{m}^2</math>, Using thermal evaporation, a 0.87<math>\mu\text{m}</math> layer of As<sub>2</sub>S<sub>3</sub> was deposited onto a thermally oxidized silicon substrate. The 2<math>\mu\text{m}</math> wide, 6.0 cm long waveguides were defined using photolithography and created using inductively coupled plasma reactive ion etching with CHF<sub>3</sub> gas to reduce the slab height by 380 nm</p> 	a 30 dB bandwidth of 750 nm	1510 nm (TM mode) TE mode in normal dispersion	1550 nm	610 fs	peak power of 68 W (60 pJ), ~0.6 mW of average power	60 mm	[2.61] CUDOS
10	As-Se based chalcogenide	<p>one ring of air holes with a core diameter of 10<math>\mu\text{m}</math> and a hole diameter to pitch ratio of 0.8</p> 	2.1 $\mu\text{m}$ to 3.2 $\mu\text{m}$	~3 $\mu\text{m}$	2.5 $\mu\text{m}$	100 fs	Ti:sapphire laser, pulse power 100 pJ	1 m	[2.62] Sanghera 2008

	Material of PCF	Structure of PCF	Range of SC / $\mu\text{m}$	ZDW of PCF/ $\mu\text{m}$	Pumping $\lambda$ / $\mu\text{m}$	Pump pulse duration /fs	Laser used	Length of PCF /mm	reference
11	$\text{As}_2\text{Se}_3$	<p>using a modified version of the standard flame brushing technique</p> 	500nm	Can be tuned to below 1550 nm	1550 nm	250 fs	7.8 W(2.2pJ)	30 mm	[2.63] CUDOS 2008
12	$\text{Te}_{20}\text{As}_{30}\text{Se}_{50}$	<p>A gallium metal coating is applied to inhibit cladding mode guidance. (<math>\Phi</math> fiber = <math>350\mu\text{m}</math>, <math>d=6\mu\text{m}</math>, <math>\Lambda=17\mu\text{m}</math>, and <math>d/\Lambda=0.35</math>). (<math>\Phi</math> fiber = <math>255\mu\text{m}</math>, <math>d=6.14\mu\text{m}</math>, and <math>\Lambda=13.77\mu\text{m}</math>). Single mode at <math>3.39\mu\text{m}</math> and <math>9.3\mu\text{m}</math> Control the temperature and pressure during fibre drawing</p> 	-	-	-	-	-	-	[2.64] France 2009
13	GLS 65% gallium sulphide, 30% lanthanum sulphide, and 5% lanthanum	-	-	-	1540 nm	200 fs	30 nJ/pulse	-	[2.65] 2008

	Material of PCF	Structure of PCF	Range of SC / $\mu\text{m}$	ZDW of PCF/ $\mu\text{m}$	Pumping $\lambda$ / $\mu\text{m}$	Pump pulse duration /fs	Laser used	Length of PCF /mm	reference
14	$\text{Ge}_{15}\text{Sb}_{20}\text{S}_{65}$ $\text{As}_{40}\text{Se}_{60}$	<p>Tubes around 12-mm OD, about 5-mm ID, and 12-cm length are obtained by the centrifugation, and finally drawn down to around 600<math>\mu\text{m}</math> OD. They were then stacked in a hexagonal lattice around a central rod of the same diameter and placed into a larger jacket tube, and drawn under positive pressure to 125<math>\mu\text{m}</math> OD.</p> <p><math>\text{Ge}_{15}\text{Sb}_{20}\text{S}_{65}</math>, <math>\Lambda=9\mu\text{m}</math>, and <math>d/\Lambda=0.31</math>, <math>A_{\text{eff}}</math> of 1.23<math>\mu\text{m}^2</math>.</p> <p><math>\text{As}_{40}\text{Se}_{60}</math>, <math>\Lambda=7\mu\text{m}</math>, and <math>d/\Lambda=0.42</math>, <math>A_{\text{eff}}</math> of 21<math>\mu\text{m}^2</math>.</p>  <p>(a) Cross section of GeSbS_2 PCF. (b) Cross section of AsSe PCF</p>	-	>1550 nm (D at 1550 nm are -421 and -760 ps/nm/km for GeSbS and AsSe)	-	-	-	-	[2.66] 2009